Shape estimation of a compliant wafer chuck in lithography systems

S.H.J. van der Kleij

Master of Science Thesis

TU Delft Delft University of Technology

Delft Center for Systems and Control
Precision and Microsystems Engineering

Shape estimation of a compliant wafer chuck in lithography systems

Master of Science Thesis
Delft University of Technology
Faculty of Mechanical, Maritime and Materials Engineering

Precision and Microsystems Engineering
Mechatronic System Design

Delft Center for Systems and Control
Systems and Control

November 24, 2014

Author: S.H.J. van der Kleij

Supervisors:
ir. J.G. Vogel
ir. R.I. Mustata
ir. J.W. Spronck
Prof. dr. ir. M.H.G. Verhaegen
Prof. ir. R.H. Munnig Schmidt

Abstract

The electronics industry aims at following Moore's law which states that the amount of transistors per unit area doubles every two years. To achieve this, the industry manufacturing Integrated Circuits (ICs) requires production technologies capable of producing smaller details. The machines capable of fulfilling these demands become more expensive and so does the cost per chip. This increase in cost is undesirable and a solution to this problem is to increase the production volumes per unit of time per machine.

The industry's approach to increase the production volumes is to increase the diameter of the wafer from 300 mm to 450 mm. The increase in size of some components in the lithography machines introduces a number of challenges to the position control of the wafer chuck in lithography machines. The main challenge is the positioning accuracy requirements of the wafer chuck with respect to the focal point of the projection optics. This is caused by the decreased stiffness of the wafer chuck, which induces undesirable deformations of the wafer resulting in decreased positioning accuracy of the chuck with respect to the focal point. Recently, two new algorithms for estimating the wafer and wafer chuck deformations have been developed that may help solve this problem.

The estimation algorithms rely on models to generate accurate estimates. In general the input, output, or both signals are not measurable. Therefore, it is not straight forward to apply system identification techniques to obtain a model. As alternative a model can be obtained from physical modeling. Both approaches are likely to result in a mathematical model with high uncertainties.

The effect of model uncertainty on one of the estimation algorithms is studied in this thesis. The model uncertainty is propagated through the algorithm to obtain a theoretical upper bound on the estimation error. The error bounds are also used to solve the constructed Least Squares (LS) problems using Robust Least Squares (RLS) algorithms where for a case study the estimation accuracy is analyzed and compared with the estimates obtained using Ordinary Least Squares (OLS). It is concluded that the usage of RLS algorithms together with the obtained error bounds increases the estimation quality under certain conditions.

Furthermore, to show that these algorithms work, experimental results are preferred over simulation results and therefore an experimental setup is designed. The setup will also be used to demonstrate the capabilities of the estimation algorithms under conditions that are topologically similar to those in a real lithography machine. Finally, the setup has been build and its performance is validated using measurements. From these measurements it is concluded that the setup's specification matches with the designed specifications.

Contents

Preface

In this preface I would like to look back at the great time I have spent at the TU Delft. It want to thank the TU Delft as organization for offering all the opportunities which I have so gratefully availed to expand my knowledge and to develop my character from a high-school student's to professional engineer's.

I started my studies with a Bachelor Mechanical Engineering at the TU Delft in 2007. Three years later I received my Bachelor of Science diploma Cum Laude.

In 2010 I started the Double Degree program by following both Masters Mechatronic System Design (MSD) and Systems and Control (S&C). MSD offers a practical approach to modern high-tech problems whereas S&C offers an academic approach to many of the same problems. By following both programs I learned to address problems from very different angles which is very helpful when seeking simple but powerful solutions.

After finishing all courses of the Master programs, I devoted one year to build, together with many fellow students, a four-wheel driven electric race care which was among the fastest accelerating electric vehicles in the world at that time. With that car we beat over a 100 other teams and by doing so we earned the "overall electric first place award" at the competition in Germany.

In 2013 I started with this final graduation project and I am very happy to present you this thesis. The graduation project is part of a large joint project between MSD and S&C, which as such provided me with a perfect framework that has enabled me to add my contribution to science by means of this thesis.

Acknowledgments

First and foremost, I want to thank my daily supervisors Ruxandra Mustata and Johan Vogel for all their help they provided me with during this project. This includes the many needed brainstorm sessions, the time spent for reviewing this report and to point out ways to improved my reporting. And off course, also all the fun and educative discussions we had.

Secondly, I want to thank professors Rob Munnig Schmidt and Michel Verhaegen for their enthusiastic lectures and talks. They truly motivated me to learn as much as possible about their fields of research during my studies. Thanks to those talks I could happily sustained all the studying and all hard work required for finalizing my masters and this project.

I also want to thank Jo Spronck for sharing his valuable experience during my studies and this project. He never failed to provide me with a different angle of attack when I required one.

Without the five persons mentioned above, this graduation project would not have been possible!

I owe thanks to many other persons, and regret that only some of them can be named here.

I want to start with Rob Luttjeboer and the other lab management staff for all design advise regarding manufacturability and all their handy solutions to many of the practical problems I have encountered while building the setup.

Likewise, I want to thank Hans Drop and the other people from the workshop for all the help while manufacturing the designed setup and for taking the time to teach me how to use the machinery. They have provided me with a valuable piece of experience.

Also, my gratitude to the PhD students from both departments for their input on this project.

I also want to thank my colleagues and students participating in the 2nd year course 'mechatronics project', where I was teaching assistant for many years. I want to thank them for the understanding I gained while teaching the basic concepts of mechatronics and control. In addition I want to thank them for all inspiring talks and the enjoyable time I had while assisting this project.

Then, I want to thank the seven project groups of first year students I have guided. I hope I guided them through a good first year and start of their studies at the TU Delft. I want to thank them for letting me experience the guiding of such groups, and for judging and steering their group-process.

And last but not least, I want to thank all my fellow students for all educative discussions, well needed coffee and lunch breaks. Without them the learning experience would not have been this great.

Executive summary

Research background (§1)

The electronics industry aims at following Moore's law which states that the amount of transistors per unit area doubles every two years. To achieve this, the industry manufacturing Integrated Circuits (ICs) requires production technology capable of producing smaller details. Lithography is the key step in determining the achievable resolution.

The lithography machines capable of fulfilling these demands become more expensive and so does the cost per chip. This increase in cost is undesired and a solution to lower the cost is to increase the production volumes per unit of time per machine. The industry's approach to reduce the cost is to increase the diameter of the wafer from 300mm to 450mm.

To handle the larger wafer, the wafer chuck in lithography machines needs to be scaled up. Due to the increased size, the weight of the wafer chuck will significantly increase when its stiffness is retained. A consequence of the increase in weight is the increased load on the actuators. This in turn results in additional heat production which is unwanted.

Therefore, there is a desire to lower the wafer chuck's weight at the cost of decreasing its stiffness. Because of the reduced stiffness, disturbances acting on the wafer chuck cause it to deform, resulting in a focal error. This focal error is significant and consumes about 10% of the focus error budget in current technology and will increase significantly when scaling up to 450mm wafer technology.

Means of actuation to compensate for the chuck deformations are present. However, compensation is only possible when the shape of the chuck is known. Measuring at the location of interest on the wafer is difficult. Currently research is being conducted at the TU Delft aiming at the development of algorithms that can estimate the shape of the wafer chuck.

Estimation algorithms (§2)

At the TU Delft two estimation algorithms are being developed. One method does shape estimation, the other estimates unknown inputs.

Shape estimation is performed by computing a linear estimator that is used to estimate the shape of the body while using a limited number of sensors. In literature, the linear estimator is often computed based on a set of fitting shapes. The new algorithms computed this estimator in an optimal manner such that the estimation error is minimized at all coordinates simultaneously. Therefore, its performance is equal or better then excising methods that use a linear estimator. This method is especially suitable when the shape of the body varies in a static manner i.e. below the first eigenfrequency of the body.

The second method is governed by the idea that the deformations are caused by disturbances. The disturbances can be considered unknown inputs of the system. When a model is available that relates these unknown inputs with measurements, then these inputs can be estimated. This method is called Receding Horizon Input (RHI) estimation and provides an effective way of doing this. Once an estimate of the unknown inputs is obtained, then these can be used to estimate the deformations. This method can also handle cases where the shape varies in a dynamic manner.

Uncertainty propagation (§3)

In order to compute an estimate of the unknown input or shape of the chuck, the estimation algorithms require a model that relates measurements to inputs or deformations. Obtaining accurate models using system identification techniques is not trivial because the inputs and/or outputs are not measurable and need therefore estimation. Because of this it is likely that the models are erroneous.

Therefore, the effect of model uncertainty on the RHI estimator is studied. The same methodology can also be applied to the shape fitting algorithm. A study is performed to see whether knowledge about the size of the model error can be propagated in order to obtain an upper bound on the resulting estimation error.

From the study it is concluded that Markov parameters provide a suitable means to study model errors. Markov Parameters are unique as opposed to state space matrices. Therefore, the difference between Markov parameters of different candidate models provide a measure of the model uncertainty. This is a contribution of this thesis.

Another contribution is that, where required, a method has been derived to construct the RHI estimator solely using Markov parameters. This is useful for propagating uncertainty of the Markov parameters through the RHI estimator.

It is shown that propagating the uncertainty on the Markov parameters result in a conservative upper-bound of the estimation error. It has been attempted to apply regularization to reduce the conservativeness which resulted in a very large estimation bias.

Inspired by the results and conclusions a different method is proposed that does compute a realistic upper bound on the estimation error. This method has been extended to provide the uncertainty on the RHI estimator matrices such that the required Least Squares (LS) problem, can be solved using Robust Least Squared (RLS).

Robust RHI estimation (§4)

Both estimations algorithms solve a LS problem and when the data used to construct this problem is erroneous the estimates will also be erroneous. The topic of obtaining more robust estimates in such scenarios has been studied extensively in literature.

Literature provide a variety of different Robust Least Squares (RLS) methods. RLS methods attempt to reduce the variance of the solution at the cost of introducing a bias. Three RLS methods are applied on the RHI estimator, to evaluate whether its estimation performance can be improved, when the used model contains errors.

A case study is performed where the RHI estimator is applied to estimate unknown disturbance forces acting on a simplified wafer chuck. A finite element model of this simplified wafer chuck has been created and realistic modeling errors are assumed. Estimation results provided by the Ordinary Least Squares (OLS) and the RLS methods are mutually compared.

Based on this case study, it is concluded that the RLS methods provide better estimates, in both RMS and maximum error sense, when discontinuous signals are estimated while OLS performs better when continuous signals are estimated. Disturbance forces are typically Zero Mean White Noise (ZMWN) which is a highly discontinuous signal and for this case it is demonstrated that RLS methods reduces the estimation error significantly. The robustness of this performance increase has been studied by applying it to 100 different perturbed models. These results are presented and studied in Chapter 4.

The methodology of this case study can also be applied to the shape fitting algorithms that computes a linear estimator by means of solving a LS problem.

Setup design (§5)

To validate the theory behind the estimation algorithms, experimental results are preferred over simulation results and therefore an experimental setup is designed. The setup will also be used to demonstrate the capabilities of the estimation algorithms under conditions that are topologically similar to the conditions in a real lithography machine.

First, basic mounting principles and conditions in a lithography machine are studied to obtain an abstract concept design of the setup. The most important choices are to partially levitated chuck, to use low stiffness actuators and to mount the sensors on a separate metrology frame.

Floor vibration measurements have been performed at the location where the setup will be operated. These measurements provide an estimate of the expected measurement noise level. Furthermore, they are used to quantify the performance increase related to the conceptual choices. They show that the sensor noise levels is the largest remaining noise source.

Then, the detailed design decisions are presented. These are based on minimizing the sensor requirements to reduce the cost of the setup. The most important sub-system, the chuck, has been optimized for this goal.

Finally, the setup has been build and its performance is validated. The closed-loop sensitivity functions of the controlled DoFs are measured to validate the performance of the controller positioning the chuck. The magnitude of the deformations are measured as function of frequency. Finally, the noise level of the deformation measurement is determined and compared with the initial analysis where expected noise level has been computed.

Chapter 1

Introduction

1-1 Research background

The electronics industry aims at following *Moore's law* which states that the amount of transistors per unit area doubles every two years. As stipulated by [1] the industry uses this law as an assumption for determining their strategic roadmap for the next decade. Moore's law is based on an observation made by Intel co-founder Gordon E. Moore. In his paper [2], he described the trend he observed. Today Moore's law is being 'adjusted' to match the current speed at which the complexity of the Integrated Circuits (ICs) increases. For the interested reader, an extensive example of such an analysis can be found in [3].

To make this increase in complexity possible, production technologies must be created in order to manufacture the smaller details of the new ICs designs. One of the key production steps determining the achievable resolution is lithography. An example of a lithography machine is shown in Figure 1-1.

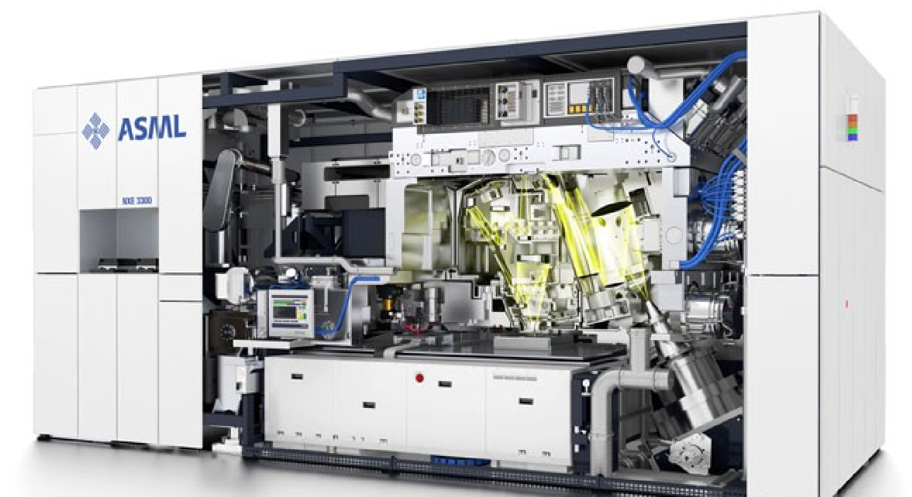

Figure 1-1: *Source: ASML. A waferscanner designed and build by ASML which is used to perform the lithography process step for manufacturing ICs.*

Lithography is a process in which a pattern is very precisely imaged on the wafer. A wafer is a round mono-crystalline silicon plate on which many ICs are manufactured. Each part of the wafer containing an IC, called a dice, is exposed separately. The exposure takes place during a scanning motion of the wafer. When a scan is complete the machine steps to the next dice. A chemical called photoresist is put on the wafer which undergoes a chemical reaction at the locations where it is exposed to the light enabling subsequent production steps e.g. deposition, etching or doping. It is very important that the wafer is perfectly positioned in the focal point of the projection optics. A much more detailed explanation of lithography machines can be found in [4].

Lithography machines are extremely complex and because of the desire to produce even smaller details they are becoming more complex. The increasing complexity also increases the cost of such a lithography machine and as a result the overall price per IC will increase. This is undesirable and research is being done to maintain or lower the price per manufactured IC. One of the options is to increase the throughput of the machine. One of the options considered by the industry is to increase the wafer size and this is the motivation for this research. Currently wafers have a diameter of 200mm or 300mm and current research focuses on increasing this to 450mm.

1-2 The need for estimation algorithms

There are many problems when modifying lithography machines to handle 450mm wafers. The problem studied in this thesis is illustrated in this section.

As is shown in Figure 1-2a, the wafer is placed on a wafer chuck. When the size of the wafer is increased, the size of the chuck needs to be increased such that the larger wafer fits on top of it. In order to maintain the stiffness of the larger chuck its thickness needs to be increased as well (Figure 1-2b). As a consequence the mass of the chuck increases and so does the load on the actuators positioning it. This in turn result in additional heat production which is unwanted.

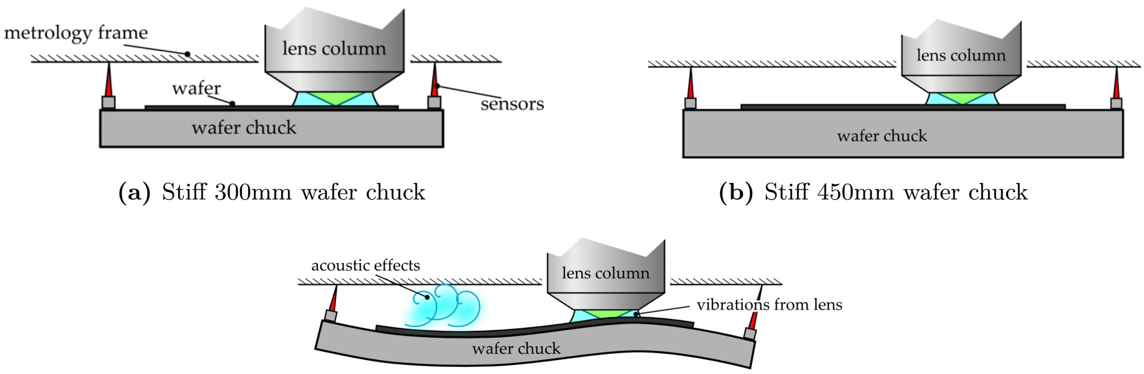

(a) Stiff 300mm wafer chuck

(b) Stiff 450mm wafer chuck

(c) Light 450mm wafer chuck

Figure 1-2: *Illustrations showing the problems related to increasing wafer size. The images are created by Vogel, J. G. in 2013.*

The mass of the chuck can simply be lowered by reducing its thickness. As a consequence, the stiffness is reduced which will lead to significant deformations due to all sorts of disturbances e.g. vibrations from the lens or evaporation of water from the water film in-between the lens and the chuck.

Parts of the wafer will not be in the focal point of the projection optics because of the deformations which is illustrated in Figure 1-2c. This is also undesirable as it will affect the achievable resolution. Currently focal errors due to wafer chuck flatness are in the order of 10nm which is significant and consumes about 10% of the focus error budget as described in [5]. When the wafer chucks are scaled up to 450 mm while reducing their stiffness, then this error will significantly increase making it difficult maintain or increase the resolution for future generation lithography machines.

However, if the disturbances or the shape of the wafer chuck are known, it is possible to compensate for these effects. Means of actuation such as repositioning the wafer chuck or adjusting the focal depth using the lens array, are available to compensate for the chucks deformations. However in order to compensate, the shape of the chuck must be known. Measuring at the location of the wafer is difficult because of all the equipment in and around the wafer chuck which is required to hold and illuminate the wafer.

Currently, research is being conducted at the TU Delft, aiming at the development of algorithms that can estimate the shape of the wafer chuck. The first algorithms is an optimal shape estimation algorithm (see [6]). It estimates the shape of the chuck using only measurements from the current time instant which is valid if the dynamics of the chuck are not of interest.

When the dynamics of the chuck are of interest, the shape can be estimated using an observer based approach such as Kalman filtering. However, the main reason for the chuck to deform is because of disturbance forces acting on the chuck. Such disturbance forces are typically not known and when they are committed as input to the observer, the shape will be poorly estimated. Therefore, the second algorithm that is being developed is an unknown input estimator (see [7]).

Both algorithms will be covered in this thesis. For an overview of their position in literature the reader is referred to respectively Subsection 2-1-1 and 2-2-3.

The estimation algorithms rely on an accurate model. Since the quantities of interest need to be estimated and cannot be measured, it might be difficult to obtain accurate models. Therefore, the available models are likely to have a relative large modeling error. In this thesis the effect of model errors on one the unknown input estimation algorithms is studied. The model error is propagated through the estimation algorithm and an upper bound on the estimated input is computed. Both estimation problems rely on solving a Least Squares (LS) problem. It is investigated whether the application of Robust Least Squares (RLS) can increase the performance of the unknown input estimator in the presence of model errors. The unknown input estimation algorithm is studied but the same methodology can be applied to the shape estimation algorithm.

Also, in this thesis a design for an experimental setup is presented. This setup can be used to test the algorithms under a wide variety of conditions. These experimental results will strengthen the work on the estimation algorithms. The setup also serves as demonstrator to show the capabilities of these algorithm in conditions topologically similar to those in a actual lithography machine.

1-3 Societal aspects

Each research has some form of societal impact. So does this work. A short impression of this impact is presented in this section. This report provides a small step in the overall research.

When the step towards 450 mm wafers can be made while maintaining the capabilities of the current lithography machines it allows for production of more advanced technology at the same cost.

In addition smaller electronics can be more efficient while the performance is maintained. This enables the creation of technology that is more sustainable while maintaining its capabilities.

Finally the current technology can also be produced more cost efficient which makes this technology accessible to less prosperous people in the world.

1-4 Research objectives

This thesis has two main objectives, both related to the performance of the estimation algorithms. The first is related to the performance of the estimation algorithms in the presence of model errors. It is investigated whether Robust Least Squares (RLS) can improve the estimation accuracy in these cases compared to Ordinary Least Squares (OLS). This study is limited to the unknown input estimator called Receding Horizon Input (RHI) estimation. Therefore, the first research objective of thesis is to answer:

"When performing RHI estimation, what will be the error bound on the estimated input in the presence of model errors? In addition, can this knowledge on the error bound in combination with RLS produce more accurate estimations compared to OLS? How does this performance difference relate to the overall estimation error introduced by model errors?"

The other objective is related to the performance of these algorithms in practice under conditions topologically similar to those in a lithography machine. Therefore, the second research objective is:

"To design and build a setup that serves both as experimental setup and as demonstrator setup on which both estimation algorithms can be applied, so that their practical performance can be evaluated and compared with simulation results."

1-5 Outline

First the ideas behind the two newly developed estimation algorithms in (see [6]) and (see [7]) are presented in Chapter 2. Then the theoretical model uncertainty bounds are propagated through the RHI estimator in Chapter 3. Several approaches are presented where one gives realistic sized upper-bounds on the estimation error. Then, by means of a case study, the effect of model errors on the RHI estimator accuracy is studied in Chapter 4. In addition the performance difference between using RLS and LS methods is studied. Finally the design of the experimental setup is presented in Chapter 5.

Chapter 2

Estimation algorithms

In this chapter, two recently developed shape estimation algorithms will be presented, such that it can be understood how they work and how they can be implemented. First, an algorithm for estimating unknown inputs is presented. Second, an algorithm for shape estimation using fitting shapes is treated. The summarized goal of this research is to improving the background of the estimation algorithms. Therefore, in this chapter a closer look is taken to these algorithms.

When the shape of a body needs to be determined one can apply shape estimation algorithms. Static and dynamic estimation can be distinguished. When the body is changing shape in a static manner then only the current measurements contain relevant information about the current shape. However, when the body changes shape in a dynamic manner, information about the past can contribute to improve the estimation of its shape.

In both cases, the estimation can be improved when information about the disturbances are known that case the body to change shape. These disturbances can be considered inputs of the system.

The first method covered in this chapter estimates the shapes based on a linear estimator. The contribution of this method is the way the linear estimator is computed. A overview of the work in [6] is presented in this chapter. Then the second method is covered. This method can be used to estimate unknown inputs. The method is called Receding Horizon Input (RHI) estimation and is originally presented in [7].

2-1 Static Shape estimation

Static shape estimation means that the shape of a body is estimated. The shape estimation methodology considered in this sections is a simple method that estimates the shape using a linear estimator. This method is suitable when the shape at the current time instant is unrelated to the shape at the previous time instant. If this condition is not met the estimation method presented in Section 2-2 might be of interest.

Shape estimation using a linear estimator is not new. In literature methods exist to compute the linear estimator based on fitting shapes. The contribution of the new work presented in [6] is a different, more optimal way, to compute the linear estimator.

First a short overview of shape fitting is provided, then the shape fitting methodology is covered and finally the new way of computing the linear estimator is presented.

2-1-1 Short overview on shape fitting

In this section a short overview of existing shape fitting methodology is provided. It positions the contribution of the work presented in [6] in the field

Often it is required to reconstruct unmeasured states. For dynamical systems this can be done using an observer such as a Kalman filter. When the state of the system varies low frequent, i.e. lower than the first eigenfrequency of the system, the states can be estimated using simpler, more intuitive methods.

One of the methods often used in literature is shape fitting. The idea of shape fitting is to estimate all Degrees of Freedom (DoF) of interest by means of only measuring a limited number of DoFs. The shape is reconstructed by fitting sensor data with fitting shapes. Fitting shapes are a set of orthogonal shapes of which it is assumed that a linear combination of these shapes can describe or estimate the shape of the body.

In contrast to Kalman filters, shape fitting can still give good results even if the input is unknown. It is possible however to incorporate knowledge about the input such as its location or size by choosing the fitting shapes carefully. This will result in better estimates since such fitting shapes will be better able to describe the shape of the body.

A limited number of measurements are used to determine the coefficients of the linear combination. For example when the out-of-plane deformations of a wafer chuck are measured at a few locations, the entire shape of the chuck can then be approximated by creating a linear combination of well chosen fitting shapes. In fact the linear estimator is thus computed based on the selected fitting shapes.

In literature a variety of possible fitting shapes can be found. [8] uses eigenmodes to reconstruct mechanical deformations based on strain measurements. However, when the dynamics of the system are not excited, these shapes will not be an optimal choice. [9] uses Proper Orthogonal Models (POMs) for estimating temperature profiles. POMs are computed based on a dataset and represent orthogonal shapes that are most apparent in the data. Depending on how the data is obtained, POMs can include information about inputs and disturbances resulting in a better estimation. In optics [10], Zernike modes are often used to reconstruct wavefronts.

The work in [6] presents a way of computing the linear estimator in an optimal way. The approach is similar when using POMS which computes the fitting shapes most apparent in the dataset and then forms a linear estimator based on these shapes. Based on such a dataset [6] computes the linear estimator directly such that it can best approximate the data in the dataset. This approach actually minimizes the estimation error instead of optimizing the selected fitting shapes.

In [6] it can be seen that the results obtained using this new linear estimator are usually generally or better then excising methods. The relevance of each fitting shape differs per considered DoF. The number of fitting shapes is limited by the number of sensors therefore, a trade-off must be made by selecting the shapes and the desired estimation accuracy of each DoF. This trade-off is avoided by directly computing the linear estimator from the dataset which explains the difference in performance.

2-1-2 Shape fitting methodology

In this section, the shape fitting methodology is explained and is based on [6].

When the shape of a bode is estimated using shape fitting, N_{fs} DoFs must be measured. The more DoFs are measured the better the estimate will be. Also N_{fs} fitting shapes must be selected that are linearly independent and can all be destination using measured DoFs. A fitting shape is denoted as s_j for $\forall j \in \mathbb{N}^+ \leq N_{\text{fs}}$.

Let N_{DoF} be the total number of considered DoFs then the matrix $S \in \mathbb{R}^{N_{\text{DoF}} \times N_{\text{fs}}}$ containing all the N_{fs} fitting shapes is defined as:

$$S = \begin{bmatrix} s_1 & \cdots & s_{N_{\text{fs}}} \end{bmatrix}.$$

Moreover, the matrix $S^{\text{meas}} \in \mathbb{R}^{N_{\text{DoF}}^{\text{meas}} \times N_{\text{fs}}}$ is defined, which contains a subset of the rows of matrix S, namely only the measured $N_{\text{DoF}}^{\text{meas}}$ DoFs, and is defined as:

$$S^{\text{meas}} = \begin{bmatrix} s_1^{\text{meas}} & \cdots & s_{N_{\text{fs}}}^{\text{meas}} \end{bmatrix}$$

Note that S^{meas}, is square since $N_{\text{fs}} = N_{\text{DoF}}^{\text{meas}}$ and invertible, since it is full column rank because of the selected shapes and sensor locations.

An estimate of the current shape $\hat{w}$ can be obtained by creating a linear combination of the fitting shapes as:

$$\hat{w} = Sa \tag{2-1}$$

where a is the vector of coefficients determining the linear combination of fitting shapes.

The linear combination depends on the measurements w and should fulfill $w = S^{\text{meas}}a$. Then a is determined as:

$$a = (S^{\text{meas}})^{-1}w$$

Substituting this in Eq. 2-1 results in:

$$\hat{w} = \underbrace{S(S^{\text{meas}})^{-1}}_{\mathcal{F}} w \tag{2-2}$$

where $\mathcal{F} \in \mathbb{R}^{N_{\text{DoF}} \times N_{\text{meas}}}$ is called the estimation matrix.

In this approach $\mathcal{F}$ is based on fitting shapes such as POMs or eigenmodes. However a linear combination of a set of shapes does not necessarily result in an optimal estimation. Some shapes could be of small significance for most DoFs, while they may be very important for a few other DoFs. Simply taking eigenmodes or POMs will therefore not result in an optimal estimation for every DoF.

Inspired by this insight [6] present a different method that computes an optimal estimation matrix $\mathcal{F}_{\text{opt}}$ that yields a minimal estimation error on DoFs.

2-1-3 Computation of an optimal estimation matrix

Inspired by the conclusion of the previous section, a method to construct an optimal estimation matrix $\mathcal{F}_{\text{opt}}$ that yields an optimal shape estimation was derived in [6]. In this section it is presented how $\mathcal{F}_{\text{opt}}$ is computed in [6].

This optimal estimation matrix is based on an initial dataset W^{true} containing data about all DoFs of interest (i.e. the measured ones and the ones that require estimation). This data can be obtained from simulations or from measurements.

Each shape w^{true} contained in the dataset W^{true} should be shapes that are typically expected when the estimation is applied. By using such a dataset more information about the expected shapes is included which results in a better estimation matrix.

Computing the optimal estimation matrix.

Let the estimation error w_e be defined as:

$$\underbrace{\begin{bmatrix} w_{e_1} \\ \vdots \\ w_{e_{N_{\text{DoF}}}} \end{bmatrix}}_{w_e} = \underbrace{\begin{bmatrix} w_1^{\text{true}} \\ \vdots \\ w_{N_{\text{DoF}}}^{\text{true}} \end{bmatrix}}_{w^{\text{true}}} - \underbrace{\begin{bmatrix} \hat{w}_1 \\ \vdots \\ \hat{w}_{N_{\text{DoF}}} \end{bmatrix}}_{\hat{w}}.$$

In addition let the dataset $W^{\text{true}} \in \mathbb{R}^{N_{DoF} \times i}$ with i shapes be of the form:

$$W^{\text{true}} = \begin{bmatrix} w^{\text{true}}(1) & \cdots & w^{\text{true}}(i) \end{bmatrix}.$$

Then the dataset $W^{\text{meas}} \in \mathbb{R}^{N_{DoF}^{meas} \times i}$ can be constructed by selecting the subset of rows from W^{true} that correspond to the measured DoFs. W^{meas} has the structure:

$$W^{\text{meas}} = \begin{bmatrix} w^{\text{meas}}(1) & \cdots & w^{\text{meas}}(i) \end{bmatrix}$$

Finally, by using these datasets the error set $W_e \in \mathbb{R}^{N_{DoF} \times i}$ can be defined as function of $\mathcal{F}_{\text{opt}}$ as:

$$W_e = W^{\text{true}} - \mathcal{F}_{\text{opt}} W^{\text{meas}}$$

In order to obtain an optimal estimation of the object, we seek to minimize every element of W_e. Let W_e^j denote every j^{th} row of W_e. Then one can formulate the minimization problem as minimizing $\left\| W_e^j \right\|_2^2$ for $\forall j \in \mathbb{N}^+ \leq N_{DoF}$. This can be done in a LS sense.

Also note that each j^{th} row in $\mathcal{F}_{\text{opt}}$ denoted as $\mathcal{F}_{\text{opt}}^j$, is responsible for the estimation quality of each element in W_e^j. Finally, let W_j^{true} denote the j^{th} row of W^{true}. Then the minimization problem can be formulated as:

$$\mathcal{F}_{\text{opt}}^j = \arg\min_{\mathcal{B}_{\text{opt}}^j} \left\| W_j^{\text{true}} - \mathcal{F}_{\text{opt}}^j W^{\text{meas}} \right\|_2^2 \tag{2-3}$$

The solution for one row j of $\mathcal{F}_{\text{opt}}$ is then given by: $\mathcal{F}_{\text{opt}}^j = W_j^{\text{true}} (W^{\text{meas}})^T [W^{\text{meas}} (W^{\text{meas}})^T]^{-1}$. From this, the solution for $\mathcal{F}_{\text{opt}}$ follows as:

$$\mathcal{F}_{\text{opt}} = W^{\text{true}} (W^{\text{meas}})^T \left(W^{\text{meas}} (W^{\text{meas}})^T \right)^{-1}$$

An important remark must be made. When estimating a variable using a linear estimate, the variable should be normally distributed. For linear systems this is the case if the inputs (e.g. disturbances) are normally distributed. When the variable is normally distributed an optimal estimator can be formulated as a linear estimator.

When the DoFs are for example uniformly distributed, a linear estimator is per definition not optimal. For this case a piece-wise linear estimator should be constructed. If in such a case, for simplicity, a linear estimator is used, the algorithm above still produces the most optimal estimator that can be formulated as a linear estimator but a more optimal estimator can be found as a piece-wise linear estimator.

2-2 Unknown input estimation

2-2-1 Necessity for unknown input estimation

In the previous section it has been seen how the shape of a body can be estimated in an optimal way when the disturbances acting on it are normally distributed. This method is suitable when the shape at the current time instance does not depend on the shape on the previous time instant.

If this condition is not met it a better approach can be thought of where the information about the past, which contains information about the present, is used. These are classic observer techniques.

If the system is not autonomous the output is often dominantly determined by the system inputs. If the inputs are known, then these can be taken into account very easily by the observer.

Almost always there are disturbances acting on a system. If the output needs to be estimated with a high accuracy, these disturbances should be taken into account. In many practical cases the disturbances cannot be measured (accurately) and can be considered unknown inputs (e.g. acoustic effects or thermal gradients). These inputs need to be estimated before the output can be estimated accurately using observer based techniques.

In this section an unknown inputs estimator called Receding Horizon Input (RHI) estimation is presented. The work in this section is based on the work presented in [7].

First the required notations are introduced, then a short overview of the state of the art about unknown input estimation is presented and finally the RHI estimator is presented.

2-2-2 Notations

In this section notations are introduced that are used throughout the thesis. Also ways to compute commonly used variables are provided so that this provides also a solid basis for implementing the methods presented in this chapter.

When a system is considered it is assumed that can be represented by a *state-space model* of order n of the form:

$$\tilde{x}(k+1) = A\tilde{x}(k) + Bu(k) + w(k) \tag{2-4a}$$
$$y(k) = C\tilde{x}(k) + Du(k) + v(k), \tag{2-4b}$$

where A, B, C, D are the state-space model system matrices, index k indicates the time instant, $\tilde{x}(k) \in \mathbb{R}^n$ is the state, $u(k) \in \mathbb{R}^m$ are inputs and $y(k) \in \mathbb{R}^\ell$ are the outputs. The process noise $w(k) \in \mathbb{R}^n$ and the measurement noise $v(k) \in \mathbb{R}^\ell$ are zero-mean noise sequences. The process noise is the result of unmodelled higher-order dynamics and non-linearities. The joint covariance matrix of the noise sequences is denoted as:

$$\mathcal{E}\left[\begin{bmatrix} w(k) \\ v(k) \end{bmatrix} \begin{bmatrix} w(k)^T & v(k)^T \end{bmatrix}\right] \triangleq \begin{bmatrix} \Sigma_w & \Sigma_{wv} \\ \Sigma_{wv}^T & \Sigma_v \end{bmatrix}.$$

When only the input output transfer is considered, a model of the form in Eq. 2-4 can be rewritten in the so called innovation form:

$$x(k+1) = Ax(k) + Bu(k) + Ke(k) \tag{2-5a}$$
$$y(k) = Cx(k) + Du(k) + e(k), \tag{2-5b}$$

where the state is given by $x(k) \in \mathbb{R}^n$, K denotes the *Kalman gain* and $e(k)$ represent a zero-mean white noise sequence. In this form it is possible to model colored measurement noise. The covariance matrix of the noise sequence $e(k)$, denoted as Σ_e, can be computed based on the noise properties of v and w and the system matrices as:

$$\Sigma_e = \Sigma_v + C\Sigma_x C^T. \tag{2-6}$$

The Kalman gain can be computed using:

$$K = \left(\Sigma_{wv} + A\Sigma_x C^T\right)\left(\Sigma_v + C\Sigma_x C^T\right)^{-1}. \tag{2-7}$$

In both Eq. 2-6 and Eq. 2-7 Σ_x denotes the covariance matrix of the state, which can be computed by solving the discrete time *Riccati equation*:

$$\Sigma_x = A\Sigma_x A^T + \Sigma_w - \left(\Sigma_{wv} + A\Sigma_x C^T\right)\left(\Sigma_v + C\Sigma_x C^T\right)^{-1}\left(\Sigma_{wv} + A\Sigma_x C^T\right)^T. \tag{2-8}$$

These last three equations are derived in [11].

2-2-3 Overview of input estimation algorithms

Before diving the details about how the RHI estimator works, the state of the art concerning unknown input estimation is studied. First the problem is approached from a basic point of view and the problem that then arises is pointed out. Then a short literature survey is provided to position the RHI estimator in the field.

A system in innovation form as denoted in Eq. 2-5 is considered. Let the unknown input be denoted by $u(k) \in \mathbb{R}^m$. Then, one can write the output of the innovation model down for a certain time interval of length s which results in:

$$\begin{bmatrix} y(k) \\ y(k+1) \\ y(k+2) \\ \vdots \\ y(k+s-1) \end{bmatrix} = \begin{bmatrix} C \\ CA \\ CA^2 \\ \vdots \\ CA^{s-1} \end{bmatrix} x(k) + \begin{bmatrix} D & 0 & 0 & \cdots & 0 \\ CB & D & 0 & \cdots & 0 \\ CAB & CB & D & \ddots & \vdots \\ \vdots & \vdots & \ddots & \ddots & 0 \\ CA^{s-2}B & CA^{s-3}B & \cdots & CE & D \end{bmatrix} \begin{bmatrix} u(k) \\ u(k+1) \\ u(k+2) \\ \vdots \\ u(k+s-1) \end{bmatrix}$$
$$+ \begin{bmatrix} I & 0 & 0 & \cdots & 0 \\ CK & I & 0 & \cdots & 0 \\ CAK & CK & I & \ddots & \vdots \\ \vdots & \vdots & \ddots & \ddots & 0 \\ CA^{s-2}K & CA^{s-3}K & \cdots & CK & I \end{bmatrix} \begin{bmatrix} e(k) \\ e(k+1) \\ e(k+2) \\ \vdots \\ e(k+s-1) \end{bmatrix}. \tag{2-9}$$

When comparing the number of equations and the number of unknowns it is easily seen that for many input-output size combinations the number of unknowns exceed the number of equations when estimating the initial state $x(k)$ and unknown inputs $[u(k)^T \cdots u(k+s-1)^T]^T$. Take for example the number of inputs m equal to the number of outputs ℓ. Then their will be $s \cdot \ell$ equations and $n + sm$ unknowns making the system of equations under-determined. This makes this approach not suitable for unknown input and state estimation. This is also described in [7].

Many attempts to overcome this problem have been done and are described in [7]. Sometimes the input is modeled using a random walk model [12], a predefined time-invariant dynamic model [13] or a constant input [14]. For such cases the state is augmented with the unknown input and a classical state estimation problem is solved to obtain an estimate of the augmented state. However the assumptions on the behavior of the input imposes large constraints on the estimates, making this approach only applicable for some systems. Another approach found in literature assumes the unknown input to be impulsive or of abrupt nature. These methods are observer based are recursive. However, they assume that no input has occurred prior to the time window limiting the practical usefulness. See e.g. [15]. In [16] another method for estimating inputs of abrupt nature is presented. Because the problem was under determined a sum-of-norms regularization term was used to force many inputs to zero. They may perform well if the sum-of-norms regularization is appropriately chosen. A third group of solutions perform simultaneous estimation of state and unknown input in a recursive manner [17]. The input can be any arbitrary sequence and no model for the unknown input is required. However, these methods do not allow regularization terms to be added when additional knowledge about the input is known.

Therefore, a new method for unknown input estimation was recently proposed in [7]. This method can handle, under mild conditions, any arbitrary sequence of inputs and is given in a receding-horizon formulation such that additional constraints can be imposed. The method is also suitable for real-time applications and is called Receding Horizon Input (RHI) estimation.

2-2-4 Receding horizon input estimation

In this section, the line of thought behind the unknown input estimator is presented and certain insight will used later in the thesis. All results in this section are based on [7], also the proofs can be found there.

Let a state-space model of the form in Eq. 2-5 be given. The unknown inputs $u(k) \in \mathbb{R}^m$ and known inputs $b(k) \in \mathbb{R}^g$ are separated. The state-space model can be denoted as:

$$\begin{aligned} x(k+1) &= Ax(k) + Bu(k) + Eb(k) + Ke(k) \\ y(k) &= Cx(k) + Du(k) + Gb(k) + e(k). \end{aligned}$$

A stationary Kalman Filter, which is unknown input free can be formulated. Let us define $\Phi = A - KC$ and $\tilde{E} = E - KG$, then a stationary Kalman Filter is given by:

$$\hat{x}(k+1) = \Phi\hat{x}(k) + \tilde{E}b(k) + Ky(k) \tag{2-11a}$$
$$\hat{y}(k) = C\hat{x}(k) + Gb(k). \tag{2-11b}$$

When the unknown inputs are non-zero, this estimates of this Kalman filter will be erroneous. The error dynamics are given by:

$$x_e(k+1) = \Phi x_e(k) + \tilde{B}u(k) \tag{2-12a}$$
$$r(k) = Cx_e(k) + Du(k) + e(k), \tag{2-12b}$$

where $\tilde{B} = B - KD$. Here $x_e(k)$ and $r(k)$ represent respectively the error state defined as $x_e(k) = x(k) - \hat{x}(k)$ and the output residual defined as $r(k) = y(k) - \hat{y}(k)$. Note that the error dynamics include the unknown input. The error is namely caused by neglecting the unknown input in the stationary unknown input free Kalman Filter.

Now, a time window of size L and ending at time instance k is selected, resulting in the time interval $[k - L + 1, k]$. The output residual over this time window is then given by:

$$\begin{aligned} \underbrace{\begin{bmatrix} r(k-L+1) \\ r(k-L+2) \\ r(k-L+3) \\ \vdots \\ r(k) \end{bmatrix}}_{r_{k,L}} &= \underbrace{\begin{bmatrix} C \\ C\Phi \\ C\Phi^2 \\ \vdots \\ C\Phi^{L-1} \end{bmatrix}}_{\mathcal{O}_L} x_e(k-L+1) \\ &+ \underbrace{\begin{bmatrix} D & 0 & 0 & \cdots & 0 \\ C\tilde{B} & D & 0 & \cdots & 0 \\ C\Phi\tilde{B} & C\tilde{B} & D & \cdots & 0 \\ \vdots & \vdots & \ddots & \ddots & \vdots \\ C\Phi^{L-2}\tilde{B} & C\Phi^{L-3}\tilde{B} & \cdots & C\tilde{B} & D \end{bmatrix}}_{\mathcal{T}_L} \underbrace{\begin{bmatrix} u(k-L+1) \\ u(k-L+2) \\ u(k-L+3) \\ \vdots \\ u(k) \end{bmatrix}}_{u_{k,L}} + \underbrace{\begin{bmatrix} e(k-L+1) \\ e(k-L+2) \\ e(k-L+3) \\ \vdots \\ e(k) \end{bmatrix}}_{e_{k,L}}. \end{aligned} \tag{2-13}$$

Eq. 2-13 can be considered a *data equation* and is denoted compactly as:

$$r_{k,L} = \mathcal{O}_L x_e(k-L+1) + \mathcal{T}_L u_{k,L} + e_{k,L}. \tag{2-14}$$

Now the time window of length L is partitioned in a past and a future time window with their respective sizes p and f, such that $p + f = L$. The future time window contains the most recent inputs. The partitioning is applied to the vectors and matrices in Eq. 2-14, which can then be written as:

$$r_{k,L} = \begin{bmatrix} r_{k-f,p} \\ r_{k,f} \end{bmatrix}, \quad u_{k,L} = \begin{bmatrix} u_{k-f,p} \\ u_{k,f} \end{bmatrix}, \quad e_{k,L} = \begin{bmatrix} e_{k-f,p} \\ e_{k,f} \end{bmatrix}, \quad \mathcal{O}_L = \begin{bmatrix} \mathcal{O}_p \\ \mathcal{O}_f\Phi^p \end{bmatrix}, \quad \mathcal{T}_L = \begin{bmatrix} \mathcal{T}_p & 0 \\ \mathcal{H}_{f,p} & \mathcal{T}_f \end{bmatrix}, \tag{2-15}$$

with $\mathcal{O}_p \in \mathbb{R}^{p\ell \times pn}$, $\mathcal{O}_f \in \mathbb{R}^{f\ell \times fn}$, $\mathcal{T}_p \in \mathbb{R}^{p\ell \times pm}$, $\mathcal{T}_f \in \mathbb{R}^{f\ell \times fm}$ and $\mathcal{H}_{f,p} \in \mathbb{R}^{f\ell \times pm}$.

Now let us define the transformation matrix:

$$T = \begin{bmatrix} I & 0 \\ -\mathcal{H}_{f,p}\mathcal{T}_p^{\dagger} & I \end{bmatrix},$$

where $(\cdot)^\dagger$ indicates the left pseudo inverse of a matrix, that is, for a matrix M such that $M^\dagger M = I$. By left multiplying Eq. 2-14 with T, the data equations Eq. 2-14 is transformed into:

$$\begin{bmatrix} \star \\ \bar{r}_{k,f} \end{bmatrix} = \begin{bmatrix} \star \\ \Gamma_f \end{bmatrix} x_e(k-L+1) + \begin{bmatrix} \mathcal{T}_p & 0 \\ 0 & \mathcal{T}_f \end{bmatrix} \begin{bmatrix} u_{k-f,p} \\ u_{k,f} \end{bmatrix} + \begin{bmatrix} \star \\ \bar{e}_{k,f} \end{bmatrix}, \tag{2-16}$$

where $\star$ indicates values of no direct interest, and where:

$$\begin{aligned} \bar{r}_{k,f} &= \begin{bmatrix} -\mathcal{H}_{f,p}\mathcal{T}_p^\dagger & I \end{bmatrix} r_{k,L}, \\ \Gamma_f &= \begin{bmatrix} -\mathcal{H}_{f,p}\mathcal{T}_p^\dagger & I \end{bmatrix} \mathcal{O}_L, \\ \bar{e}_{k,f} &= \begin{bmatrix} -\mathcal{H}_{f,p}\mathcal{T}_p^\dagger & I \end{bmatrix} e_{k,L}. \end{aligned} \tag{2-17}$$

When only the bottom line of the transformed data equation Eq. 2-16 is considered it reduces to:

$$\bar{r}_{k,f} = \Gamma_f x_e(k-L+1) + \mathcal{T}_f u_{k,f} + \bar{e}_{k,f}. \tag{2-18}$$

It is shown in [7] that when Φ is stable, and the transfer Ψ from r to u, is stable, the product $\Gamma_f x_e(k-L+1)$ will go to zero for $p \to \infty$. An expression for Ψ is given in Lemma 2 and Lemma 3 on on page 36. K should be chosen such that both matrices are simultaneously stabilized. When p is finite but sufficiently large, $\Gamma_f x_e(k-L+1)$ will be small and only a small error is introduced when it is neglected. With this result, Eq. 2-18 reduces to:

$$\bar{r}_{k,f} \simeq \mathcal{T}_f u_{k,f} + \bar{e}_{k,f}. \tag{2-19}$$

This equation can be solved for the unknown input vector using a Least Squares (LS) problem. The LS problem can be formulated to solve Eq. 2-19 for $u_{k,f}$ as:

$$\hat{u}_{k,f} = \arg\min_{u_{k,f}} \left\| \bar{r}_{k,f} - \mathcal{T}_f u_{k,f} \right\|_2^2. \tag{2-20}$$

When $\mathcal{T}_f$ is full column rank, the solution of Eq. 2-20 is given by:

$$\hat{u}_{k,f} = \left(\mathcal{T}_f^T \mathcal{T}_f \right)^{-1} \mathcal{T}_f^T \bar{r}_{k,f}. \tag{2-21}$$

It needs to be noted that the LS problem Eq. 2-20 can be solved without constraining the inputs when $m \leq \ell$. Furthermore it is possible to add constraints to the LS problem to incorporate prior knowledge on the input.

When the matrix D has no full column rank the current input $u(k)$ which is the last element of the vector $u_{k,f}$, cannot be estimated since insufficient data about this input is present in the output data. To be able to solve the LS problem Eq. 2-20, $\mathcal{T}_f$ should be made full column rank despite D not being full column rank.

This can be done by removing the first ℓ elements of $\bar{r}_{k,f}$ and the last m columns and the first ℓ rows of $\mathcal{T}_f$. Then by solving the LS problem as in Eq. 2-21 one obtains $\hat{u}_{k-1,f-1}$ instead of $\hat{u}_{k,f}$. This is the best that can be done since the current output contains no information about the current input.

Chapter 3

Propagating model uncertainty

A fundamental problem in applying estimation algorithms is that a model is required. When accurate estimates are desired naturally accurate models are required. On the other hand, in case the input, the output, or both can not be measured, it is not trivial to use System IDentification (SID) techniques since they required input/output data of the system.

An option to obtain an model is to use a different or modified setup such that the inputs and output can be measured. Another option is to use physical modeling. In both cases the obtained model will have a certain error.

In this chapter it is studied how the modeling error can be propagated through the Receding Horizon Input (RHI) estimator such that an upper-bound on the estimation error is obtained. The RHI estimator is chosen as a case study but the same methodology can be applied for the static shape estimator.

First, the estimation problem is formulated and the modeling errors will be introduced. Then, Markov parameters are introduced as an effective way to study model uncertainty. Then, it is discussed how the Markov parameters and their uncertainty can be obtained. Hereafter, it is shown how the RHI estimator can be constructed using Markov parameters only.

Finally, it will be presented how the uncertainty on the Markov parameters can be propagated such that an upper-bound on the estimation error is obtained. Different approaches are considered of which the last determines a realistic upper-bound on the estimation error.

3-1 Problem formulation

Both estimation algorithms discussed in Chapter 2 are based on solving the Least Squares (LS) problems Eq. 2-3 on page 21 and Eq. 2-20 on page 25 respectively. In the presence of modeling error an extension to this formulation is required which is presented in this section.

In the presence of modeling errors the LS problem denoted in Eq. 2-20 which for ease of the reader is repeated here,

$$\hat{u}_{k,f} = \arg\min_{u_{k,f}} \left\| \bar{r}_{k,f} - \mathcal{T}_f u_{k,f} \right\|_2^2 . \tag{3-1}$$

From now on to $\mathcal{T}_f$ and $\bar{r}_{k,f}$ is also referred to as respectively *LS data matrix* and *LS measurement vector*.

The matrix $\mathcal{T}_f$ is computed based on system matrices. When the model is uncertain, so is $\mathcal{T}_f$. The same is true for vector $\bar{r}_{k,f}$ which is computed based on measurements and system matrices. Clearly, $\mathcal{T}_f$ and $\bar{r}_{k,f}$ are uncertain so is the estimated input $\hat{u}_{k,f}$.

In order to denote the size of the uncertainty the operator $\delta(\cdot)$ is introduced which is formally defined in the following definition.

Definition. Operator $\delta(\cdot)$

The operator $\delta(\cdot)$ that gives an upper-bound on uncertainty on the elements of its operand. For example the uncertainty on the elements of matrix $M \in \mathbb{R}^{a\times b}$ is given by the elements of matrix $\delta(M) \in \mathbb{R}^{a\times b}$ such that the true value $M_{true} \in \mathbb{R}^{a\times b}$:

$$M_{true} \subseteq M \pm \delta(M).$$

$\delta(M)$ contains only positive elements. The true sign and size of the error on M is unknown.

In the prescience of model uncertainty, Eq. 3-1 becomes:

$$\hat{u}_{k,f} + \delta(\hat{u}_{k,f}) = \arg\min_{u_{k,f}} \left\| \Big(\bar{r}_{k,f} + \delta(\bar{r}_{k,f})\Big) - \Big(\mathcal{T}_f + \delta(\mathcal{T}_f)\Big) u_{k,f} \right\|_2^2. \tag{3-2}$$

The goal of this section is to compute $\delta(\hat{u}_{k,f})$ which represents an upper bound on the uncertainty on the estimated input. In addition $\delta(\mathcal{T}_f)$ and $\delta(\bar{r}_{k,f})$ are computed which are used to compute $\delta(\hat{u}_{k,f})$. In addition they can be used by solving Eq. 3-2 in a robust manner using Robust Least Squares (RLS) methods. They attempt to reduce the uncertainty at the cost of adding bias. The RLS methods and their performance will be investigated in Chapter 4.

3-2 Markov parameters and model uncertainty

Before proceeding with propagating the model uncertainty through the RHI estimator, first a way of studying this model uncertainty needs to be determined. A certain input/output transfer can be represented by an infinite number of state-space realizations. Therefore, it is difficult to compare different candidate state-space models.

In this section it will be proven that Markov parameters are invariant to the state-space realization of the system. In other words, they are unique. This makes them a suitable tool for studying model uncertainty since different candidate Markov parameters can be compared. Their difference provide a measure for the uncertainty.

The Markov parameters are defined as:

$$\begin{aligned}
\mathcal{B}_j &= \begin{bmatrix} C\Phi^{j-1}\tilde{B} & C\Phi^{j-2}\tilde{B} & \cdots & C\tilde{B} \end{bmatrix} \\
\mathcal{K}_j &= \begin{bmatrix} C\Phi^{j-1}K & C\Phi^{j-2}K & \cdots & CK \end{bmatrix} \\
D &= D,
\end{aligned}$$

where $j \in \mathbb{N}^+$. Each block element in $\mathcal{B}_j$ or $\mathcal{K}_j$ denotes a Markov parameter. D is also a Markov parameter.

In this section it will be proven that hey are unique and suitable methods to obtain a model and its uncertainty are discussed.

3-2-1 Uniqueness of Markov parameters

In order to prove that Markov parameters are unique, assume a transformation matrix T that transforms state x into state $q = Tx$. Then the transformed system matrices (denoted with subscript q) are given by:

$$A_q = TAT^{-1}, \quad B_q = TB, \quad C_q = CT^{-1}, \quad D_q = D, \quad K_q = TK.$$

Then the Markov parameters are given by:

$$\begin{aligned}
C_q\Phi_q^i\widetilde{B}_q &= C_q\left(A_q - K_qC_q\right)^i\left(B_q - K_qD_q\right) \\
&= CT^{-1}\left(TAT^{-1} - TKCT^{-1}\right)^i\left(TB - TKD\right) = CT^{-1}\left(T(A-KC)T^{-1}\right)^i T\left(B - KD\right) \\
&= CT^{-1}T(A-KC)^iT^{-1}T\left(B-KD\right) = C(A-KC)^i\left(B-KD\right) \\
&= C\Phi^i\widetilde{B}.
\end{aligned}$$

In addition we can conclude that $\Phi_q = T\Phi T^{-1}$ and $\widetilde{B}_q = T\widetilde{B}$. This will be used to simplify a proof presented later in this chapter.

From the latter proof it can be concluded that the Markov parameters are indeed unique. They are thus independent of the choice of state coordinates in a State Space model. This is a big advantage when analyzing model uncertainty. While it might be hard to compare two different realizations of slightly different state space models it is much easier to compare the Markov parameters since their difference gives an impression of the size of the modeling difference.

3-2-2 Obtaining a model and its uncertainty

Now we know how to compare multiple models. It is interesting to provide a small background on how to obtain a model and its associated uncertainty. When a model and its uncertainty are available, the uncertainty on the RHI estimator matrices can be computed. Two approaches are considered. The first approach is to obtain a model from SID experiments. The second approach is to obtain a model from physical modeling. Both approach are covered in this subsection.

System identification techniques

From an academic point of view, it is interesting to address the matter of obtaining a model starting from a SID experiment. From practical point of view, this experiment can be executed on, for example, a system that is modified such that both the inputs and outputs are measurable. The resulting model will however be perturbed because of measurement noise and process noise in combination with a limited number of samples.

In order to identify a model using SID techniques, first a suitable SID method must be selected. A very short summary of available techniques will given such that a suitable method can be selected.

Output-error vs subspace methods Typically, the model to be identified is first parametrized, that is, its structure is fixed within a class of models. Then, a cost function of the model parameters is formulated which is optimized using an optimization framework to obtain the model parameters. These approaches can be classified as *output-error parametric model estimation*. When the goal is to obtain the parameters of a parametrized predictor model or Kalman filter, they can be classified as *prediction-error parametric model estimation* which follows a very similar methodology as the output-error methods.

The system under consideration, a wafer chuck, is in general a Multiple-Input Multiple-Output (MIMO) system. In general, the output-error or prediction-error methods will result for MIMO systems in a cost-function that is non-convex (see e.g. [18]). This makes it hard to solve the formulated optimization problem efficiently.

Another class of SID methods are based on projecting data onto linear subspaces mainly by using LS [19]. These methods are called subspace identification methods and are much more suitable for estimating MIMO models because they do not rely on parametrization and optimization.

Since the considered system is clearly a MIMO systems the subspace identification methodology is selected.

Subspace identification techniques There are many subspace identification methods. In the past, mainly open-loop methods where developed. However, for many practical applications it was also desirable to perform the identification experiments under closed-loop conditions. For subspace identification this posed a challenge for many years but recently closed-loop algorithms have been developed, such as the Predictor Based Subspace IDentification (PBSID) method [18].

There are many open-loop methods. An overview can be found in [20] amoung which we mention the: Multivariable Output-Error State-sPace (MOESP), Numerical algorithm for Subspace IDentification (N4SID) and Canonical Variate Analysis (CVA) methods. Many of these algorithms show similarities and there are unifying theorems such as the one presented in [21].

Figure 3-1 shows a concise summary illustrating the different approach between the open and closed-loop methods. In essence the open-loop methods have in common that they compute a subspace matrix based on the input output data. The subspace matrix enjoys the property that it can be factorized in an extended observability matrix and another matrix whose properties depend on the selected method.

In contrast, the closed-loop method PBSID computes the Markov parameters. This makes PBSID an interesting option since we require the Markov parameters to study model uncertainty. When the Markov parameters are obtained directly less numerical operations are performed which makes the the results more traceable. Furthermore PBSID can be used in closed-loop scenarios making it more flexible. PBSID also provides means to compute the estimation uncertainty on the estimated Markov parameters. For the interested reader the working principles of PBSID is explained in more detail in Chapter A.

A remark must be made when using any SID technique to obtain a model. When the system is modified to make the inputs and outputs and outputs measurable that the system might be changed. The estimated model will correspond to this different system and as such the model might be biased. The estimation uncertainty obtained from PBSID will relate to the estimation uncertainty of the modified system and not the uncertainty with respect to the original unmodified system.

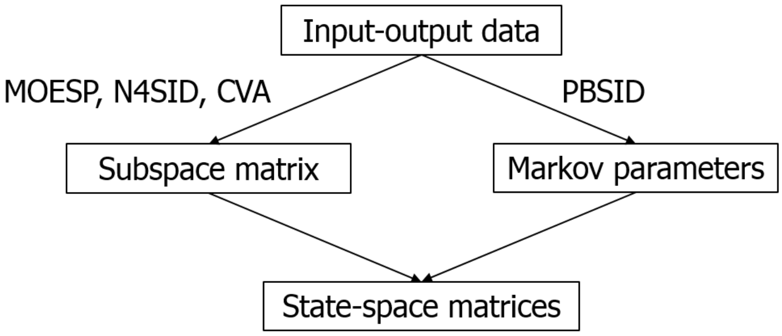

Figure 3-1: *A short overview of the fundamental difference between the mentioned different subspace methods.*

Physical modeling

We have seen that PBSID is a suitable SID method to obtain a model. There might be scenarios where performing a SID experiment is impossible or undesired. Then one can use physical modeling to obtain an estimate of the model.

One can write down all physical relations and solve the system of equations. Alternatively models can be discretized using finite elements. Such a model can (if required) be linearized and converted to a discrete time state-space model of the form Eq. 2-5. Then the Markov parameters can be computed based on the system matrices. This way one can acquire a model and the Markov parameters.

The next step is to get an estimate of the model uncertainty. Usually several parameters of the model are uncertain e.g. the density, the effective stiffness or the amount of damping. One can create several models for different, extreme choices, of these parameters. Then the largest difference between these Markov parameters and the expected Markov parameters give a measure of the uncertainty. This approach can be classified as a Monte Carlo approach.

3-2-3 Construct the RHI estimator using only Markov parameters

Now it is known that Markov parameters are an effective method to study model uncertainty. It has also been seen how models can be obtained and the corresponding Markov parameters. This includes also their uncertainty.

The next step is to propagate these uncertainties to the RHI estimator matrices. However, the RHI estimator requires system matrices for which we have discussed that it is difficult to obtain their uncertainty. Therefore, it is first analyzed how the RHI estimator can be formulated using Markov parameters only. Then the uncertainty of the Markov parameters can be propagated to the RHI estimator matrices. For ease of the reader we start by repeating the definitions of the most important variables.

Definitions

In Section 2-2 definitions for certain parameters have been introduced. The most important once are now repeated for ease.

First of all, a time window of size L is chosen, and later it is partitioned in a past time window of size p and a future time window of size f, such that $L = p + f$. Based on these time windows, in Eq. 2-13 on page 24 the matrix $\mathcal{T}_L$ is first defined and later in Eq. 2-15 on page 24 is partitioned as:

$$\mathcal{T}_L = \begin{bmatrix} \mathcal{T}_p & 0 \\ \mathcal{H}_{f,p} & \mathcal{T}_f \end{bmatrix} = \begin{bmatrix} D & 0 & 0 & \cdots & 0 \\ C\tilde{B} & D & 0 & \cdots & 0 \\ C\Phi\tilde{B} & C\tilde{B} & D & \cdots & 0 \\ \vdots & \vdots & \ddots & \ddots & \vdots \\ C\Phi^{L-2}\tilde{B} & C\Phi^{L-3}\tilde{B} & \cdots & C\tilde{B} & D \end{bmatrix}. \tag{3-3}$$

The parts of this partitioned matrix will be used later in this chapter.

Next, in Eq. 2-11 on page 24 the unknown input free Kalman filter is formulated and the output residual can be computed by evaluating:

$$\hat{x}(k+1) = \Phi\hat{x}(k) + \tilde{E}b(k) + Ky(k) \tag{3-4a}$$

$$\hat{y}(k) = C\hat{x}(k) + Gb(k) \tag{3-4b}$$

$$r(k) = y(k) - \hat{y}(k). \tag{3-4c}$$

Then the output residual over the time window L is denoted as $r_{k,L}$, and is partitioned as:

$$r_{k,L} = \begin{bmatrix} r_{k-f,p} \\ r_{k,f} \end{bmatrix}. \tag{3-5}$$

Next in Eq. 2-17 on page 25 the output residual is transformed as:

$$\bar{r}_{k,f} = \begin{bmatrix} -\mathcal{H}_{f,p}\mathcal{T}_p^{\dagger} & I \end{bmatrix} r_{k,L}, \tag{3-6}$$

where $(\cdot)^{\dagger}$ indicates the left pseudo inverse of a matrix, that is, for a matrix M such that $M^{\dagger}M = I$.

Finally, the RHI estimator is defined in Eq. 2-20 on page 25 as:

$$\hat{u}_{k,f} = \arg\min_{u_{k,f}} \left\| \bar{r}_{k,f} - \mathcal{T}_f u_{k,f} \right\|_2^2. \tag{3-7}$$

The RHI estimator effectively consists of two parts, matrix $\mathcal{T}_f$ and vector $\bar{r}_{k,f}$.

Constructing $\mathcal{T}_f$ from Markov parameters

As was seen in Eq. 3-7 , the RHI estimator effectively consists of two parts, matrix $\mathcal{T}_f$ and vector $\bar{r}_{k,f}$. The matrix $\mathcal{T}_f$ only consists of model information. By close inspection of Eq. 3-3 it can be seen that $\mathcal{T}_f$ only consists of Markov Parameters. Therefore, it can be constructed directly from the Markov parameters, together with its uncertainty $\delta(\mathcal{T}_f)$ based on the uncertainty on the Markov parameters denoted as $\delta(\mathcal{B}_f)$, $\delta(\mathcal{K}_f)$ and $\delta(D)$.

This also holds for $\mathcal{T}_p$, $\delta(\mathcal{T}_p)$, $\mathcal{H}_{f,p}$ and $\delta(\mathcal{H}_{f,p})$ defined in Eq. 3-3 which are intermediate results required for computing the vector $\bar{r}_{k,f}$ and $\delta(\bar{r}_{k,f})$.

Computing the output residual using Markov parameters

As has been seen, the matrix $\mathcal{T}_f$ and $\delta(\mathcal{T}_f)$ can be directly constructed from the Markov parameters. This is not the case for $\bar{r}_{k,f}$.

The vector $\bar{r}_{k,f}$ is computed in Eq. 3-6. In order to compute it, we require: $\mathcal{H}_{f,p}$, $\mathcal{T}_p$ and $r_{k,L}$. It has been seen that $\mathcal{H}_{f,p}$ and $\mathcal{T}_p$ can also be constructed by using solely Markov parameters. However, this is not the case for $r_{k,L}$. The vector $r_{k,L}$ can be computed by evaluating Eq. 3-4 recursively which requires the system matrices.

In this section a method is presented to compute $r_{k,L}$ also only based on the Markov Parameters, without requiring the actual system matrices. This method is later used to compute $\delta(\bar{r}_{k,f})$ based on the uncertainty on the Markov parameters.

The output residual can be obtained by recursively solving Eq. 3-4. The first h time instants can are written as:

$$\begin{aligned}
r(0) &= y(0) - Cx(0) - Gb(0) \\
r(1) &= y(1) - C\Phi x(0) - C\widetilde{E}b(0) - CKy(0) - Gb(1) \\
r(2) &= y(2) - C\Phi^2 x(0) - C\Phi\widetilde{E}b(0) - C\widetilde{B}u(1) - C\Phi Ky(0) - CKy(1) - Gb(2) \\
r(3) &= y(3) - C\Phi^3 x(0) - C\Phi^2\widetilde{E}b(0) - C\Phi\widetilde{B}u(1) - C\widetilde{B}u(2) - C\Phi^2 Ky(0) - C\Phi Ky(1) - CKy(2) - Gb(3) \\
&\vdots \\
r(h) &= y(h) - C\Phi^h x(0) - \sum_{j=0}^{h-1} C\Phi^j \widetilde{E}b(h-1-j) - \sum_{j=0}^{h-1} C\Phi^j Ky(h-1-j) - Gb(h).
\end{aligned}$$

This shows that $r(h)$ is dependent on the Markov parameters, input/output data and the term $C\Phi^h x(0)$. In order to compute $r(h)$ only in terms of Markov parameters this last term needs to be eliminated. For systems with a stable Φ, this can be done by selecting h large enough such that the term $C\Phi^h x(0)$ becomes small. The inputs and outputs data are known so they pose no problem.

Selecting the initial state. The expressions above assumes that the time instant of the initial state is equal to the time instant of the oldest computed output residual over the time window. When inputs and outputs from before this time instant are known, they can be used to express the equations in terms of an initial state before the time instant of this oldest computed output residual. Here it is assumed that these required inputs and outputs are known and the goal is to selected a suitable initial state.

With respect to the initial state, the output residual r can be considered over a time window in two ways, namely:

- from an initial state that is i steps before the oldest computed output residual in the time window;
- from an initial state that is i steps before each computed output residual in the time window.

Both methods can be used but both have clear advantages and disadvantages.

An advantage of the first option would be that: $||C\Phi^{i+j}x(0)||_F \backsimeq 0$ becomes a better approximation when increasing $j \in \mathbb{N}^0$. This comes at the cost of relying more on the model information. When the model contains errors these errors will accumulate. The second option uses less Markov parameters in total. In the presence of model errors, the error will remain approximately constant. The assumption $||C\Phi^{i}x(0)||_F \backsimeq 0$ remains equally valid.

If $||C\Phi^{i}x(0)||_F \backsimeq 0$ needs to be better approximated it is easy to choose a bigger i. Requiring the Markov parameters to be more certain can in practice be a difficult problem to solve. Therefore, the second option is the logical choice.

For stable predictor models it holds that:

$$\lim_{i\to\infty} \left\|C\Phi^i x\right\|_F = 0.$$

In a practical case, when i is chosen sufficiently large then $||C\Phi^{i}x||_F \backsimeq 0$. Remember from Section 2-2 that the RHI estimation required a choice of the past window p such that $||C\Phi^{p}x||_F \backsimeq 0$. Therefore, a good choice is $i = p$ which will be used in the sequel.

Expressing the output residual in terms of this initial state. The solution is constructed step by step. Now the output residual is written over a time window of size L starting on time instant p up to time instant $p + L - 1$. It is expressed relative to the choice initial state which is p time instances before each output residual's time instant. This results in:

$$\begin{aligned}
r(p) =& y(p) - C\Phi^p x(0) - \sum_{j=0}^{p-1} C\Phi^j \widetilde{E} b(p-j-1) - \sum_{j=0}^{p-1} C\Phi^j K y(p-j-1) - Gb(p) \\
r(p+1) =& y(p+1) - C\Phi^p x(1) - \sum_{j=0}^{p-1} C\Phi^j \widetilde{E} b(p-j) - \sum_{j=0}^{p-1} C\Phi^j K y(p-j) - Gb(p+1) \\
r(p+2) =& y(p+2) - C\Phi^p x(2) - \sum_{j=0}^{p-1} C\Phi^j \widetilde{E} b(p-j+1) - \sum_{j=0}^{p-1} C\Phi^j K y(p-j+1) - Gb(p+2) \\
&\vdots \\
r(p+L-1) =& y(p+L-1) - C\Phi^p x(L-1) - \sum_{j=0}^{p-1} C\Phi^j \widetilde{E} b(p-j+L-2) - \sum_{j=0}^{p-1} C\Phi^j K y(p-j+L-2) \\
&- Gb(p+L-1).
\end{aligned}$$

When p is chosen properly, as it should be in order to successfully construct the RHI estimator, then $||C\Phi^{p}x||_F \backsimeq 0$ which is in the sequel considered zero.

Shifting the output residual window towards the current time instant. Now consider the output residual r over the time window L from time instant $k - L + 1$ up to the current time instant k. This time window is also used by the RHI estimator presented in Section 2-2. The expression for the output residual then becomes:

$$r(k-L+1) = y(k-L+1) - \sum_{j=0}^{p-1} C\Phi^j \widetilde{E} b(k-L-j) - \sum_{j=0}^{p-1} C\Phi^j K y(k-L-j) - Eb(k-L+1) \quad \text{(3-8a)}$$

$$\vdots$$

$$r(k) = y(k) - \sum_{j=0}^{p-1} C\Phi^j \widetilde{E} b(k-1-j) - \sum_{j=0}^{p-1} C\Phi^j K y(k-1-j) - Eb(k), \quad \text{(3-8b)}$$

which consists of only Markov parameters and input/output data. This can be denoted in matrix form, which is advantageous when implementing code, as:

$$\begin{aligned}
&\underbrace{\begin{bmatrix} r(k-L+1) & r(k-L+2) & \cdots & r(k) \end{bmatrix}}_{R_{k-L+1,1,L}} = \\
&\qquad \underbrace{\begin{bmatrix} y(k-L+1) & y(k-L+2) & \cdots & y(k) \end{bmatrix}}_{Y_{k-L+1,1,L}} \\
&\qquad - \underbrace{\begin{bmatrix} (C\Phi^{p-1}\widetilde{E}) & (C\Phi^{p-2}\widetilde{E}) & \cdots & (C\widetilde{E}) \end{bmatrix}}_{\mathcal{E}_p} \underbrace{\begin{bmatrix} b(k-L+1-p) & \cdots & b(k-p-1) & b(k-p) \\ b(k-L+2-p) & \cdots & b(k-p) & b(k-p+1) \\ \vdots & & \vdots & \vdots \\ b(k-L) & \cdots & b(k-2) & b(k-1) \end{bmatrix}}_{B_{k-L+1-p,p,L}} \\
&\qquad - \begin{bmatrix} (C\Phi^{p-1}K) & (C\Phi^{p-2}K) & \cdots & (CK) \end{bmatrix} \underbrace{\begin{bmatrix} y(k-L+1-p) & \cdots & y(k-p-1) & y(k-p) \\ y(k-L+2-p) & \cdots & y(k-p) & y(k-p+1) \\ \vdots & & \vdots & \vdots \\ y(k-L) & \cdots & y(k-2) & y(k-1) \end{bmatrix}}_{Y_{k-L+1-p,p,L}} \\
&\qquad - D \underbrace{\begin{bmatrix} b(k-L+1) & b(k-L+2) & \cdots & b(k) \end{bmatrix}}_{B_{k-L+1,1,L}}.
\end{aligned}$$

Note the *Hankel structure* of the underbraced matrices (except for $\mathcal{E}_p$). $\mathcal{E}_p$ resembles the Markov parameters corresponding to the known inputs. By using these observations, the equations can be denoted compactly as:

$$R_{k-L+1,1,L} = Y_{k-L+1,1,L} - \mathcal{E}_p B_{k-L+1-p,p,L} - \mathcal{K}_p Y_{k-L+1-p,p,L} - DB_{k-L+1,1,L}. \quad \text{(3-9)}$$

3-3 Propagating model uncertainty to the RHI estimator

In the previous sections it has been shown that Markov parameters are an effective way to analyze model uncertainty. It has also been shown how to construct the RHI estimator from only the Markov parameters.

In order to address the problem stated in Eq. 3-2 in a scientific way it is desired to know the size of $\delta(\mathcal{T}_f)$ and $\delta(\bar{r}_{k,f})$. In this section an attempt will be made to derive an upper bound on the size of $\delta(\mathcal{T}_f)$ and $\delta(\bar{r}_{k,f})$.

3-3-1 Computing the uncertainty of the LS data matrix

As introduced in Section 3-1, the matrix $\mathcal{T}_f$ is also called the LS data matrix.

In Subsection 3-2-3 it was shown that the matrices $\mathcal{T}_f$, $\mathcal{H}_{f,p}$ and $\mathcal{T}_p$, all originating from $\mathcal{T}_L$ shown in Eq. 3-3 and it was pointed out that they can all be directly constructed from Markov parameters. Therefore, their respective uncertainties $\delta(\mathcal{T}_f)$, $\delta(\mathcal{H}_{f,p})$ and $\delta(\mathcal{T}_p)$ can be constructed directly from the uncertainty on the Markov parameters denoted as $\delta(\mathcal{B}_j)$, $\delta(\mathcal{K}_j)$ and $\delta(D)$.

Determining the uncertainty on $\bar{r}_{k,f}$ is more complicated therefore, the next subsection is devoted to this topic.

3-3-2 Computing the uncertainty of the LS measurement vector

The vector $\bar{r}_{k,f}$ is also called the LS measurement vector, as was introduced in Section 3-1.

In this section the uncertainty on the LS measurement vector i.e. $\delta(\bar{r}_{k,f})$ will be computed. When this uncertainty bound is obtained, the problem given in Eq. 3-2 robustly in a scientific way. In order to do this, remember from Eq. 3-6 that $\bar{r}_{k,f}$ is computed as:

$$\bar{r}_{k,f} = \begin{bmatrix} -\mathcal{H}_{f,p}\mathcal{T}_p^{\dagger} & I \end{bmatrix} r_{k,L}. \tag{3-10}$$

In order to propagate $\delta(\mathcal{B}_j)$, $\delta(\mathcal{K}_j)$ and $\delta(D)$ to $\delta(\bar{r}_{k,f})$ the intermediate results $\delta(\mathcal{H}_{f,p})$, $\delta(\mathcal{T}_p^{\dagger})$ and $\delta(r_{k,L})$ must be determined. Note that especially computing $\delta(\mathcal{T}_p^{\dagger})$ poses a challenge.

The uncertainty on $\delta(\mathcal{H}_{f,p})$ has been obtained in the previous subsection. In this subsection first the propagation of uncertainties through multiplication studied. Then it is shown how to compute the uncertainty $\delta(r_{k,L})$, then it is shown how to compute the uncertainty $\delta(\mathcal{T}_p^{\dagger})$.

Uncertainty propagation through multiplication

First the uncertainty propagation is studied when two uncertain matrices are multiplied. For this the following lemma is introduced. The lemma is also valid for matrix-vector multiplications since a vector can be interpreted as a matrix with one column or row.

Lemma 1. *Uncertainty propagation of multiplication of uncertain matrices*

Let $A \in \mathbb{R}^{m\times n}$ and $B \in \mathbb{R}^{n\times o}$ be a matrix where the uncertainty on their elements are given respectively by $\delta(A) \in \mathbb{R}^{m\times n}$ and $\delta(B) \in \mathbb{R}^{n\times o}$. Furthermore, m, n, $o \in \mathbb{N}^+$, and a matrix obtained from the $\delta()$ operation contains only positive elements. The uncertain product is defined as:

$$M \pm \delta(M) = (A \pm \delta(A))\,(B \pm \delta(B))\,.$$

Then the upper bound on the uncertainty on the elements of M denoted as $\delta(M)$ is computed by:

$$\delta(M) = |A|\,\delta(B) + \delta(A)\,|B| + \delta(A)\delta(B).$$

Proof. $M \in \mathbb{R}^{m\times o}$ is the product between A and B where $\delta(M) \in \mathbb{R}^{m\times o}$ gives the uncertainty on each element of M. It is unknown whether the uncertainties $\delta(A)$ and $\delta(B)$ should be (partially) added or subtracted from A and B in order to obtain their true value. Since an upper bound is computed the worst case scenario should be considered i.e. where all uncertainties add up. By taking the absolute values of the coefficients makes sure they will only add up. □

Computing the uncertainty bound on the output residual

In Subsection 3-2-3 it is shown how to compute $r_{k,L}$ based on only Markov parameters. Remember that $r_{k,L}$ is obtained from Eq. 3-8. In the presence of perturbation on the Markov parameters, denoted as $\delta(C\Phi^j\widetilde{B})$, $\delta(C\Phi^j K)$ and $\delta(D)$ for $0 \le j \le p-1$, then there will be a also perturbation present on $r_{k,L}$ denoted as $\delta(r_{k,L})$. The task at hand is to compute an upper bound on $\delta(r_{k,L})$. Recall that $r_{k,L}$ was actually partitioned as shown in Eq. 3-5 therefore, the results that is pursued is not an upper bound on $\delta(r_{k,L})$, but actually the upper bounds on $\delta(r_{k-f,p})$ and $\delta(r_{k,f})$.

When measurements are assumed to be noiseless and the perturbations are assumed to be exactly known, it is straight forward to see from Eq. 3-8 that $\delta(r_{k,L})$ can be computed as:

$$\begin{aligned}
\delta\left(r(k-L+1)\right) &= -\sum_{j=0}^{p-1}\delta\left(C\Phi^j\widetilde{E}\right)b(k-L-j) - \sum_{j=0}^{p-1}\delta\left(C\Phi^j K\right)y(k-L-j) - \delta\left(G\right)b(k-L+1)\\
&\vdots\\
\delta\left(r(k)\right) &= -\sum_{j=0}^{p-1}\delta\left(C\Phi^j\widetilde{E}\right)b(k-1-j) - \sum_{j=0}^{p-1}\delta\left(C\Phi^j K\right)y(k-1-j) - \delta\left(G\right)b(k).
\end{aligned}$$

Now assume that the perturbations are not exactly known but only an upper bound is known. Then by application of Lemma 1 one obtains:

$$\begin{aligned}
\delta\left(r(k-L+1)\right) \leq & \sum_{j=0}^{p-1} \delta\left(C\Phi^j \widetilde{E}\right) |b(k-L-j)| + \sum_{j=0}^{p-1} \delta\left(C\Phi^j K\right) |y(k-L-j)| \\
& + \delta\left(G\right) |b(k-L+1)| \\
& \vdots \\
\delta\left(r(k)\right) \leq & \sum_{j=0}^{p-1} \delta\left(C\Phi^j \widetilde{E}\right) |b(k-1-j)| + \sum_{j=0}^{p-1} \delta\left(C\Phi^j K\right) |y(k-1-j)| \\
& + \delta\left(G\right) |b(k)|,
\end{aligned}$$

Just as is the case for Eq. 3-8, this can be denoted in matrix form which reads:

$$\begin{aligned}
&\begin{bmatrix}\delta\left(r(k-L+1)\right) & \delta\left(r(k-L+2)\right) & \cdots & \delta\left(r(k)\right)\end{bmatrix} \leq \\
&\quad \begin{bmatrix}\delta\left(C\Phi^{p-1}\widetilde{E}\right) & \delta\left(C\Phi^{p-2}\widetilde{E}\right) & \cdots & \delta\left(C\widetilde{E}\right)\end{bmatrix}
\begin{bmatrix}
|b(k-L+1-p)| & \cdots & |b(k-p-1)| & |b(k-p)| \\
|b(k-L+2-p)| & \cdots & |b(k-p)| & |b(k-p+1)| \\
\vdots & & \vdots & \vdots \\
|b(k-L)| & \cdots & |b(k-2)| & |b(k-1)|
\end{bmatrix} \\
&\quad + \begin{bmatrix}\delta\left(C\Phi^{p-1}K\right) & \delta\left(C\Phi^{p-2}K\right) & \cdots & \delta\left(CK\right)\end{bmatrix}
\begin{bmatrix}
|y(k-L+1-p)| & \cdots & |y(k-p-1)| & |y(k-p)| \\
|y(k-L+2-p)| & \cdots & |y(k-p)| & |y(k-p+1)| \\
\vdots & & \vdots & \vdots \\
|y(k-L)| & \cdots & |y(k-2)| & |y(k-1)|
\end{bmatrix} \\
&\quad + \delta\left(G\right)\begin{bmatrix}|b(k-L+1)| & |b(k-L+2)| & \cdots & |b(k)|\end{bmatrix},
\end{aligned}$$

which again can ease programming when the Hankel structures are noted.

This result can be partitioned in $\delta(r_{k-f,p})$ and $\delta(r_{k,f})$ which are the desired quantities. Next it will be shown how to compute an upper bound on the uncertainty of $\mathcal{T}_p^\dagger$.

The uncertainty of the pseudo inverse of $\mathcal{T}_p$

In the previous section it is shown how the upper bounds of the uncertainties $\delta(r_{k-f,p})$ and $\delta(r_{k,f})$ can be computed. Only the uncertainty on $\mathcal{T}_p^\dagger$ has to be computed in order to obtain an upper bound on $\delta(\bar{r}_{k,f})$.

Initially the problem was approached by determining the uncertainty on $(\mathcal{T}_p^T\mathcal{T}_p)^{-1}$ because:

$$\mathcal{T}_p^\dagger = \left(\mathcal{T}_p^T\mathcal{T}_p\right)^{-1}\mathcal{T}_p^T.$$

This problem was solved under the assumption that the size of the uncertainty of $\mathcal{T}_p$ fulfills some conditions. It can be shown that these conditions are only met for very small uncertainties for this application. In this case the uncertainties are so small that an uncertainty analysis is usually not desired and as such the contribution is very small. When the assumption is violated the obtained bound equals $\delta(\mathcal{T}_p^\dagger) = \infty$, which is clearly to conservative. This work may be useful for other application and can be found in Appendix B. Here another approach is presented that yields much smaller and realistic bounds.

This method starts by showing how to compute $\mathcal{T}_p^\dagger$ analytically. Based on this analytic expression the size of $\delta(\mathcal{T}_p^\dagger)$ can be derived. By definition of the (left) pseudo inverse:

$$T_p^\dagger T_p = I.$$

By noting that the matrix T_p is lower triangular allows us to denote the previous equations as:

$$\underbrace{\begin{bmatrix} V & W \\ X & Y \end{bmatrix}}_{T_p^\dagger}\underbrace{\begin{bmatrix} K & 0 \\ H & L \end{bmatrix}}_{T_p} = \begin{bmatrix} I & 0 \\ 0 & I \end{bmatrix}.$$

Noting that K, L and H are knowns, four equations can be formed and solved for the unknowns V, W, X and Y. This yields the following result:

$$T_p^\dagger = \begin{bmatrix} K^\dagger & 0 \\ -L^\dagger H K^\dagger & L^\dagger \end{bmatrix}.$$

As can be seen only the pseudo inverse of K and L are required. Note that these matrices have the exactly the same structure as T_p but have smaller dimensions. Because of this, this computation can be applied recursively on $K^\dagger$ and $L^\dagger$. This can be done until only the pseudo inverse of the block $C\widetilde{B}$ or D is required, depending whether or not the model has a feed-through term. Because of this dependence of the final result's formulation, the result is presented in two lemmas, one for each case.

Lemma 2. *When the model as given in Eq. 2-10 has a feed-trough term D, then:*

$$\mathcal{T}_p = \begin{bmatrix} D & 0 & 0 & \cdots & 0 \\ C\tilde{B} & D & 0 & \cdots & 0 \\ C\Phi\tilde{B} & C\tilde{B} & D & \cdots & 0 \\ \vdots & \vdots & \ddots & \ddots & \vdots \\ C\Phi^{p-2}\tilde{B} & C\Phi^{p-3}\tilde{B} & \cdots & C\tilde{B} & D \end{bmatrix},$$

and $T_p^\dagger$ can be computed as:

$$\mathcal{T}_p^\dagger = \begin{bmatrix} \bar{D} & 0 & 0 & \cdots & 0 \\ \bar{C}\bar{B} & \bar{D} & 0 & & 0 \\ \bar{C}\Psi\bar{B} & \bar{C}\bar{B} & \bar{D} & \ddots & \vdots \\ \vdots & \vdots & \ddots & \ddots & 0 \\ \bar{C}\Psi^{p-2}\bar{B} & \bar{C}\Psi^{p-3}\bar{B} & \cdots & \bar{C}\bar{B} & \bar{D} \end{bmatrix},$$

where $\Psi = \Phi + \widetilde{B}D^\dagger C$, $\bar{B} = \widetilde{B}D^\dagger$, $\bar{C} = -D^\dagger C$ and $\bar{D} = D^\dagger$.

Lemma 3. *When the model as given in Eq. 2-10 has no feed-trough term D, then:*

$$\mathcal{T}_p = \begin{bmatrix} C\tilde{B} & 0 & \cdots & 0 \\ C\Phi\tilde{B} & C\tilde{B} & \ddots & \vdots \\ \vdots & \vdots & \ddots & 0 \\ C\Phi^{p-2}\tilde{B} & C\Phi^{p-3}\tilde{B} & \cdots & C\tilde{B} \end{bmatrix},$$

and $T_p^\dagger$ can be computed as:

$$\mathcal{T}_p^\dagger = \begin{bmatrix} \bar{D} & 0 & 0 & \cdots & 0 \\ \bar{C}\bar{B} & \bar{D} & 0 & & 0 \\ \bar{C}\Psi\bar{B} & \bar{C}\bar{B} & \bar{D} & \ddots & \vdots \\ \vdots & \vdots & \ddots & \ddots & 0 \\ \bar{C}\Psi^{p-2}\bar{B} & \bar{C}\Psi^{p-3}\bar{B} & \cdots & \bar{C}\bar{B} & \bar{D} \end{bmatrix},$$

where $\Psi = (I + \widetilde{B}(C\widetilde{B})^\dagger C)\Phi$, $\bar{B} = \widetilde{B}(C\widetilde{B})^\dagger$, $\bar{C} = -(C\widetilde{B})^\dagger C\Phi$ and $\bar{D} = (C\widetilde{B})^\dagger$.

The particular notation for computing $T_p^\dagger$ in Lemma 2 and 3 is selected to show the structure of $\mathcal{T}_p^\dagger$ that is exploited. It is shown that $\mathcal{T}_p^\dagger$ is again build from Markov parameters which relate to a state-space model with different system matrices namely: Ψ, $\bar{B}\,\bar{C}\,\bar{D}$, as defined in Lemma 2 and 3. These system matrices can be computed based on the original system matrices Φ, $\widetilde{B}$, C, D. When these Markov parameters are also independent of the similarity transformation of the original state-space model, then their uncertainty can also be computed as explained in Subsection 3-2-1.

Now it will be shown that $\bar{D}$ and $\bar{C}\Psi^{p-2}\bar{B}$ are unique for all $p \in \mathbb{N} \geq 2$ and independent of the similarity transformation of the original system matrices A, B, C, D. As in Subsection 3-2-1, consider a transformation matrix T that transforms state x into state $q = Tx$, then the transformed system matrices, denoted with subscript q, are given by:

$$\Phi_q = T\Phi T^{-1}, \quad \widetilde{B}_q = T\widetilde{B}, \quad C_q = CT^{-1}, \quad D_q = D.$$

For the case of Lemma 3, this leads to:

$$\begin{aligned}\Psi_q =&(I + \widetilde{B}_q(C_q\widetilde{B}_q)^\dagger C_q)\Phi_q = (TT^{-1} + T\widetilde{B}(CT^{-1}T\widetilde{B})^\dagger CT^{-1})T\Phi T^{-1}\\ =&T\Psi T^{-1}\\ \\ \bar{B}_q =&\widetilde{B}_q(C_q\widetilde{B}_q)^\dagger = T\widetilde{B}(CT^{-1}T\widetilde{B})^\dagger\\ =&T\bar{B}\\ \\ \bar{C}_q =&-(C\widetilde{B}_{qq})^\dagger C_q\Phi_q = -(CT^{-1}T\widetilde{B})^\dagger CT^{-1}T\Phi T^{-1}\\ =&\bar{C}T^{-1}\\ \\ \bar{D}_q =&(C_q\widetilde{B}_q)^\dagger = (CT^{-1}T\widetilde{B})^\dagger\\ =&\bar{D}\end{aligned}$$

Then via a proof identical to that presented in Subsection 3-2-1 it follows that the Markov parameters related to this different model are also unique. This proof can be repeated for Lemma 2 with the same result.

Therefore, multiple candidate models can be used to compute the candidate Markov parameters. The largest difference between the candidates is a measure for the uncertainty on these Markov parameters. For the case of Lemma 2 the proof follows the same reasoning and will yield the same conclusion.

The uncertainty on these Markov parameters are denoted as: $\delta(\bar{D})$, $\delta(\bar{C}\bar{B})$, $\cdots$, $\delta(\bar{C}\Psi^{p-2}\bar{B})$ and the uncertainty on $T_p^\dagger$ is thus given by:

$$\delta(\mathcal{T}_p^\dagger) = \begin{bmatrix} \delta(\bar{D}) & 0 & 0 & \cdots & 0\\ \delta(\bar{C}\bar{B}) & \delta(\bar{D}) & 0 & & 0\\ \delta(\bar{C}\Psi\bar{B}) & \delta(\bar{C}\bar{B}) & \delta(\bar{D}) & \ddots & \vdots\\ \vdots & \vdots & \ddots & \ddots & 0\\ \delta(\bar{C}\Psi^{p-2}\bar{B}) & \delta(\bar{C}\Psi^{p-3}\bar{B}) & \cdots & \delta(\bar{C}\bar{B}) & \delta(\bar{D}) \end{bmatrix}. \tag{3-11}$$

Before proceeding with deriving the uncertainty on the estimated unknown input, one question needs to be answered. In Subsection 3-2-2 it is explained that PBSID can be used to construct the RHI-estimator. However, in order to propagate the uncertainty through the RHI-estimator, also the state-space model with system matrices Ψ, $\bar{B}\,\bar{C}\,\bar{D}$ should be identifiable using PBSID. This problem is addressed next.

Identifying the inverse system

In this thesis it has been shown that $\mathcal{T}_p^\dagger$ and $\delta(\mathcal{T}_p^\dagger)$ can be obtained from the Markov parameters corresponding to a state-space model with system matrices Ψ, $\bar{B}\,\bar{C}\,\bar{D}$. It can be shown, as is done in [7], that this model describes the transfer of the inverse system i.e. from output residual r to unknown input u.

The Markov parameters corresponding to the inverse system can be computed based on the original system matrices as shown in Lemma 2 and 3. Then the uncertainty on these Markov parameters can be obtained using a Monte Carlo approach as explained in Subsection 3-2-2.

However, Subsection 3-2-2 discusses a different approach that acquires the Markov parameters and their uncertainty directly from a system identification experiment. However, the Markov parameters corresponding to the inverse system need to be estimated also based on the available input output data. Now it is shown how these Markov parameters can be identified using PBSID based on the same input output data.

Again there are small, but non trivial difference between the case where the original model has or does not have a feed-through term. Therefore, we can again distinguish two case, which will be discussed in the sequel.

Case where the model has a feed-trough term D. Using the methodology presented in [7], it can be shown that the state-space model corresponding to the inverse system i.e. from output residual r to unknown input u is given as:

$$x_e(k+1) = \Psi x_e(k) + \bar{B}r(k) \tag{3-12a}$$
$$\hat{u}(k) = \bar{C}x_e(k) + \bar{D}r(k). \tag{3-12b}$$

Furthermore, let us introduce the notations:

$$\breve{x}(k) = \begin{bmatrix} x_e(k) \\ \hat{x}(k-1) \end{bmatrix}, \qquad \breve{u}(k) = \hat{u}(k),$$

as they will be required later but are introduced here since their definition is case specific.

Case where the model has no feed-trough term D. In [7] it is shown that the state-space model corresponding to the inverse system i.e. from output residual r to unknown input u is given as:

$$x_e(k) = \Psi x_e(k-1) + \bar{B}r(k) \tag{3-13a}$$
$$\hat{u}(k-1) = \bar{C}x_e(k-1) + \bar{D}r(k). \tag{3-13b}$$

Furthermore, let us introduce the notations:

$$\breve{x}(k) = \begin{bmatrix} x_e(k-1) \\ \hat{x}(k-1) \end{bmatrix}, \qquad \breve{u}(k) = \hat{u}(k-1),$$

as they will be required later but are introduced here since their definition is case specific.

Note that the difference between Eq. 3-12 and Eq. 3-13 is the time instance of the system's output. In Eq. 3-13 the output of the system is $\hat{u}(k-1)$ i.e. the input is from the previous time instant since in that case, the system is assumed to have no feed-through term D and does therefore not contain information about the input at the current time instant.

Recall from Subsection 2-2-4 that the output residual $r(k)$ was defined as $r(k) = y(k) - \hat{y}(k)$, and recall that $\hat{y}(k)$ is governed by state-space model given in Eq. 2-11 on page 24 which is for ease repeated:

$$\hat{x}(k+1) = \Phi\hat{x}(k) + \tilde{E}b(k) + Ky(k) \tag{3-14a}$$
$$\hat{y}(k) = C\hat{x}(k) + Gb(k). \tag{3-14b}$$

By using Eq. 3-14, the output residual can be rewritten as:

$$\begin{aligned} r(k) =& y(k) - C\hat{x}(k) - Gb(k) \\ =& y(k) - C\Phi\hat{x}(k-1) - CKy(k-1) - Gb(k) - C\tilde{E}b(k-1), \end{aligned} \tag{3-15}$$

where the equality: $\hat{x}(k) = \Phi\hat{x}(k-1) + \tilde{E}b(k-1) + Ky(k-1)$ is used which is obtained from Eq. 3-14a. Then by defining:

$$\breve{y}(k) = \begin{bmatrix} y(k) \\ y(k-1) \end{bmatrix}, \qquad \breve{b}(k) = \begin{bmatrix} b(k) \\ b(k-1) \end{bmatrix},$$

and by substituting Eq. 3-15 into Eq. 3-12 or Eq. 3-13 one obtains the state-space system:

$$\breve{x}(k+1) = \underbrace{\begin{bmatrix} \Psi & -\bar{B}C\Phi \\ 0 & \Phi \end{bmatrix}}_{\breve{\Psi}} \breve{x}(k) + \underbrace{\begin{bmatrix} \bar{B} & -\bar{B}CK \\ 0 & K \end{bmatrix}}_{\breve{B}} \breve{y}(k) + \underbrace{\begin{bmatrix} -\bar{B}G & -\bar{B}C\widetilde{E} \\ 0 & \widetilde{E} \end{bmatrix}}_{\breve{E}} \breve{b}(k) \tag{3-16a}$$

$$\breve{u}(k) = \underbrace{\begin{bmatrix} \bar{C} & -\bar{D}C\Phi \end{bmatrix}}_{\breve{C}} \breve{x}(k) + \underbrace{\begin{bmatrix} \bar{D} & -\bar{D}CK \end{bmatrix}}_{\breve{D}} \breve{y}(k) + \underbrace{\begin{bmatrix} -\bar{D}G & -\bar{D}CE \end{bmatrix}}_{\breve{G}} \breve{b}(k). \tag{3-16b}$$

It must be noted that $\breve{y}(k)$ and $\breve{b}(k)$ consist of elements corresponding to the current and previous time instant so that the upper triangular structure is obtained in $\breve{\Psi}$, $\breve{B}$ and $\breve{E}$ which is essential for our goal as will be explained next.

Now note that the system in Eq. 3-16 can be identified using PBSID since both inputs and outputs of this system are available. Remember from Subsection 3-2-2 that for the system identification experiment the unknown input must be measurable.

Also note that now the Markov parameters of the system in Eq. 3-16 will have the structure:

$$\breve{C}\breve{\Psi}^i\breve{B} = \begin{bmatrix} \bar{C}\Psi^i\bar{B} & \star \end{bmatrix} \qquad \text{for} \qquad \forall i \in \mathbb{N}^0,$$

where $\star$ indicate a block value of no interest. The desired Markov parameters $\bar{C}\Psi^i\bar{B}$ can be obtained by dropping the part denoted with $\star$.

Now an analytic expression is available to compute $\mathcal{T}_p^\dagger$ and its uncertainty $\delta(\mathcal{T}_p^\dagger)$ can be computed. It has also been shown that the required matrices can be obtained using the same techniques as presented in Subsection 3-2-2 used to obtain the state-space model with system matrices Φ, $\widetilde{B}$, C, D. Also, $\delta(r_{k-f,p})$ and $\delta(r_{k,f})$ have been computed. The next step is to compute $\delta(\mathcal{H}_{f,p}\mathcal{T}_p^\dagger)$ so that the uncertainty on $\bar{r}_{k,f}$ can be determined.

The uncertainty of $\delta(\mathcal{H}_{f,p}\mathcal{T}_p^\dagger)$

Up until now, it has been shown how to obtain the uncertainties: $\delta(r_{k-f,p})$, $\delta(r_{k,f})$, $\delta(\mathcal{H}_{f,p})$, and $\delta(\mathcal{T}_p^\dagger)$. In order to obtain our final result, the uncertainty $\bar{r}_{k,f}$, the uncertainty on the product $\mathcal{H}_{f,p}\mathcal{T}_p^\dagger$ denoted as $\delta(\mathcal{H}_{f,p}\mathcal{T}_p^\dagger)$ must be computed.

The uncertainty $\delta(\mathcal{H}_{f,p}\mathcal{T}_p^\dagger)$ can be computed by application of Lemma 1 and yield:

$$\delta(\mathcal{H}_{f,p}\mathcal{T}_p^\dagger) \leq |\mathcal{H}_{f,p}|\,\delta(\mathcal{T}_p^\dagger) + \delta(\mathcal{H}_{f,p})\left|\mathcal{T}_p^\dagger\right| + \delta(\mathcal{H}_{f,p})\delta(\mathcal{T}_p^\dagger).$$

Merging the latter results to compute an upper bound on $\delta(\bar{r}_{k,f})$

Recall that $\bar{r}_{k,f}$ is computed using Eq. 3-10. All ingredients, namely the upper bounds on $\delta(\mathcal{H}_{f,p}\mathcal{T}_p^\dagger)$, $\delta(r_{k-f,p})$ and $\delta(r_{k,f})$ are know, thus an upper bound on $\delta(\bar{r}_{k,f})$ can be computed. By application of Lemma 1 this results in:

$$\delta(\bar{r}_{k,f}) \leq \delta(\mathcal{H}_{f,p}\mathcal{T}_p^\dagger)\,|r_{k-f,p}| + \left|\mathcal{H}_{f,p}\mathcal{T}_p^\dagger\right|\delta(r_{k-f,p}) + \delta(\mathcal{H}_{f,p}\mathcal{T}_p^\dagger)\delta(r_{k-f,p}) + \delta(r_{k,f}). \tag{3-17}$$

3-4 Upper bounds on the estimated input

In this section it will be shown how a bound on the estimated input can be computed. This is based on the previous results from this chapter.

3-4-1 Computing the upper bound

The unknown input is computed by solving Eq. 3-7. The explicit solution is given by:

$$\hat{u}_{k,f} = \mathcal{T}_f^\dagger \bar{r}_{k,f}. \tag{3-18}$$

As can be seen, $\bar{r}_{k,f}$ and $\mathcal{T}_f^\dagger$ are required. The uncertainty on the estimated inputs originates from the uncertainty on these matrices. The uncertainty $\delta(\bar{r}_{k,f})$ has been computed in Eq. 3-17. Both $\mathcal{T}_f^\dagger$ and $\delta(\mathcal{T}_f^\dagger)$ can be computed in the the same way as $\mathcal{T}_p^\dagger$ and $\delta(\mathcal{T}_p^\dagger)$ by applying Lemma 2 or Lemma 3 depending on the presence of a full rank feed-through term in the system.

The uncertainty on $\hat{u}_{k,f}$, denoted as $\delta(\hat{u}_{k,f})$, can be obtained by applying Lemma 1, which results in:

$$\delta(\hat{u}_{k,f}) \leq \left|\mathcal{T}_f^\dagger\right|\delta(\bar{r}_{k,f}) + \delta(\mathcal{T}_f^\dagger)\,|\bar{r}_{k,f}| + \delta(\mathcal{T}_f^\dagger)\delta(\bar{r}_{k,f}). \tag{3-19}$$

3-4-2 Numerical example to illustrate the results

In the previous subsection an upper bound on the estimated input is computed. In this subsection a numerical example is shown to illustrate the quality of the computed bound.

For this a very simple mass-spring-damper model has been used with a mass of 1 kg, a stiffness of 1000 N/m and a damping coefficient of 10 Ns/m. The selected sampling frequency is 10 times the eigenfrequency. As input, a force of 1 N is applied as a square-wave. For the example the RHI estimator is constructed using a future window of $f = 1$ and a past window of $p = 100$. A smaller value of p resulted in biased estimates.

For this experiment it is assumed that the real model is known and a perturbed model has been selected as the model where the stiffness is perturbed by a very small amount of +1%. Because the real model is known, the magnitude of the model errors, i.e. uncertainties are also exactly known.

Simulations are performed where the input is estimated using a RHI estimator constructed based on the real and the perturbed model. The simulation results are shown in Figure 3-2.

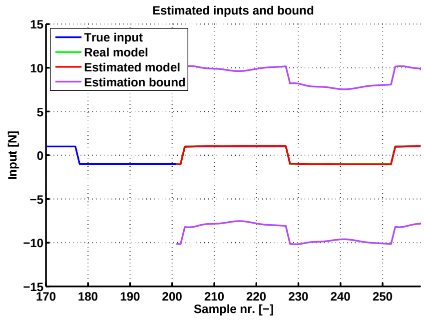

(a) The true input and estimated input based on the estimated and real model. The estimate corresponding to the real model is difficult to see because it is overlapped by the line corresponding to the estimated model. The uncertainty bound is computed using Eq. 3-19.

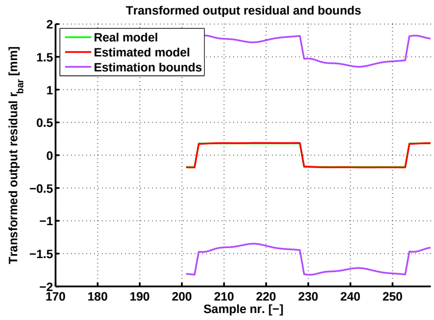

(b) The transformed output residual based on the estimated and real model. The estimate corresponding to the real model is difficult to see because it is overlapped by the line corresponding to the estimated model. The uncertainty bound is computed using Eq. 3-17.

Figure 3-2: *Computation of RHI estimator signals using the estimated and real model. The uncertainty bounds are computed based on the theory presented in Section 3-3.*

As is shown in Figure 3-2a, the actual error is very small. It is so small that the two lines in the graph are practically overlapping. The computed bound however is very large, and is clearly too conservative, which makes the bound not very useful. This bound is computed using Eq. 3-19. As is shown in Figure 3-2b the computed bound on the transformed output residual $\bar{r}$ is also very large. This is computed using Eq. 3-17.

In Table 3-1 Frobenius norms of all intermediate computed matrices and their computed uncertainties are shown for, where required, time instant $k = 210$. This allows us to study where the conservative bound originates from. As can be seen, the norms of the uncertainty of the matrices are small compared

Table 3-1: *Frobenius norms of various RHI estimator matrices, vector and their uncertainties.*

	$\hat{u}_{k,f}$	$\bar{r}_{k,f}$	$\mathcal{T}_f^\dagger$	$\mathcal{H}_{f,p}$	$\mathcal{T}_p^\dagger$	$\mathcal{H}_{f,p}\mathcal{T}_p^\dagger$	$r_{k-f,p}$	$r_{k,f}$
$\lVert\cdot\rVert_F$	1.03	0.185	5.59	0.374	246	4.48	8.97	0.870
$\lVert\delta(\cdot)\rVert_F$	9.90	1.77	0.000117	0.00317	0.0311	0.229	0.150	0.0260

to the estimated matrices. However, some norms of the estimated matrices are big, such as $||\mathcal{T}_f^\dagger||_F$, $||\mathcal{T}_p^\dagger||_F$, $||\mathcal{H}_{f,p}\mathcal{T}_p^\dagger||_F$ and $||r_{k-f,p}||_F$. In Eq. 3-19 and Eq. 3-17 the the small uncertainties get multiplied by these relative large numbers, resulting in large uncertainties on $\bar{r}_{k,f}$ and $\hat{u}_{k,f}$.

In order to solve this problem, a modification to this approach is presented in the next subsection.

3-4-3 Reducing the conservativeness of the uncertainty bound

In the previous section it is proposed to compute the estimation error bound using Eq. 3-19. However, this resulted in a very conservative bound, and the main reason is that $||\mathcal{T}_f^\dagger||_F$ is large. The 2-norm $||\mathcal{T}_f^\dagger||_2$ is also large which is caused by the fact that $\mathcal{T}_f$ has a small minimum singular value, implying that $\mathcal{T}_f$ is close to singular. Because $\mathcal{T}_f$ is close to singular, the solution of the least squares problem Eq. 3-1 is sensitive for perturbations on $\mathcal{T}_f$. This results, in the presence of uncertainty, in a large uncertainty bound on the solution of Eq. 3-1.

In order to reduce this sensitivity, one could apply regularization where, at the cost of introducing bias, the variance of the solution is reduced. Such an approach is presented in more detail in Subsection 4-1-2 and referred to as Classic Robust Least Squares (C-RLS). C-RLS is studied in more detail in e.g. [22]. The regularized least squares approach presented in [22] shows that, given the bounded uncertainties:

$$\|\delta(\mathcal{T}_f)\|_2 \leq \eta_{\mathcal{T}_f}, \qquad \|\delta(\bar{r}_{k,f})\|_2 \leq \eta_{\bar{r}},$$

the least squares problem in Eq. 3-1 transforms into:

$$\hat{u}_{k,f} = \arg\min_{u_{k,f}} \left(\|\bar{r}_{k,f} - \mathcal{T}_f u_{k,f}\|_2 + \eta_{\mathcal{T}_f} \|u_{k,f}\|_2 + \eta_{\bar{r}} \right),$$

which provides an optimized trade-off between adding bias and reducing the variance, in the sense that the worst case residual is minimized. The solution is given as:

$$\hat{u}_{k,f} = \underbrace{\left(\mathcal{T}_f^T \mathcal{T}_f + \alpha I\right)}_{\breve{\mathcal{T}}_f}{}^{-1} \mathcal{T}_f^T \bar{r}_{k,f}.$$

Note the similarity with Eq. 3-18 where, in this case, the well-posedness of inverse is regularized by the constant α. [22] shows how to compute α analytically as function of $\eta_{\mathcal{T}_f}$ and $\eta_{\bar{r}}$. Alternatively α can be tuned manually, which reduces the solution to a standard L_2 regularized least squares solution.

An upper bound on the 2-norm of $\delta(\breve{\mathcal{T}}_f^{-1})$ can be computed using Lemma 5 in Appendix B on page 110. By application of Lemma 1 an upper bound on $\delta(\mathcal{T}_f^T \bar{r}_{k,f})$ can be computed as:

$$\delta(\mathcal{T}_f^T \bar{r}_{k,f}) \leq \left|\mathcal{T}_f^T\right| \delta(\bar{r}_{k,f}) + \delta(\mathcal{T}_f^T) \left|\bar{r}_{k,f}\right| + \delta(\mathcal{T}_f^T)\delta(\bar{r}_{k,f}).$$

Then using Lemma 4 in Appendix B on page 109 an upper bound on the 2-norm of the uncertainty on estimated input can then be computed as:

$$\|\delta(\hat{u}_{k,f})\|_2 \leq \left\| \left|\breve{\mathcal{T}}_f^{-1}\right| \delta(\mathcal{T}_f^T \bar{r}_{k,f}) \right\|_2 + \left\| \delta(\breve{\mathcal{T}}_f^{-1}) \right\|_2 \left\|\mathcal{T}_f^T \bar{r}_{k,f}\right\|_2 + \left\| \delta(\breve{\mathcal{T}}_f^{-1}) \right\|_2 \left\|\delta(\mathcal{T}_f^T \bar{r}_{k,f})\right\|_2. \tag{3-20}$$

In order to test this new approach, the same simulation has been performed as described in Subsection 3-4-2. The results are shown in Figure 3-3. As can be seen in Figure 3-3a, the solution is practically identical to the solution presented in Figure 3-2a. Because of the small perturbation on the model, the uncertainty on $\mathcal{T}_f$ is small, which results in the fact that the optimal value of α is very small.

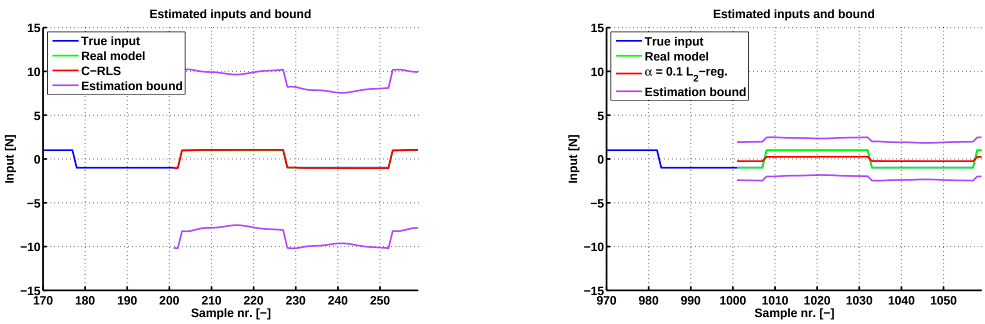

(a) Optimal choice of α as described in [22]. **(b)** L_2-regularization.

Figure 3-3: *The true input and estimated input based on the estimated and real model. The estimate corresponding to the real model is difficult to see because it is overlapped by the line corresponding to the estimated model. The uncertainty bound is computed using Eq.* 3-20.

Alternatively, α can be tuned to make the trade-off between added bias and reduced variance manually. This has been done, and the simulation result is shown in Figure 3-3b. As can be seen, the uncertainty bounds have reduced significantly but remain conservative while the added bias is of unacceptable magnitude.

The results can be explained by noting that Lemma 1 and Lemma 4 assume the worst case scenario where all uncertainties add up. Apparently this is a very conservative assumption since in practice the errors on the Markov parameters seem to cancel each other out such that the actual error much smaller. However, in general, there is no scientific basis to know to what extend the uncertainties will cancel out. One approach could be to use tuning, which can be very time consuming. Therefore, in the next section a different approach is proposed that takes this structure of the perturbations into account.

Still, regularization may be a very useful tool to apply when performing RHI estimation in the presence of modeling errors. Therefore, this is studied in more detail in Chapter 4.

3-5 Obtaining realistic bounds

In the previous section a method has been presented to compute an upper-bound on the estimated input and other RHI estimator matrices, such as the LS data matrix and the LS measurement vector. This was based on uncertainties of the models Markov parameters. As concluded in the previous section, the obtained bounds are very conservative. Therefore, a different approach is presented in this section. It will be shown that the obtained bounds are much more realistic.

3-5-1 The comparison method

The newly proposed method is called *the comparison method* and aims at obtaining more realistic bounds on the estimated input uncertainty caused by model errors.

This method is inspired by the fact that the previous method, based on Lemma 1, assumes that all perturbations are such that they add up. It has been shown that this is very conservative and surely the uncertainties cancel each other out to some extent. Clearly, the modeling error contains a structure. In order to obtain smaller bounds, this structure on the uncertainties must be exploited. This is the basic idea behind the formulation of this method.

Assume an estimate model $\mathfrak{m}_e$ is available and that a certain uncertainty bound for this model is given such that the model set $\mathcal{M}$ can be defined as containing exactly all possible models within this uncertainty bound. The real model $\mathfrak{m}_r$ is assuming to be in $\mathcal{M}$, i.e. $\mathfrak{m}_r \in \mathcal{M}$. In addition, assume a worst case model $\mathfrak{m}_w \in \mathcal{M}$ defined as:

$$\mathfrak{m}_w = \arg\max_{\mathfrak{m}\in\mathcal{M}} \left(\|\hat{u}_{k,f}(\mathfrak{m}) - \hat{u}_{k,f}(\mathfrak{m}_e)\|\right),$$

where the estimated input $\hat{u}_{k,f}$ is denoted as a function of the used model $\mathfrak{m}$. Then the difference $||\hat{u}_{k,f}(\mathfrak{m}_\mathfrak{w}) - \hat{u}_{k,f}(\mathfrak{m}_e)||$ provides the estimation norm-bound on the estimated input. By computing the bound this way, it is possible that the for the model differences cancel out instead of adding up. Therefore, the bound will be much less conservative and be realistic. This is presented in Theorem 1.

Theorem 1. *Computation of uncertainty norm-bounds on the estimated input.*

Given an estimated model $\mathfrak{m}_e$ and an uncertainty bound on this model, the model set $\mathcal{M}$ can be defined such that it contains exactly all models within this uncertainty bound. It is assumed that the real model $\mathfrak{m}_r$ is confined in this set, i.e. $\mathfrak{m}_r \in \mathcal{M}$. Then, assume the worst case model $\mathfrak{m}_w \in \mathcal{M}$ defined as:

$$\mathfrak{m}_w \triangleq \arg\max_{\mathfrak{m}\in\mathcal{M}} \left(\|\hat{u}_{k,f}(\mathfrak{m}) - \hat{u}_{k,f}(\mathfrak{m}_e)\|\right).$$

Then, a RHI estimator can be constructed for both models $\mathfrak{m}_e$ and $\mathfrak{m}_w$. Both estimators can be used to estimate an input sequence which is denoted as $\hat{u}_{k,f}(\mathfrak{m}_e)$ and $\hat{u}_{k,f}(\mathfrak{m}_w)$. Then, the norm-bound on the estimated input is obtained as:

$$\|\delta(\hat{u}_{k,f})\| = \|\hat{u}_{k,f}(\mathfrak{m}_w) - \hat{u}_{k,f}(\mathfrak{m}_e)\|,$$

where $||\cdot||$ can be any norm.

Proof. The norm-bound on the uncertainty is provided by $||\hat{u}_{k,f}(\mathfrak{m}_w) - \hat{u}_{k,f}(\mathfrak{m}_e)||$ since the worst case model $\mathfrak{m}_w \in \mathcal{M}$ is selected such that this term is maximized and since the real model is also contained in the set $\mathcal{M}$.

□

The real challenge in applying Theorem 1 is to find the worst case model. When the model is obtained from physical modeling, it might be possible to predict the worst case choice of parameters. However, this might not be trivial in general. As an alternative, a Monte Carlo based approach is proposed, where the unknown input is estimated using many different models in $\mathcal{M}$. The model generating the estimated inputs which differs most from the estimated input, obtained using the estimated model, will be classified as the worst-case model.

It should be noted that the choice of the worst case model can depend on the time instant k. If depending on the time instant different worst case models can be defined, then Theorem 1 can be applied for each model and the largest $\delta(\hat{u}_{k,f})$ can be selected at each time instant.

Another remark is that, when Monte Carlo based approach is selected it is not proven that the obtained bound is an upper-bound. However, the obtained bound will well approximate the upper-bound when enough probable models are considered. The obtained bound will be much more practical then the bound obtained using the method presented in Section 3-3.

3-5-2 Numerical example to illustrate the results

In order to illustrate the performance of the comparison method presented in the previous subsection the numerical example presented in Subsection 3-4-2 is repeated but here the bounds are computed using the comparison method.

The example model is again the same simple mass-spring-damper system with a mass of 1 kg, a stiffness of 1000 N/m and a damping coefficient of 10 Ns/m. The selected sampling frequency is 10 times the eigenfrequency. As input a force of 1 N is applied in a square-wave manner. The RHI estimator is constructed using a future window of $f = 1$ and a past window of $p = 100$. A smaller value of p resulted in biased estimates.

For this experiment it is assumed that the real model is unknown. The estimated model has been selected as the model where the stiffness is perturbed by a much larger amount as before, namely +10%. Furthermore, it is assumed that this estimated model has an uncertainty on the stiffness of ±18% around the perturbed model. This results in two candidate worst case models namely one with a stiffness of −10% and +30% relative to the real model. The simulation results are shown in Figure 3-4. It can be

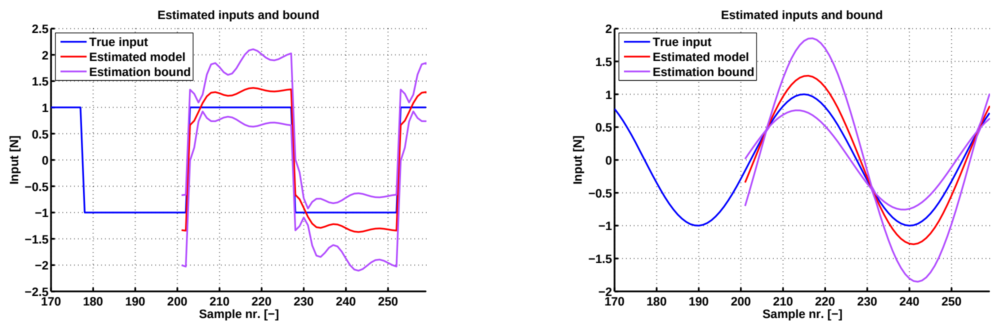

(a) square-wave shaped input. **(b)** Sine-wave shaped input.

Figure 3-4: *Both the true input and the estimated input are shown. The estimated input is obtained using RHI estimation. The estimation bounds are computed using the comparison method presented Theorem 1.*

seen, the computed uncertainty bounds are much smaller compared to the uncertainty bounds shown in Figure 3-2a. It can be seen that the true input falls nicely within the bounds. This happens for both the square-wave and sine-wave input signals. For the sinusoidal input signal a clear phase shift can be observed caused by the shifted eigenfrequency of the estimated model compared to the real model.

Based on this numerical experiment, it can be concluded that a more realistic upper-bound can be obtained via the comparison method, instead of propagating the model uncertainty through the RHI estimator.

3-5-3 Extension to the comparison method

The comparison method presented in Subsection 3-5-1 aims at obtaining more realistic bounds on the estimated input. In contrast to this aim, it might be more interesting to obtain bounds on other RHI estimator matrices, such as the LS data matrix and the LS measurement vector. When these bounds are available they can be used to address the problem stated in Eq. 3-2 in a robust way by taking the bounds into account in order to reduce $\delta(\hat{u}_{k,f})$. This will be the topic of Chapter 4. In this subsection the bounds on the LS data matrix and on the LS measurement vector will be determined in an approach similar to the one proposed in Theorem 1.

Inspired by Theorem 1, two new, very similar theorems are now introduced. First, a theorem providing means to compute the uncertainty on the LS data matrix is presented.

Theorem 2. *Computation of uncertainty norm-bounds on the LS data matrix*

Let $\mathfrak{m}_e$, $\mathfrak{m}_r$ and $\mathcal{M}$ be defined as in Theorem 1. Then, by redefining the worst case model $\mathfrak{m}_w$ as:

$$\mathfrak{m}_w \triangleq \arg\max_{\mathfrak{m}\in\mathcal{M}} \left(\|\mathcal{T}_f(\mathfrak{m}) - \mathcal{T}_f(\mathfrak{m}_e)\| \right),$$

the uncertainty norm-bound on $\mathcal{T}_f$ is given by:

$$\|\delta(\mathcal{T}_f)\| = \|\mathcal{T}_f(\mathfrak{m}_w) - \mathcal{T}_f(\mathfrak{m}_e)\|,$$

where $||\cdot||$ *can be any norm.*

Proof. The construction of the proof is identical to the proof presented in Theorem 1. □

It should be emphasized that, given a certain estimated model and a uncertainty on $\mathcal{T}_f$ is independent of time i.e. constant. Actually this definition of $\delta(\mathcal{T}_f)$ is identical to the definition for the method presented in Section 3-3. Here it is constructed from the uncertainty on the Markov parameters which are defined, when obtained from physical modeling, as the largest difference between possible Markov parameters and the expected Markov parameters.

The second theorem provides means to compute the uncertainty on the LS measurement vector.

Theorem 3. *Computation of uncertainty norm-bounds on the LS measurement vector*
Let $\mathfrak{m}_e$*,* $\mathfrak{m}_r$ *and* $\mathcal{M}$ *be defined as in Theorem 1. Then, by redefining the worst case model* $\mathfrak{m}_w$ *as:*

$$\mathfrak{m}_w \triangleq \arg\max_{\mathfrak{m}\in\mathcal{M}} \left(\|\bar{r}_{k,f}(\mathfrak{m}) - \bar{r}_{k,f}(\mathfrak{m}_e)\|\right),$$

the uncertainty norm-bound on the transformed output residual is given by:

$$\|\delta(\bar{r}_{k,f})\| = \|\bar{r}_{k,f}(\mathfrak{m}_w) - \bar{r}_{k,f}(\mathfrak{m}_e)\|,$$

where $||\cdot||$ *can be any norm.*

Proof. The construction of the proof is identical to the proof presented in Theorem 1. □

Here it should be noted that the same remarks as for Theorem 1 are applicable, namely that the worst case model can be time varying.

Furthermore, it should be noted that the worst case models, as defined in Theorem 1, Theorem 2 and Theorem 3 are not necessarily identical.

Finally, the obtained bound $\delta(\bar{r}_{k,f})$ is time varying even when $\mathfrak{m}_w$ is constant. This is a desired feature, which ensures that at a given time instant the bound is not unnecessarily conservative or optimistic. As it will be seen in Chapter 4, applying the RLS methods using these uncertainty bounds will contribute to obtain much better estimates in certain scenarios.

3-6 Conclusion

It has been shown that the Markov parameters are a powerful tool to study the effects of model uncertainty on RHI estimation because they are unique. This makes it possible to compare Markov parameters of several candidate models, as opposed to a state-space system matrices which are depended on the state transformation. It has also been shown how the RHI estimator can be completely constructed from only Markov parameters so that the actual system matrices are not required.

The Markov parameters can be obtained from physical modeling and their uncertainty can be obtained by comparing multiple models withing the model uncertainty bound. Markov parameters and their uncertainty can also be obtained directly from a SID experiment, where it is required that the unknown input must be measurable during such an experiment.

Furthermore has been shown that, when the exact size and sign of the perturbation on the Markov parameters are unknown, that propagation of this uncertainty through the RHI estimator results in a conservative uncertainty bound on the estimated input. To reduce the uncertainty, regularization of the LS problem has been attempted which resulted in an unacceptably large bias on the solution.

Therefore, a different method is proposed which estimates the input using both the estimated model and a predetermined worst case model. The estimation difference provides a realistic norm-bound on the input estimation uncertainty.

This approach is also applied to determine realistic norm-bounds on the LS estimation matrix and on the LS data vector, two matrices constructed in order to form the RHI estimator. When the uncertainties on these quantities are known, they can be taken into account to obtain more robust estimates of the unknown input. This will be the topic of the next chapter.

Chapter 4

Robust RHI estimation

As discussed before, the presented framework for shape and input estimation in Chapter 2 relies on models of the system. These model can be in accurate if it is difficult or impossible to measure the inputs and/or outputs. In this chapter it is therefore studied what the influence of modeling errors is on the RHI estimator.

In the previous chapter methods have been presented to obtain error bounds on several RHI estimator quantities. Knowledge about these bounds can be used to improve the robustness of the estimations. This is also a topic of this chapter. Three Robust Least Squares (RLS) algorithms are introduced and are used to solve in a robust way the estimation problem given in Eq. 3-2.

Simulations are performed for different perturbed models, different uncertainty sizes and a variety of input signals. The results are discussed and the conclusions are presented.

4-1 Robust Least Squares

It has been seen in Section 3-1 that an estimate of the unknown input is obtained by solving:

$$\bar{r}_{k,f} = \mathcal{T}_f u_{k,f}, \tag{4-1}$$

which in general has no exact solution since it is an overdetermined set of equations. In Subsection 2-2-4 this equation is solved by forming a least squares (LS) problem shown in Eq. 3-1 which is repeated below:

$$\hat{u}_{k,f} = \arg\min_{u_{k,f}} \left\| \bar{r}_{k,f} - \mathcal{T}_f u_{k,f} \right\|_2^2. \tag{4-2}$$

This problem can be solved using Ordinary Least Squares (OLS) . In the presence of model uncertainty the problems transforms into Eq. 3-2, which is also repeated:

$$\hat{u}_{k,f} + \delta(\hat{u}_{k,f}) = \arg\min_{u_{k,f}} \left\| \Big(\bar{r}_{k,f} + \delta(\bar{r}_{k,f})\Big) - \Big(\mathcal{T}_f + \delta(\mathcal{T}_f)\Big) u_{k,f} \right\|_2^2. \tag{4-3}$$

In this equation, $\delta(\mathcal{T}_f)$ and $\delta(\bar{r}_{k,f})$ are uncertainties of the matrices $\mathcal{T}_f$ and $\bar{r}_{k,f}$ respectively. The uncertainty originates from the fact that the model has some degree of uncertainty caused by e.g. uncertain parameters of a parametrized model, or when a System IDentification (SID) experiment is considered, because of measurement noise and a limited number of samples. Because of this uncertainty the estimated input has also a certain uncertainty denoted as $\delta(\hat{u}_{k,f})$.

An interesting question is whether the LS problem formulated in Eq. 3-2, can be solved in an robust way. Meaning that the sizes of the uncertainties $\delta(\mathcal{T}_f)$ and $\delta(\bar{r}_{k,f})$ are taken into account such that a better estimate of the unknown input can be obtained i.e. such that $\delta(\hat{u}_{k,f})$ is decreased. Performance indicators of estimation accuracy are: *average, RMS* or *maximum* error.

In this section three different Robust Least Squares (RLS) methods are presented which are denoted by TLS, C-RLS and R-RLS. In Section 4-2 the model used for simulations is introduced. Then in Section 4-3, these methods will be applied in simulations to investigate their typical performance in different scenarios. A more complete overview of RLS method can be found in [23] and [24].

4-1-1 Total Least Squares (TLS)

An old and well studied RLS method is Total Least Squares (TLS). Many variations have been created over time and an overview of them can be found in [25]. Here, the classical TLS approach is presented, to which is referred to using TLS.

The TLS approach seeks the smallest perturbations, in Frobenius norm sense, such that the system of equations presented in Eq. 4-1 becomes exactly solvable. This can mathematically be denoted as:

$$\hat{u}_{k,f} = \arg\min_{u_{k,f}} \min_{\delta(\mathcal{T}_f),\,\delta(\bar{r}_{k,f})} \left\| \begin{bmatrix} \delta(\mathcal{T}_f) & \delta(\bar{r}_{k,f}) \end{bmatrix} \right\|_F \quad \text{s.t.} \quad \Big(\bar{r}_{k,f} + \delta(\bar{r}_{k,f})\Big) - \Big(\mathcal{T}_f + \delta(\mathcal{T}_f)\Big) u_{k,f} = 0.$$

This RLS approach can be classified as optimistic since it assumes that the system of equations in Eq. 4-1 should be solvable and that this is prevented by the perturbations.

In [25] this optimization problem is solved by first computing the Singular Value Decomposition (SVD):

$$\begin{bmatrix} \mathcal{T}_f & \bar{r}_{k,f} \end{bmatrix} = U \begin{bmatrix} \Sigma_1 & 0 \\ 0 & \Sigma_2 \end{bmatrix} \begin{bmatrix} V_{11} & V_{12} \\ V_{21} & V_{22} \end{bmatrix}^T,$$

where $V_{11} \in \mathbb{R}^{m \times m}$ and $V_{22} \in \mathbb{R}^{\ell \times \ell}$. Then, the solution is given by:

$$\hat{u}_{k,f} = -V_{12} V_{22}^{-1}.$$

In [25] it is denoted that the solution can also be written as:

$$\hat{u}_{k,f} = \left(\mathcal{T}_f^T \mathcal{T}_f + I \sigma_{\min}^2(\begin{bmatrix} \mathcal{T}_f & \bar{r}_{k,f} \end{bmatrix})\right)^{-1} \mathcal{T}_f^T \bar{r}_{k,f},$$

where $\sigma_{\min}(\cdot)$ provides the minimum singular value of its operand. As can be seen, the solution is actually deregularized. It tries to remove bias from the solution which at the cost of variance.

4-1-2 Min-max approach (C-RLS)

Another RLS method widely mentioned in literature the min-max approach to which is referred to in the sequel as Classic Robust Least Squares (C-RLS). A thorough analysis of the method is presented in [26] or [22]. It seeks to minimize the worst case residual of Eq. 4-3. This approach differs from TLS in two ways. It requires bounds on the perturbations or the estimated input or $\hat{u}_{k,f}$ will always be estimated as zero. Furthermore, in contrast to the TLS, this method can be classified as pessimistic. This is because the min-max approach actually optimizes the worst case scenario which might be conservative if the perturbation bounds are not selected tightly.

Mathematically, the min-max method can be denoted as:

$$\hat{u}_{k,f} = \arg\min_{u_{k,f}} \max_{\delta(\mathcal{T}_f),\,\delta(\bar{r}_{k,f})} \left\| \Big(\bar{r}_{k,f} + \delta(\bar{r}_{k,f})\Big) - \Big(\mathcal{T}_f + \delta(\mathcal{T}_f)\Big) u_{k,f} \right\|_2 \text{ s.t. } \|\delta(\mathcal{T}_f)\|_2 \leq \eta_{\mathcal{T}_f},\ \|\delta(\bar{r}_{k,f})\|_2 \leq \eta_{\bar{r}}.$$

In [26] it is shown that this optimization problem is equivalent to:

$$\hat{u}_{k,f} = \arg\min_{u_{k,f}} \left(\|\bar{r}_{k,f} - \mathcal{T}_f u_{k,f}\|_2 + \eta_{\mathcal{T}_f} \|u_{k,f}\|_2 + \eta_{\bar{r}} \right),$$

which is continuous and convex.

This cost function has the analytical solution:

$$\hat{u}_{k,f} = \left(\mathcal{T}_f^T \mathcal{T}_f + \alpha I\right)^{-1} \mathcal{T}_f^T \bar{r}_{k,f},$$

where it can be seen that the well-posedness of inverse is regularized by the constant α and as such trying to reduce the sensitivity of the estimate due to the uncertainties $\delta(\mathcal{T}_f)$ and $\delta(\bar{r}_{k,f})$. [26] and [22] shows how to compute α analytically as function of $\eta_{\mathcal{T}_f}$ and $\eta_{\bar{r}}$. Alternatively α can be tuned manually which reduces the analytical solution to a standard L_2 regularized least squares solution.

Alternatively the convex optimization problem can be solved in Matlab using the CVX toolbox [27]. Finally, is should be noted that when the uncertainty bounds are set to zero, the problem reduces to a OLS problem.

4-1-3 Regret based min max approach (R-RLS)

The C-RLS method is a conservative approach because it optimizes the worst case scenario. Another method was found in trying to temper this conservative nature, which is referred to in the sequel as R-RLS. It defines a regret for not using the OLS estimator, then the worst case regret is minimized. In other words the R-RLS method seeks an estimate that is as close as possible to the OLS solution for all possible perturbations. This way a trade-off between performance and robustness is implemented. A detailed analysis of the approach can be found in [28] where the authors classify the method as a novel approach.

Mathematically, the regret is defined as:

$$\mathcal{R}\big(\delta(\mathcal{T}_f), \delta(\bar{r}_{k,f})\big) = \left\| \Big(\bar{r}_{k,f} + \delta(\bar{r}_{k,f})\Big) - \Big(\mathcal{T}_f + \delta(\mathcal{T}_f)\Big) u_{k,f} \right\|_2^2 - \min_{\bar{u}_{k,f}} \left\| \Big(\bar{r}_{k,f} + \delta(\bar{r}_{k,f})\Big) - \Big(\mathcal{T}_f + \delta(\mathcal{T}_f)\Big) \bar{u}_{k,f} \right\|_2^2,$$

and the R-RLS seeks the solution of the optimization problem:

$$\hat{u}_{k,f} = \arg\min_{u_{k,f}} \max_{\delta(\mathcal{T}_f),\, \delta(\bar{r}_{k,f})} \mathcal{R}\big(\delta(\mathcal{T}_f), \delta(\bar{r}_{k,f})\big) \quad \text{s.t.} \quad \|\delta(\mathcal{T}_f)\|_F \leq \eta_{\mathcal{T}_f},\ \|\delta(\bar{r}_{k,f})\|_F \leq \eta_{\bar{r}}.$$

For completeness it is shown in [28] that this problem is equivalent to the convex semi-definite programming problem:

$$\min_{u_{k,f},\, \gamma,\, \tau,\, \theta} (\gamma) \quad \text{s.t.} \quad \begin{bmatrix} \gamma + \xi - \tau - \theta & L^T & \eta_{\mathcal{T}_f} c^T & \eta_{\bar{r}} b^T \\ L & I & \eta_{\mathcal{T}_f} U & -\eta_{\bar{r}} I \\ \eta_{\mathcal{T}_f} c & \eta_{\mathcal{T}_f} U^T & \tau I & 0 \\ \eta_{\bar{r}} b & -\eta_{\bar{r}} I & 0 & \theta I \end{bmatrix} \geq 0, \quad \tau, \theta \geq 0,$$

where $c = -2(\mathcal{T}_f(\mathcal{T}_f^T\mathcal{T}_f)^{-1}\mathcal{T}_f^T\bar{r}_{k,f}\bar{r}_{k,f}^T\mathcal{T}_f(\mathcal{T}_f^T\mathcal{T}_f)^{-1} + \bar{r}_{k,f}\bar{r}_{k,f}^T\mathcal{T}_f(\mathcal{T}_f^T\mathcal{T}_f)^{-1})$, $b = 2(I - \mathcal{T}_f\mathcal{T}_f^\dagger)\bar{r}_{k,f}$, $\xi = {}^1\!/_2\bar{r}_{k,f}^T b$, $L = (\mathcal{T}_f u_{k,f} - \bar{r}_{k,f})$ and $U = (I \otimes u_{k,f})^T$. This convex optimization problem can also be solved in Matlab using the CVX toolbox [27]. Also for this case, when the bounds are selected as zero, the problem reduces to a normal OLS problem.

4-2 Model

In order to perform simulations a model is required which is introduced in this section. The model represents a heavily simplified wafer chuck for 450 mm wafers which is modeled as a flat plate. The behavior of the plate is modeled using finite elements techniques. Finally, the model is put in discrete time state-space form.

4-2-1 Impression

In this subsection the model is introduced. The model resembles a heavily simplified wafer chuck for 450 mm wafers depicted in Figure 4-1. The wafer chuck is modeled as a uniform Zerodur square chuck. The exact parameters can be found in Table 4-1. The model is based on a finite element model of a uniform plate as presented in [29]. This finite element model has been implemented in Matlab by [30] where also some corrections of the work in [29] have been made.

4-2-2 Refining the model

Conversion to state-space form

From the results in [29] a mass matrix M and stiffness matrix K are derived that define the second order differential equation as:

$$M\ddot{x} + Kx = F, \tag{4-4}$$

where F are the forces acting on the nodes. In this second order differential equation x is expressed in *nodal* coordinates. Nodal coordinates describes all DoFs of each node. This model contains no damping. To add damping in an easy way the model is converted to *modal* coordinates denoted as q. Modal coordinates describe the amplitude of each eigenmode (also called modeshapes). The chape of the chuck is obtained by summing all eigenmodes, each multiplied with their respective amplitude. For this purpose,

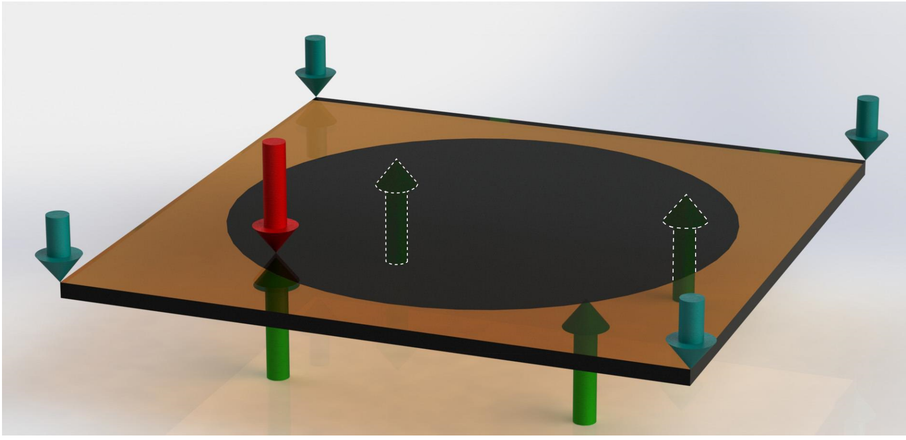

Figure 4-1: *A graphical representation of the constructed model. The green arrows are reaction forces from a controller to keeping the chuck at its position. The red arrow represents a disturbance force that is considered an input of the model and the blue arrows are displacement sensors which are considered the outputs of the model.*

Table 4-1: *Parameters describing the modeled chuck.*

Parameter	value	Comment
Number of elements	4x4	Limited to reduce simulation time.
Width	550mm	
Depth	550mm	
Thickness	14mm	
Actuator Position	140mm	Distance from each side.
Material	Zerodur	Used to make wafer chucks.
Young's modulus E_{nom}	$91 \cdot 10^9 \mathrm{N/m}^2$	
Density ρ_{nom}	$2.5 \cdot 10^3 \mathrm{kg/m}^3$	
Poisson's ratio ν_{nom}	0.24	
Relative damping ratio ζ_{nom}	0.05	Assumed constant over all modes.

a matrix V is defined of which its column V_i contain the shape of the ith eigenmode. In mathematical terms, we described the relation: $x = Vq$. Then by differentiating x twice one obtains: $\ddot{x} = V\ddot{q}$. Note that the amplitude of the eigenmodes follow a sinusoidal motion thus $\ddot{q}_i = -\omega_i^2 q_i$ where ω_i denotes the ith eigenfrequency. By substituting these results in Eq. 4-4, one obtains:

$$-MV_i\omega_i^2 q_i + KV_i q_i = F. \tag{4-5}$$

When a system is oscillating in one or more eigenmode at the corresponding frequency, the inertia forces are equal to the internal forces of the system. Energy is converted from potential energy to kinetic energy and back. When no damping and external force is present, then this motion continues indefinitely In order to compute V and all ω, the external forces F in Eq. 4-5 are put to zero and the problem reduces to the eigenvalue problem:

$$(K - M\omega_i^2)V_i = 0,$$

which can be solved to obtain ω_i and V_i.

Now one can write down the system in modal coordinates as:

$$MV\ddot{q} + KVq = F.$$

Then by multiplication with $\left(V^T MV\right)^{-1} V^T$ from the left, we obtain:

$$\ddot{q} + \underbrace{\left(V^T MV\right)^{-1} V^T KV}_{\Omega^2} q = \underbrace{\left(V^T MV\right)^{-1} V^T}_{V_F} F,$$

where V_F is defined for brevity a and $\Omega^2 = \mathrm{diag}(\left[\omega_1^2, \cdots, \omega_n^2\right])$. The reason that $\Omega^2 = \left(V^T M V\right)^{-1} V^T K V$ can be found by studying the fact that the eigenmodes are orthogonal to the mass and stiffness matrices [31] which is too ambiguous to treat in this thesis. Using these results the differential equations reduces to $\ddot{q} + \Omega^2 q = V_F F$. As a last step, a damping term can be added in the same way as is often done in linear second order systems by adding: $2\Omega\zeta\dot{q}$. This adds constant modal damping to the system, which is valid for small values of ζ, since then practically no energy is exchanged between the modes. Finally, the differential equation that includes damping becomes:

$$\ddot{q} + 2\Omega\zeta\dot{q} + \Omega^2 q = V_F F$$

For the simulations, two models are considered. One model, based on the parameters as given in Table 4-1, is used and for simulation purposes assumed to be the real model. Finally, this set of second order differential equation can be converted to a set of first order differential equations in state-space form as:

$$A = \begin{bmatrix} 0 & I \\ -\Omega^2 & -2\Omega\zeta \end{bmatrix}, \qquad B = \begin{bmatrix} 0 \\ V_F \end{bmatrix}, \qquad C = \begin{bmatrix} V & 0 \end{bmatrix}, \qquad D = [0],$$

where the relation $x = Vq$ was used to have nodal coordinates as output. Finally, only the desired outputs are selected by selecting the corresponding rows of the C matrix, and only the desired inputs are selected by selecting the corresponding columns from the B matrix.

Stabilizing the marginally stable model

The created model is marginally stable. The first 6 eigenvalues of the A matrix are 0 which correspond to the rigid body motions of the chuck. These modes must be stabilized or they will make the system unstable when the model is discretized. 6 PID-controllers are designed to stabilize the 6 marginal stable modes. In Subsection 5-2-2 the tuning rules of these PID-controller are presented.

Selecting outputs

Furthermore, this system has dynamics of which its speed is in a different order of magnitude. These are the relative slow dynamics of the chuck positioned by the PID-controllers, and the much faster eigenfrequencies of the chuck. A sampling frequency sufficiently high to capture the most important eigenfrequencies of the chuck is required. However, the slow, not highly damped, dynamics are then described by a large number of samples.

Therefore, a very large past window p is required as is explained in Section 2-2. Because of this required large choice of p, very large matrices need to be formed to construct the RHI estimator, making the algorithm very slow. This is undesired and therefore, it has been decided to only look at the chuck's deformations, defined as a translation of a point on the chuck, relative to the chuck's position in space. Then the slow dynamics corresponding to the chuck's position in space are made unobservable and do not influence the measurements. Therefore, a much smaller p can be selected resulting in much smaller RHI estimation matrices.

Unobservable and uncontrollable modes

The model is a 3D model which contains all 6 Degrees of Freedom (DoF) whereas in this study we only look at the 3 DoFs out of the chuck's plane i.e. out-of-plane in the sequel. Therefore, the model contains unobservable and uncontrollable modes. This means the model order can be reduced which yield a reduction of the computation complexity. The unobservable and uncontrollable modes are removed by computing the Kalman decomposition and by dropping the uncontrollable and unobservable parts. This will result in the same input-output response since in our case the states are not required to have specific initial conditions.

Discretizing the model

The estimation algorithms presented in Chapter 2 will be used in a discrete-time manner. Samples are collected and the available time until the next samples need to be collected will be used to perform the required computations. The RHI estimator is expressed in terms of a discrete time model. Therefore, this model is discretized by assuming piecewise constant inputs over the sampling time i.e. Zero-Order

Hold (ZoH). In practice this will be the case for the known control inputs. However, the disturbance force will not be constant over the sampling time. Still this discretization method will provide a sufficiently accurate and intuitive discrete-time approximation of the model. The disturbance forces considered in these simulations are well below the sampling frequency, therefore the exact discretization methodology it not very important.

4-3 Simulations and results

RHI estimation simulations have been performed where the problem given in Eq. 4-3 has been solved in different ways. The OLS solution is compared with the solutions obtained using TLS, RLS and R-RLS. This provides a background of the performance of the RHI estimation in the presence of modeling errors. In addition, it will be seen whether RLS algorithms provide better estimates than OLS.

4-3-1 Description of the numerical experiments

Before proceeding with presenting the simulation results, a thorough description of the experiments is provided.

First, a constant real model is assumed with the parameters as presented in Section 4-2 and Table 4-1. Then, we assume a perturbed model where the parameters E, ρ and ζ are assumed to be uncertain and perturbed. The perturbed parameters are denoted with subscript *per*, while to the nominal parameters denoted with subscript *nom*.

Two models are studied, one with a normal sized perturbation and one with a larger perturbation. The perturbed model parameters are shown in Table 4-2.

In Table 4-2 the uncertainty of the perturbed parameters is also presented. These are chosen such that the real model is contained withing these uncertainty bounds.

Table 4-2: *Parameters of perturbed models denoted with subscript per relative to the nominal parameters denoted with subscript nom.*

Model	E_{per}	$\delta(E_{per})$	ρ_{per}	$\delta(\rho_{per})$	ζ_{per}	$\delta(\zeta_{per})$
Lightly perturbed	$0.9E_{nom}$	$\pm10\%$	ρ_{nom}	$\pm10\%$	$0.9\zeta_{nom}$	$\pm150\%$
Severely perturbed	$1.2E_{nom}$	$\pm20\%$	$0.9\rho_{nom}$	$\pm20\%$	$0.5\zeta_{nom}$	$\pm300\%$

Before the RHI estimator is constructed for both perturbed model, a proper past and future window size need to be determined. The future window size has been selected to be f=1. This has been selected for simplicity and computational efficiency. The past window size is selected using simulations for different past window sizes.

Different estimates of the unknown input are obtained by solving Eq. 4-3 using OLS, TLS, C-RLS and R-RLS. The bounds on $\delta(\mathcal{T}_f)$ and $\delta(\bar{r}_{k,f})$ are obtained as described in Theorem 2 and 3 respectively. They require to select a model from the set of possible models which produces the largest different $\mathcal{T}_f$ and $\bar{r}_{k,f}$ with respect to the estimated model. This worst case model is estimated using a Monte Carlo approach.

Then, the unknown input is estimated using the perturbed models and their uncertainty bound and the unknown input estimation errors are discussed.

4-3-2 Choice of past window size p

Before the RHI estimator can be implemented, a past window size p must be selected. A too small p results in large estimation errors while a too large p makes the RHI estimation computationally necessarily heavy. In order to select a suitable value of p , the RHI estimator has been implemented for many different values of p and the estimation errors are compared.

The RHI estimator is constructed for the lightly perturbed, severely perturbed and for the real model. A square-wave input with an amplitude of 1 N is selected. As performance indicator, the estimation error in terms of RMS and maximum error in the considered time window are used. The considered time window is one period of the square-wave which is about 80ms. These estimation errors as function of the past window size p are shown in Figure 4-2.

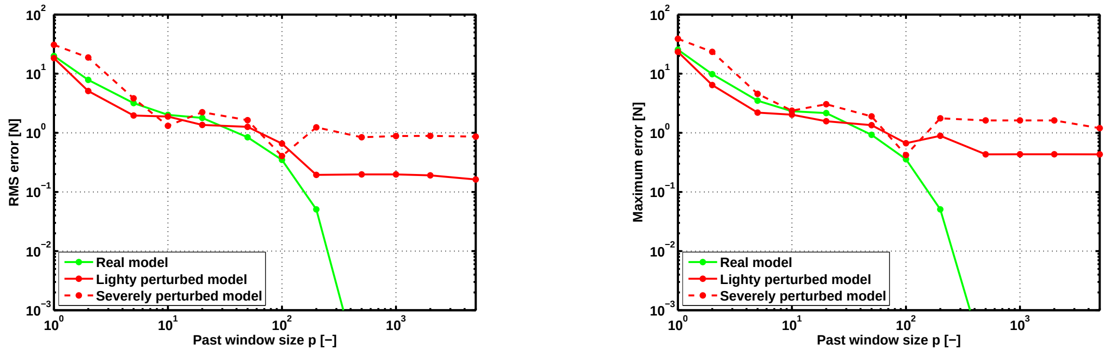

(a) RMS estimation error.

(b) Maximum estimation error.

Figure 4-2: *Estimation errors as function of the past window size.*

It can be seen that the errors are very large for small values of p and decrease for increasing value of p. When the real model is used, the error keeps decreasing for increasing value of p. However, when the perturbed model is used, the error settles at a certain value.

To understand why, remember that the RHI estimator relies on the assumption $||C\Phi^p x||_F \simeq 0$. While the value p is increased, this assumption becomes more valid, at the cost of adding model information by using additional Markov parameters. When the model is correct then the error decreases. When the model is has a certain error, then the error still decreases initially. However, the Markov parameters, $C\Phi^p\widetilde{B}$, will be very small for large p and $\lim_{p\to\infty}(C\Phi^p\widetilde{B}) = 0$ when Φ is stable. In addition, note that the errors on $C\Phi^p\widetilde{B}$ are large for small p and decrease for increasing p. At some point the small Markov parameters (and errors) make no difference to the already included large errors. Therefore, increasing the value of p after a certain value has virtually no effect on the estimation error. This is well illustrated by the result shown in Figure 4-2. For models with a larger error a smaller value of p can be used without increasing the estimation error significantly.

In this chapter, the estimation error caused by model errors is studied. Therefore, the value of p should be chosen such that the error for the perturbed model is minimal which is the case for $p = 300$. In order to be insensitive for small changes when different perturbed models are used a value of $p = 500$ is selected. The resulting computational load is acceptable for this value and introduces no restriction on the desired size of the value p.

4-3-3 Bound selection

The next task is to determine the bounds on $\delta(\mathcal{T}_f)$ and $\delta(\bar{r}_{k,f})$, so that the RLS methods can be implemented. The bounds are determined using a worst case model as presented in Theorem 2 and Theorem 3. The worst case model for both perturbed models is determined in this subsection using a Monte Carlo based approach.

This can be done in two ways: one could *randomly* generate models in the set of models falling within the uncertainty bound, or a *structured set* of models can be evaluated. The latter option is selected because it might reveal a trend in the worst case model which can be used to select (an approximate) worst case model intuitively. This approach is much faster than a Monte Carlo based approach.

The evaluated models relating to both the lightly and severely perturbed model are shown in Table 4-3. As can be seen, 27 models are evaluated. Every uncertain parameter is evaluated at 3 points: at both extremes possibilities and at their estimated value. Then, every possible combination of these parametric values represents a model. As shown in Table 4-3, this results in 27 different models where model nr. 14 represents the estimated model.

The LS data matrix $\mathcal{T}_f$ is computed for all models and the largest difference with respect to model 14 is selected as $\delta(\mathcal{T}_f)$. The worst case model used for computing the uncertainty on the LS measurement vector can vary over time. This can be taken into account but the difference will be very small. In order to simplify the analysis and speed up the simulations the LS measurement vector $\bar{r}$ is also computed over a time window and the maximum-, RMS- and mean-difference is used as measure to determine a time independent worst case model. The results are shown in Figure 4-3 for the lightly perturbed model, and

Table 4-3: *Structured set of models that are evaluated to obtain an estimate of the worst case model.*

		Model nr.	**1**	**2**	**3**	**4**	**5**	**6**	**7**	**8**	**9**	**10**	**11**	**12**	**13**	**14**
Lightly perturbed		E [% E_{per}]	90	100	110	90	100	110	90	100	110	90	100	110	90	100
		ρ [% ρ_{per}]	90	90	90	100	100	100	110	110	110	90	90	90	100	100
		ζ [% ζ_{per}]	67	67	67	67	67	67	67	67	67	100	100	100	100	100
Severely perturbed		E [% E_{per}]	80	100	120	80	100	120	80	100	120	80	100	120	80	100
		ρ [% ρ_{per}]	80	80	80	100	100	100	120	120	120	80	80	80	100	100
		ζ [% ζ_{per}]	33	33	33	33	33	33	33	33	33	100	100	100	100	100

		Model nr.	**15**	**16**	**17**	**18**	**19**	**20**	**21**	**22**	**23**	**24**	**25**	**26**	**27**
Lightly perturbed		E [% E_{per}]	110	90	100	110	90	100	110	90	100	110	90	100	110
		ρ [% ρ_{per}]	100	110	110	110	90	90	90	100	100	100	110	110	110
		ζ [% ζ_{per}]	100	100	100	100	150	150	150	150	150	150	150	150	150
Severely perturbed		E [% E_{per}]	120	80	100	120	80	100	120	80	100	120	80	100	120
		ρ [% ρ_{per}]	100	120	120	120	80	80	80	100	100	100	120	120	120
		ζ [% ζ_{per}]	100	100	100	100	300	300	300	300	300	300	300	300	300

in Figure 4-4 for the severely perturbed model.

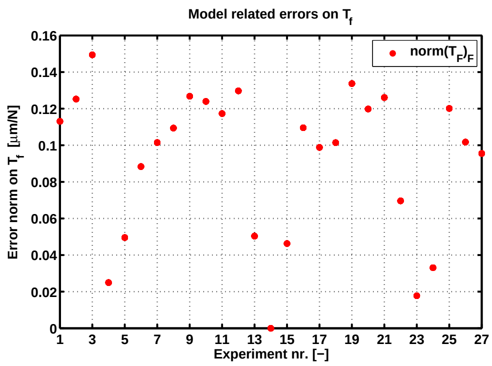

(a) Norm of the difference in $\mathcal{T}_f$ as function of the selected model. The largest difference is used as $\delta(\mathcal{T}_f)$.

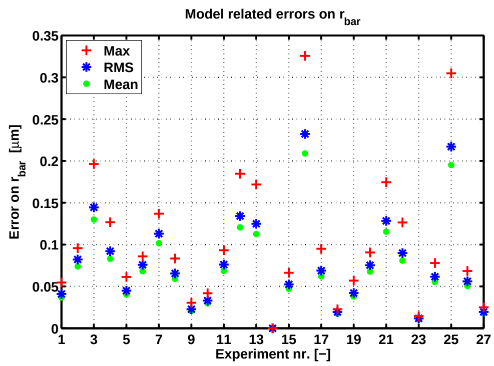

(b) Differences on $\bar{r}$ as function of the selected model. The model giving the largest difference is used to generate the time varying uncertainty $\delta(\bar{r}_{k,f})$.

Figure 4-3: *Error on the LS data matrix and LS measurement vector as function of possible models. These results correspond to the lightly perturbed model.*

By comparison of the figures it is shown unsurprisingly that the errors for the severely perturbed model are much larger. Furthermore, it can be seen that model 14 results in a zero error since that represents the estimated model. Also the pattern is similar although not identical. Roughly spoken, when a candidate model generates a large error for the lightly perturbed model, it does also perform inadequately for the severely perturbed model and vice versa.

It can be seen in Figure 4-3b that model 3, 7, 16 and 25 generate the largest $\delta(\bar{r}_{k,f})$. These models correspond to perturbations where an extreme value of $\delta(E_{per})$ is selected while an opposite extreme value for $\delta(\rho_{per})$ is selected e.g. $\delta(E_{per}) = +20\%$ and $\delta(\rho_{per}) = -20\%$. Such changes result in the largest change of the systems dynamics and apparently also result in the largest errors on $\mathcal{T}_f$ and $\bar{r}$.

In Figure 4-4b the models 6, 16 and 24 generate the largest $\delta(\bar{r}_{k,f})$. Here the same reasoning is true but in case of model 6 en 24 for extremes of $\delta(E_{per})$ and $\delta(\zeta_{per})$.

As is shown, model 3 results in the largest $\delta(\mathcal{T}_f)$ and this value must thus be selected in accordance with Theorem 2. The worst case model used to determine $\delta(\bar{r}_{k,f})$ differs for the lightly and severely perturbed case which poses no problem.

4-3-4 Performance of RHI estimator when using perturbed models

The RHI can be constructed using the selected past and future window size. Simulations can be performed to evaluate its performance in the presence of modeling errors. Given the model uncertainty on the perturbed models, also uncertainty bounds on the LS data matrix and LS measurement vector have been determined which can be used to obtain estimates using RLS.

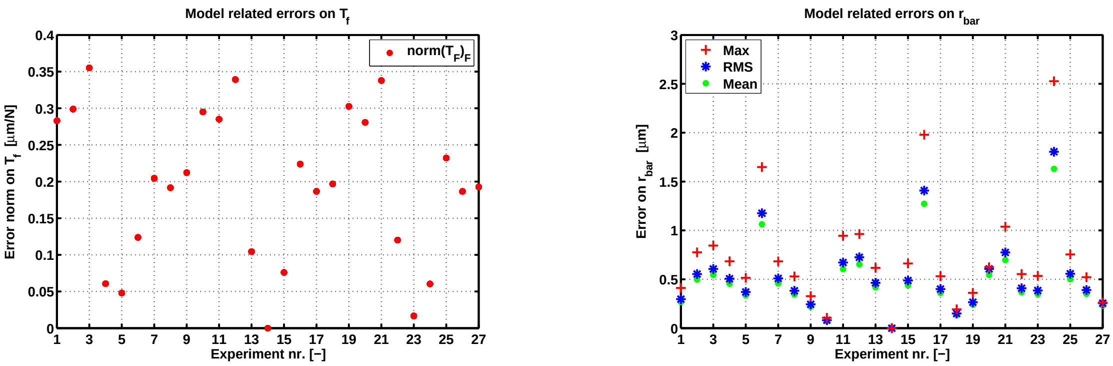

(a) Norm of the difference in $\mathcal{T}_f$ as function of the selected model. The largest difference is used as $\delta(\mathcal{T}_f)$.

(b) Differences on $\bar{r}$ as function of the selected model. The model giving the largest difference is used to generate the time varying uncertainty $\delta(\bar{r}_{k,f})$.

Figure 4-4: *Error on the LS data matrix and LS measurement vector as function of possible models. These results correspond to the severely perturbed model.*

For both the lightly and severely perturbed model the RHI estimator is constructed. This boils down to constructing Eq. 4-3. Then this equation is solved using OLS, TLS, C-RLS and R-RLS when several different shaped unknown inputs are supplied. These inputs are square, sinusoid and triangularly shaped, and in addition, a Zero Mean White Noise (ZMWN) input signal is used. The resulting estimated inputs are plotted against the true input and the estimation error is also plotted.

Furthermore, it is investigated what the influence of over and under estimating the uncertainty bounds is on the performance of the RLS algorithms. Therefore, two additional cases are evaluated where the found uncertainty bound for the severely perturbed model is applied to the lightly perturbed model and visa versa.

The lightly perturbed model using its uncertainty bounds.

First the lightly perturbed model is evaluated using the bounds found in Subsection 4-3-3. The graphical results can be seen in Figure 4-5 and the numerical results in Table 4-4. As can be seen there is no method that clearly performs better. Depending on the input signal shape and time instant, each method out- or under-performs with respect to the other methods.

Table 4-4: *Input estimation errors for different input signals and LS algorithms. The RHI estimator is constructed using the lightly perturbed model and the obtained uncertainty bounds on $\delta(\mathcal{T}_f)$ and $\delta(\bar{r}_{k,f})$.*

Error type	Method	ZMWN	Square	Triangle	Sine
RMS	**OLS**	0.624	0.145	0.070	0.085
	TLS	0.633	0.154	0.074	0.090
	C-RLS	0.582	0.125	0.069	0.081
	R-RLS	0.548	0.228	0.129	0.161
Maximum	**OLS**	1.742	0.476	0.100	0.122
	TLS	1.767	0.523	0.104	0.129
	C-RLS	1.616	0.392	0.120	0.144
	R-RLS	1.439	0.314	0.198	0.226

It can be seen that the OLS and TLS produce very similar estimates. It is hard to say for sure why this is, but likely is that TLS only assumes very small perturbations resulting in practically the same estimates as OLS.

For the sine-wave, a small phase shift can be observed between the estimated sine-waves and the actual input signal. This is caused by the dynamics of the lightly perturbed perturbed model, which has changed because it assumes a lower stiffness coefficient. The largest error component on the estimated sine-waves is caused by the phase shift. Except for the R-RLS method where the largest error component is caused by underestimating the amplitude.

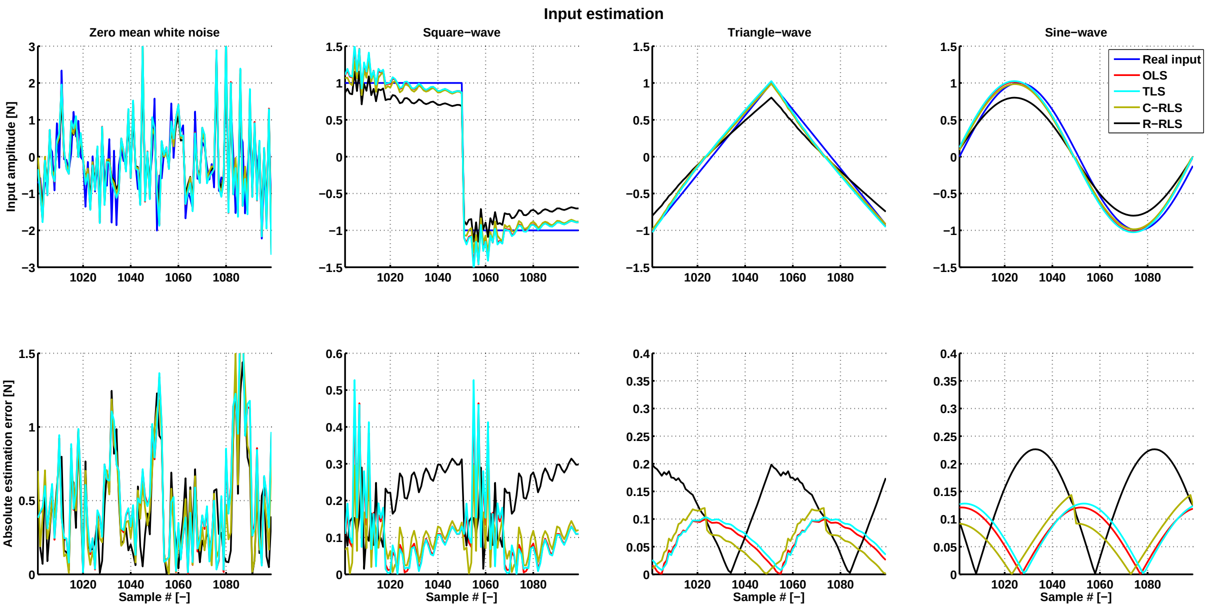

Figure 4-5: *This figure shows the input estimation results using the RHI estimator where the LS problem shown in Eq. 4-3 is solved using OLS, TLS, C-RLS and RLS. The estimate inputs are plotted together with the real input and the corresponding estimation error is shown. The estimation is performed on different kind of input signals. The RHI estimator has been constructed based on the lightly perturbed model and the corresponding uncertainty bounds* $\delta(\mathcal{T}_f)$ *and* $\delta(\bar{r}_{k,f})$*. The OLS solution is sometimes hard to see because it is overlapped by the TLS solution. The maximum and RMS errors are shown in Table 4-4.*

The RLS methods are expected to produce more conservative estimates. This simulation result suggest that the R-RLS method produces too conservative estimates. For all input signals it under-estimates the amplitude. However, in the case of the ZMWN signal this seems to be an advantage. The C-RLS method is less conservative but is still more conservative than the OLS estimate. The conservativeness of C-RLS (determined by the used bounds, $\delta(\mathcal{T}_f)$ and $\delta(\bar{r}_{k,f})$), seems to be properly balanced and it outperforms the OLS estimate most of the time. The large estimation noise present at each jump of the square-wave gets filtered out by this conservative attitude, while the amplitude is estimated almost just as good as the OLS estimate. C-RLS also estimates the ZMWN sequence better then OLS.

The numerical results, shown in Table 4-4, show that C-RLS produces always a lower RMS error then OLS. When considering discontinuous input signals i.e. the square-wave and the ZMWN sequence, both C-RLS and R-RLS perform better when comparing the maximum errors. They under-perform when continuous input signals such as the sine-wave and triangle-wave are considered in the maximum error sense compared to the OLS solution.

The TLS solution is very similar to the OLS solution, but its estimation error is always slightly larger. The method under-performs most of the time compared to the other methods. Apparently, its optimistic nature is not the correct approach for this estimation problem.

The lightly perturbed model using the severely perturbed model's uncertainty bounds

In the previous results it is shown that the RLS methods, especially C-RLS can reduce the estimation error. It is interesting to see what would happen if the uncertainty bounds are conservatively estimated. This is simulated by using the uncertainty bounds of the severely perturbed model on the lightly perturbed model. The results are presented in Figure 4-6 and Table 4-5.

The OLS and TLS estimates remain the same since they do not use the uncertainty bounds. The estimates produced using C-RLS and R-RLS have changed.

As can be seen, the amplitudes estimated by C-RLS and R-RLS are lower. They produce more conservative estimates because of the increased uncertainty bounds. However, the difference is not very large. The under-estimated amplitude result typically in a larger maximum error. However, the increased conservativeness decreases the error at some moments in time resulting in only a small increase of the RMS error. The overall performance of C-RLS has decreased but is still better then the performance of

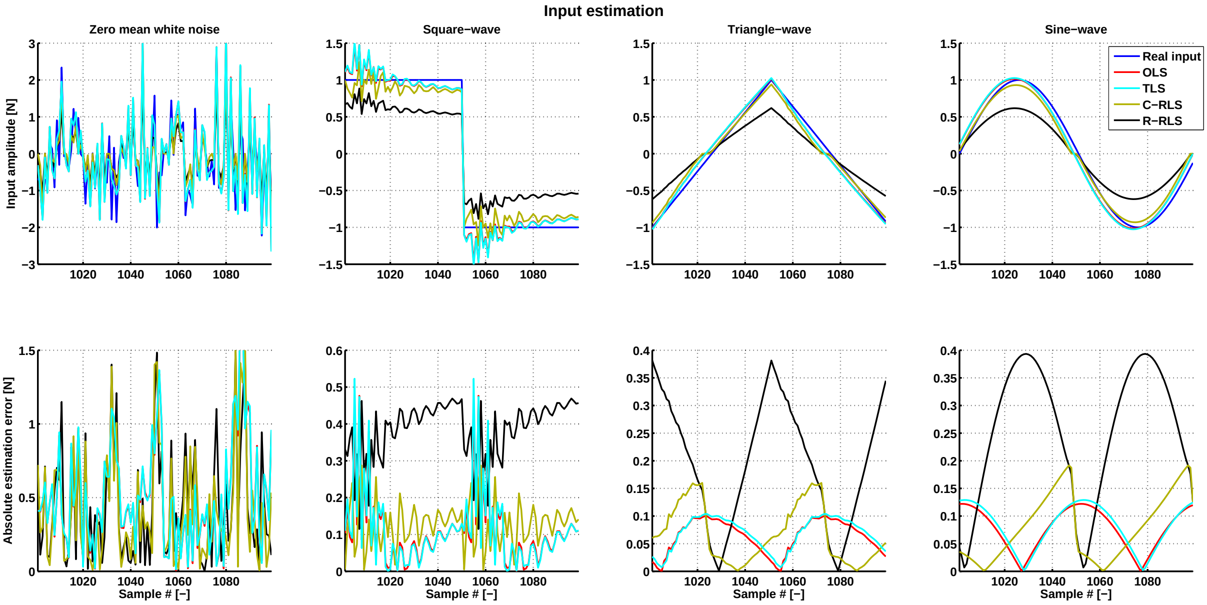

Figure 4-6: *This figure shows the input estimation results using the RHI estimator where the LS problem shown in Eq. 4-3 is solved using OLS, TLS, C-RLS and RLS. The estimate inputs are plotted together with the real input and the corresponding estimation error is shown. The estimation is performed on different kind of input signals. The RHI estimator has been constructed based on the lightly perturbed model and the uncertainty bounds $\delta(\mathcal{T}_f)$ and $\delta(\bar{r}_{k,f})$ corresponding to the severely perturbed model. The OLS solution is sometimes hard to see because it is overlapped by the TLS solution. The maximum and RMS errors are shown in Table 4-5.*

Table 4-5: *Input estimation errors for different input signals and LS algorithms. The RHI estimator is constructed using the lightly perturbed model and the used uncertainty bounds $\delta(\mathcal{T}_f)$ and $\delta(\bar{r}_{k,f})$ correspond to the severely perturbed model. This to show the effect of overestimating the uncertainty bounds of a model.*

Error type	Method	ZMWN	Square	Triangle	Sine
RMS	**OLS**	0.624	0.145	0.070	0.085
	TLS	0.633	0.154	0.074	0.090
	C-RLS	0.568	0.141	0.085	0.099
	R-RLS	0.577	0.394	0.227	0.282
Maximum	**OLS**	1.742	0.476	0.100	0.122
	TLS	1.767	0.523	0.104	0.129
	C-RLS	1.541	0.287	0.160	0.192
	R-RLS	1.522	0.469	0.381	0.393

OLS when the discontinuous input signals are considered. When continuous input signals are considered, then OLS produces better estimates.

R-RLS seems to under-perform compared to the other methods in this scenario.

The severely perturbed model using its uncertainty bounds.

Next the severely perturbed model is considered. The RHI estimator is now constructed using the severely perturbed model and the corresponding uncertainty bounds, which have been found in Subsection 4-3-3 are used. The graphical results can be seen in Figure 4-7 and the numerical results in Table 4-6. As can be seen the overall estimation error is much larger then for the lightly perturbed model.

It can be seen that the estimation difference between OLS and TLS has increased. In case of the square-wave input, TLS performs significantly better than all other algorithms.

A notable part of this result is that the shape of the square and triangle-wave cannot be recognized from the estimated input any more. Only the shape of the sine-wave gets reproduced accurately but with a more increased phase difference responsible for the largest error component.

C-RLS and R-RLS tend to underestimate the amplitudes in this case. It can also be seen that C-RLS

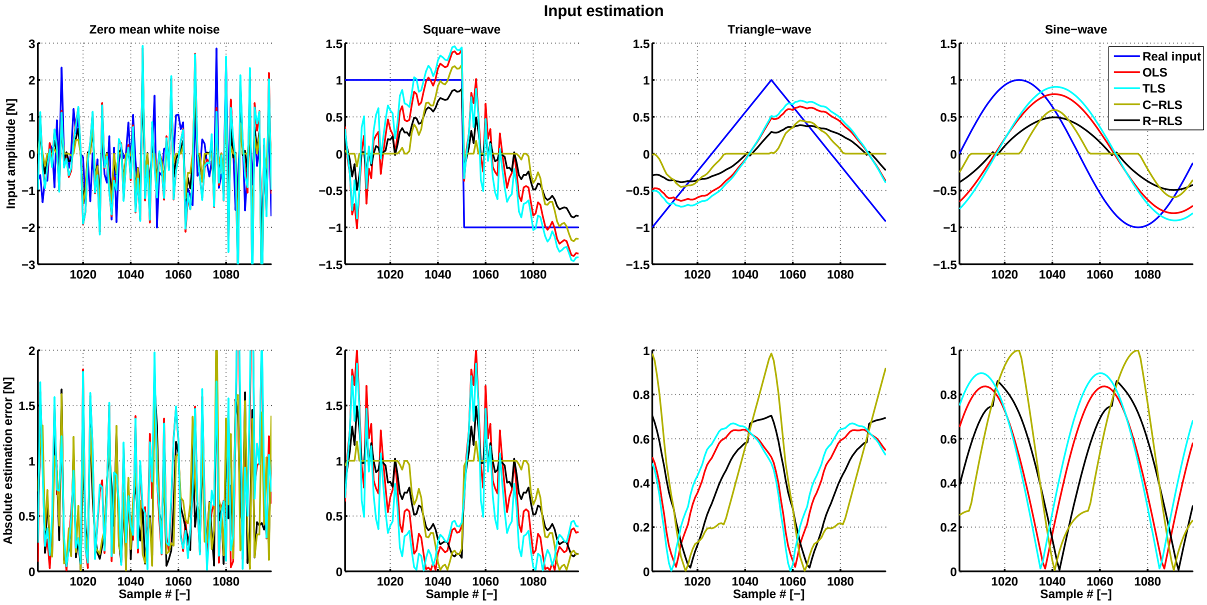

Figure 4-7: *This figure shows the input estimation results using the RHI estimator where the LS problem shown in Eq. 4-3 is solved using OLS, TLS, C-RLS and RLS. The estimate inputs are plotted together with the real input and the corresponding estimation error is shown. The estimation is performed on different kind of input signals. The RHI estimator has been constructed based on the severely perturbed model and the corresponding uncertainty bounds $\delta(\mathcal{T}_f)$ and $\delta(\bar{r}_{k,f})$. The maximum and RMS errors are shown in Table 4-6.*

Table 4-6: *Input estimation errors for different input signals and LS algorithms. The RHI estimator is constructed using the severely perturbed model and the obtained uncertainty bounds on $\delta(\mathcal{T}_f)$ and $\delta(\bar{r}_{k,f})$.*

Error type	Method	ZMWN	Square	Triangle	Sine
RMS	**OLS**	0.938	0.842	0.494	0.608
	TLS	0.970	0.588	0.493	0.638
	C-RLS	0.796	0.793	0.504	0.606
	R-RLS	0.739	0.784	0.467	0.575
Maximum	**OLS**	2.880	2.014	0.641	0.837
	TLS	3.099	1.880	0.669	0.897
	C-RLS	2.357	1.174	0.985	1.000
	R-RLS	2.076	1.493	0.704	0.861

sometimes produces very conservative estimates namely zero amplitude however, at moments in time this is indeed favorable and decreases the estimation error compared to OLS and TLS.

Again for the discontinuous input signals, the RMS and maximum error corresponding to the C-RLS and R-RLS estimates are lower compared to the OLS estimate. For the continuous input signals OLS provides again the best estimates.

The severely perturbed model using the lightly perturbed model's uncertainty bounds

Finally, one case has not been studied. The case where the bounds $\delta(\mathcal{T}_f)$ and $\delta(\bar{r}_{k,f})$ are underestimated. This is also an interesting case to evaluate and is simulated by using the bounds of the lightly perturbed model on the severely perturbed model. The results are presented in Figure 4-8 and Table 4-7.

The OLS and TLS results have again not altered since they do not use the uncertainty bounds. Furthermore, it can be seen that because of the smaller bounds C-RLS and R-RLS are less conservative and estimate larger amplitudes and in addition C-RLS does estimate less often a zero amplitude input. The advantages and disadvantages cancel out for the most part and compared to the previous case the errors have not changed much.

Again, C-RLS and R-RLS perform best for the discontinuous signals and performs best while for the continuous signals OLS is preferred. The change in performance of the RLS algorithms, caused by

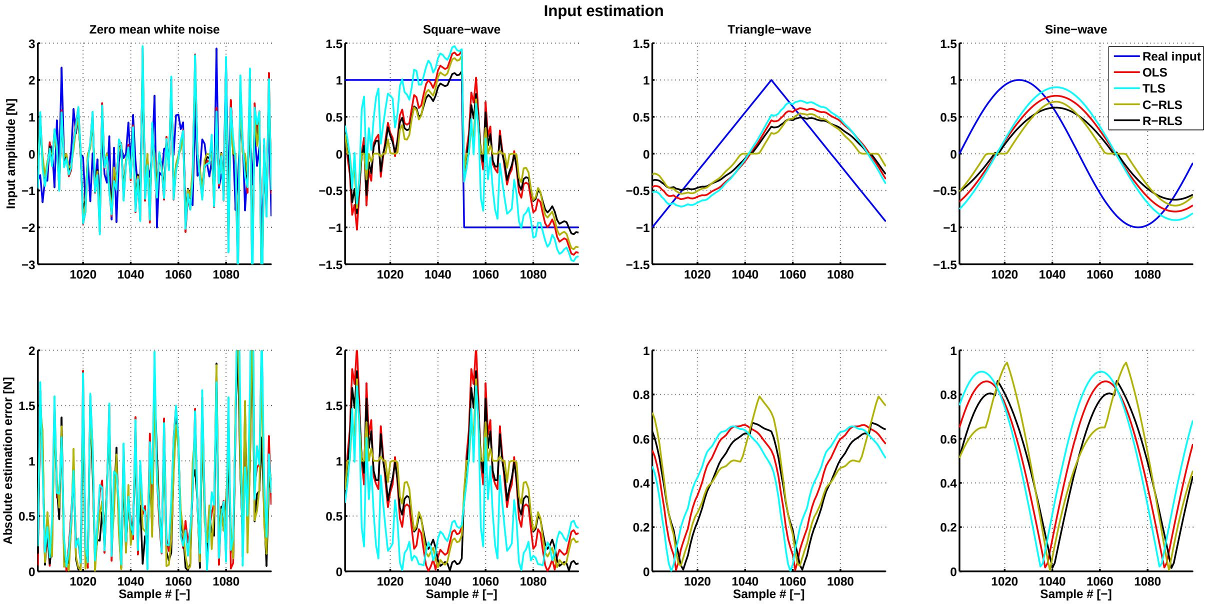

Figure 4-8: *This figure shows the input estimation results using the RHI estimator where the LS problem shown in Eq. 4-3 is solved using OLS, TLS, C-RLS and RLS. The estimate inputs are plotted together with the real input and the corresponding estimation error is shown. The estimation is performed on different kind of input signals. The RHI estimator has been constructed based on the severely perturbed model and the uncertainty bounds on $\delta(\mathcal{T}_f)$ and $\delta(\bar{r}_{k,f})$ corresponding to the lightly perturbed model. The maximum and RMS errors are shown in Table 4-7.*

Table 4-7: *Input estimation errors for different input signals and LS algorithms. The RHI estimator is constructed using the lightly perturbed model and the used uncertainty bounds $\delta(\mathcal{T}_f)$ and $\delta(\bar{r}_{k,f})$ correspond to the severely perturbed model. This to show the effect of underestimating the uncertainty bounds of a model.*

Error type	Method	ZMWN	Square	Triangle	Sine
RMS	**OLS**	0.938	0.842	0.494	0.608
	TLS	0.970	0.588	0.493	0.638
	C-RLS	0.852	0.803	0.486	0.595
	R-RLS	0.795	0.809	0.473	0.584
Maximum	**OLS**	2.880	2.014	0.641	0.837
	TLS	3.099	1.880	0.669	0.897
	C-RLS	2.350	1.739	0.791	0.944
	R-RLS	2.111	1.812	0.673	0.861

underestimating the uncertainty bounds, is not large. The RLS results have become qualitatively more similar to the OLS solution. Intuitively it makes sense because the estimation error size is related to the modeling error. When the uncertainty bounds are chosen relatively small, the RLS algorithms become more similar to a OLS problem. When the bounds are zero, they fully reduce to an OLS problem.

4-3-5 Robustness of RLS algorithms

In the previous section it is shown that C-RLS and R-RLS can reduce the estimation error, especially when discontinuous input signals are estimated. However, only four cases have been studied and it should be investigated if the use of C-RLS and R-RLS usually result in better estimations or only occasionally.

Therefore, for both the square-wave and ZMWN case 100 simulations have been performed each using a randomly generated model. The set of models from which the models are generated is defined as the real model with uncertainty bounds which are equal to those of the severely perturbed model namely: $k_{per} \subseteq k_{nom} \pm 20\%$, $E_{per} \subseteq E_{nom} \pm 20\%$ and $\zeta_{nom}/3 \leq \zeta_{per} \leq 3\zeta_{nom}$. Here the subscript *nom* again indicates the parameter value of the real model and subscript *per* the parameter value of the perturbed model. A plot of the RMS and maximum input estimation error for each experiment are shown in Figure 4-9 and 4-10. The errors are sorted from small to large. It should be noted that the error is plotted on a logarithmic scale and depending on the on the section of the graph, the same distance between lines can represent an estimation error that differs an order of magnitude.

Square-wave input signal

First, the results for the square-wave input signals, shown in Figure 4-9, are discussed.

As is shown, R-RLS provides a nearly constant RMS error for all experiments but this error is typically larger then the other algorithms except for the 6 worst case experiments. The maximum error of R-RLS is typically lower than that of the other algorithms except for the 25 best experiments. Clearly, R-RLS provides a trade-off between maximum and RMS error for this system.

C-RLS shows the same characteristics as R-RLS except that the differences are smaller. The difference of RMS error compared to OLS is slightly larger but C-RLS performs in the worst case also better then OLS. The maximum error of C-RLS is for the best 62 % of the experiments slightly larger then OLS but for the other 38 % its performance is much better.

Finally, the TLS algorithm performs usually very similar to OLS. However, the error is equal or larger to that of OLS and for the worst case scenarios the performance of TLS is unacceptably bad.

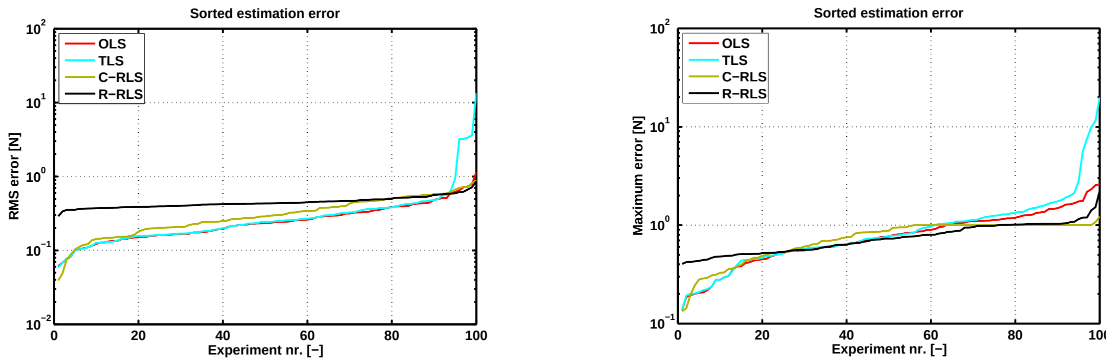

(a) RMS estimation error.

(b) Maximum estimation error.

Figure 4-9: *Sorted estimation error of RHI estimates using different LS algorithms. A square-wave input signal is estimated for 100 randomly generated perturbed models.*

Regarding C-RLS, it is concluded that the performance is slightly lower or much better then OLS, based on these 100 experiments. Therefore, C-RLS is a good choice when a discontinuous input signal such as a square-wave is considered for this model. TLS is not a suitable choice.

ZMWN input signal

Figure 4-10 shows the same graphs as in the latter, but then for a ZMWN input signal. The results are similar to those presented in Figure 4-9, but their are some clear difference in the favor of C-RLS and R-RLS.

As can be seen, R-RLS produces again a nearly constant RMS estimation error but, as opposed to the latter, wich is also typically lower then the other algorithms. R-RLS performs also better compared to the other algorithms in a maximum error sense. C-RLS also performs very good in these scenarios, it also performs typically equal or better then OLS. Finally, TLS again performs equally or much poorer then OLS. Even more so in the case a ZMWN input signal, it can be concluded that C-RLS and also R-RLS are a very suitable choice. They perform typically better then OLS in both an RMS and maximum error sense. TLS is again an unsuitable choice.

Detailed results regarding the square-wave input signal

As is shown, especially C-RLS is a tempting choice when the unknown input has a square-wave shape. The RMS estimation error is similar to that of OLS but performs better in the worst case scenarios. C-RLS performs also well compared to OLS in terms of maximum error which is comparable or much better.

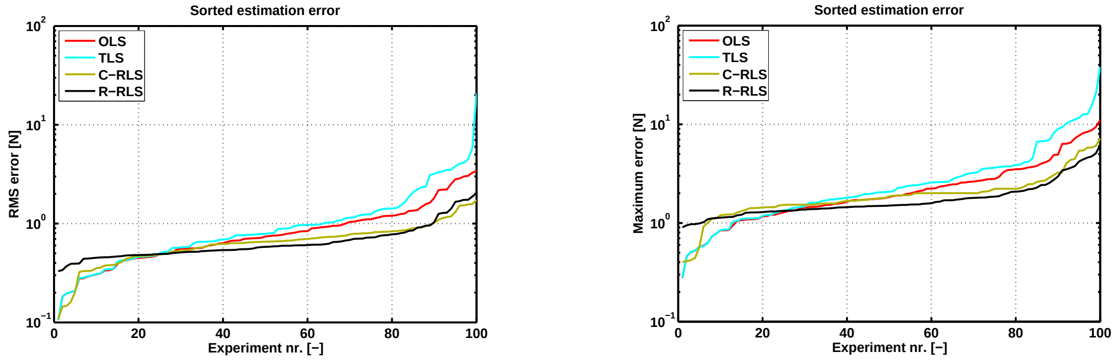

(a) RMS estimation error. **(b)** Maximum estimation error.

Figure 4-10: *Sorted estimation error of RHI estimates using different LS algorithms. A ZMWN input signal is estimated for 100 randomly generated perturbed models.*

In order to understand where this performance difference originates from, the results shown in Figure 4-9 are studied in more detail. Here a square-wave shaped input signals with an amplitude of 1 N is estimated. Box-plots are created that illustrates the distribution of the estimation error magnitude in time of each experiment. They are sorted by the RMS estimation error size and are shown in Figure 4-11.

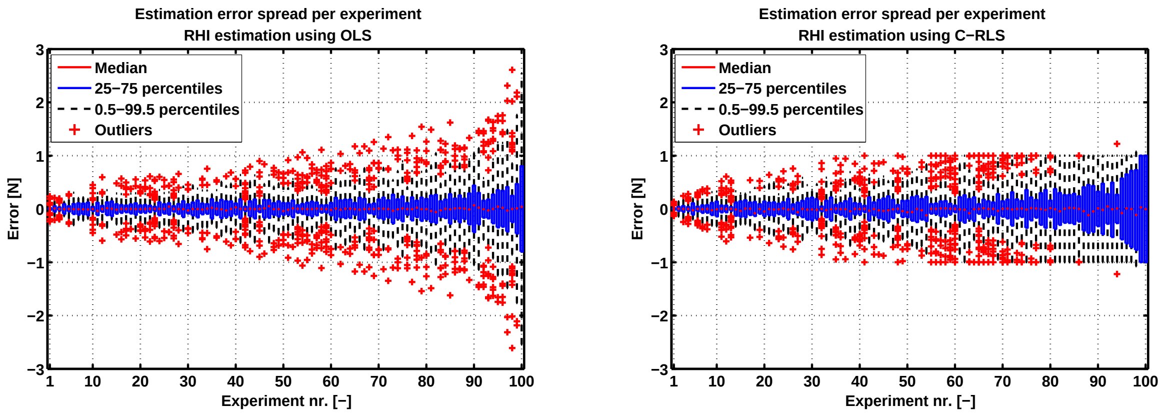

(a) RHI estimation using OLS **(b)** RHI estimation using C-RLS

Figure 4-11: *Figure 4-9 shows the sorted RMS and maximum estiomation error for 100 experiments where a square-wave input signal is estimated. These figures shows the estimation error spread per experiment for where the RHI estimation has been performed using OLS and C-RLS. It can be seen that their performance is comparable but that C-RLS has a limited maximum error because, it rather produces a conservative zero estimate, than a very uncertain but potentially more accurate estimate. OLS follows the latter approach, which results in much larger maximum errors.*

As can be seen, OLS performs well in the best case scenarios but also very bad in the worst case scenarios. C-RLS performance is very similar when the best case scenarios are considered. However, in the worst case scenarios the maximum errors are clipped because of the conservative nature of C-RLS resulting in a significantly reduced estimation error. C-RLS rather estimates a zero input (resulting in an error of 1) then risking to obtain an estimate in the wrong direction resulting in a larger estimation error. The price that is payed for limiting the maximum error of many samples, is that the error of many other samples, samples that would have been estimated reasonably, are also estimated as zero resulting in a much larger average error. Still, because of the significant reduction of maximum errors, C-RLS performs better then OLS in a RMS sense, in these worst case scenarios.

4-4 Conclusion

From the above simulations and results, several conclusions can be drawn. They are based on the simulations and results presented in this chapter.

First of all, it is shown that RLS can produce more accurate results then OLS. The performance does depend on the shape of the signal that needs to be estimated. Furthermore, using a more accurate model makes a larger differences than applying the right RMS method. Therefore, it is better to spend resources on improving the model than on tuning the RLS approach. However, when the model is 'as is' then RLS can improve the estimates.

First of all, TLS seems to be a bad choice since it almost always has the biggest RMS and maximum error. On the other hand, the performance of R-RLS produces conservative results for models with small perturbations. When the perturbation is increased, the estimation accuracy of R-RLS increases relative to the other algorithms. The performance of C-RLS and OLS are comparable.

C-RLS performs better for discontinuous input signals e.g. a square-wave or ZMWN. OLS performs better for continuous input signals such as a sine-wave or a triangle-wave. When the shape of the input signal is known, a preferred algorithm can be selected.

C-RLS and R-RLS performed especially better while estimating ZMWN input signals. Disturbance forces are typically of such a type and for such cases C-RLS and R-RLS do significantly increase the estimation performance.

Furthermore the performance of especially C-RLS is typically better based on simulations considering 100 differently perturbed models. The performance of C-RLS and OLS are similar and when the difference increases C-RLS typically is the better performing algorithm.

C-RLS and R-RLS rely on adequate estimates of the uncertainty bounds on $\delta(\mathcal{T}_f)$ and $\delta(\bar{r}_{k,f})$. When small model perturbations are considered, Theorem 2 and 3 provide useful estimates of these bounds for C-RLS such that in general, its performance is comparable to OLS. The performance of R-RLS is too conservative when these uncertainty bounds are used and smaller bounds are desired, even-though they are smaller then the actual uncertainty. When larger model perturbations are considered, Theorem 2 and Theorem 3 provide useful estimates for both C-RLS and R-RLS such that their general performance is comparable to OLS.

Finally, overestimating the uncertainty bound did decrease the performance of the RLS algorithms. On the other hand, underestimating the uncertainty bounds had a much smaller effect on their overall performance. When the bounds are estimated as zero, the RLS algorithms reduce to OLS problems.

This section is concluded with a remark. These conclusions are based and valid for this model with the assumed perturbations. If a different model is chosen, or different sized perturbations the results may be different. Therefore, it is always required to perform such a study when working with a different model.

Chapter 5

Setup Design

Experimental results are always preferred over simulations as foundation for validation of new theories. In order to obtain experimental results a setup is required. Besides experiments it is also important to demonstrate that the algorithms work under conditions that are comparable to the conditions present in their application. Therefore, an setup is designed that serves both as demonstrator and experimental setup. This design is presented in this chapter.

First the basic requirements are presented in Section 5-1. Then the analysis on which the concept design is based is presented in Section 5-2. Noise measurements have been done to quantify the performance increase related to the conceptual choices. These measurements and their analysis is presented in Section 5-3. Then the detailed design is presented in Section 5-4. In this section the analysis and conclusions are presented which lead to the final design. In Section 5-5 the performance of the manufactured and assembled setup is validated. Finally, this chapter is concluded with an overview of the conclusions in Section 5-6.

5-1 Setup requirements

The setup is designed to fulfill certain functions. They can be translated to requirements on the setup design such that these functions are implemented. These functions and requirements are presented in this section.

The setup is used to evaluate the developed estimation algorithms presented in Chapter 2. The setup must serve two goals. It should be usable as an *experimental setup* and as a *demonstrator setup*.

Both top-level functions are very abstract and can be divided in more specific sub-functions.

An experimental setup must be *modifiable* so that many different scenarios under different conditions can be evaluated. It should be *repeatable* in the sense that after modifications are made undone, new measurements must be comparable with initially obtained results. Finally, results must be *traceable* such that artifacts in the results can traced down to their origin in order to gain a better understanding of the results and algorithms.

A demonstrator setup should simulate *topologically similar conditions* of a wafer chuck in a real lithography machine. In this way it demonstrates that the estimation algorithms can be used in such applications successfully.

In the following sections the setup design is presented. The design is implemented such that all these requirements are fulfilled.

5-2 Conceptual design

The design phase starts by making conceptual choices. Conceptual choices should be made such that the system concept fulfills the required function in a good way. When done properly a good detailed design can then result in a very good system. When done improperly a good detailed design may result in an acceptable but never a perfect system.

The conceptual choices are based on the functions and requirements as stated in Section 5-1. First the most basic system layout is considered. From this analysis conclusions will be drawn on how to mount the essential components to the mechanical ground. A result will be to partially levitate the chuck. Then all advantage of a levitated chuck are discussed. Finally, the feasibility of a setup with levitated chuck is studied.

5-2-1 Basic system layout

The setup will be used to study the performance of the estimation algorithms in estimate the shape of a wafer chuck. The deformations are caused by disturbance forces. Already it can be concluded that at least three basic components will be required, namely: a *chuck*, *sensors* and *actuators*. The sensors are required to measure the shapes of the chuck at several locations. At least one actuator is required to apply disturbance forces to the chuck that cause it to deform. Furthermore, at least one additional sensor is required to measure the shape of the chuck at the *Point of Interest* (PoI). This measurement must be compared with the estimates produced by the shape fitting algorithms in order to validate the algorithms performance.

These components must be fixed with respect to the mechanical ground. Figure 5-1a shows a basic scheme from doing this. There, the chuck is supported by two supports and the actuators and sensors are mounted on the mechanical ground.

The actuator stiffness should be low. A high actuator stiffness will influence the shape of the chuck, which makes modeling more difficult and is as such less traceable. An actuator with zero stiffness allows the chuck to be freely deformable depending on the applied forces.

Furthermore, it is a well known fact is that the mechanical ground is not as vibration free as desired for performing high precision measurements. These floor vibrations propagate to the chuck causing unintended deformations which are measured as measurement noise. When the actuator stiffness is low, vibrations from the floor are not transferred via the actuator which results in better noise free measurements.

The concept shown in Figure 5-1a has several disadvantages. The supports supporting the chuck add parasitic effects such friction and hysteresis forces that will influence the shape of the chuck. Furthermore, floor vibrations propagate through the supports to the chuck causing unintended deformations which are measured as measurement noise.

This concept can by improved by levitating the chuck as is illustrated in Figure 5-1b. This removes the parasitic effects introduced by the chuck supports and floor vibrations cannot propagate through them anymore. In order to levitate the chuck a controller is required to compensate for the applied disturbance forces. This controller uses (some of) the sensors and actuators to position the chuck.

Yet, the sensors that are still mounted on the mechanical ground and will therefore measure the floor vibrations which will be interpreted as measurement noise. This problem can be solved by mounting the sensors to the mechanical ground using a low stiffness connections i.e. by mounting the sensors on a metrology frame. This is illustrated in Figure 5-1c. Low stiffness is defined such that the eigenfrequency of the sensors and their connection lies well below the lowest frequency of interest.

The concept as presented in Figure 5-1c reject floor vibrations very well by design. Furthermore, the chuck is positioned and measured in a contactless manner which avoids the introduction of unwanted friction and hysteresis forces.

5-2-2 Leviation

In the previous subsection it has been concluded that the setup should have a levitated chuck. However, a levitated chuck complicates the setup design significantly. Their are more reasons to require a levitated chuck. In this subsection these additional advantages are presented. Thereafter, the feasibility of the levitated concept is studied.

Advantages of levitation

One of the most fundamental decisions is to design a setup where the chuck is levitated. This choice is being considered because it rejects floor vibrations and positions the chuck in a contactless manner as explained in the previous subsection.

However, a levitated chuck has more advantages. A real lithography machine also has a levitated wafer chuck. Therefore, levitation can be considered a requirement such that the setup simulates topologically similar conditions as to a real lithography machine.

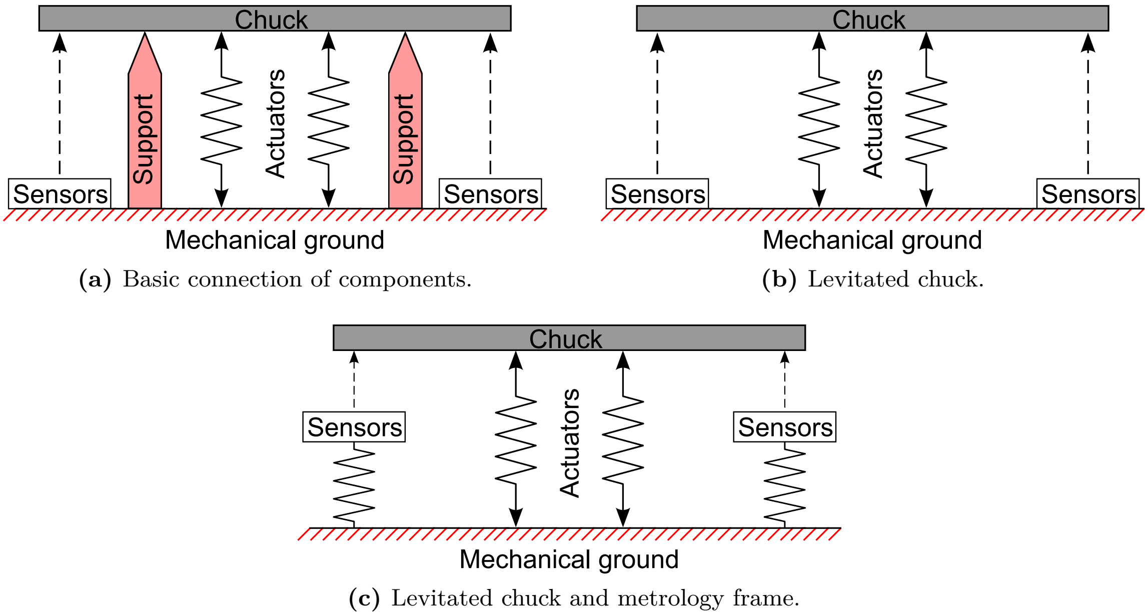

Figure 5-1: *Illustrations that show how the basic components namely: the chuck, sensors and actuators, can be fixed with respect to the mechanical ground.*

Furthermore, a levitated chuck is positioned using actuators. When proper estimates of the shape of the chuck are being produced by the shape estimation algorithms then these actuators can also be used to reposition the chuck to compensate for the deformations.

A levitated chuck also offers an additional interesting effect that can be studied. Repositioning the chuck by applying actuation forces will cause the chuck to change shape. The effect of these known actuation forces should be taken into account while compensating for the chuck deformations. When a levitated chuck is used, this coupling between positioning of the chuck and chuck deformations can also be studied.

It is possible to create a 6 Degrees of Freedom (DoFs) levitated stage however it would make the setup quite complex. Note that the deformations of interest happen in the space spanned by the 3 out-of-plane DoFs. The in-plane DoFs are therefore less of interest. Therefore, a hybrid solutions is proposed where the 3 out-of-plane DoFs are levitated while the 3 in-plane DoFs are kinematically fixed. The in-plane fixation is thoroughly designed and studied in Subsection 5-4-6.

The levitated concept

Finally, a concept design can be presented. Here the chuck is levitated using low stiffness actuators and the sensors are mounted on a vibration isolated frame. Only, the 3 in-plane suspended DoFs need to be kinematically fixed.

To avoid the entrance of floor noise trough this fixation this in-plane fixation should not be mounted directly to the mechanical ground. It should be mounted on its own, vibration isolated frame. However, then two vibration isolation arrangements are required which are expensive and will be unpractical to realize.

Therefore, it is decided to mount the in-plane fixation frame on the vibration isolation arrangement of the sensors. The in-plane fixation must fixate the in-plane DoFs while leaving the out-of-plane DoFs free. Therefore, the in-plane fixation introduces ideally no out-of-plane forces on the vibration isolated metrology frame. In addition, no in-plane forces will be acting on the chuck therefore no significant in-plane forces are introduced to the vibration isolated metrology frame.

By combining the abstract concept in Figure 5-1c with the decision to fixate the in-plane DoFs on the vibration isolated metrology frame one obtains the concept design shown in Figure 5-2.

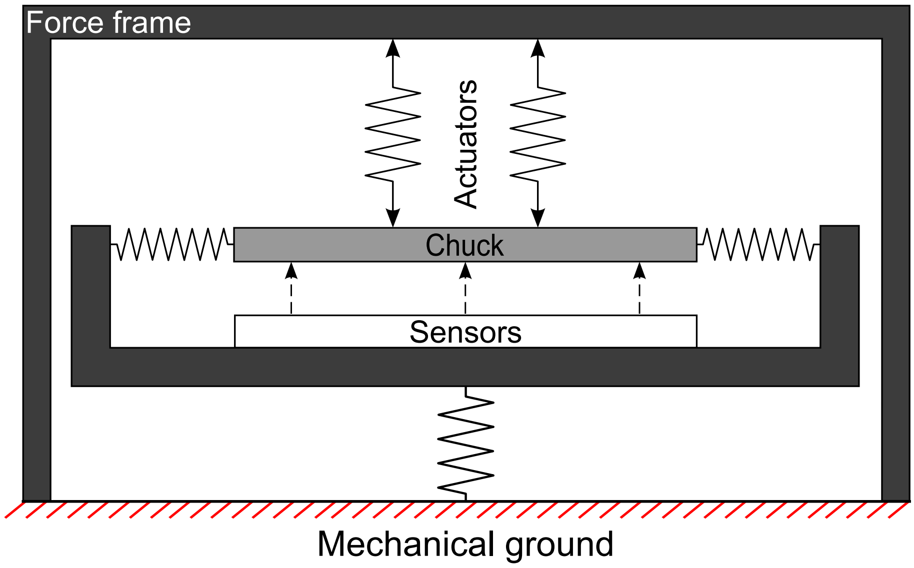

Figure 5-2: *This image illustrates the levitated concept. The sensors are mounted on a vibration isolated metrology frame. Actuators are used to position the chuck's out-of-plane DoFs i.e. partially levitate the chuck. The in-plane DoFs are fixated. No in-plane forces are acting on the chuck and the in-plane fixation introduces no forces in the out-of-plane direction. Therefore, the in-plane fixation is mounted to the vibration isolated metrology frame.*

Feasibility of the levitation controller

Before levitated concept is designed in detail, the feasibility of this concept is studied. The controller positioning the chuck is referred to as the *levitation controller*. Ideally, to simplify the design process, the design of the setup should be separated from the design of the levitation controller. This is only possible when the achievable controller bandwidth is very high. If the achievable bandwidth turns out is to be very low, the concept is unfeasible. Therefore, the aim of this feasibility study is to determine the maximum bandwidth of this levitation controller.

As explained in the latter, 3 out of 6 DoFs are controlled. Intuitively, the DoFs are orthogonal with respect to each other since they are defined in a standard Cartesian coordinate system. The transfer function matrix shown in Figure 5-3a confirms this thought. This transfer function matrix is created using the model introduced in Section 4-2. As can be seen, the transfers of off-diagonal elements, describing the interaction between the DoFs, are very small compared to the transfers of the diagonal elements. Therefore, the levitation controller will be implemented using 3 simple SISO controllers instead of 1 complex MIMO controller.

System dynamics typically limit the achievable controller bandwidth. A trick that can be performed is to collocate the actuators and sensors used by the controller. In this way the system dynamics are mostly masked and will not limit the controller bandwidth. An example of a typical open-loop transfer of such a system is shown in Figure 5-3b. As can be seen, the chuck's eigenfrequencies are visible but the phase stays bounded and goes never below -180 degrees.

When the sensors and actuators are assumed to be collocated, other aspects than the system dynamics are limiting the controller bandwidth, in this case the sampling frequency. Because the setup serves as an experimental setup it should be possible to perform additional tasks in the loop without having to worry about computationally efficiency. Therefore, the by design required sampling frequency should not be too high. To accommodate this requirement the maximum required sampling frequency is set at one 1kHz.

As will be seen in Subsection 5-4-1 the first eigenfrequency of the chuck in the setup will be around 100 Hz. As can be seen in Figure 5-3b, the next eigenfrequencies follow each other up quickly with relatively high resonance peaks. A constant relative damping ratio of $\zeta = 0.005$ is assumed for all modes which is a rather high value based on [32]. In order to avoid aliasing the system response should be practically 0 after 500 Hz. When the controller bandwidth is selected too high, this will clearly not be the case.

Filtering can be applied but, in order for a first order filter to have significant effect, its cut-off frequency should be well placed below the 500 Hz, for example at 50 Hz. This filter will already add

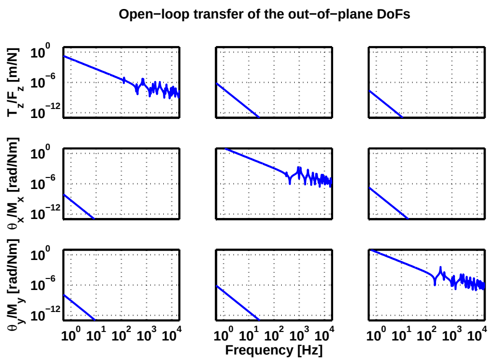

(a) Transfer function matrix of the chuck's 3 out-of-plane DoFs that are controlled by the levitation controller. The inputs are forces or moments where F_z denote a force in the z-direction and M_x and M_y denote moment around respectively the x and y-axis. The outputs are positions or angles where T_z, θ_x and θ_y are respectively translations in z-direction and rotations around the x and y-axis.

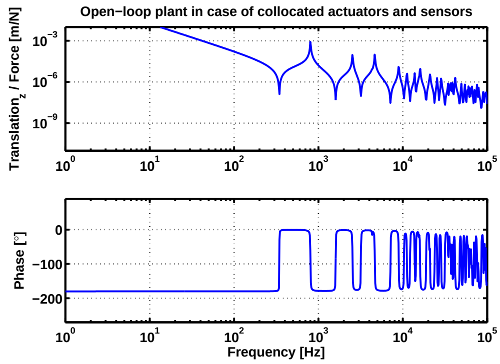

(b) This figure shows a typical transfer function of a system with collocated actuators and sensors. The special property is that the phase is not going to $-\infty$ but never comes below -180 degrees.

Figure 5-3: *Two important system properties used designing the levitation controller such that its feasibility can be studied.*

45 degrees of phase lag at this frequency. Then, if a phase margin of 30 degrees is required, not much margin for error is left. When using a higher order low-pass filter the cut-off frequency can be placed at a higher frequency, but it will also add more phase at this frequency. Because the phase starts dropping well before the cut-off frequency the usage of a higher-order low-pass filter does not solve this problem. Therefore, it is concluded that adding a low-pass filter does not allow the controller bandwidth to be increased significantly.

In order to illustrate the bandwidth limitations related to the sampling frequency, some simulations have been performed using the model introduced in Section 4-2. The number of elements has been increased to 8x8, the relative damping ratio is selected as $\zeta = 0.005$ and an aluminum chuck with the dimensions given in Subsection 5-4-1 are used. A step shaped force of 1 N is applied at time 0.01 seconds at the center of the chuck. The translation in z-direction of four points on the chuck are measured. The difference in their response is caused by deformations of the chuck. The first eigenfrequency of the chuck lies at 120 Hz. The controller is a *PID-controller* which is tuned using the rules-of-thumb that can be found in [33]. A short summary of these rules is provided now.

The PID-controller that is considered is of the form:

$$\begin{aligned} C =& K_p + \frac{K_d s}{\frac{s}{N}+1} + K_i \frac{1}{s} \\ =& K_p \left(1 + \frac{\tau_d}{\frac{s}{N}+1} s + \frac{1}{\tau_i s}\right). \end{aligned}$$

Here K_p is the proportional gain, K_d the differentiator gain and K_i the integrator gain. N controls the differentiator cut-off. The gains K_d and K_i can be expressed in respectively the time constants $\tau_d = K_d/K_p$ and $\tau_i = K_p/K_i$. These time constants are related to frequencies as $f_d = 1/(2\pi\tau_d)$ and $f_i = 1/(2\pi\tau_i)$. The desired bandwidth f_{bw} is selected manually. Then the differentiator frequency is placed as $f_d = f_{bw}/3$. The integrator frequency is placed as $f_i = f_{bw}/10$. The differentiator cut-off is computed as $N = 2\pi \cdot 3f_{bw}$. Finally K_p is computed using the systems open-loop gain at frequency f_{bw} denoted as $G\left(2\pi f_{bw}\right)$. Using this number K_p is obtained by evaluating: $K_p = 1/\left(3G\left(2\pi f_{bw}\right)\right)$.

Simulations have been performed based on this controller for different selected controller bandwidths f_{bw}. The results can be seen in Figure 5-4. As can be seen in Figure 5-4a, with a bandwidth of 12 Hz and a sampling frequency of 1 kHz, the chuck will move about 750 μm. The deformations are in the order of 10 μm. In Figure 5-4b, the bandwidth has been increased to 50 Hz and the sampling frequency is unaltered. Now the system becomes unstable. Then the result in Figure 5-4c, is obtained using the same controller bandwidth of 50 Hz but for an higher sampling frequency of 10 kHz. As can be seen, the

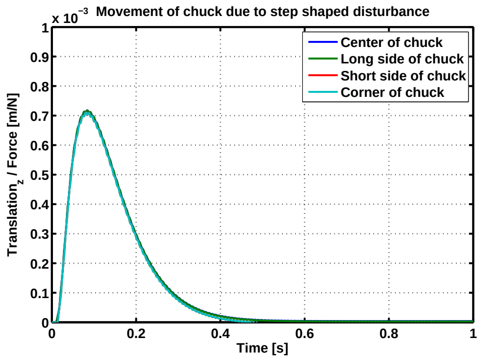

(a) Controller bandwidth of 12Hz and a sampling frequency of 1kHz.

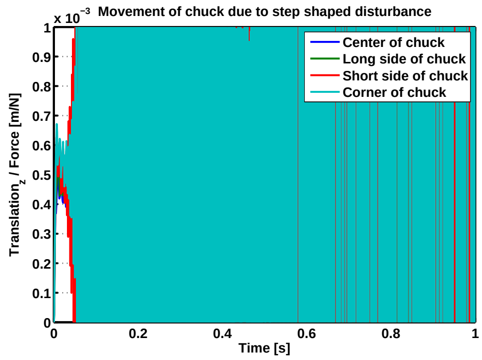

(b) Controller bandwidth of 50Hz and a sampling frequency of 1kHz.

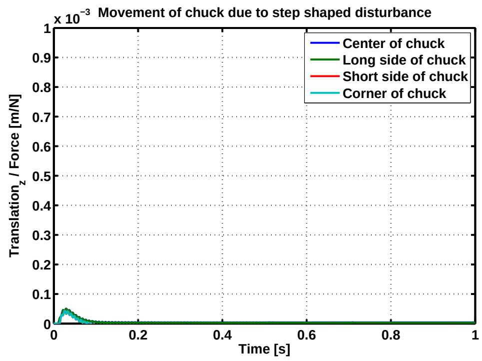

(c) Controller bandwidth of 50Hz and a sampling frequency of 10kHz.

Figure 5-4: *These plots show the response of multiple points on a levitated chuck. The movement is cased by a step shaped disturbance force of 1 N acting on the center of the chuck. The difference in the response of the points is due to deformations of the chuck. The experiment is repeated for three combinations of controller bandwidth and sampling frequencies.*

system is stable again and the movement of the chuck is much smaller because of the higher controller bandwidth. Unfortunately demanding a sampling of 10 kHz is limiting the flexibility of the experimental setup and as explained 1 kHz is chosen as upper limit on the minimum required sample frequency. Based on many of these simulations, a good choice for the controller bandwidth is: $f_{bw} = f_1/10$. Here f_1 denotes the first eigenfrequency of the chuck.

From this analysis it can be concluded that the controller bandwidth, and thus controller stiffness, is limited. When collocating the actuators and sensors, the limitation is caused by the limited sample frequency. Because of the limited controller stiffness, the chuck will experience relative large movements when disturbance forces are acting on the chuck are inflicting deformations.

Based on this analysis it is concluded that the levitation controller bandwidth is not very low. To be more specific, the ratio between translations and deformations of the chuck is small enough such that the sensor requirements are reasonable. However, the levitation controller bandwidth can also not be very high. Therefore, the levitation controller must be considered during the detailed design of the setup.

5-3 Measurement noise

Measurement noise should always be considered when designing a high-performance system.This is also the reason why the analysis in Section 5-2 about noise rejection has been performed. Measurements noise is limiting what can and cannot be measured.

Measurement noise consists not only of sensor noise. It is a sum of a variety of *noise sources* acting on the system. One can think of sources such as: *floor vibrations*, *electronic noise* and *sensor noise*.

Floor noise are the vibrations of the floor due activity in the building. Electronic noise, is noise from transducers such as current amplifiers or Analog to Digital Converters (ADCs). Sensor noise is actually a form of electronic noise. By taking smart design decisions the measurement noise can be reduced enormously by decreasing and/or removing the influence of different noise sources.

Noise measurements are performed in order to quantify the performance increase related to the conceptual decisions presented in Section 5-2. The results are presented in this section.

5-3-1 The measurements and their analysis

Working principle of geo-phone

In order to measure the ground vibration velocities, geo-phones of type GS-11D are used. The working principle is that a permanent magnet is moving relative to a coil, both inside the geo-phone. Because of the changing flux through the coil, a potential difference is induced that can be measured. The changing flux is proportional to the relative velocity of the two parts. One of the parts is fixed to the geo-phone's casing and the other is mounted via a suspension to this casing. When the casing is moving so will the magnet relative to the coil. The casing will move because the surface where the geo-phone is mounted on moves.

It is not difficult to shown that the transfer function describing the output voltage as function of ground velocities equals:

$$\frac{V}{\dot{x}_0} = \frac{G\left(\dot{x}_1 - \dot{x}_0\right)}{\dot{x}_0} = \frac{-Gms^2}{ms^2 + cs + k},$$

A derivation can be found in e.g. [34]. In this equation, V denotes the output voltage which is proportional with gain G to the velocity difference between the mover and the geo-phone's casing described respectively by $\dot{x}_1$ and $\dot{x}_0$. m is the mass of the mover and the stiffness and damping coefficient of the mover's suspension are respectively denoted by k and c. A bode plot of this transfer function is shown in Figure 5-5. The selected parameters correspond to geo-phone type GS-11D which can be found in [35]. This plot provides the sensitivity of the geo-phone as function of frequency. As can be seen, for low

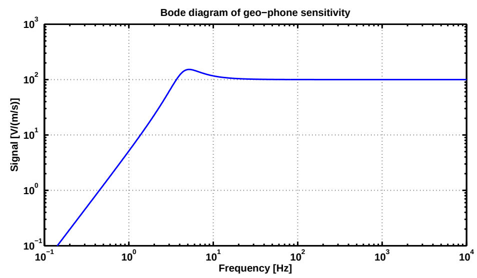

Figure 5-5: *Transfer between output voltage and casing velocity of a GS-11D geo-phone with open leads.*

frequencies the geo-phone has a very low sensitivity, then a well damped resonance occurs and finally for higher frequencies the sensitivity becomes constant.

Analysis of measurements

Here the measurements, including their analysis are presented and it is shown that the method used for analysis is numerically stable and physically sound.

The measurements are obtained as a time series of points representing an potential difference at each time step. The signals need to be filtered in order to get an reliable velocity estimate. In addition, the influence of these floor velocities on the setup need to be evaluated.

Before the measurements are digitized using an ADC, they are low-pass filtered using a first order filter in the analog domain with a cut-off frequency of 1 kHz. The sampling frequency is 10 kHz. Then in the digital domain, the measurements are compensated for the transfer shown in Figure 5-5. This is done by multiplying the obtained measurements by the inverse transfer of the geo-phone. Of course, the signal has a certain noise level so for very low frequencies only noise will be present in the signal. Therefore, a high pass filter needs to be applied. Finally, the obtained velocities need to be converted to deformations of the chuck since these will be measured and interpreted as measurement noise. This can be summarized in the block scheme presented as in Figure 5-6.

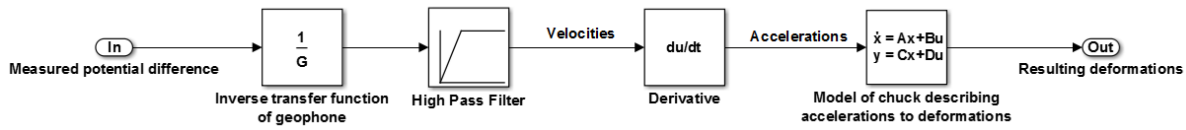

Figure 5-6: *Measurement post-processing steps to obtain an estimate of the chuck deformations caused by floor vibrations. These deformations are unwanted and show up as measurement noise in measurements obtained from the experimental setup.*

Figure 5-7 shows the filters in more detail. First the measurements are filtered with the inverse of

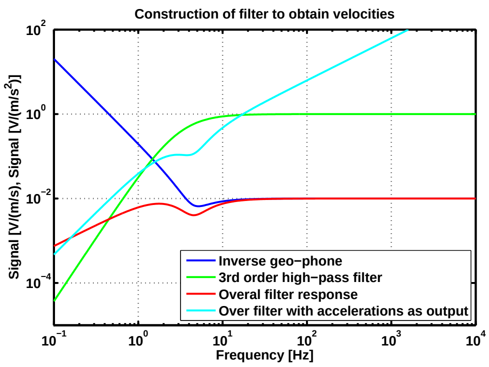

(a) This figure shows how the filter is constructed that is used to obtain velocity values based on the measured potential differences from the geo-phone. Finally, the velocities are converted to accelerations which makes it easier to predict the chuck's deformations.

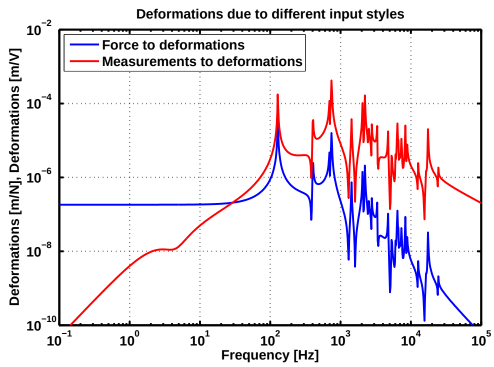

(b) This figure shows the size of a typical deformations of the chuck due to two different causes. The blue line shows deformations due to forces acting on the chuck. The red line shows the transfer of measured potential differences from the geo-phone to chuck's deformations for the case of a levitated chuck.

Figure 5-7: *These plots show in more detail than Figure 5-6 how the measurement signals are processed. As will be explained in the text it will be concluded that these filters yield reliable results.*

the geo-phone transfer. At low frequencies the measurement will contain only noise because of the low sensitivity of the sensor. To avoid unrealistic results, this low frequency content will be filtered out using a high pass filter. Since the inverse transfer of the geo-phone has a -2 slope in the considered low frequency region, the high pass filter must be at least of 3rd order and therefore a 3rd order filter is selected. Finally, the signals are converted to accelerations because it allows for easier calculations of the resulting chuck deformations. This sequence of filters is shown in Figure 5-7a.

The system response due to disturbance forces is shown in Figure 5-7b. Accelerations cause forces that in turn cause the undesired deformations. The red line in Figure 5-7b shows the total filter response. As expected low frequencies will cause almost no deformations since the accelerations and thus forces are very low. High frequencies will cause also almost no deformations. This is because the inertia of the mechanical system is limiting the movement of the portions mass of the chuck. The frequencies in between will contribute most to the deformations. These results are in line with the expectations. Next the filters are implemented and tested for numerical stability.

Implementation of filter and discussion of results

At least two often used methods can be considered to filter measurements, namely: *time domain* analysis and *frequency domain* analysis. Time domain analysis has as advantage that it is very intuitive and can be adjusted easily. On the down side it is computationally much more demanding and less robust. Frequency domain analysis, when performed properly, is numerically much more stable but harder to adjust for different scenario.

The time domain analysis boils down to a sequence of filters that will filter the data. The system model can also be seen as a filter with a certain transfer between input and output.

Only the magnitude has been taken into account with the performed frequency domain analysis. The phase of the noise signals are not of any interest and is therefore omitted. The frequency analysis boils down to creating an amplitude spectrum of the measurements, multiplying it with the magnitude line of all transfers, and finally an output amplitude spectrum is obtained.

The steps shown in Figure 5-6 are performed using time domain and frequency domain analysis. Both methods are investigated and the results are compared. For this study a typical measurement has been used. The obtained conclusion is also valid for the other measurements. Conclusions on the actual noise level will be drawn in Subsection 5-3-2. Now only the measurement processing methodologies are tested and compared.

In Figure 5-8 the results are shown. In Figure 5-8a a typical measured amplitude spectrum of the floor noise is shown. This noise is clearly spread widely around 10Hz. Most of it comes from the building and suspension of the lab itself. The clear dynamic resonances are likely due to the large 700kg granite block that is suspended on a three steel points.

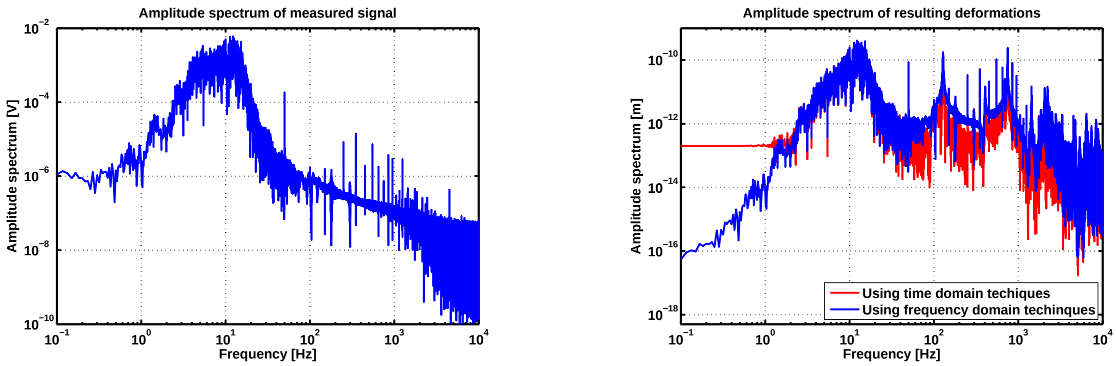

(a) The amplitude spectrum of a typical measurement obtained using a geo-phone which is used for the noise analysis.

(b) The amplitude spectra of the resulting deformations due to the noise spectrum shown in Figure 5-8a. Both the time domain and frequency domain analysis results are drawn so that they can be compared.

Figure 5-8: *Amplitude spectra of the measured noise signal and the resulting deformations. Two numerically different methods used to obtain the output spectrum are compared.*

In Figure 5-8b the amplitude spectra of the resulting deformations are shown. The spectrum corresponding to the blue line is computed using frequency domain techniques and the spectrum corresponding the red line is computed by filtering the signals in a time domain sense. Both methods result in similar results but their are clear differences. The time domain methods produces a more noisy output spectrum, caused by numerics. It was found that the performance of the high-pass is very bad cause by the large ratio between (high) sampling frequency and (low) cut-off frequency.

The frequency domain methods outperform the time domain methods. Therefore, the frequency domain methods are used in the subsequent analysis.

5-3-2 Noise sources

There are many noise sources contributing to the total amount of measurement noise. The noise sources that are expected to be the most important are investigated. This is done in order to quantify the performance increase related to the conceptual decisions presented in Section 5-2. Each case illustrated in Figure 5-1 on page 63 is considered.

Because the sensor noise specifications are specified as Peak-to-Peak (P-P) the results are presented in terms of peak to peak. Here the convention is used that the P-P = 8RMS which is a commonly used factor. In Appendix C it is shown that this is a very good approximation.

Sensor noise

Sensor noise is one important measurement noise sources. When the sensor was selected the noise level was specified to be 12 nm P-P when a bandwidth of 1kHz is considered. In order to measure a deformation 5 sensors will be used. As is presented in Subsection 5-4-4 and 5-4-5, four sensors are used to measure the position of the chuck as if it was a rigid body. Then, the remaining sensor measures the position of the chuck at the PoI. Therefore, the measurement noise due to sensor noise is, when assuming the sensor noise us uncorrelated, $\sqrt{5} \cdot 12\,\text{nm P-P} = 27$ nm P-P.

This noise level can be lowered at the cost of using better and thus more expensive sensors. Detailed information about the sensor selection can be found in Subsection 5-4-5.

Floor vibration measurements

First we look at the contribution of floor vibrations to the total measurement noise. The first thing that is of interest is what has exactly been measured and this will be discussed now.

The setup will be placed on the granite table shown in Figure 5-9a. The granite block is suspended on three steel pivots mounted on a solid steel frame. The granite block will move in 6 DoF and the vibrations can be clearly felt when it is pushed. Only the 3 out-of-plane DoFs of the chuck are studied, and therefore only floor vibrations that will have significantly affect in these directions are measured which are also the out-of-plane DoFs of the granite block. Because only 4 geo-phones where available, 2 horizontal, and 2 vertical variant, the measurements had to be performed in two parts. Both measurement conditions are shown in Figure 5-9.

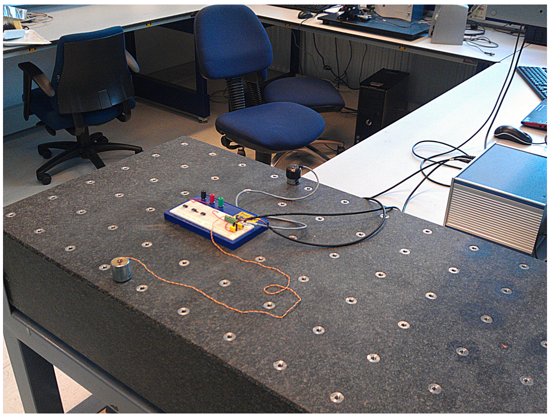

(a) The place where the setup will be constructed. This is at this end of the granite table. The two geo-phones on top measure a rotational DoF.

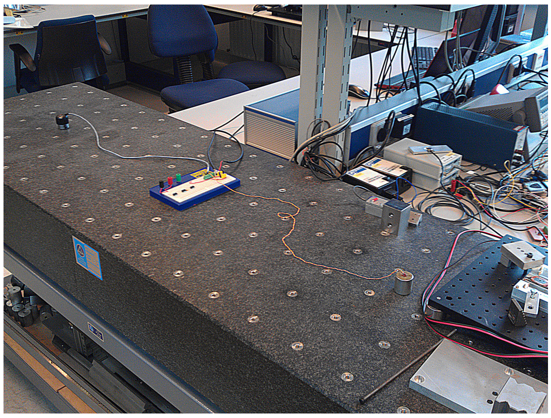

(b) Two geo-phones mounted to measure the translational and the other rotational DoF.

Figure 5-9: *These figures show the location of the setup and the sensor placement in order to measure the floor vibrations.*

Finally, one large datasets is created which contains for the DoFs of interest the vibrations of the table top. These are filtered as described in Subsection 5-3-1 such that an estimate of the the resulting chuck deformations due to these vibrations are obtained. This shown Figure 5-10.

As is shown, the amount of measurement noise caused by floor vibrations for a non-levitated chuck will be 27 nm P-P which is a significant amount of noise compared to the sensor noise. When the chuck is levitated this is reduced to 20 nm P-P which is only a small reduction.

It is trivial that when the chuck will deform when it is supported on a mechanical ground that vibrates. Based on the measurements this results in an expected measurement noise contribution of 27 nm P-P. When the chuck is levitated, but the sensors are mounted on the mechanical ground, will makes that the sensors still move. The controller makes the chuck follow these movements, and as a result, actuator forces are applied to the chuck which cause it deformation. These deformations are expected to have a magnitude of 20 nm P-P.

The reduction comes from the fact that the controller has a limited bandwidth as is discussed in Subsection 5-2-2. Because of this limited bandwidth only the floor vibrations with a frequency within the controller bandwidth will result in controller forces on the chuck. This means that the the floor vibrations

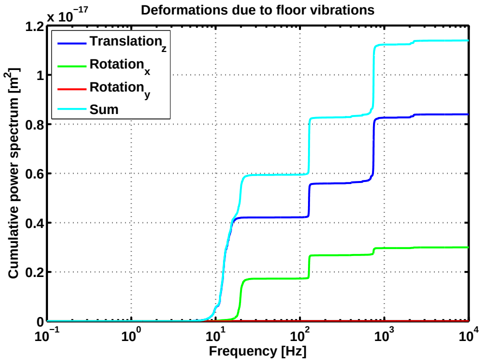

(a) Contribution of the measurement noise due to the floor vibrations for a non-levitated chuck. This corresponds to the scenario illustrated in Figure 5-1a.

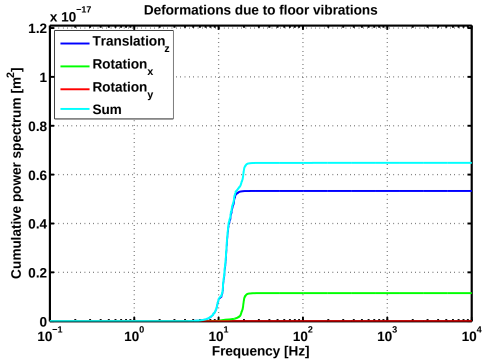

(b) Contribution of the measurement noise due to the floor vibrations for a levitated chuck without metrology frame. This corresponds to the scenario illustrated in Figure 5-1b.

Figure 5-10: *This figure shows the contribution of floor vibrations to the overall measurement noise.*

are effectively low-pass filtered before they are transferred to the chuck. Thus, the high frequent floor vibration components are not transferred and therefore the measurement noise level is decreased. An additional measure that can be taken to reduce floor vibrations is by mounting the sensors on a vibrations isolation table which is discussed in Subsection 5-2-1 and illustrated in Figure 5-1c. This measure will be discussed in the conclusion of this subsection.

Vibrations due to reaction forces

The actuators are connected to the mechanical ground. When forces are applied to the chuck reaction forces will be acting on the mechanical ground. Because of these forces the floor can start to vibrate. An unfortunate property of these vibrations is that they show up as noise which is correlated with the measurements signals since the applied disturbance force induces the effect that is studied on the setup. Longer measurements will therefore not cancel out this noise.

To get an idea of the influence of the reaction forces on the vibrations of the mechanical ground its transfer has been identified experimentally. This is done using an impact hammer as shown in Figure 5-11a. The impact hammer uses a soft tip in order to concentrate the impact energy in the lower frequency regions. A typical measurement obtained from the experiment can be seen in Figure 5-11b. From such a result the transfer from forces to the resulting floor vibrations can be estimated. The influence of these floor vibrations is estimated in the same way as for the latter results.

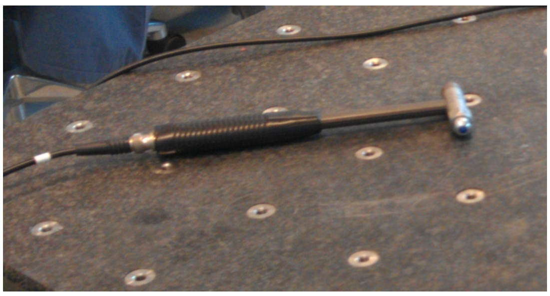

(a) The used impact hammer with soft tip to concentrate the impact energy in the lower frequency regions.

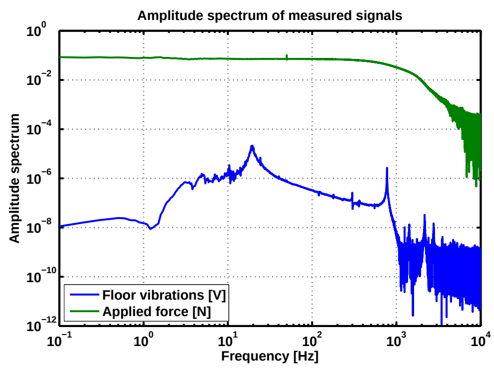

(b) A typical measurement result of the measured floor vibrations when the granite table (shown in Figure 5-9a) is hit by the impact hammer.

Figure 5-11: *These figures show how the floor vibrations induced by reaction forces are measured. These are used to estimate the corresponding measurement noise component.*

A typical force acting on the chuck is the intentionally applied disturbance force to induce the deformations that we wish to measure. This force can be freely selected and a logical candidate is a sinusoidal disturbance force of different frequencies. From the identified transfer a frequency can be identified where it will produced the largest amount of floor vibrations. The setup should also function as expected for this worst case choice of disturbance force. Therefore, this force is chosen to benchmark the noise performance.

When the chuck is supported low frequent reaction forces of the actuator are compensated by low frequent reaction forces of the support. The floor will only start vibrating when these reaction forces are out of phase. This happens at the first eigenfrequency of the chuck which is about 120 Hz. When the chuck is levitated, the reaction forces of the disturbance force are only compensated by the reaction forces of the levitation controller's actuators when the disturbance force's frequency is within the levitation controller's bandwidth. In Subsection 5-2-2 this is estimated at 12 Hz. Therefore, the worst frequency of the disturbance force is in this case 21 Hz, as can be seen in Figure 5-11b. The considered amplitude of the disturbance force is 1 N.

The analysis is performed in a similar fashion as the latter. Except in this case, we look at a specific frequency. Cumulative power spectra plots are therefore not of any interest since they are a tool to show results over a frequency range.

For a supported chuck the expected measurement noise 19 nm P-P. When the chuck is levitated the expected measurement noise is reduced to 5 nm P-P. This large decrease of noise can be explained because 21 Hz lies outside the controller bandwidth and is therefore again filtered out when floor vibrations are transferred to the chuck.

Noise from current amplifiers

In order to apply forces, actuators are required. As explained in Subsection 5-2-1 low stiffness actuators are desired, and it will be discussed in Subsection 5-4-4, that Lorenz actuators are a good choice. In order to apply forces, the current through these actuators must be controlled and for this purpose current amplifiers are used. As for every device, current amplifiers are also not perfect and they have a certain noise level at their output. The noise level of a current amplifiers of the type we intend to use, is measured. A stack of these amplifiers is shown in Figure 5-12a.

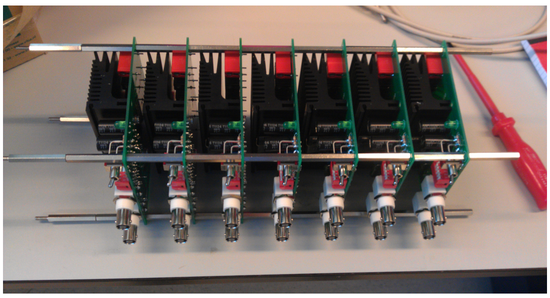

(a) Current amplifier stack of 7 current amplifiers which are used in the setup. All soldered by hand

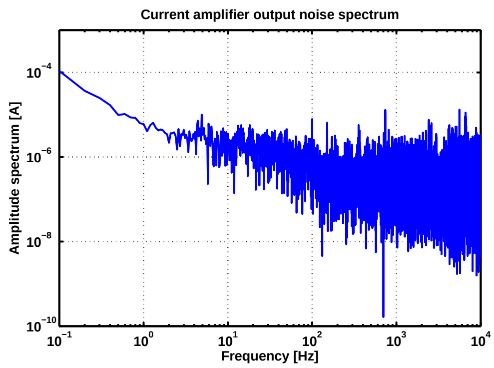

(b) This figure shows the output spectrum of a constant current.

Figure 5-12: *The current amplifiers that are used and there output noise spectrum.*

Figure 5-12b shows the amplitude spectrum of and constant output current of 2 A. The experiment was repeated for a 10 times lower current of 200 mA and the measured noise level was similar. Therefore, it is concluded that the noise level is independent of the output current.

A noise spectrum as shown in Figure 5-12b will result in unintended force on the chuck causing it to deform. Theses forces come from the actuator used to apply the disturbance force and, in case when the chuck is levitated, also from the actuators used for levitating it. The resulting deformations due to these forces are estimated in a similar way as described in Subsection 5-3-1 but fortunately the processing of the measurement signal is far simpler. The magnitude of the resulting deformations are shown in Figure 5-13.

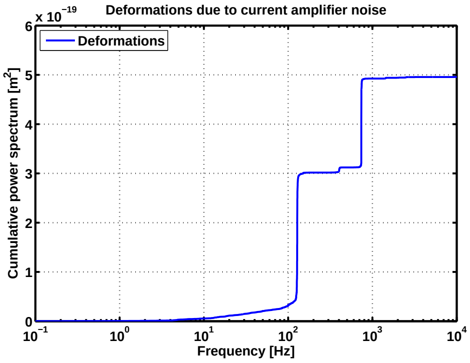

(a) Contribution of the measurement noise due to the current amplifier noise for a non levitated chuck. This corresponds to the scenario illustrated in Figure 5-1a.

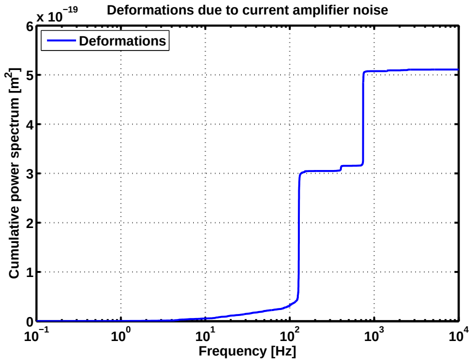

(b) Contribution of the measurement noise due to the current amplifier noise for a levitated chuck. This corresponds to the scenario illustrated in Figure 5-1b.

Figure 5-13: *This figure shows the contribution of current amplifiers output noise to the overall measurement noise.*

As is shown in these figures, the noise levels are respectively 5.6 nm P-P for a non-levitated chuck and 5.7 nm P-P for a levitated chuck. Since more actuators and current amplifiers are required when the chuck is levitated, the noise level is slightly higher in this case. The largest deformations are caused by the actuator applying the disturbance forces which is present in both topologies. Therefore, the noise levels are similar.

Conclusions

In this section the four most important sources of measurements noise have been analyzed. Their contributions are computed for a non-levitated chuck and a levitated chuck. In order to clearly see how the conclusions from Section 5-2 influence the noise performance of the setup, a short overview is presented here. A summary of the computed noise levels can be found in Table 5-1. Some interesting conclusions can be drawn from these results.

Table 5-1: *This table provides a summary of the expected measurement noise sources and there sum. These sources are assumed to be uncorrelated.*

	Non-levitated (See Figure 5-1a)	**Levitated** (See Figure 5-1b)	**Levitated with metrology frame** (See Figure 5-1c)
Floor vibrations [nm P-P]	27	20	<0.20
Reaction forces [nm P-P]	19	5.0	<0.050
Current amplifiers [nm P-P]	5.6	5.7	5.7
Noise of 5 sensors [nm P-P]	27	27	27
Total [nm P-P]	**43**	**34**	**28**

First of all the the non-levitated case is considered. All noise sources are in the same order of magnitude as the sensor noise. Selecting a better sensor will thus be of no use if a lower noise level is desired.

Second, it can be seen that levitating the chuck indeed does lower the total noise level. Especially, the transmission of measurement noise due to reaction forces is significantly lowered. The floor vibrations however, still form the biggest noise source.

Levitation does not change much about the measurement noise level caused by the current amplifiers. This is not a big limitation because their noise level are of an acceptable level.

Finally, as mentioned before in this section, the transmission of the floor vibrations can be reduced by mounting the sensors on a separate, vibration isolated, metrology frame. This topic is discussed in Subsection 5-4-2 where it will be explained that a commercial vibration isolation table is selected to serve as metrology frame.

The transmissibility of, all of the considered commercially available vibration isolation tables, is at most 0.01 at 10 Hz. The transmissibility follows a -2 slope for higher frequencies. When this reduction in transmission of floor vibrations is taken into account it becomes clear that the influence of floor vibrations almost vanish. The final measurement noise levels are of acceptable levels since the sensor noise is clearly limiting the performance. This is desired since otherwise, cheaper sensors should be selected.

5-4 Detailed design

In Section 5-2 the conceptual choices where discussed. These choices are to use a metrology frame and to levitate the chuck's out-of-plane DoFs wile fixating the in-plane DoFs. In this section the detailed design is presented. Then the choices are made such that the final design will fulfill the (sub)-requirements stipulated in Section 5-1. In addition, the setup should be well manufacturable.

First, the most important part is sized: the chuck. Then the metrology and force frame are discussed. Hereafter, the actuators are selected, the sensor requirements are determined and the in-plane fixation is designed. Finally, some choices regarding the other hardware are presented.

5-4-1 Chuck dimensions

The most important part of the setup will be the chuck. The estimation algorithms will be applied to estimate the shape of this chuck. The chuck has been analyzed thoroughly and its size and shape are based on the results.

Recall the conclusions from Section 5-2. The chuck will be levitated partially, and the achievable controller stiffness is limited. Therefore, the chuck will undergo relative large movements which determines the required range of the sensors. Furthermore, the sensors should not be required to have a extremely high resolution over this entire range. This means the deformations of the chuck should not be to small compared to the movements of the chuck. For this reason, a parametric analysis is performed in order to minimize the ratio between chuck movement and deformation. In other words, the sensor requirements are minimized and as such their cost is minimized. The sensor cost is largest part of the total cost of the setup.

Basic decision about chuck shape

First, of all recall the requirement that results should be traceable. This means that a complex, near real wafer chuck is not desired since that is a very complex part. Therefore, it is chosen so simulate the wafer chuck using a simple flat plate. This makes modeling easier and results more traceable.

Second, it has been decided to use a rectangular plate. For a square plate all eigenfrequencies will occur double. In practice the eigenfrequencies will not be the same but very close together. Then, even for a very small amount of damping, energy will be transferred from one mode to the other. These effects make results less traceable which is undesirable. Therefore, it has been decided to use a rectangular plate.

Parametric analysis to reduce sensor requirements

A parametric analysis is performed in order to minimize the ratio between chuck movement and deformation. In order to perform this analysis first the size of the deformations are studied. For this a benchmark deformation is used. As benchmark the deformation of the center of the chuck is studied when a force is applied at the center of the chuck. This case is selected as benchmark because of its symmetry which makes it possible to compute an analytic estimate which is required for the parametric analysis.

Consider a plate as shown in Figure 5-14a. The controller keeping the chuck at its place is simulated using two rollers. This is a rough approximation but the trends of how parameters will influence the chuck stiffness will be similar. In Figure 5-14b a side view can be seen. This is the same chuck which is drawn as a beam supported by two rollers. This model where the chuck is modeled as a beam is stiffer than the actual chuck, but we are interested in the parametric trends and not the actual stiffness and the trend is similar. The stiffness k of the beam, defined as the applied force at the location as drawn in Figure 5-14b divided over the maximum deformation which can be computed using:

$$k = \frac{48EI}{a^3} = \frac{4Ebh^3}{a^3} \qquad \text{where: } I = \frac{bh^3}{12}. \tag{5-1}$$

In this equation E is the Young's modulus, I the moment of inertia, a is the length of the longest side and b the length of the shortest side of the chuck and h represents the thickness of the chuck. This equation can also be found in [36]. Off course, the trend of k relative to parameter b is invalid because this equation assumes the chuck is supported by two rollers which is not the case. In fact, the influence of b on k will be the same as the influence of a on k. Therefore, it is concluded that the stiffness is proportionality to the chuck's parameters as:

$$k \propto \frac{Eh^3}{a^3 b^3}. \tag{5-2}$$

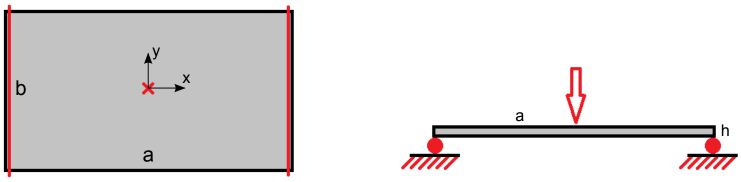

(a) Top view of a on both size on rollers supported chuck. The middle is marked, this is where the force is acting.

(b) Side view of a on both sides on rollers supported chuck. The arrow represents a force in the middle.

Figure 5-14: *These plots shows a schematic representation of a on roller supported the chuck with a force acting on it in the center. This simplification is used to find an expression describing the proportionality of the chuck's deformation magnitude relative to the chuck's design parameters.*

Now the trend is known that describes the size of the chuck's deformation as function of the chuck's design parameters. Next it is time to study the levitation controller stiffness. The levitation controller stiffness is related to the controller bandwidth in a quadratic manner. To understand this, imagine the controller has a bandwidth that is twice as high. In order for the chuck to follow sinusoidal motions with double the frequency, the acceleration has to be four times as high, since the amplitude of the accelerations scales with the frequency squared. The accelerations are linearly related to the required forces and the stiffness of the controller is proportional to the forces. Therefore, the levitation controller stiffness is quadratically related to the controller bandwidth.

In order to increase the levitation controller stiffness, the first eigenfrequency of the chuck has to be increased. Recall from Section 5-2 that, as rule of thumb, the levitation controller bandwidth is 1/10th of the first eigenfrequency. The eigenfrequency increases by increasing stiffness of the chuck, which is a contradicting requirement with respect to the deformations of the chuck. Still, changing the stiffness influences one requirement stronger then the other and as such it is still possible to bring the requirements together. In short, the goal is to lower the stiffness in Eq. 5-2 and to increase the controller stiffness by increasing the first eigenfrequency of the chuck.

The first eigenfrequency of a plate can be computed analytically as is presented in [37]. In this paper it is shown that the first eigenfrequency f_1 of a free plate is given by:

$$f_1 = \lambda_1 \cdot \frac{1}{2\pi\sqrt{12}} \cdot \frac{\sqrt{E}}{\sqrt{\rho\,(1-\nu^2)}} \cdot \frac{h}{a^2}, \tag{5-3}$$

where ρ denotes the density of the material and ν denotes Poisson's ratio.

λ_1 is a dimensionless constant which depends on the ratio between a and b. In [37], the constant λ_1 has been computed for some ratios a and b. A plot of the values can be seen in Figure 5-15a. A quadratic fit:

$$\lambda_1 \approx -6.2\left(\frac{a}{b}\right)^2 + 26.4\left(\frac{a}{b}\right) - 6.2 \qquad \text{for: } 0.4 \leq \frac{a}{b} \leq 2.5, \tag{5-4}$$

has been constructed. The coefficients of the second order polynomial have been obtained in a least squares (LS) sense. As can be seen in Figure 5-15a, the fit describes of the table data accurately.

Eq. 5-4 can be substituted in Eq. 5-3 to obtain an estimate of the first eigenfrequency as function of the chuck dimensions and material properties. The result is:

$$f_1 \approx \frac{1}{2\pi\sqrt{12}} \cdot \frac{\sqrt{E}}{\sqrt{\rho\,(1-\nu^2)}} \cdot h \cdot \left(\frac{26.4}{ab} - \frac{6.2}{a^2} - \frac{6.2}{b^2}\right). \tag{5-5}$$

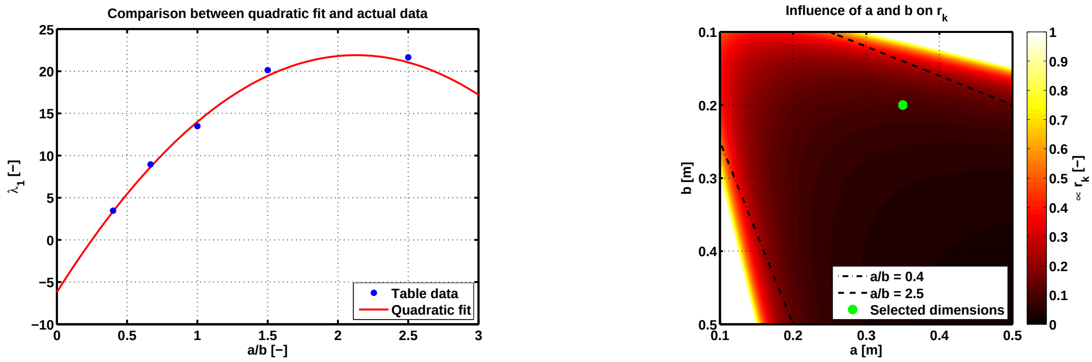

(a) The blue line shows the table data of λ_1 which can be used to compute the first eigenfrequency of a free plate. The values are obtained from a table in [37]. The red line represents a quadratic fit of the table data. The coefficients of the second order polynomial where obtained in a LS sense.

(b) This figure shows the evaluation of: $\left(a^3b^3\left(\frac{26.4}{ab}-\frac{6.2}{a^2}-\frac{6.2}{b^2}\right)^2\right)^{-1}$ as function of a and b. This term is a part of Eq. 5-7. The dot represent the finally chosen values for a and b. It must be denoted that the figure is valid in the region where $0.4 \leq \frac{a}{b} \leq 2.5$ since it is based on Eq. 5-4.

Figure 5-15: *These figures show important results used for analyzing the chuck's design.*

Finally taking the quadratic nature between f_1 and controller stiffness K_p into account one obtains:

$$\begin{aligned} K_p \propto & f_1^2 \\ \propto & \frac{E}{\rho\left(1-\nu^2\right)} \cdot h^2 \cdot \left(\frac{26.4}{ab}-\frac{6.2}{a^2}-\frac{6.2}{b^2}\right)^2 \end{aligned} \tag{5-6}$$

Now that the trends for both the chuck's deformations and the levitation controller stiffness are known, it is time to analyze them and see how the ideal chuck should look like. Remember that the way to achieve this was to lower the stiffness given in Eq. 5-1 and to increase the first eigenfrequency given in Eq. 5-6. In other words the stiffness ratio r_k:

$$\begin{aligned} r_k = & \frac{k}{K_p} \\ \propto & \frac{\left(1-\nu^2\right)\rho h}{a^3b^3\left(\frac{26.4}{ab}-\frac{6.2}{a^2}-\frac{6.2}{b^2}\right)^2} \end{aligned} \tag{5-7}$$

must be minimized.

First, consider the material properties. They cannot be freely chosen but come in fixed combinations depending on the chosen materials. Clearly, changing E does not influence the ratio. The Poisson ratio ν can make a difference when it is close to one, but for common materials it takes a value of around 0.3, as can be seen in [38]. Therefore, the Poisson ratio will not make a big difference. From Eq. 5-7 it is concluded that a material with low density is desired. However, when metals such as steel, aluminum or titanium are considered the density will not vary orders of magnitude.

Then the dimension of the chuck can be changed. Decreasing the thickness h will lower the ratio in a linear way. Still h will need to be decrease a lot in order to bring the ratio significantly together.

Lastly, the dimensions a and b remain to be analyzed. It is not immediately clear how a and b affect Eq. 5-7. To ease the analysis Figure 5-15b has been created. From this figure it can clearly be seen that in order to decrease r_k, the dimensions a and b should be chosen as large as possible. However, the largest gradient of r_k can be observed for very small dimensions, for larger dimensions they have to increase a lot for a small reduction of r_k. Finally, an aspect ratio of $a/b = 1$ results in the lowest r_k when the chuck's area is kept constant. However, changing the aspect ratios does not influence r_k much except when it become very large such as 0.4 or 2.5.

Chuck design decisions

Now a theoretical basis is provided that can be used to make design decisions regarding the chuck for the setup. However, there are also some practical issues that should not be forgotten. The chuck should not be to large because it should fit in the lab on the granite tabletop as shown in Figure 5-9a.

In addition, it must be possible to mount additional sensors such as accelerometers to the chuck. Also the actuators mounted to the chuck have a certain weight. The chuck should not be too light in order to prevent that the chuck's properties completely change when such weights are added to it. A very thin and large chuck should be designed according to the theoretical analysis. Based on practical considerations it is desired to have a medium sized and heavy chuck.A trade-off need to be made between these aspects. The trade-off has been made and the result is: an aluminum chuck, with dimensions 350x200x3mm which will weight approximately 567 grams and has a ratio of $a/b = 1.75$. A render of the chuck is shown in Figure 5-16.

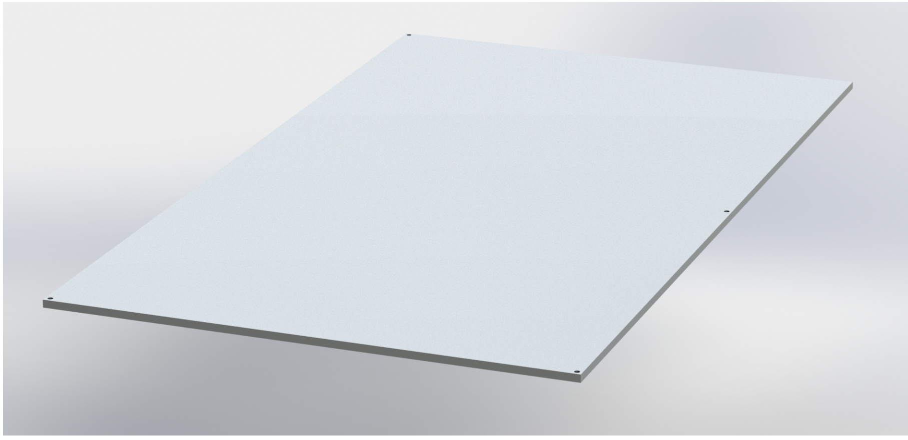

Figure 5-16: *A render of the designed chuck. The small holes on the edges are for the in-plane fixation designed in Subsection 5-4-6.*

A ratio of $a/b = 1.75$ is selected which results in a non-square chuck, as required in the beginning of this subsection. Still this is no extreme ratio and based Figure 5-15b it will not affect the theoretical ideals much.

In addition, a conductive material with a relatively low density can be selected. Aluminum is a good and practical material choice and is therefore selected.

Finally, the chuck dimensions makes it fit easily on the table top in the lab while some space around it is left for other equipment such as the in-plane fixation. Furthermore, as can be seen in Figure 5-15b, these dimensions are well outside the domain where gradient with respect to r_k is large. Therefore, to obtain a significant improvement on r_k the dimensions have to be improved a lot which makes the chuck impractically large.

To summarize, in this section a minimization problem has been solved manually that is constrained by practical issues. The final design of the chuck has a weight that is high enough such that small sensors and actuators can be mounted on it while its properties remain similar. Furthermore, the sensor requirements remained acceptable which will be studied in more detail in Subsection 5-4-5.

5-4-2 Metrology frame

Sensors are mounted on the metrology frame. The metrology frame should be designed such that it allows for high quality measurements which are noise free and repeatable. Noise rejection is achieved by implementing the vibration isolation as discussed in Subsection 5-2-1. Repeatability is achieved by using a kinematic mounts. Finally, attention is payed to manufacturability.

Vibration isolation

As discussed in Section 5-2 and 5-3, the sensors should be mounted to a frame that is vibration isolated with respect to the floor. Vibration isolation will increase the measurement quality of the setup. The vibration isolation is implemented by buying a commercial product.

After a short market survey the Minus K Technology BM-4 has been selected which is a cost effective, fully mechanical vibration isolation table. It was about 5 times cheaper than the other considered alternatives with comparable specifications. The detailed specifications of the Minus K Technology BM-4 can be found in [39]. It has an eigenfrequency of 0.5 Hz. From here the transmissibility follows a -2 slope resulting at 10 Hz in a transmissibility of 0.004. As has seen shown in Figure 5-8a, most of the floor noise frequency content is centered around 10 Hz, therefore the vibration isolation tables are compared using their specification at this frequency.

The setup will contain many sensors that measure the chuck's deformations. Each sensor requires a cable. These cables will transmit floor vibrations directly to the vibration isolated table top. The cables can be oriented such that they have a low stiffness of about 1 N/m that connects the table top with the floor. Therefore, the stiffness of the table top with respect to ground will increase. This is undesired since a vibration isolation system is used to make this stiffness as low as possible.

Therefore, the Minus K Technology BM-4 variant that can carry the highest payload is selected. It can carry payloads up to 93 kg. Because of this choice, forces are acting on the vibration isolation table top, will have significantly less effect because of the large inertia on the table top. In addition, this model has the same eigenfrequency of 0.5 Hz which means that $\omega = \sqrt{k/m}$ remains constant[1]. In order for this ratio to remain constant for larger m, a larger k is required. This also means that a small contribution of additional stiffness from the cables has less effect. In addition the vertical stiffness of this vibration isolation table can be adjusted, so it is possible to compensate for the added vertical stiffness coming from the sensor cables.

Figure 5-17 shows render of the vibration isolation arrangement. The black part is the vibration isolation table. The red parts are shipping collars that should be removed during operation and placed back when making changes to the payload. On top of the vibration isolation table lie 11 steel plates of 4mm thick. These are used to increase the weight of the total construction on top to near the maximum payload of 93 kg. The notches in the steel plates are designed so it is possible to place and remove the

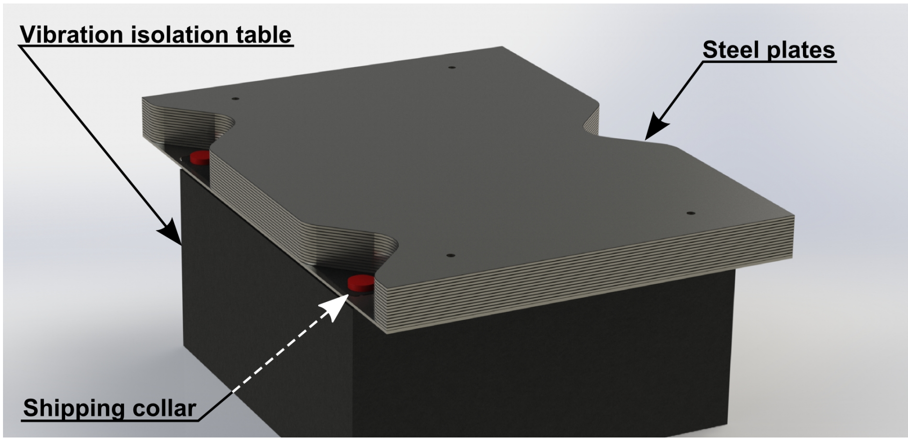

Figure 5-17: *A render of the designed vibration isolation arrangement. The black part is the vibration isolation table and the red parts are shipping collars. These shipping collars must be removed during operation and placed back when making changes to the payload. In addition, the space that is left when the shipping collars are removed can be used to verify the alignment of the table top with respect to the frame of the vibration isolation table. The 11 gray plates on top of the vibration isolation table consists are steel plates of 4mm thick. These are used to increase the weight of the total construction on top to get near the maximum payload of 93 kg. The lowest steel plate is used to position the payload accurately on the table top.*

shipping collars easily. Furthermore, the holes that are left when the shipping collars are removed can be used to verify the alignment of the table top with respect to the frame of the vibration isolation table. The lowest steel plate has 3 contact points that can be used to easily center this payload on the table top. The four holes can be used to bolt everything together so it becomes a rigid block.

Kinematic mount for repeatability

Another important requirement for the measurements is that they are repeatable. Since the setup is an experimental setup, modifications must be made quite often. Every time the sensor configuration is altered and then altered back to the original situation, the new measurements must remain comparable

[1] In this equations is ω the eigenfrequency in rad/s, k the vibration isolation table stiffness and m the mass of the tabletop including the payload.

to the original measurements. For this it is important that the metrology frame returns to its original position after it has been remounted. A kinematic mount can be used for this purpose.

A kinematic mount is a support that fixes a part in a statically determined way. It can be implemented by placing a ball bearing ball in a groove. The groove limits the ball by 2 DoF, namely the ball cannot roll in the direction perpendicular to the groove and it cannot fall down. If the ball and the groove are flat rotation is still possible. Then, by using three properly oriented grooves, a part can be constrained in precisely 6 DoF. Once the parts is remounted it will return to its statically determined orientation.

To put this in perspective, a render has been created that can be seen in Figure 5-18. On top of the vibration isolation arrangement shown in Figure 5-17, the metrology arrangement is placed. The metrology arrangement consists of a thick aluminum plate which serves as basis. The sensors consist of long probes which are illustrated in Figure 5-19a. Room for these probes must be made below the metrology frame which is done by placing the metrology frame on top of three pillars.

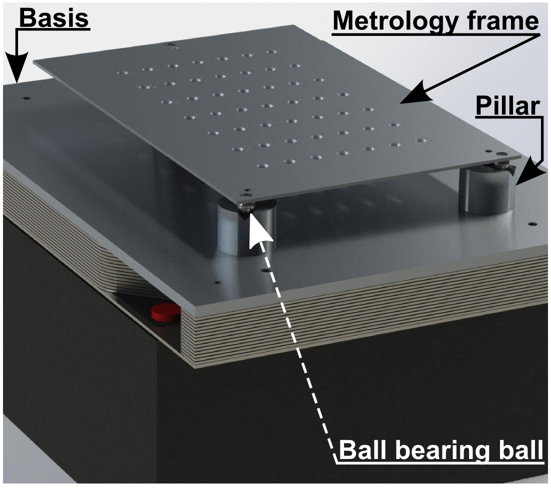

(a) On top of the vibration isolation arrangement shown in Figure 5-17, the metrology arrangement is placed. This consists of a 10 mm thick aluminum plate which serves as basis. The sensors are long probes and room must be made below the metrology frame which is done by placing the metrology frame on top of three pillars.

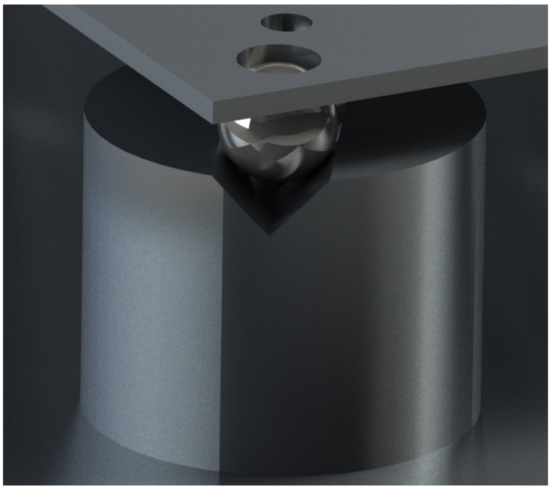

(b) Close-up of one pillar to clearly show the ball bearing ball in the horizontal groove. The combination of the three pillars form the quasi-kinematic mount to fixate the metrology frame.

Figure 5-18: *A render of the metrology frame with a close-up of the quasi-kinematic mount.*

Horizontal grooves have been made in the pillars. The metrology frame is supported on ball bearing balls that rest in these grooves. Ideally the metrology frame should also have grooves. For easy of production it has been chosen to make just holes. The balls can still rotate in the holes but not translate in any direction. This mount is also called a quasi-kinematic mount in [40].

When the sensor arrangement is altered, the metrology frame must be removed. When it is placed back it should be placed at the same place. The same place means within 0.1 mm and then it is expected that the measurements will not be changed significantly. A kinematic mount provides repeatability up to 0.1μm, based on [40]. According to [40] a quasi-kinematic mount provides a repeatability in the order of 10μm which is still a factor 10 better as required.

The metrology frame is made out of stainless steel plate. It can be manufactured using water or laser cutting. These technologies can handle stainless steel with the same ease as steel or aluminum. Stainless steel has been chosen to increase the stiffness. In addition, it is non-ferromagnetic, which is important because actuators containing magnets are placed on the chuck which is within 15 mm of the metrology frame.

A plate has been selected such that the sensors can be placed anywhere below the chuck. A prepared grid of holes has been created so the sensors can be moved easily. A plate allowed for quick production of all these features during the one production step. The downside of a plate is that it is relatively compliant and has a first eigenfrequency slightly higher but in the same order as the chuck. A thicker plate could have been selected since it will be a lot stiffer. However, the laser-cutter available at the university's faculty can only cut plates up to 4 mm.

Sensor clamp

The sensor probes, illustrated in Figure 5-19a, have to be mounted on the metrology frame. For this sensor clamps have been designed shown in Figure 5-19b . They have been designed such that the probe is clamped in a well conditioned way.

The large hole in the middle is where the probe is placed. The hole on the side is used to clamp the probe. Instead of one large hole in the middle three notches have been placed on its side. This is done to better condition the surface used to clamp the probe. Now for sure the sensor is clamped on the 3 sides. Otherwise, if only one hole was used, it would become an oval when the clamping force is applied and then the exact contact with the probe is poorly defined.

The two other holes are for mounting the probe to the metrology frame. Because the chuck can come very close the the sensor probe, the bolt heads may not extend out of the sensor clamp.

(a) Source: Micro-Epsilon. Sensor probe and connector.

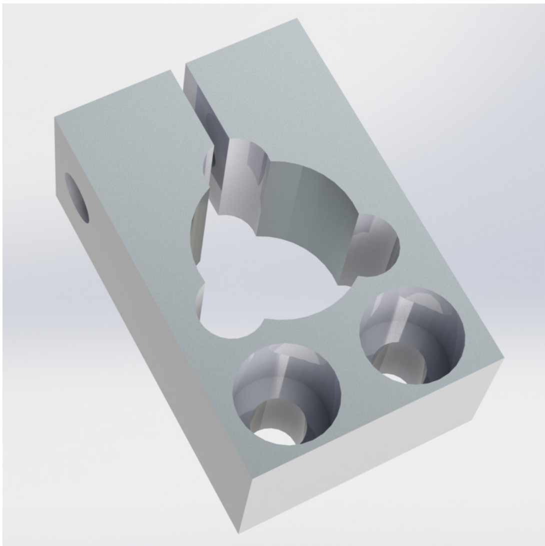

(b) A render of a sensor clamp. The large hole in the middle is where the probe is placed. The hole on the side is used to clamp the probe. The two small holes are to bolt it to the metrology frame.

Figure 5-19: *These figures show the sensor probe and sensor clamp.*

Overall metrology frame design

A render of the total metrology arrangement including the vibration isolation and sensor clamps with sensor probes can be seen in Figure 5-20.

5-4-3 Force frame

When the actuators produce the desired forces on the chuck, then they will also produce reaction forces. These reaction forces need to be guided to the mechanical ground which is done via the force frame. A separate force frame is used to prevent contamination of the metrology frame with vibrations caused by these reaction forces.

Figure 5-21 shows a render of the force frame. It consists of three pillars used to lift the frame over the setup. The force frame is again mounted using a quasi-kinematic mount as described in Subsection 5-4-2. Finally, the actuators are mounted on the force frame plate that will be spanned over the chuck.

The setup is placed on the granite table shown in e.g. Figure 5-9a. This granite block has M8 threaded inserts. The force frame should be fixed to the granite block using these inserts. Therefore, pillars have been aligned with them.

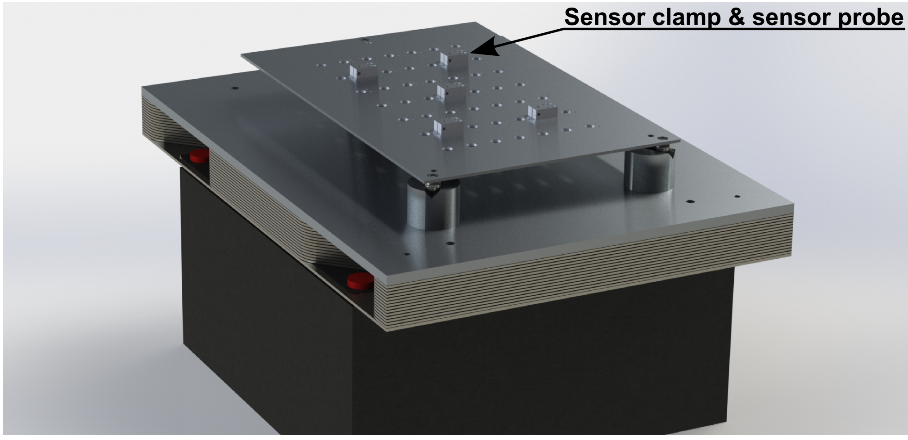

Figure 5-20: *A render of the total metrology arrangement including the vibration isolation table, metrology frame and sensor clamps with sensor probes.*

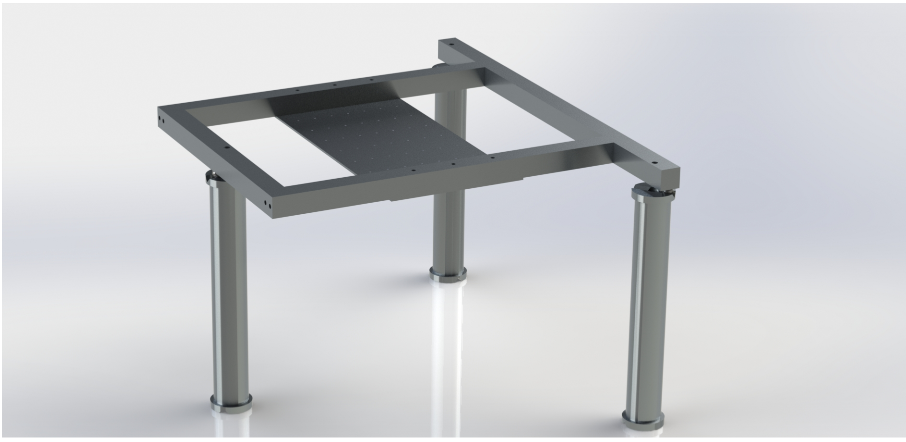

Figure 5-21: *A render of the force frame. It consists of three pillars used to lift the frame over the setup. The force frame is again mounted using a quasi-kinematic mount as described in Subsection 5-4-2.*

The actual force frame is constructed from staff material. This has been done so that later, if required, additional devices can be mounted to the force frame. Additional holes can be drilled easily and thread can be cut if necessary.

It should also be possible to mount the actuators anywhere on the chuck and therefore, a plate is spanned over the chuck. A grid of holes has been prepared in this plate so the location of the actuators can be changed easily. From manufacturability point of view, a plate is a very good choice because it can be shaped using one production step such as water or laser cutting.

When the actuators or sensors are relocated, the force frame must be removed. The actuators are voice coils as will be explained in Subsection 5-4-4. The voice coil actuators have only a very small total air gap size of 0.64 mm. This means a clearance of 0.32 mm per side. When the force frame is put back, it should be placed back with an accuracy of at least 0.1mm to avoid contact between the actuator mover and stator. This is achieved using a quasi kinematic mount as described in Subsection 5-4-2. Horizontal grooves are placed on the pillars and holes are drilled in the force frame.

Finally, the force frame should be stiff. The voice coil actuators have in theory zero stiffness but in practice they have a low stiffness since the motor constant depends on the position. Because of this stiffness, forces due to movements of the force frame will still be transmitted to the chuck. For this reason the force frame is created from staff material which makes it stiffer. For the same reason the force frame plate is manufactured from stainless steel.

In additional, stainless steel has been selected over steel because it is again non-ferromagnetic. The voice coil actuator mover, which contains magnets, is mounted on the chuck which can be as close as 5mm away from the force frame plate.

5-4-4 Actuators

Actuators are required to levitate the chuck and to apply disturbance forces. The actuators are also used to compensate for the weight of the chuck since no gravity compensation means are included in the design. In this subsection the actuator selection and placement is described. Finally, it is presented how the actuators are connected to the chuck.

Selected actuator type

As will be described in Subsection 5-4-5 the sensors that have been selected have a range of at least 1 mm. In that subsection it is also presented that the chuck will move about 1mm when disturbance forces of 1N are applied to the chuck. Therefore, the actuators should be able to produce force in the order of 1 N continuously. The chuck's response of a step shaped input force of 1 N is shown Figure 5-4a.

Another requirement on the actuators that they must have a low stiffness, as is explained in Subsection 5-2-1. In addition, low friction and low hysteresis forces are required since these effects will cause unintended deformations of the chuck which is measured as measurement noise. In addition, they should not be too heavy since adding additional weight to the chuck will alter its behavior.

Voice coils are a class of actuators that fulfill these requirements very well. They can provide the required forces, they have theoretically a zero stiffness and they are contactless which means they introduce no friction and hysteresis.

After a market survey the selected actuator is a Moticont lvcm-016-013-01 and detailed specification can be found in [41]. This was the cheapest and lightest actuator found. It can exert a continuous force of 1.8 N and has a stroke of 6.4 mm. The stator weighs 7 grams, and the mover, mounted to the chuck weights 12 grams. It has an operating point where the stiffness is exactly zero, and over a stroke of ±0.5 mm around this point the stiffness will not exceed 30 mN/mm which is very low. This means the maximum stiffness forces are smaller than 30mN which is acceptable.

The selected actuators can deliver a continuous force that is almost twice as high as the required force. Therefore, of this their heat production will be limited when they create forces with a maximum of 1 N Root Mean Square (RMS).

Placement and number of actuators

A tasks that remains regarding the levitation controller is to decide on the amount and placement of the actuators. These design decisions are presented now.

Only 3 DoFs are controlled by the levitation controller so a minimum of 3 actuators are required. The actuators are placed such that the first modeshapes are not or minimally excited. By doing this they will not show up in the transfer shown in e.g. Figure 5-3a. This makes it possible to achieve a higher controller bandwidth which in turn reduces the sensor requirements. A modeshape is not excited when the actuators are place on its nodal lines. Another way to avoid excitation is to placed the actuators such that the mode is excited equally in positive and negative direction. In order to excite modes as such, a symmetric placement of the actuators is preferred. Therefore, 4 actuators are used which allow for placement with two symmetry lines.

In Figure 5-22 the modeshapes of the chuck have been drawn together with their nodal lines. Figure 5-22a shows the first modeshape. As can be seen, the first modeshape, the umbrella shape, has two curved nodal lines. The actuators can be placed anywhere on those for lines and then this mode will in theory not be excited. The second mode, shown in Figure 5-22b has only two intersection points of its nodal lines with the nodal lines of the first modeshape. This provides only two possible placement locations for the actuators which is not enough since at least three actuators are required.

However, by inspection of the second modeshape, excitation can be avoided by placing the actuators in a symmetrical way. When two symmetry lines are are drawn the chuck is divided in four quadrants. By placing the actuators in a symmetric way in each quadrant, on the nodal lines of the first modeshape, neither mode will be excited.

A similar analysis can be performed for the other modes shown in Figure 5-22. The reasoning for the second mode is also valid for the third mode shown in Figure 5-22c. However, the fourth mode, shown in Figure 5-22d will always excited when rotating the chuck around y-axis which is defined in Figure 5-14a. This cannot be avoided, except when the actuators are placed on the shape's nodal lines. However, they do not coincide with the nodal lines of the first modeshape. The first mode gets priority since it is lower frequent and has therefore an higher magnitude when constant modal damping is assumed.

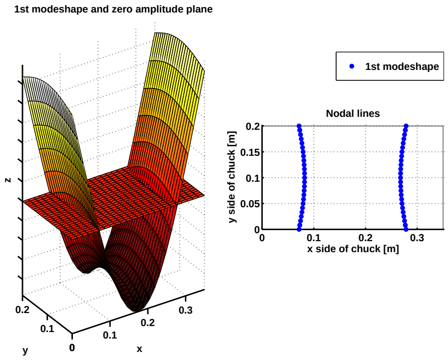

(a) First modeshape (122 Hz).

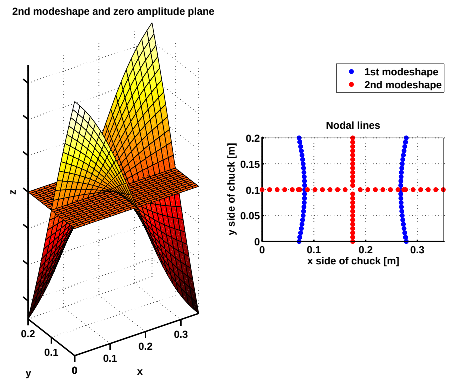

(b) Second modeshape (146 Hz).

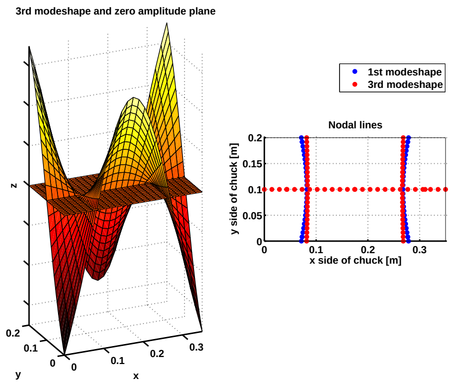

(c) Third modeshape (298 Hz).

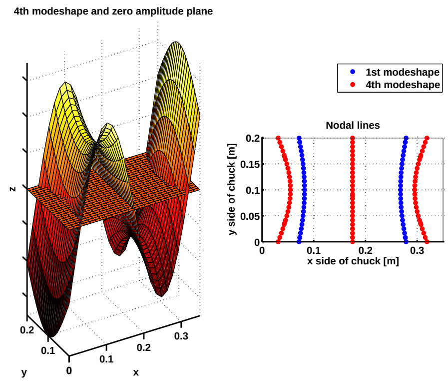

(d) Fourth modeshape (331 Hz).

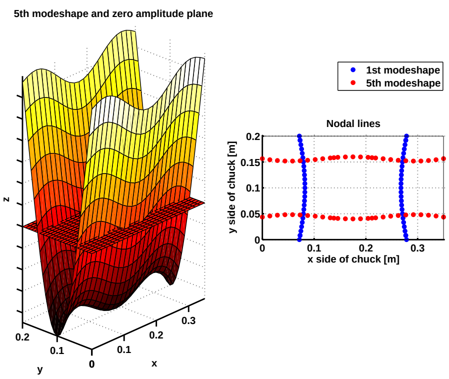

(e) Fifth modeshape (435 Hz).

Figure 5-22: *Each figure shows a modeshape and the amplitude zero plane on the left side. The right part the nodal lines are drawn which are the intersection of the modeshape with the zero amplitude plane. The nodal lines of the first modeshape are repeated in every figure.*

Finally, we arrive at the fifth mode shown in Figure 5-22e. This shape is similar to the first shape and has again two curved nodal lines. As can be seen, there are four intersection points between the nodal lines of the first and fifth mode shape where each intersection also lies each of the four quadrants defined by the two symmetry lines of the chuck. As such, these intersection points mark the location of the 4 actuators.

This part is concluded with a remark. By adding the mass of the actuator movers to the chuck the mode shapes will change a bit. It is difficult to model the exact effect of this mass. However, the shapes will only change a little bit and by placing the actuators as presented the resonance peaks of the lower modes will have a small magnitude. Therefore, it is possible to increase the levitation controller's bandwidth a bit further which reduces the sensor requirements.

Actuator connection to chuck

The actuators must be connected to the chuck with a very high position tolerance with respect to each other. As stated before the clearance between the stator and mover is about 0.32 mm. If they are placed inaccurately not all movers will fit properly in the stator.

Therefore, an connection type is chosen that allows for easy (dis)mounting of the actuators such that they can be (re)aligned. Small magnets are glued to the chuck and the actuators are placed on them. The part of the actuators mounted to the chuck consist of ferromagnetic material, therefore it will be pulled to the glued magnet by reluctance force. The body is fixed by friction forces.

The actuator's mover contains magnets and therefore magnetic flux is already present in the iron. The iron can saturate which must be avoided since saturation will lower the motor constant of the actuator. Therefore, the flux originating from the magnet which is mounting the actuator to the chuck should counteract the flux already present inside the actuators iron.

The flux direction inside this iron is unknown is first be determined relative to the magnet mounting the actuator to the chuck. Then this magnet can be properly oriented. A small test has been designed to detect the proper orientation. In Figure 5-23 illustrations are made to help explain the test.

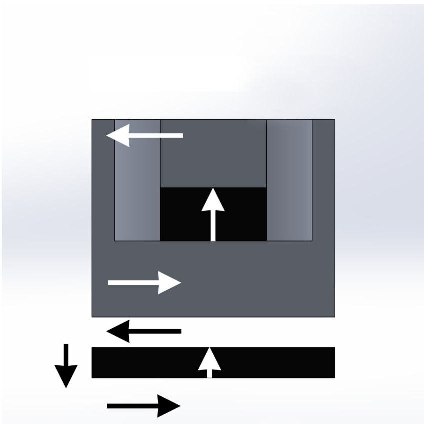

(a) Ideal flow direction of the magnetic flux inside the iron of the actuator.

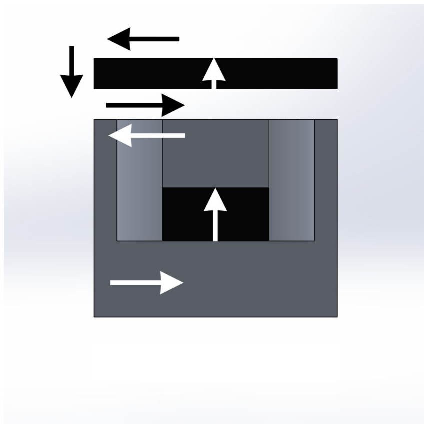

(b) Illustration of the flow direction of the magnetic flux that is used to detect the magnetization direction of the magnet inside the actuator relative to the magnetization direction of an external magnet.

Figure 5-23: *These images show a cross-sectional view of an actuator mover. The black parts are magnets and the arrows indicate the flow of the magnetic flux. The gray parts are iron of the actuator mover.*

In Figure 5-23a the ideal situation of the flow direction of the magnetic flux is drawn. The flux flows in opposite direction which avoids saturation in the iron. Figure 5-23b shows how the magnetization direction of the magnet inside the actuator can be found relative to the magnetization direction of an external magnet. In the situation as drawn the magnetic flux lines inside the air gap flow in opposite direction. Now a clear attraction force will be felt. In this situation the reluctance force is relatively small because of the air gap. If the field inside the actuator would be reversed, a clear repelling force can be felt, then it is known that the external magnet must be rotated before gluing it to the chuck.

In order to position the magnets accurately a mold was made. It is shown in Figure 5-24. It is a out of PMMA laser cut plate of the same size as the chuck. A grid of squares has been cut out such that when the magnets are placed against the two on the mold indicated sides they are positioned well within the required tolerances.

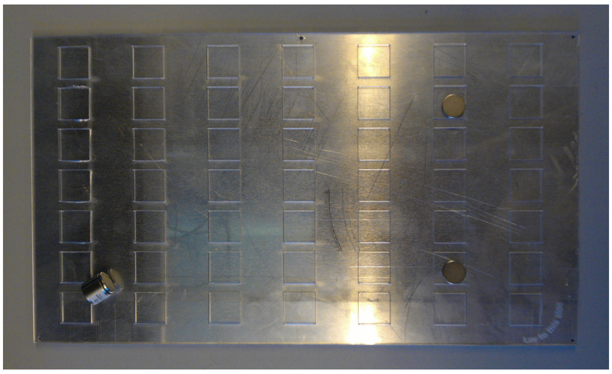

Figure 5-24: *Photo of the mold used to position the magnets on which the actuators are mounted accurately. The mold is manufactured from transparent PMMA and below it the chuck can be seen. On the left two magnets have already been glued to the chuck. An actuator body, with magnet attached to it, lies on the mold in the bottom right corner of the photograph.*

5-4-5 Sensor selection

The sensor selection is one of the most important design decisions that needs to be made. Sensors are used to measure the position of the chuck and to measure its deformations. The selection of the sensors had to be made early in the design process because of the relatively long lead time.

A long analysis on which the sensor selection is based on has already been done. In Section 5-2 the metrology concept is presented and the levitation concept is introduced. Then in Subsection 5-4-1 the chuck has been designed such that the difference between chuck movements and chuck deformations is minimized. In this subsection, the capabilities of the levitation controller are investigated which determines partially the sensor requirements.

Sensor placement

In Subsection 5-2-2 it has been explained that the sensors will be placed collocated with the actuators. The actuator location has been determined in Subsection 5-4-4. Therefore, the location of the sensors used by the levitation controller are also determined.

A grid on which the sensor clamps can be fixed has been prepared such that different sensor locations can by considered while investigating the estimation algorithms. Because of this, non-collocated sensor-actuator configurations can also be considered, when desired.

Range vs resolution

Next, the minimum sensor range and minimum sensor resolution need to be determined. The minimum sensor range is determined by the maximum movement that the chuck will undergo. The minimum sensor resolution will be determined by the magnitude of the deformations of the chuck.

Based on the controller design presented in Subsection 5-2-2 and on the model of the chuck presented in Section 4-2. In Figure 5-25, the expected translations and deformations are shown when a force as described in the figure caption is acting on the chuck.

First, take a close look at Figure 5-25a. When the disturbance force has a very low frequency, the chuck will not move at all. This is because the integrator in the controller compensates for this force low frequent disturbance. At high frequencies the chuck dynamics can be seen but the overall movement is also small which is caused by the inertia of the chuck. For some intermediate frequency the maximum translation occurs. In that case the integrator does not have enough time to integrate the error, while the event happens slow enough such that the inertia is not limiting the amplitude of the movement a lot. This maximum amplitude occurs at a frequency of about 20 Hz. Then the chuck's corner will move about 1 cm when a force of 1 N is applied at the same location. This point on the chuck is selected since this point undergoes the largest translations. This system property determines the required sensor range.

Next take a look at Figure 5-25b. This figure shows the deformation of the center of the chuck when a force is applied there. This is used as a measure to determine the size of the deformations. The deformation is defined as the movement of the chuck's center relative to the chuck's as used by the levitation controller. It can be seen that this system behaves, as one would expect, as a mass spring

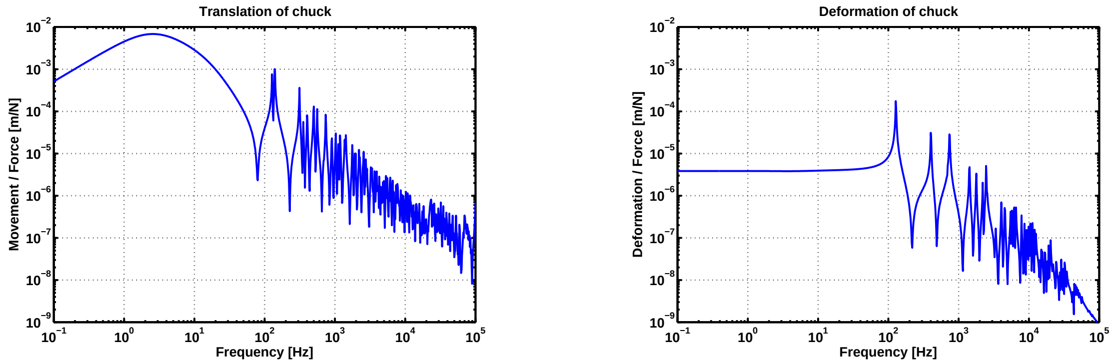

(a) This figure shows as function of frequency the translation of the corner of the chuck due to an input force on the corner of the chuck. These are the worst case translations that will occur.

(b) This figure shows as function of frequency the deformations of the chuck when a force is applied at the center of the chuck. The deformation is measured as difference in distance between the chuck center and the position of the chuck as measured by the levitation controller.

Figure 5-25: *These figures show transfer functions from which the sensor requirements are distilled.*

system. At low frequencies, the stiffness of the chuck is limiting the deformation. And after a certain frequency the mass of the middle part of the chuck decouples from the sides of the chuck. This happens at the first eigenfrequency. After the first eigenfrequency more and more parts of the chuck start to decouple. In the low frequency part, where the deformation is frequency independent, the deformation is about 5 μm when a force of 1 N is applied at the center of the chuck. This system property determines the required sensor resolution.

The results shown in Figure 5-25 are relative to the actuator force. If the actuator force is 10 times smaller then the range can be 10 times smaller and the resolution should increase by a factor 10. Therefore, it is interesting to look at the ratio r_s between required range and resolution. The ratio is:

$$r_s \approx \frac{1\text{cm}}{5\mu\text{m}} = 2 \cdot 10^3$$

This means a sensor that has a range over resolution ratio of $2 \cdot 10^3$ must be selected.

The deformation shown in Figure 5-25b is among the largest deformations that will occur in the chuck. Preferably deformations that are a factor 10 times smaller should also be measurable. In addition this deformation should be measured with an accuracy between 10% to 1%. This increases the required ratio to $r_s \geq 2 \cdot 10^5$ and the preferred ratio to $r_s \geq 2 \cdot 10^6$.

Discussion

A remark need to be made. The translation of 1 cm is a worst case result. If the actuator is not placed at the corner of the chuck but somewhat more towards the center, the translations will be a lot smaller. Then, larger forces can be applied and the size of the deformations will increase. The typical expected translations are about 1 mm when a force of 1 N is applied. This means that a sensor having $r_s \geq 2 \cdot 10^5$ can measure the expected deformations with an accuracy of about 1% without increasing the cost. As can be seen in Appendix C, sensors with a ratio of $r_s = 2 \cdot 10^5$ are expensive but affordable. Sensors with a ratio over $r_s = 10^6$ are about three times as expensive and are considered to expensive for this project.

For this reason, sensors with a range of 1 mm are selected. Then actuators that can apply disturbance forces in the order of 1 N can be used. As discussed in Subsection 5-4-4, these are of reasonable size and weight with respect to the designed chuck.

Sensor selection

The sensor range and resolution requirements have been established. The next task is to select a suitable sensor. This topic is studied in great detail and its presentation is out of the scope of the main matter. However, a summary is provided here and the complete studie can therefore be found in Appendix C.

Several sensor technologies have been considered and capacitive sensors have been selected as the most suitable choice because they can achieve the desired r_s in a contactless and relatively cost effective manner.

After an extensive market survey Micro-Epsilon CapaNCDT6200 with DL6230 amplifiers has been selected. This sensor was based on the by manufacturers provided information the best performing sensor that was while their was no clear difference in the final cost. Furthermore, this system is the only one that provides besides an analog interface also an digital interface. This can greatly simplify the required wiring and filtering as an some filter settings can be configured in the sensors that will only affect the output of the digital interface. The digital interface that will be used is an EtherCAT interface.

Before the system was ordered a test system was requested for which the noise levels where validated. The results are presented in Figure C-2 on page 116. It is concluded that this system performs as best as specified.

Furthermore, when digital interface applies some internal filtering such as anti aliasing filtering is applied. However, what exactly happens is badly documented and therefore the frequency response of the analog and digital interface are compared. The results are presented in Figure C-3 on page 118.

It is concluded that the EtherCAT interface has sufficient performance for our goal and will therefore be used. EtherCAT can be used using a standard Intel based network card. Because of this, no expensive ADC array that is compatible with the control system has to be ordered which saves about € 2.000,-.

5-4-6 Design of in-plane fixation

The last important subsystem of the setup is the in-plane fixation. The levitation controller handles 3 out-of-plane DoFs which means that the 3 other, in-plane DoFs, need to be fixed or suspended. For this reason, multiple concepts have been considered and analyzed. Based on the conclusions the final design is created.

Requirements

The analysis is started by determining the in-plane fixation's requirements. The in-plane fixation has certain requirements.

First of all, it should be stiff enough such that the amplitude of the chuck's in-plane movements do in not exceed the clearance of the voice coils which is 0.32 mm. The expected disturbance forces are estimated to be at most 10% of the actuation forces which are in the order of 1 N. If a movement of 0.1mm is accepted then a minimum stiffness of 1 N/mm is required.

Next, a lot of effort has been made to handle the chuck in a contactless manner. The main reason for this is to avoid friction and hysteresis. The in-plane fixation should also be frictionless with no hysteresis.

In addition, the chuck is levitated for noise rejection reasons presented in Section 5-2. Therefore, the in-plane fixation should introduce no stiffness in the out-of-plane directions.

Concepts

Many concepts have been considered in order to implement the in-plane fixation. The most promising where: *repelling magnates*, *a ferrofluid bearing* or strings. Each concept is now discussed shortly.

The repelling magnets concept has been studied thoroughly. The performed analysis can be found in Appendix D. The concept uses repelling magnet pairs on both sides of the chuck to keep it in place. Devices using this concepts are used to implement gravity compensation, which could be a very handy bonus feature for our setup to reduce the load on the actuators. Above all, this concept would implement the in-plane fixation in a contactless manner, resulting in a chuck that is kept in place in a completely contactless. Unfortunately, as can be seen in the conclusion in Appendix D, it is not possible to use this concept to create a sufficiently stiff in-plane fixation when using rectangular magnets. It might be possible however when more complex shaped magnets are considered. It was decided that the required analysis is to complicated and outside the scope of this thesis project. Therefore, a simpler concept is selected.

The next concept suspend the chuck using a in-plane ferrofluids bearing. Based on work in [42] it should be possible to achieve a sufficient stiff suspension this way. Unfortunately, such a bearing shows small hysteresis effect. The ferrofluid bearing introduces some out-of-plane viscous friction and damping when the chuck is moving in out-of-plane direction. The damping is expected to be in the order of 0.01 Nm/s. This will result in forces of about 1% of the actuation forces. The ferrofluid concept is an interesting option but would cost a considerable amount of time to design properly. This time was spend on the repelling magnets concept. It was decided to go for a simpler concept.

The concept that is is selected and implemented is the concept to suspend the chuck with strings. The idea is to fix 3 or 4 strings to the chuck to fix its in-plane DoFs. A very high stiffness can be achieved when very stiff strings are used. Since the strings remain strained they will only bend at two pivot points near the chuck and near the fixture to the in-plane fixation frame. Very thin strings will be used since the loads are very low. Therefore, this bending of the strings is expected to happen without any significant hysteresis. When the strings are long, the out-of-plane DoFs of the chuck experience near zero stiffness. This concept is simple and can be implemented quickly. This is the most important reason why concept is chosen.

Location and number of strings

As explained in the beginning of this subsection, 3 DoFs need to be constrained. Therefore, at least 3 strings are required where each string constrains 1 DoF.

A string is only stiff when pulled. To overcome this issue they should be prestressed. The pretension force should be at least be as high as the largest disturbance force in that direction. In order to add the pretension, a 4th string is required. Therefore, four strings are used.

The strings are mounted near the corners of the chuck. This is being done in order to create a high rotational stiffness. The pretension can be selected such that the strings are stiff enough to handle the disturbance forces, but not stiffer than required so that the out-of-plane stiffness is kept as low as possible.

Location and direction of pretension string

The string responsible for the pretension force is placed carefully. It is placed such that all strings are equally prestressed. In Figure 5-26, the red arrows represent the prestressed strings. In y-direction, 2 strings are used to overcome the disturbance forces in y-direction. In x-direction only 1 string is used. In order for the in-plane fixation to handle disturbance forces of the same magnitude in both x and y-direction, the string in x-direction requires a double amount of pretension. Now the exact location and

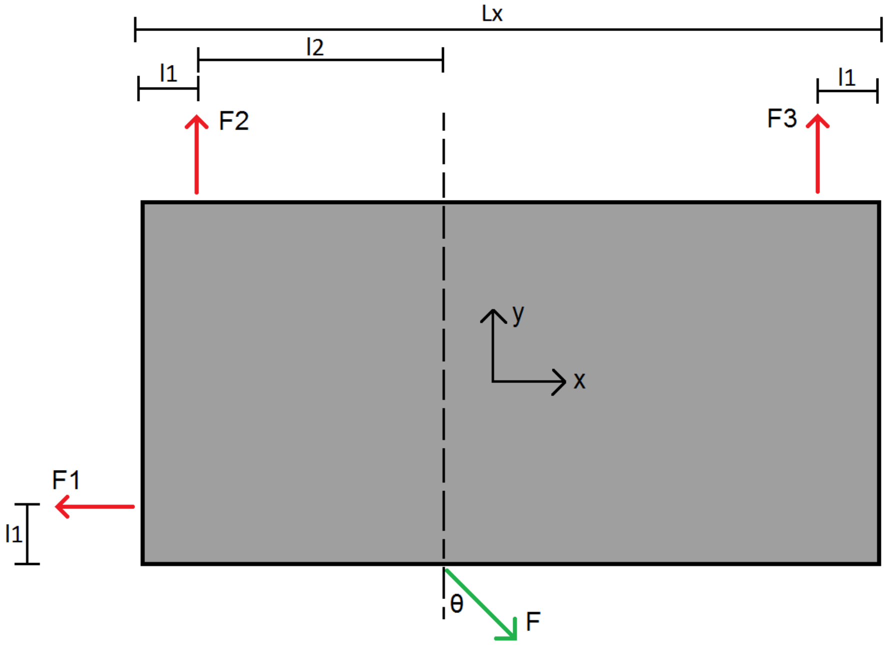

Figure 5-26: *Free-body diagram of the chuck in the xy-plane showing the in-plane forces acting on the chuck caused by the in-plane fixation strings.*

direction of the pretension string is determined. For the definition of the used symbols please refer to Figure 5-26. The force exerted by the pretension string is represented by a green arrow and denoted by

F. The direction of the force can be computed by solving the force equilibrium in x and y-direction:

$$\sum F_x = 0 : \qquad F_1 = \sin(\theta)F, \tag{5-8a}$$

$$\sum F_y = 0 : \quad F_2 + F_3 = \cos(\theta)F. \tag{5-8b}$$

As explained, the pretension in strings 2 and 3 should be equal and the pretension in string 1 should be double that. This can mathematically be denoted in terms of the desired pretension as:

$$F_1 = 2F_2 = 2F_3 = F_p. \tag{5-9}$$

By substituting this in (5-8b) and solving for the direction θ, one obtains:

$$\theta = 45°, \tag{5-10}$$

Then, the distribution of the pretension force F_p over the strings 2 and 3 can be influenced by the location of the pretension string. The location of the pretension string is determined by l_2. From the equilibrium equation of moments around a point on the chuck the proper choice for l_2 can be derived. For ease the moment around the point of application of force F is chosen and then the equilibrium equation is given by:

$$\sum M_z : \quad 0 = F_p \left(l_1 - \frac{1}{2} l_2 + \frac{1}{2}(L_x - l_2 - 2l_1) \right). \tag{5-11}$$

By solving Eq. 5-11 for l_2 one finds that the solution is given by:

$$l_2 = \frac{1}{2} L_x,$$

which is independent of the choice of l_1. Then, the required force F in the pretension string for achieving the desired pretension force F_p in the strings can be computed from Eq. 5-8a and Eq. 5-10 which results in:

$$F = \frac{F_p}{\sin(\theta)} = \sqrt{2} F_p \tag{5-12}$$

The distance l_1 can be chosen freely but it is desired to choose l_1 small since that will result in a high rotational stiffness.

Force and stiffness in out-of-plane directions

Another important requirement on the in-plane fixation is that the magnitude of the forces acting in out-of-plane directions must be very low. This will be the case when the out-of-plane stiffness is very low. It should be noted that when the chuck is at its nominal position, halfway the sensor range, the stiffness is indeed zero. However, when it moves up or down, it will experience a small, non-zero stiffness.

The expected magnitude of this stiffness and out-of-plane forces can be computed. For this the length of the strings is denoted by l. Four strings are connected to the chuck where their pretension force is given by Eq. 5-9 and Eq. 5-12 as function of the desired in-plane pretension force F_p. Then, using basic trigonometry, it can be computed that when the chuck moves upward (or downward) by an amount of Δ_z, the downward force component, denoted by F_d, is given by:

$$F_d = \frac{\Delta_z \left(2 + \sqrt{2}\right) F_p}{\sqrt{l^2 + \Delta_z^2}}.$$

The maximum out-of-plane stiffness k_d is given by:

$$k_d = \frac{F_d}{\Delta_z} = \frac{\left(2 + \sqrt{2}\right) F_p}{\sqrt{l^2 + \Delta_z^2}}.$$

The length l of the strings is designed to be 111 mm. Note that the chuck will move maximal $\Delta_z = 0.5$ mm upward or downward since it should stay within the sensor range of 1 mm. Furthermore, as stated in the requirements, the pretension force F_p is selected to be 0.1 N. Therefore, the maximum out-of-plane force will be $F_d = 1.3$ mN and the maximum stiffness will be $k_p = 2.5$ mN/mm which is very small.

Furthermore, remember from Subsection 5-4-2 that the mass of the total construction on the vibration isolation table is 93 kg. Such small forces acting on such a large mass can be neglected. The same is true for the two out-of-plane rotations, and for brevity, this analysis is therefore omitted from this report.

In-plane fixation design

Based on these finding the in-plane fixation had been designed. A render can be seen in Figure 5-27. As can be seen, the in-plane fixation uses a separate frame where the components are mounted on. This will be called the in-plane fixation frame. Now all the features are covered step by step.

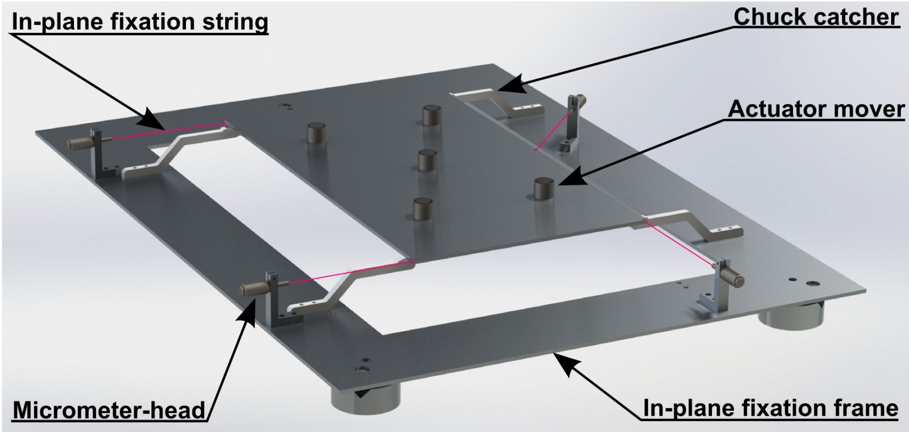

Figure 5-27: *A render of the in-plane fixation. The chuck with the actuator movers is shown in the middle. On the sized, on-top of the in-plane fixation frame, micrometers-heads are mounted. The chuck is connected to these micrometers-heads using strings to fix the chuck's in-plane DoFs. Furthermore white parts can be seen, which are called chuck catchers. Their function is to support the chuck when the in-plane fixation frame is removed along witch the chuck to avoid large strings in the strings connecting the chuck to the in-plane fixation frame.*

It need to be noted that the chuck is connected to this frame with strings. When the sensor locations need to be altered the chuck needs to be removed. Therefore, the entire in-plane fixation frame must be removable. This frame is also mounted using a quasi-kinematic mount as described in Subsection 5-4-2 such that the chuck will return to its previous location.

Furthermore, micrometer-heads can be seen in Figure 5-27. The strings are connected to the frame via these heads. If some realigning of the chuck is required with respect to the force frame then this can be done easily and accurately using the micrometer-heads. Also, the pretension string uses a micrometer-head. This can be used to accurately control the pretension force. In order to avoid torsion in the strings, micrometer-heads with non-rotating spindle are selected.

Finally, we see white curved beams which are called chuck catchers. When the in-plane suspension frame is removed the entire weight of the chuck will by carried by the strings. By handling the overall in-plane fixation frame with the chuck connected in this way very large strains are expected in the strings which will probably change their length or break them. Now the chuck will rest on the catchers when the in-plane fixation frame is removed and as such the strain in the strings is limited.

5-5 Validation of design

After the detail design has been completed all parts of the setup have been manufactured and assembled. After these steps have been completed measurements are performed to validate the setups performance and behavior. A photo of the assembled setup is shown in Figure 5-28.

5-5-1 Sensitivity function of the levitation controller

The first property that is studied is the performance of the controller levitating the chuck. The controller has been configured with the parameters as obtained from the rules of thumb described in Subsection 5-2-2. Then, the controller parameters have been fine tuned to increase its performance

The controllers performance is studied by determining its ability to reject disturbances i.e. obtaining the system's closed-loop sensitivity function. The sensitivity function is obtained experimentally. Thereafter, the results are compared with the theoretical sensitivity function obtained from the model introduced in Section 4-2. The 11 samples delay the digital sensor interfaces introduces as shown in Figure C-3, presented, appendix C-3-2 on page 117,

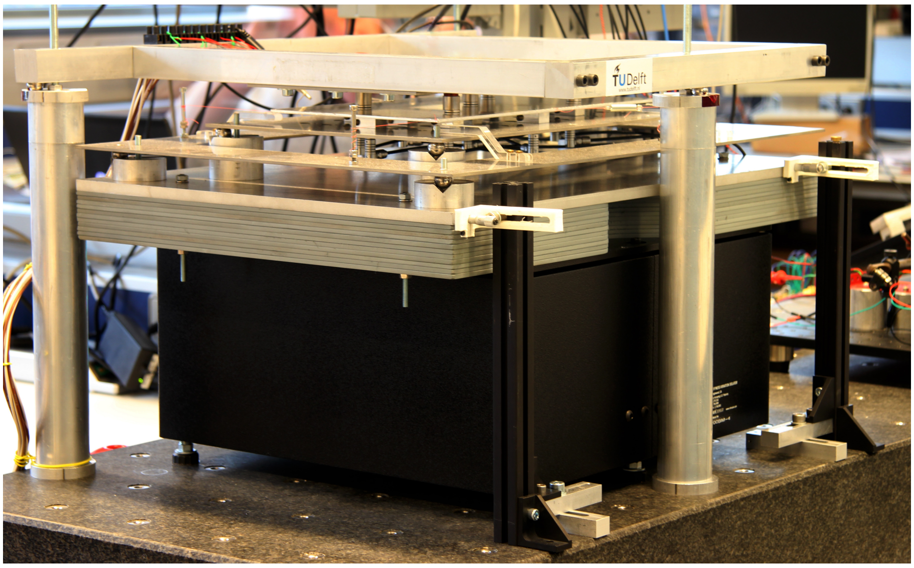

Figure 5-28: *Photograph of the manufactured and assembled setup.*

Each experiments lasts 6 minutes and a square wave input disturbance force with a cycle time of 20 seconds is used. During the 6 minutes 18 responses are obtained which are averaged to reduce the influence of noise. Then, amplitude spectra of both the input and output are computed where use is made of a hanning window. The ratio of these amplitude spectra provides the closed-loop sensitivity function describing the transfer from disturbance to output. The results are shown in Figure 5-29.

First, the sensitivity functions corresponding to the designed controller settings are discussed. It can be seen that the measured sensitivity is about equal or lower as the predicted sensitivity. The biggest difference is that, in Figure 5-29a and 5-29b, the model seems to have a maximum around 2 Hz which is much lower for the actual system. This can have many reasons, one could be that, because this controller has a very limited stiffness, only a small disturbance force could be applied resulting in a biased estimate of the transfer at these low frequencies. Another difference is that that some resonances are predicted by the model which do show up in practice. This can be explained by the fact that the actuators and sensors are placed on nodal lines. In the real setup this has been done exactly, while the model is based on a finite element model of 8 times 8 elements. The actuators and sensors had to be placed to the nearest nodes causing some resonances and anti-resonances not to be at exactly the same frequency but only almost.

The controller was tuned to increase its performance while maintaining good stability margins. For the case shown in Figure 5-29a, the model matches very well with the measured sensitivity function and the maximum sensitivity has been reduced. For the case shown in Figure 5-29b and 5-29c, the controller gains could not increased much. Therefore, their is only little change and no significant improvement. For these cases, the stability margins have mainly been improved.

5-5-2 Deformations

In the previous subsection the performance of the controller was investigated. The task of this controller is to keep the chuck in range of the sensors when disturbance forces are applied. The actual purpose of the setup is to investigate deformations of the chuck. Therefore, the deformation, which was used as benchmark during the design phase, is compared to the measured deformation. This is the deformation of the center of the chuck with respect to its position as used by the controller. The result is shown in Figure 5-30.

As is shown, the measured deformation matches very well with the deformations obtained from the model. The static deformation is in reality about 1 μm smaller. The most likely explanation for this is the curvature of the plate. The model assumes a perfectly flat plate while the used chuck has an very small umbrella shaped curvature. It is well known that curvatures of thin walled structures makes them stiffer.

Furthermore, the measured frequency of the resonance peaks matches very well with the model while

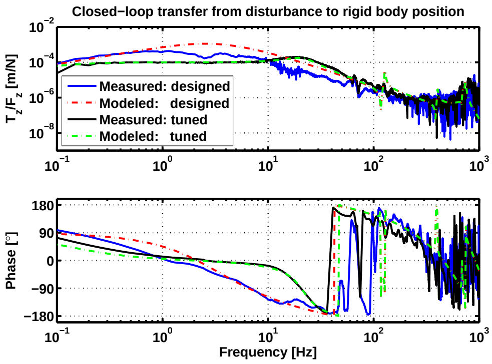

(a) Sensitivity function from disturbance force to z-translation of chuck.

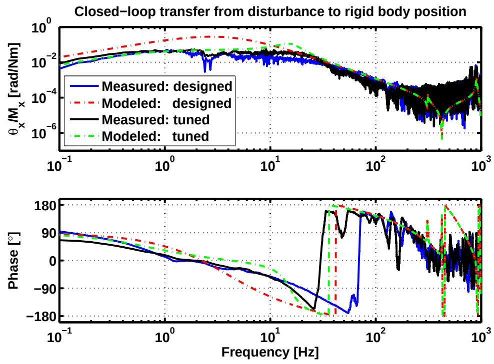

(b) Sensitivity function from disturbance to rotation of chuck around x-axis as defined in Figure 5-26.

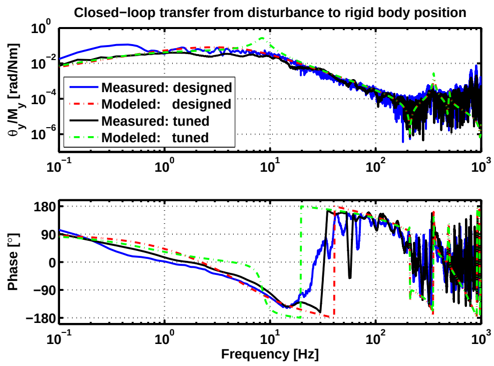

(c) Sensitivity function from disturbance to rotation of chuck around y-axis as defined in Figure 5-26.

Figure 5-29: *Sensitivity functions of the closed-loop system of each of the three out-of-plane DoFs positioned by the levitation controller. Modeled and measured transfer functions are compared for two different controllers, namely: the designed controller and a by tuning improved controller.*

their amplitudes are are also in the same order of magnitude. From this it is concluded that the assumed damping model as mentioned in Subsection 5-2-2 is a good approximation.

5-5-3 Noise level

Finally, some measurements have been performed to quantify the measurement noise level which is compared with the in Section 5-3 obtained theoretical noise level. The setup is used to measure deformations of the chuck and use them in the shape estimation algorithms. The smallest deformations that can be reliable measured is limited by the measurement noise.

Therefore, a constant disturbance force is applied to the chuck which should result in a constant deformation. This deformation is measured over 6 minutes. A power spectral density is computed via Welch's method. This power spectral density is converted to an amplitude spectrum of the measured deformation. Figure 5-31a clearly shows that the amplitude spectrum is non-zero which is caused by the measurement noise.

As is shown, for high frequencies the measurement noise is small while at low frequencies a very large amount of measurement noise is present. In addition, concentration of frequency content can be seen at 1 Hz, 2 Hz and 10 Hz. The vibration isolation table, as discussed in Subsection 5-4-2 has an eigenfrequency of 0.5 Hz. However, this frequency can be tuned and also depends on the mass of the setup. Likely, the actual eigenfrequency of this vibration isolation table in its current configuration is 1 Hz. Furthermore, the vibration isolation table has rotational eigenfrequencies of which probably one lies at 2 Hz. Furthermore, as discussed in Subsection 5-3-1, most of the floor vibration frequency content is centered around 10 Hz and this is where the 3rth peek originates from.

The measurement noise level is quantified via a cumulative power spectrum shown in Figure 5-31b.

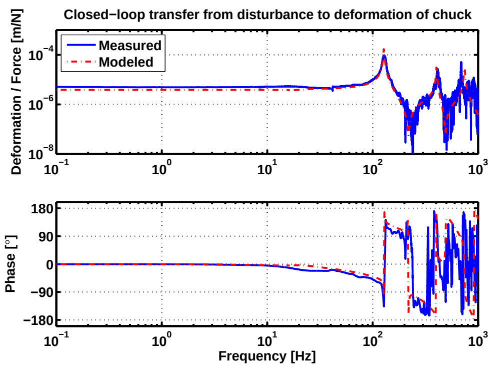

Figure 5-30: *Modeled and measured deformation of the center of the chuck relative to its position as used by the controller.*

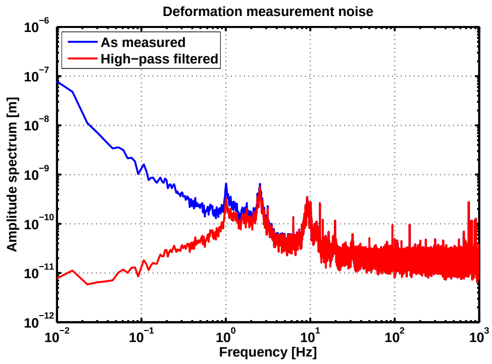

(a) Amplitude spectrum of a measured deformation. Both the measured and a high-pass filtered version of the measurement is shown.

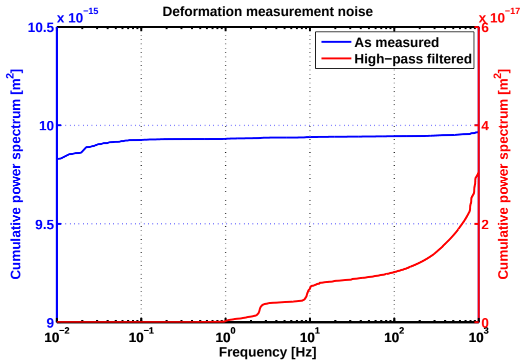

(b) Cumulative power spectrum of a measured deformation. Both the measured and a high-pass filtered version of the measurement is shown.

Figure 5-31: *These figures show spectra of a measured deformation. A constant disturbance force was applied which should result in a constant deformation. Clearly, the spectra are non-zero which is cause by measurement noise.*

As can be seen, the noise level is quite high, about 800 nm P-P, where again use is made of the rule of thumb: the RMS noise level times 8 is the approximated P-P noise level. However, practically all noise power is concentrated in the low frequency part of the frequency range. The vibration isolation table does not filter out these frequencies since they are below its eigenfrequency. These low frequencies are not of any interest for our experiments and are therefore filtered out using a 2nd order high-pass filter with a cut-off frequency at 1 Hz. Then a measurement noise level of 53 nm P-P remains.

In Section 5-3 it is presented that the expected measurement noise level of each sensor is 28 nm P-P. From this analysis it is concluded that the actual noise level is in the same order of magnitude as the predicted noise level.

5-6 Overview of conclusions

In this section a summary of the conclusions and results in this chapter is provided. It is created to give the reader a compact overview.

Requirements (§5-1)

The setup is designed to fulfill certain functions. These functions are stated here.

The setup is used to evaluate the developed estimation algorithms presented in Chapter 2. The setup must serve two goals. It should be usable as an experimental setup and as a demonstrator setup. Both functions can be divided in sub-functions.

An experimental setup must be modifiable, such that many different scenarios under different conditions can be evaluated. It should be repeatable, in the sense that after modifications are made undone, new results must be comparable with initially obtained results. Finally, results must be traceable so that artifacts in the results can traced down to the source to gain a better understanding of the algorithms.

A demonstrator setup should simulate relevant conditions of an actual lithography machine. In this way it can be demonstrates that the estimation algorithms can be used in such applications successfully. In addition, it should perform optimally so the true potential of the estimation algorithms is demonstrated.

Conceptual design (§5-2)

In Section 5-2, basic mounting principles and conditions in a lithography machine are studied to obtain an abstract concept design of the setup. Furthermore, the feasibility of this concept is studied.

It has been concluded that a separate metrology and force frame are desired. The metrology frame should be connected via a low stiffness to the mechanical ground. The actuator stiffness should be low. Furthermore, it is concluded that a levitated chuck provides several advantages namely: it rejects floor noise, it is contactless, it resembles conditions in a lithography machine and it provides means to actuate the chuck.

For simplicity it has been decided to only levitate the 3 out-of-plane DoFs. These DoFs are most of interest because the deformations of interest happen in these directions. The other 3 in-plane DoFs are fixated.

Finally, the capabilities of this levitation controller are studied. Design decisions have been made to separate this controller design from the setup design as much as possible. However, the sample frequency limits the achievable controller bandwidth. Therefore, the levitation controller's capabilities had to be taken into account during the remainder of the design process.

Noise measurements (§5-3)

Floor vibration measurements have been performed at the setup's location. These measurements provide an estimate of the expected measurement noise level. Furthermore, they are used to quantify the performance increase related to the conceptual choices.

After analysis the following conclusions have been drawn: by omitting a separate metrology and force frame and by supporting the chuck on the mechanical ground, the measurement noise is expected to be 43 nm P-P. When the chuck is levitated using low stiffness actuators this reduces to 34 nm P-P. Then, when the sensors are mounted on a vibration isolated metrology frame, the measurement noise level is further reduced to 28 nm P-P. The corresponding sensor noise level is 27 nm P-P which is clearly the largest remaining noise source.

Detailed design (§5-4)

The detailed design choices are made to minimize the sensor requirements, thereby reducing the cost of the setup.

The chuck has been designed to maximize its deformations while maximizing the levitation controller's stiffness. This optimization problem was constrained by practical considerations namely, a minimum weight and maximum size of the chuck.

After the chuck had been designed the metrology frame was designed. The vibration isolation property is implemented by using a commercial vibration isolation table. In order to guarantee repeatability, it is mounted using a quasi-kinematic mount explained in Subsection 5-4-2. Finally, manufacturability was a very important requirement. Therefore, use was made of plates which can be manufactured in one production step using the laser-cutter of the university's faculty. These considerations have led to a force frame design which uses the same features to guarantee repeatability and ease of manufacturability.

The actuators have been selected to be voice coil actuators. Voice coil actuators are contactless and have a low actuator stiffness. The actuators used by the levitation controller have been placed on the nodal lines of the first modeshapes such that the controller bandwidth could be improved resulting in a better signal to noise ratio when the chuck's deformations are measured.

Once the chuck design has been optimized, the sensor requirements have been determined. Thereafter, capacitive sensors where selected as being most suitable for the task. They can achieve the required range over resolution ratio in a contactless manner while being relatively cost effective. The sensor specifications have been validated and in Appendix C the results are presented. The selected sensor has digital interface.

The performance of this interface has been experimentally evaluated and was found to perform sufficiently with respect to our requirements. This allows for a cleaner and simpler way to interface the sensors with the controller.

Finally, the in-plane fixation is designed. After discarding a thoroughly studied concept, which has been proven to be unfeasible given the available design time, the final concept was chosen for its simplicity. It fixates the in-plane DoFs of the chuck using strings, while it introduces only a very low stiffness in out-of-plane directions. Micrometer-heads have been added such that alignment issues between the chuck and the force frame can be solved easily and accurately

Validation (§5-5)

After the setup has been built, experiments have been performed to validate the designed specifications.

From these measurements it is concluded that the performance of the controller positioning the chuck, when using the designed controller parameters, is about equal or better than the expected performance compared to the predicted performance. The controller's parameters are tuned to increase its the performance while maintaining good stability margins.

The deformation of the center of the chuck has been used as benchmark during the design phase. The deformation is measured and matches very well with the predicted deformations. The (anti)-resonance peaks are at the same frequency and of comparable magnitude.

Finally, the noise level of the deformation measurement has been determined. It has been found that this is in the same order of magnitude as the expected noise level.

Based on these results it is concluded that the setup will function as expected and can be used very well for its purpose.

Chapter 6

Conclusions and recommendations

6-1 Conclusions

This section provides the conclusions obtained in this research. The section numbers in the margin refer to the corresponding section on which the conclusion is based.

6-1-1 Propagation of model uncertainty

In order to study model uncertainty, a measure for it uncertainty must be available. Markov parameters, §3-2 which describe the impulse response of a system, are proven to be invariant to the state-space realization of the system. Therefore, Markov parameters of different candidate models can be compared and their difference provides a measure of the model uncertainty. The Markov parameters and their uncertainty can §3-2-2 be obtained using physical modeling or using system identification when the signals that need estimation can be made measurable for such an experiment. Predictor Based System IDentification (PBSID) is considered to be the most suitable System IDentification (SID) technique since PBSID estimates the Markov parameters directly and provides their estimation covariance which is a measure for their uncertainty.

The Receding Horizon Input (RHI) estimator can be constructed using only Markov parameters. The §3-2-3 uncertainty on Markov parameters can be propagated through the RHI estimator so that an upper bound §3-3 on estimation error of the the unknown input is obtained.

However, when it is assumed that the exact size and sign of the error on each Markov parameter is §3-4 unknown, but only an upper bound on this error is available, this approach results in a large error bound on the estimated input. Because an upper-bound on the estimation error is computed the worst case scenario must be assumed where all errors are of maximum size and all add up.

However, the RHI estimator is more robust to model errors and these large error bounds are conservative. §3-4-3 The errors introduced by mismodelling do not add up but cancel out for the most part. The modeling error was found to contain a structure. Therefore, a different method named, the comparison method, is proposed. It determines the estimation error bound caused by mismodelling, while taking the structure of the model error into account.

By determining the potentially valid model, that produces the largest estimation difference, compared §3-5-1 to the estimated model, a realistic estimation error bound is obtained. This method is presented in Theorem 1 on page 42.

Finally, the latter approach can be applied to determine accurate error bounds on Least Squares (LS) §3-5-3 data matrix and the LS measurement vector which are required for the construction of the RHI estimator. These error bounds can be used to solve the LS problem using Robust Least Squares (RLS) in order to obtain robust estimations of the unknown input.

The methodology for studying the effect of model uncertainty on RHI estimator can also be applied §3 to the computation of the linear estimator used for shape fitting.

"Based on the latter sub-conclusions, it is concluded that the first part of the first research objective has been achieved. This objective was to answer:

When performing RHI estimation, what will be the error bound on the estimated input in the presence of model errors? In addition, can this knowledge on the error bound in combination with RLS produce *more accurate estimations compared to OLS? How does this performance difference relate to the overall estimation error introduced by model errors?*

It is concluded that it is possible to obtain an estimation error-bound when performing RHI estimation in the presence of model errors. In addition, error-bounds on the LS data matrix and on the LS measurement vector can be computed and can be used to apply RLS methods to solve the LS problems posed by the RHI estimator."

6-1-2 Applying robust least squares algorithms

§4-1 The RHI estimation solves a LS problem in order to produce an estimate of the unknown input. The LS problem is constructed from the LS data matrix and the LS measurement vector, which are uncertain if the model is uncertain. In the previous subsection it has been concluded that accurate error bounds on these variables can be obtained.

§4-1 The LS problem can then be solved using RLS techniques to obtain a robust estimate of the unknown input. RLS techniques attempt to reduce the variance at the cost of adding bias to the solution. How this trade-off is made depends on the specific RLS method and the provided error bounds. Three RLS methods have been applied namely: TLS, C-RLS and R-RLS respectively detailed in Subsection 4-1-1, 4-1-2 and 4-1-3.

§4-3-4 The following conclusions are based on the case-study performed in Chapter 4. First of all, it is concluded that reducing the modeling error results in a larger reduction of the estimation error than applying RLS methods. Furthermore, it is concluded that TLS is not a suitable method for obtaining robust RHI estimates in the presence of modeling errors. TLS produces almost always bigger Root Means Square (RMS) and maximum estimation error.

§4-3-4 Zero Mean White Noise (ZMWN) input signals get usually estimated much better when using C-RLS or R-RLS instead of using LS, both in RMS and maximum estimation error sense.

§4-3-5 For other discontinuous signal types, such as a square wave, C-RLS performs also typically better then Ordinary Least Squares (OLS). This conclusion is based on the comparison of 100 estimation errors that are obtained from simulations using different perturbed models. OLS tend, to give better estimates when continuous input signals are considered. Based on these results it is concluded that information about the typical shape of the input that needs estimation will provide a basis for the most suitable LS methodology.

§4-3-4 Furthermore, it is concluded that the computed error bounds on the LS data matrix and the LS measurement vector, based on Theorem 2 and 3, provide proper sized bounds in such way that, when they are used to configure the RLS methods, they do produce consequently better estimates when considering discontinuous signals.

§4-3-4 Finally, it is concluded that overestimating the uncertainty bounds on LS data matrix and LS measurement vector degenerate the performance of the RLS methods while underestimating the bounds has a much smaller effect.

"Based on the latter sub-conclusions, it is concluded that the second part of the first research objective has also been achieved. This objective was to answer:

When performing RHI estimation, what will be the error bound on the estimated input in the presence of model errors? In addition, can this knowledge on the error bound in combination with RLS produce more accurate estimations compared to OLS? How does this performance difference relate to the overall estimation error introduced by model errors?

It is concluded that RLS methods can reduce the estimation error significantly in both RMS and maximum error sense. For the performed case-study this happened for discontinuous input signals. The specific choice of the RLS method is a very important factor, which determines the increase in performance. Finally, the estimation performance will increase more when the model accuracy is improved than when a properly selected RLS method is successfully deployed using realistic uncertainty bounds on the LS data matrix and LS measurement vector."

6-1-3 Setup design

Requirements

To validate the theory behind the estimation algorithms, experimental results are preferred over simulation results and therefore an experimental setup is designed. The setup must also serve as demonstrator to show the capabilities of the estimation algorithms in conditions topologically similar to those in a lithography machine. §5-1

An experimental setup must be modifiable so that many different scenarios under different conditions can be evaluated. It should also be repeatable, in the sense that after modifications are made undone, new measurements must be comparable to the original measurements. Furthermore, the results must be traceable, so that artifacts in the results can be traced to their origin, in order to gain a better understanding of the results and algorithms. A demonstrator setup, on the other hand, should simulate relevant conditions in a lithography machine. §5-1

Conceptual design

The setup requires at least sensors, actuators and a chuck, which all needed to be connected the mechanical ground. To reject measurement noise caused by floor vibration, the sensors must be connected to the mechanical ground via a low stiffness connection and low stiffness type actuators should be mounted directly to the mechanical ground. The chuck must be levitated using these actuators and sensors in the control-loop. §5-2-1

Levitation offers more advantages namely: it provided actuation means to compensate for the estimated deformations which can be used to demonstrate the usefulness of the estimations. Furthermore, the chuck is then suspended in a manner topologically similar to that in a real lithography machine. Finally, levitation can be implemented contactless, which eliminates friction and hysteresis forces that would cause degradation of the performance of the estimation algorithms. §5-2-2

The phenomena of interest, the chuck's deformations, occur in the out-of-plane directions. Therefore, it has been decided to only 'levitate' these directions and to kinematically fix the in-plane Degrees of Freedom (DoFs).

The the levitated chuck concept was proven to be feasible. The bandwidth of the controller levitating the chuck is limited by the sampling frequency. However, the achievable controller stiffness is low and therefore, the controller limitations must be taken into account during the detailed design phase. §5-2-2

Noise measurements

To quantify the performance increase related to the conceptual choices. The four most important noise sources, floor vibrations, vibrations due to actuator reaction forces, current amplifier output noise and sensor noise were considered. Floor vibration measurements have been performed at the location where the setup will be operated. Also, current amplifier output noise measurements have been performed. These measurements provide an estimate of the expected measurement noise level. They showed that for the proposed conceptual design, the sensor noise level is the largest remaining measurement noise source. §5-3-1

Analysis of the measurements showed that without metrology frame and with a non-levitated chuck the measurements noise would be 43 nm Peak-to-Peak (P-P). When the chuck is levitated this is reduced to 34 nm P-P because not all floor vibrations are passed to the chuck as a result of the limited controller bandwidth. Finally, if the sensors are placed on a metrology frame the measurement noise is further reduced to 28 nm P-P. In this case, the sensor specifications are limiting the performance of the setup. The corresponding sensor noise level is 27 nm P-P, which is clearly the largest remaining noise source. §5-3

Detailed design

The most important part of the setup is the chuck. It has been designed to minimize the displacement sensor requirements, thereby reducing the cost of the setup. Specifically the required range and resolution are reduced which was achieved by minimizing the ratio between the chuck deformations and chuck displacements. §5-4-1

The metrology frame is suspended by a commercial vibration isolation table. Components that are occasionally demounted, are positioned using a quasi-kinematic mount in order to guarantee repeatability. Manufacturability is an important requirement, so many parts are made from plates which can be manufactured in one production step using the laser-cutter of the university's faculty. §5-4-2

§5-4-3 These considerations led to a force frame design that uses the same features to guarantee repeatability and ease of manufacturability. Furthermore, it is made stiff to reduce the influence of vibrations, which propagate via the parasitic stiffness of the voice coil actuators to the chuck.

§5-4-4 Voice coil actuators have been selected because they have low stiffness and are contactless. They have been placed on the nodal lines of lower model shapes so that they are not excited. Furthermore, four actuators have been selected to attain a symmetrical placement on the chuck, thereby also avoiding excitation of mode shapes.

§5-4-5 Capacitive sensors have been selected because they are contactless, and can meet the range/resolution requirements while being cost effective.

§5-4-6 Finally, the in-plane fixation has been designed to kinematically fixate the in-plane DoFs of the chuck while introducing no significant stiffness in the out-of-plane directions. Initially, a contactless concept using repelling magnets was considered, which was shown to be unfeasible given the available design time. Therefore, a simpler concept was selected which fixates the chuck's in-plane DoFs using strings. The strings are connected to micrometer-heads that makes it possible to solve alignment issues between the chuck and the force frame accurately.

§5-5-1 After the design has been completed the setup has been built and its performance is validated. The controller positioning the chuck performs about equal or better compared to the predicted performance. The controller has been tuned to increase its performance further while maintaining good stability margins.

§5-5-2 The deformation that is used as benchmark for designing the setup was accurately modeled, as it matched well with the measured deformation of the chuck at that location. The (anti)-resonance peaks are at the expected frequency and of comparable magnitude.

§5-5-3 Finally, the noise level of the deformation measurement has been determined. This is in the same order of magnitude as the predicted noise level.

"Based on the latter sub-conclusions, it is concluded that the second research objective has been achieved. This objective was:

To design and build a setup that serves both as experimental setup and as demonstrator setup on which both estimation algorithms can be applied, so that their practical performance can be evaluated and compared with simulation results.

The performance of the setup has been experimentally validated and was found to perform as designed. Therefore, it is concluded that the setup can be used to experiment with the estimation algorithms and to demonstrate their capabilities in conditions topologically similar to those in a lithography machine. Furthermore, the experimental results will compare well to the simulation results."

6-2 Recommendations

Although much work has been done within this graduation project, there are related and interesting topics left unstudied. The following recommendations are suggestions for a possible continuation of the work presented in this thesis.

- An experimental setup has been built and its performance has been validated. However, its characteristics should be mapped accurately and a model relating inputs and outputs should be obtained so that the estimation algorithms can be implemented. The model can be obtained, as described in this thesis in Subsection 3-2-2, using PBSID.
- The obtained model should be used to implement the shape fitting algorithm and RHI estimator in order to demonstrate their performance on the setup. In addition, many different experiments can be conducted to evaluate the performance of the estimation algorithms in different scenarios.
- The algorithms should also be implemented using a perturbed model and the performance decrease should be evaluated. In addition, the RLS methodologies can be applied to solve the required LS problem as proposed in this thesis. Then the practical estimation performance should be evaluated using the setup. The results should be compared with the simulation results presented in this thesis in Chapter 4.

- Once accurate estimates of chuck's shape are obtained using the estimation algorithms, these estimates should be used to reposition the chuck to compensate for the chuck's deformations. This recommendation can be split in two tasks, a theoretical and practical task.
  - The chuck is repositioned by applying forces to it and these known actuation forces will also cause the chuck to change its shape. This effect must be studied and a theoretical background should be provided such that, given an estimated shape of the chuck, suitable actuation signals can be determined.
  - Furthermore, once this theoretical background is available, it should be tested on the setup to validate that the positioning accuracy of the PoI can indeed be improved by using the estimation algorithms.
- Finally, the effect of model uncertainty on the RHI estimator has been studied. The effect of model uncertainty on the shape fitting algorithms presented in Section 2-1 should also be studied. The methodology used to study the effects of model uncertainty on the RHI estimator provide a good starting point for this study.

These are only a few suggestions of possible future work. However, these recommendations are a serious amount of work that will easily fill another graduation project.

Appendix A

Predictor Based Subspace Identification (PBSID)

A-1 The subspace identification algorithm

A-1-1 Computing the Markov parameters

One of the most popular methods for closed-loop subspace identification is the PBSID algorithm which will be explained in this section. This section is based on [18] unless otherwise referred.

Let the goal be to seek a realization of the innovation model in Eq. 2-5 in the one-step ahead predictor form. This is for ease repeated here:

$$x(k+1) = \Phi x(k) + \tilde{B}u(k) + Ky(k) \tag{A-1a}$$

$$y(k) = Cx(k) + Du(k) + e(k), \tag{A-1b}$$

where $\Phi = A - KC$ and $\tilde{B} = B - KD$. Recall that index k indicates the time instant, $\tilde{x}(k) \in \mathbb{R}^n$ is the state, $u(k) \in \mathbb{R}^m$ are inputs and $y(k) \in \mathbb{R}^\ell$ are the outputs and $e(k) \in \mathbb{R}^\ell$ denotes a Zero-Mean White-Noise (ZMWN) sequence.

When propagating Eq. A-1 for p time instants, with $p \geq 1$, the following equation can be obtained:

$$\begin{aligned} y(k+p) = C\Phi^p x(k) &+ \underbrace{\begin{bmatrix} C\Phi^{p-1}\tilde{B} & C\Phi^{p-2}\tilde{B} & \cdots & C\tilde{B} \end{bmatrix}}_{\mathcal{B}_p} \begin{bmatrix} u(k) \\ \vdots \\ u(k+p-1) \end{bmatrix} + Du(k+p) \\ &+ \underbrace{\begin{bmatrix} C\Phi^{p-1}K & C\Phi^{p-2}K & \cdots & CK \end{bmatrix}}_{\mathcal{K}_p} \begin{bmatrix} y(k) \\ \vdots \\ y(k+p-1) \end{bmatrix} + e(k+p). \end{aligned} \tag{A-2}$$

The block elements in $\mathcal{B}_p$ and $\mathcal{K}_p$ together with D are known as the Markov parameters of the predictor form Eq. A-1.

For brevity the following notation for matrices with a *Hankel structures* is introduced:

$$Y_{i,s,N} = \begin{bmatrix} y(i) & y(i+1) & \cdots & y(i+N-1) \\ y(i+1) & y(i+2) & \cdots & y(i+N) \\ \vdots & \vdots & \ddots & \vdots \\ y(i+s-1) & y(i+s) & \cdots & y(i+N+s-2) \end{bmatrix},$$

where i denotes the first sample, s denotes the number of block rows and N the number of columns. Likewise defining $X_{i,s,N}$, $U_{i,s,N}$ and $E_{i,s,N}$ are defined. Then time shifted versions of Eq. A-2 are repeated N times, then one obtains:

$$Y_{p,1,N} = C\Phi^p X_{0,1,N} + \mathcal{B}_p U_{0,p,N} + DU_{p,1,1} + \mathcal{K}_p Y_{0,p,N} + E_{p,1,N}, \tag{A-3}$$

which is called the *PBSID data equation*.

Now note that for a strictly stable matrix Φ (i.e. all eigenvalues within the unit circle), it can be shown that $\lim_{p\to\infty} ||C\Phi^p X_{0,1,N}||_F = 0$. For a finite, sufficiently large value of p, Φ can be made arbitrarily small and $||C\Phi^p X_{0,1,N}||_F \approx 0$. Assuming p is selected such that $||C\Phi^p X_{0,1,N}||_F$ can be considered zero, then the data equation in Eq. A-3 reduces to:

$$Y_{p,1,N} \simeq \mathcal{B}_p U_{0,p,N} + DU_{p,1,1} + \mathcal{K}_p Y_{0,p,N} + E_{p,1,N}. \tag{A-4}$$

Now the influence of the initial state is eliminated. Note that $\mathcal{B}_p$, D and $\mathcal{K}_p$ are the unknown quantities that contain the information we wish to retrieve. Furthermore, $E_{p,1,N}$ is also not known. Eq. A-4 can be solved in a least-squares sense for $[\mathcal{B}_p \, D \, \mathcal{K}_p]$ as:

$$\begin{bmatrix}\hat{\mathcal{B}}_p & \hat{D} & \hat{\mathcal{K}}_p\end{bmatrix} = \arg \min_{[\mathcal{B}_p \, \mathcal{K}_p]} \left\| Y_{p,1,N} - \begin{bmatrix}\hat{\mathcal{B}}_p & \hat{D} & \hat{\mathcal{K}}_p\end{bmatrix} \begin{bmatrix} U_{0,p,N} \\ U_{p,1,1} \\ Y_{0,p,N} \end{bmatrix} \right\|_F^2. \tag{A-5}$$

A unique solution to this problem exist if $[U_{0,p,N}^T \, U_{p,1,1}^T \, Y_{0,p,N}^T]^T$ has full rank.

This Least squares problem can be solved using the LQ factorization:

$$\begin{bmatrix} \begin{bmatrix} U_{0,p,N} \\ U_{p,1,1} \\ Y_{0,p,N} \end{bmatrix} \\ Y_{p,1,N} \end{bmatrix} = \begin{bmatrix} L_{11} & 0 & 0 \\ L_{21} & L_{22} & 0 \end{bmatrix} \begin{bmatrix} Q_1 \\ Q_2 \\ Q_3 \end{bmatrix}, \tag{A-6}$$

where, for clarity: $L_{11} \in \mathbb{R}^{m(p+1)+lp \times m(p+1)+lp}$, $L_{21} \in \mathbb{R}^{l \times m(p+1)+lp}$, $L_{22} \in \mathbb{R}^{l \times l}$ and $Q_2 \in \mathbb{R}^{l \times N}$. It can be shown that $L_{21} = [\mathcal{B}_p \, D \, \mathcal{K}_p] L_{11}$ and an estimate of the Markov parameters can be obtained by computing:

$$\begin{bmatrix}\hat{\mathcal{B}}_p & \hat{D} & \hat{\mathcal{K}}_p\end{bmatrix} = L_{21} L_{11}^{-1}. \tag{A-7}$$

The noise sequence $E_{p,1,N}$ is given by:

$$E_{p,1,N} = L_{22} Q_2. \tag{A-8}$$

A-1-2 Extracting the system matrices

After the Markov parameters $[\mathcal{B}_p \, D \, \mathcal{K}_p]$ are estimated, there are multiple ways to obtain a state-space realization (A, B, C, D). A few possibilities are given in [18]. One way is to directly formulate the system matrices using the Markov parameters as:

$$\bar{x}(k+1) = \begin{bmatrix} 0 & I & 0 & \cdots & 0 \\ 0 & 0 & I & \ddots & \vdots \\ \vdots & \vdots & \ddots & \ddots & 0 \\ 0 & 0 & \cdots & 0 & I \\ 0 & 0 & \cdots & 0 & 0 \\ C\Phi^{p-1}[\tilde{B}\, K] & \cdots & \cdots & C\Phi[\tilde{B}\, K] & C[\tilde{B}\, K] \end{bmatrix} \bar{x}(k) + \begin{bmatrix} 0 \\ 0 \\ \vdots \\ 0 \\ I \\ D \end{bmatrix} u(k) + \begin{bmatrix} 0 \\ 0 \\ \vdots \\ 0 \\ 0 \\ I \end{bmatrix} e(k) \tag{A-9a}$$

$$y(k) = \begin{bmatrix} C\Phi^{p-1}[\tilde{B}\, K] & \cdots & \cdots & C\Phi[\tilde{B}\, K] & C[\tilde{B}\, K] \end{bmatrix} \bar{x}(k) + Du(k) + e(k). \tag{A-9b}$$

Obtaining the system matrices like this is very simple. However, the model order of $p(m+\ell)$, is usually very large. This may, from numerical point of view, be undesirable if the model is used in more complicated algorithms such as for example control design. If this poses a problem, standard model order reduction techniques can be applied to reduce order of the model. An interesting observation is that the state is measurable since it is composed of delayed input and output samples. Another nice feature is that the variance on the elements of the state-space matrices can directly be obtained from the least squares problem Eq. A-5.

Alternatively, a method very similar to the open-loop method N4SID can be used to obtain the system matrices. An advantage of this method is that a SVD is used to select a proper model order. First the state sequence is estimated, and then, using the state sequence, a realization of the system matrices is obtained. Observe the following:

$$CX_{p,N} = \begin{bmatrix}\mathcal{B}_p & D & \mathcal{K}_p\end{bmatrix} \begin{bmatrix} U_{0,p,N} \\ U_{p,1,1} \\ Y_{0,p,N} \end{bmatrix}.$$

The row space of $CX_{p,N}$ is contained in that of $X_{p,N}$, i.e. $CX_{p,N} \subseteq X_{p,N}$. However, for a general C matrix the two row spaces are not equal which can be interpreted as a loss of information about the state sequence. A more 'richer' matrix product should thus be formed to preserve the information. Let us now introduce the extended observability matrix of the predictor model $\mathcal{O}_f \in \mathbb{R}^{f\ell \times n}$ as $\mathcal{O}_f = [C^T \; (C\Phi)^T \; \cdots \; (C\Phi^{f-1})^T]^T$, then it can be shown that:

$$\mathcal{O}_f X_{p,N} = \Gamma_{p,f} \begin{bmatrix} U_{0,p,N} \\ Y_{0,p,N} \end{bmatrix}, \tag{A-10}$$

where an estimate of $\Gamma_{p,f}$ denoted as $\hat{\Gamma}_{p,f}$ can be constructed based on the estimated Markov parameters as:

$$\hat{\Gamma}_{p,f} = \begin{bmatrix} \widehat{C\Phi^{p-1}[\tilde{B}\,K]} & \widehat{C\Phi^{p-2}[\tilde{B}\,K]} & \cdots & \widehat{C[\tilde{B}\,K]} \\ 0 & \widehat{C\Phi^{p-1}[\tilde{B}\,K]} & \cdots & \widehat{C\Phi[\tilde{B}\,K]} \\ \vdots & \ddots & \ddots & \vdots \\ 0 & & & \widehat{C\Phi^{f-1}[\tilde{B}\,K]} \end{bmatrix}.$$

An $f \geq n$ is required. It should be noted that the zeros in this matrix are due to the assumption $\Phi^p \simeq 0$ for a sufficiently large finite choice of p. Now, the right hand side of Eq. A-10 can be computed using $\hat{\Gamma}_{p,f}$. Then, the SVD of the right hand side of Eq. A-10 is partitioned it as:

$$\hat{\Gamma}_{p,f} \begin{bmatrix} U_{0,p+1,N} \\ Y_{0,p,N} \end{bmatrix} = \begin{bmatrix} U_1 & U_2 \end{bmatrix} \begin{bmatrix} \Sigma_1 & 0 \\ 0 & \Sigma_2 \end{bmatrix} \begin{bmatrix} V_1^T \\ V_2^T \end{bmatrix}.$$

The system order can be determined based on the magnitude of the singular values. Let the singular values with high magnitudes be contained in Σ_1, and assume the other singular values in Σ_2 are approximately equal to zero. Then, an estimate of the state sequence can be obtained from:

$$\hat{X}_{p,N} = \Sigma_1 V_1^T.$$

Finally, the system matrices can be determined by solving the least squares problems:

$$\hat{X}_{p+1,N-1} = \begin{bmatrix} \hat{A} & \hat{B} & \hat{K} \end{bmatrix} \begin{bmatrix} \hat{X}_{p,N-1} \\ U_{p,1,N-1} \\ E_{p,1,N-1} \end{bmatrix}, \tag{A-11a}$$

$$Y_{p,1,N} = \begin{bmatrix} \hat{C} & \hat{D} \end{bmatrix} \begin{bmatrix} \hat{X}_{p,N} \\ U_{p,1,N} \end{bmatrix} + E_{p,1,N}. \tag{A-11b}$$

First Eq. A-11b should be solved. Then the resulting residual $E_{p,N}$ should be used to solve Eq. A-11a.

A-2 Estimation uncertainty

The Markov parameters are estimated by solving Eq. A-4 in a least squares sense, as given in Eq. A-5. This equation is solved using an LQ factorization. Alternatively, it can be solved directly and the Markov parameters are then given by:

$$\underbrace{\begin{bmatrix} \mathcal{B}_p & D & \mathcal{K}_p \end{bmatrix}}_{\hat{M}_p} = Y_{p,1,N} \begin{bmatrix} U_{0,p,N} \\ U_{p,1,1} \\ Y_{0,p,N} \end{bmatrix}^T \left(\begin{bmatrix} U_{0,p,N} \\ U_{p,1,1} \\ Y_{0,p,N} \end{bmatrix} \begin{bmatrix} U_{0,p,N} \\ U_{p,1,1} \\ Y_{0,p,N} \end{bmatrix}^T \right)^{-1}, \tag{A-12}$$

The covariance the elements of this estimate can be computed by using:

$$\Sigma_{M_p} \triangleq \mathcal{E}[\mathrm{vec}(\hat{M}_p - M_p)\mathrm{vec}(\hat{M}_p - M_p)^T] \tag{A-13}$$

$$= \left(\begin{bmatrix} U_{0,p,N} \\ U_{p,1,1} \\ Y_{0,p,N} \end{bmatrix} \begin{bmatrix} U_{0,p,N} \\ U_{p,1,1} \\ Y_{0,p,N} \end{bmatrix}^T \right)^{-1} \otimes \Sigma_e, \tag{A-14}$$

where by the definition of a zero mean noise sequence, the covariance matrix Σ_e is constant and is defined as:

$$\Sigma_e \triangleq \mathcal{E}[e(k)e(k)^T]$$

The matrix Σ_{M_p} can also be computed numerically in a more efficient way using the LQ factorization in Eq. A-6 as:

$$\begin{aligned}\Sigma_{M_p} &\triangleq \mathcal{E}[\text{vec}(\hat{M}_p - M_p)\text{vec}(\hat{M}_p - M_p)^T] \\ &= (L_{11}^{-1})^T L_{11}^{-1} \otimes \Sigma_e.\end{aligned} \tag{A-15}$$

Both Eq. A-14 and Eq. A-15 are proven in Section A-3. These covariances can be used to obtain uncertainty bounds on the estimated Markov parameters which are used in this thesis.

A-3 Proofs

Proof of Eq. A-14

As is given by Eq. A-12:

$$\hat{M}_p = Y_{p,1,N} \begin{bmatrix} U_{0,p,N} \\ U_{p,1,1} \\ Y_{0,p,N} \end{bmatrix}^{\ddagger}, \tag{A-16}$$

where $A^{\ddagger}$ indicates the right pseudo inverse such that $AA^{\ddagger} = I$. And where $Y_{p,1,N}$ is given by Eq. A-4. Let us denoted $M_p = [\mathcal{B}_p \, D \, \mathcal{K}_p]$, then, the data equation Eq. A-4 can be written as:

$$Y_{p,1,N} \simeq M_p \begin{bmatrix} U_{0,p,N} \\ U_{p,1,1} \\ Y_{0,p,N} \end{bmatrix} + E_{p,1,N}. \tag{A-17}$$

Substituting Eq. A-17 in Eq. A-16, it follows that:

$$\begin{aligned}\hat{M}_p &= \left(M_p \begin{bmatrix} U_{0,p,N} \\ U_{p,1,1} \\ Y_{0,p,N} \end{bmatrix} + E_{p,1,N} \right) \begin{bmatrix} U_{0,p,N} \\ U_{p,1,1} \\ Y_{0,p,N} \end{bmatrix}^{\ddagger} \\ &= M_p + E_{p,1,N} \begin{bmatrix} U_{0,p,N} \\ U_{p,1,1} \\ Y_{0,p,N} \end{bmatrix}^{\ddagger}.\end{aligned}$$

Then:

$$\hat{M}_p - M_p = E_{p,1,N} \begin{bmatrix} U_{0,p,N} \\ U_{p,1,1} \\ Y_{0,p,N} \end{bmatrix}^{\ddagger}. \tag{A-18}$$

Substituting Eq. A-18 in Eq. A-13 and following the stochastic least squares procedure as presented in [43], one obtains:

$$
\begin{aligned}
\Sigma_{M_p} &\triangleq \mathcal{E}[\mathrm{vec}(\hat{M}_p - M_p)\mathrm{vec}(\hat{M}_p - M_p)^T] \\
&= \mathcal{E}\left[\mathrm{vec}\left(E_{p,1,N}\begin{bmatrix}U_{0,p,N}\\U_{p,1,1}\\Y_{0,p,N}\end{bmatrix}^{\ddagger}\right)\mathrm{vec}\left(E_{p,1,N}\begin{bmatrix}U_{0,p,N}\\U_{p,1,1}\\Y_{0,p,N}\end{bmatrix}^{\ddagger}\right)^T\right] \\
&= \left(\left(\begin{bmatrix}U_{0,p,N}\\U_{p,1,1}\\Y_{0,p,N}\end{bmatrix}\begin{bmatrix}U_{0,p,N}\\U_{p,1,1}\\Y_{0,p,N}\end{bmatrix}^T\right)^{-1}\begin{bmatrix}U_{0,p,N}\\U_{p,1,1}\\Y_{0,p,N}\end{bmatrix}\otimes I\right)\mathcal{E}[\mathrm{vec}(E_{p,1,N})\mathrm{vec}(E_{p,1,N})^T]\times \\
&\qquad\qquad \left(\left(\begin{bmatrix}U_{0,p,N}\\U_{p,1,1}\\Y_{0,p,N}\end{bmatrix}\begin{bmatrix}U_{0,p,N}\\U_{p,1,1}\\Y_{0,p,N}\end{bmatrix}^T\right)^{-1}\begin{bmatrix}U_{0,p,N}\\U_{p,1,1}\\Y_{0,p,N}\end{bmatrix}\otimes I\right) \\
&= \left(\left(\begin{bmatrix}U_{0,p,N}\\U_{p,1,1}\\Y_{0,p,N}\end{bmatrix}\begin{bmatrix}U_{0,p,N}\\U_{p,1,1}\\Y_{0,p,N}\end{bmatrix}^T\right)^{-1}\begin{bmatrix}U_{0,p,N}\\U_{p,1,1}\\Y_{0,p,N}\end{bmatrix}\otimes I\right)(I\otimes\Sigma_e)\times \\
&\qquad\qquad \left(\left(\begin{bmatrix}U_{0,p,N}\\U_{p,1,1}\\Y_{0,p,N}\end{bmatrix}\begin{bmatrix}U_{0,p,N}\\U_{p,1,1}\\Y_{0,p,N}\end{bmatrix}^T\right)^{-1}\begin{bmatrix}U_{0,p,N}\\U_{p,1,1}\\Y_{0,p,N}\end{bmatrix}\otimes I\right) \\
&= \left(\begin{bmatrix}U_{0,p,N}\\U_{p,1,1}\\Y_{0,p,N}\end{bmatrix}\begin{bmatrix}U_{0,p,N}\\U_{p,1,1}\\Y_{0,p,N}\end{bmatrix}^T\right)^{-1}\otimes\Sigma_e,
\end{aligned}
\tag{A-19}
$$

Proof of Eq. A-15

From Eq. A-6 it can be seen that:

$$
\begin{bmatrix}U_{0,p,N}\\U_{p,1,1}\\Y_{0,p,N}\end{bmatrix} = L_{11}Q_1. \tag{A-20}
$$

By substitution of Eq. A-20 and using the property $Q_1Q_1^T = I$ if follows that:

$$
\left(\begin{bmatrix}U_{0,p,N}\\U_{p,1,1}\\Y_{0,p,N}\end{bmatrix}\begin{bmatrix}U_{0,p,N}\\U_{p,1,1}\\Y_{0,p,N}\end{bmatrix}^T\right)^{-1} = \left(L_{11}L_{11}^T\right)^{-1} = (L_{11}^{-1})^T L_{11}^{-1}. \tag{A-21}
$$

Then, Eq. A-15 follows from substituting Eq. A-21 in Eq. A-14.

Appendix B

Matrix inversion uncertainty

In Section 3-3 the model uncertainty is propagated through the RHI estimator. For this the uncertainty of the left pseudo inverse of $\mathcal{T}_p$, denoted as $\mathcal{T}_p^\dagger$, must be determined. In Section 3-3 this is done by computing an analytic expression of this pseudo inverse which is then used to compute its uncertainty.

Initially a different approach was taken based on the equation:

$$\mathcal{T}_p^\dagger = \left(\mathcal{T}_p^T \mathcal{T}_p\right)^{-1} \mathcal{T}_p^T.$$

It was attempted to compute uncertainty on the inverse: $(\mathcal{T}_p^T \mathcal{T}_p)^{-1}$. This was achieved using a result found in literature. However, the results turned out to be very unsuitable for this application. It is still presented in this appendix because it can be very useful for other problems. As will become clear, this attempt only succeed in computing an upper bound on the norm $||\mathcal{T}_p^\dagger||_2$.

B-1 The uncertainty of a pseudo inverse of a uncertain matrix

Computing $\delta(\mathcal{T}_p^T \mathcal{T}_p)$.

The analysis is started with computing $\delta(\mathcal{T}_p^T \mathcal{T}_p)$. For this Lemma 1 on page 34 can be used.

Norm inequalities

Before moving on a lemma about matrix-vector norm inequalities is provided. This lemma will be useful later in the next part of this appendix.

Lemma 4. *Matrix 2-norm inequalities.*
For matrices $A \in \mathbb{R}^{m\times n}$, $B \in \mathbb{R}^{m\times n}$, $C \in \mathbb{R}^{n\times o}$ and $x \in \mathbb{R}^n$ it holds that:

$$\|A + B\|_2 \leq \|A\|_2 + \|B\|_2 \,,$$

$$\|AC\|_2 \leq \|A\|_2 \|C\|_2 \,,$$

and

$$\|Ax\|_2 \leq \|A\|_2 \|x\|_2 \,.$$

Proof. The proofs can be found in [44]. □

Computing $\delta((\mathcal{T}_p^T \mathcal{T}_p)^{-1})$

The next step is to compute $\delta((\mathcal{T}_p^T \mathcal{T}_p)^{-1})$. We are dealing with an inversion uncertainty. A very important detail one should be aware of is that the magnitude of the perturbation $\delta(\mathcal{T}_p^T \mathcal{T}_p)$ must be bounded such that perturbation cannot be such that $\mathcal{T}_p^T \mathcal{T}_p + \delta(\mathcal{T}_p^T \mathcal{T}_p)$ becomes singular. If $\mathcal{T}_p^T \mathcal{T}_p + \delta(\mathcal{T}_p^T \mathcal{T}_p)$ can become singular, then the inversion uncertainty will be ∞. This can be avoided when the structure of the perturbation is taken into account. This structure is taken into account by the method presented in Section 3-3 , but is not taken into account by the method presented in this appendix.

A solution to this perturbed inversion problem is present in literature when the perturbation is considered to be unstructured. The solution provides an upper bound on the norm $||\delta((\mathcal{T}_p^T\mathcal{T}_p)^{-1})||_2$. This work is presented in [45]. The for our study relevant result from [45] is presented in Lemma 5.

Lemma 5. *Propagation of uncertainty through a matrix inversion as presented in* [45].

Let M be a matrix and $\delta(M)$ an additive uncertainty. Note that $\|M\|_2$ equals to the maximum singular value of M denoted as $\sigma_{\max}(M)$ and $\left\|(M)^{-1}\right\|_2^{-1}$ equals to the minimum singular value of M denoted as $\sigma_{\min}(M)$. Then if the condition:

$$\sigma_{\max}(\delta(M)) < \sigma_{\min}(M), \tag{B-1}$$

is satisfied, $||\delta\left(M^{-1}\right)||_2$ can be computed as:

$$\left\|\delta\left(M^{-1}\right)\right\|_2 \leq \frac{\sigma_{\max}(\delta(M))}{\sigma_{\min}(M)\left(\sigma_{\min}(M) - \sigma_{\max}(\delta(M))\right)}.$$

Proof. The proof can be found in [45]. In [45] an upper bound on $||\delta(M^{-1})||_2$ relative to the size of the perturbation $\sigma_{\max}(\delta(M))$ is derived. That is:

$$\frac{\left\|\delta\left(M^{-1}\right)\right\|_2}{\sigma_{\max}(\delta(M))} \leq \frac{1}{\sigma_{\min}(M)\left(\sigma_{\min}(M) - \sigma_{\max}(\delta(M))\right)}.$$

By multiplying this result with the size of the actual perturbation $\sigma_{\max}(\delta(M))_2$ the result in the lemma is obtained. This concludes the proof. □

By applying Lemma 5 the upper bound on $||\delta((\mathcal{T}_p^T\mathcal{T}_p)^{-1})||_2$ can be computed as:

$$\left\|\delta\left((\mathcal{T}_p^T\mathcal{T}_p)^{-1}\right)\right\|_2 \leq \frac{\sigma_{\max}\left(\delta(\mathcal{T}_p^T\mathcal{T}_p)\right)}{\sigma_{\min}\left(\mathcal{T}_p^T\mathcal{T}_p\right)\left(\sigma_{\min}\left(\mathcal{T}_p^T\mathcal{T}_p\right) - \sigma_{\max}\left(\delta(\mathcal{T}_p^T\mathcal{T}_p)\right)\right)}.$$

This results is only valid as long as the assumption:

$$\sigma_{\max}\left(\delta(\mathcal{T}_p^T\mathcal{T}_p)\right) < \sigma_{\min}(\mathcal{T}_p^T\mathcal{T}_p) \tag{B-2}$$

is met.

This assumption can be translated to an upper bound on $||\delta(\mathcal{T}_p)||_2$. By application of Lemma 1 on page 34 and on the preceding page the following inequality can be constructed:

$$\left\|\delta(\mathcal{T}_p^T\mathcal{T}_p)\right\|_2 \leq 2\left\|\mathcal{T}_p\right\|_2\left\|\delta(\mathcal{T}_p)\right\|_2 + \left\|\delta(\mathcal{T}_p)\right\|_2^2.$$

Then using this result the assumption in Eq. B-2 can be denoted as:

$$\left\|\delta(\mathcal{T}_p^T\mathcal{T}_p)\right\|_2 \leq 2\left\|\mathcal{T}_p\right\|_2\left\|\delta(\mathcal{T}_p)\right\|_2 + \left\|\delta(\mathcal{T}_p)\right\|_2^2 < \sigma_{\min}(\mathcal{T}_p^T\mathcal{T}_p).$$

By solving this quadratic equation for $||\delta(\mathcal{T}_p)||_2$ and discarding the negative root one obtains the requirement:

$$0 \leq \left\|\delta(\mathcal{T}_p)\right\|_2 < \sqrt{\left\|\mathcal{T}_p\right\|_2^2 + \sigma_{\min}(\mathcal{T}_p^T\mathcal{T}_p)} - \left\|\mathcal{T}_p\right\|_2. \tag{B-3}$$

Now an upper bound on $||\delta(\mathcal{T}_p)||_2$ is available such that an upper bound on $||\delta((\mathcal{T}_p^T\mathcal{T}_p)^{-1})||_2$ can be computed. This result can be used to obtain an upper bound on $||\delta(\mathcal{T}_p^\dagger)||_2$ by application of Lemma 1 on page 34 and Lemma 4 one obtains:

$$\left\|\delta\left(\mathcal{T}_p^\dagger\right)\right\|_2 \leq \left\|\delta\left((\mathcal{T}_p^T\mathcal{T}_p)^{-1}\right)\right\|_2\left\|\mathcal{T}_p\right\|_2 + \left\|\left|(\mathcal{T}_p^T\mathcal{T}_p)^{-1}\right|\delta(\mathcal{T}_p)\right\|_2 + \left\|\delta\left((\mathcal{T}_p^T\mathcal{T}_p)^{-1}\right)\right\|_2\left\|\delta(\mathcal{T}_p)\right\|_2.$$

Which is the result that is aimed for.

B-2 Discussion of result

In the previous section a methodology is presented that provides an upper bound on $||\mathcal{T}_p^\dagger||_2$. However, this result is based on an assumption and as will be discussed in the section, this assumption is limiting the suitability for our application enormously.

This assumption is given in Eq. B-2 which for ease is repeated:

$$\sigma_{\max}\left(\delta(\mathcal{T}_p^T\mathcal{T}_p)\right) < \sigma_{\min}(\mathcal{T}_p^T\mathcal{T}_p). \tag{B-4}$$

This assumption has been translated into Eq. B-3 which is also repeated:

$$0 \leq \|\delta(\mathcal{T}_p)\|_2 < \sqrt{\|\mathcal{T}_p\|_2^2 + \sigma_{\min}(\mathcal{T}_p^T\mathcal{T}_p)} - \|\mathcal{T}_p\|_2\,. \tag{B-5}$$

Structure of the Markov parameters and $\mathcal{T}_p$

Remember from e.g. Eq. 3-3 that $\mathcal{T}_p$ is build from Markov parameters. These Markov parameters defined as $C\Phi^j\widetilde{B}$ where $j \in \mathbb{N}^0$, show a certain structure. They typically non-zero for low j and decrease for increasing j since for any systems with a stable Φ it holds that $\lim_{j\to\infty}||C\Phi^j\widetilde{B}||_F = 0$. Note that the past window p must be selected such that $\|C\Phi^p x(0)\|_F \approx 0$, which ensures that also the very small Markov parameters are included in $\mathcal{T}_p$. In order to illustrate the typical structure of the Markov parameters, Figure B-1 has been created. In this figure it can also be seen that for a perturbed model, the error (i.e.

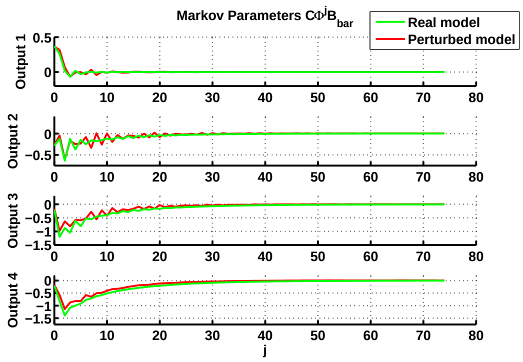

Figure B-1: *Markov parameters of a system with a one input and four outputs. Two sets of Markov parameters are shown, one set belonging the the supposed real model and one set to a perturbed version of this model.*

uncertainty) on the Markov parameters are in the same order of magnitude as the Markov parameters themselves for small j. These errors decrease (together with the Markov parameters themselves) for increasing j.

The product $\mathcal{T}_p^T\mathcal{T}_p$ can be structured as:

$$\mathcal{T}_p^T\mathcal{T}_p = \begin{bmatrix} A_1 \\ A_2 \end{bmatrix},$$

where A_1 contains relative big numbers because of the Markov parameters with low j and A_2 contains relatively small numbers corresponding to Markov parameters with high j. Because of this, $\sigma_{\min}(\mathcal{T}_p^T\mathcal{T}_p)$ will be a small value compared to $||\mathcal{T}_p||_2 = \sigma_{\max}(\mathcal{T}_p)$. The singular value$\sigma_{\max}(\mathcal{T}_p)$ is larger because of the larger Markov parameters corresponding to low values of j.

Effect of the structure on the assumption

By analysis of the structure of the Markov parameters it has been concluded that:

$$\sigma_{\min}(\mathcal{T}_p^T\mathcal{T}_p) \ll ||\mathcal{T}_p||_2,$$

then Eq. B-5 can be approximated as:

$$\begin{aligned}0 \leq \|\delta(\mathcal{T}_p)\|_2 &< \sqrt{\|\mathcal{T}_p\|_2^2 + 0} - \|\mathcal{T}_p\|_2 \\ &< 0,\end{aligned}$$

Which has no unfeasible solution resulting in $||\mathcal{T}_p^\dagger||_2 = \infty$. In practice $\sigma_{\min}(\mathcal{T}_p^T\mathcal{T}_p) \neq 0$ but is a very small number, this leaves room for a very small perturbation on $\mathcal{T}_p$ such that $||\mathcal{T}_p^\dagger||_2 < \infty$.

Conclusion

The presented theory in this appendix is only valid for small perturbation on $\mathcal{T}_p$. This is because of the assumed unstructured nature of the perturbation $\delta(\mathcal{T}_p)$. When this perturbation is too large it the uncertainty on $(\mathcal{T}_p^T\mathcal{T}_p)^{-1}$ becomes ∞ because $(\mathcal{T}_p^T\mathcal{T}_p)$ can be singular. It is shown that for the particular structure of $\mathcal{T}_p$ and the Markov parameters, only very small perturbations $\delta(\mathcal{T}_p)$ are allowed.

In such a scenario where the model errors are only small it is less interesting to study propagation of modeling errors. Therefore, this contribution is somewhat small and put in the appendix. In Section 3-3, a more general way is proposed that takes the structure of $\mathcal{T}_p$ and $\delta(\mathcal{T}_p)$ into account allowing $\delta(\mathcal{T}_p)$ to be much larger.

Appendix C

Sensor selection and performance

In Subsection 5-4-5 the sensor requirements are derived. The actual sensor selection is more involved and is presented in this appendix. It is omitted from the main matter because of it is not a fundamental problem that needs attention but rather a practical part of the work.

The sensors should be selected such that their performance is sufficient and cost effective. In addition, it is required that the sensors are suitable for future use when the setup has fulfilled its purpose and is taken apart. Because of this, sensors that are commonly used in the lab are considered. This has as advantage that there is experience within the PME department with these sensors. Therefore, an extensive literature survey is omitted.

First the sensor technology is selected, then typical features of this technology are discussed. A short overview of commercial products is provided. After a sensor has been selected, its performance is validated. Finally, the digital output interface is compared with the analog output interface.

C-1 Sensor technology

In this section the sensor technology is selected. The sensors are required to measure the deformations of the chuck in the experimental setup designed in Chapter 5. The selection is mainly confined to technology where the PME department has experience with. One of the reasons is that the sensors should be useful for future setups. Another reason is that the probability to encounter (expensive) unforeseen problems is lower.

C-1-1 Sensor technologies

The following technologies have been considered:

- capacitive sensors;
- eddy-current sensors;
- interferometers;
- encoders.

All of the above technologies can be implemented in a contactless manner. This is an requirement because it ensures that no additional friction or hysteresis forces are introduced.

An additional requirements is that the sensors should have a high resolution relative to their range. This ratio must be at least 10^5 as was computed in 5-4-5. Encoders and interferometers can have a very high resolution and range. Capacitive sensors have a more limited range but can also provide sufficient resolution in this range. Eddy current sensors usually have an slightly worse resolution to range ratio. A quick search for available eddy current sensors revealed that they could barely do the job according the the presented requirements in Subsection 5-4-5. Capacitive sensors can do the job according the the specification just like interferometers and encoders.

Interferometers are very expensive and quite large. Encoders are unpractical since the grid has to be physically connected to the chuck also called target. If they need to be moved, this may leads to unnecessary complications.

Therefore, capacitive sensors are selected as the best choice. It is a suitable solution that is flexible and cost effective.

C-1-2 Characteristics of capacitive sensors

Next typical characteristics of capacitive sensor systems are discussed. The information in this subsection is a summary of [46]. First, a few definitions are introduced. The actual sensor interacting with the setup is called the *sensor probe*. The object of which the position is measured is referred to as the *target*. The amplifier is traducing the probe's capacitance to signals representing a distance of the probe to the target.

A requirement is that the target must be conductive. Normally, a target is grounded and the sensors work by measuring the AC-current flow from the probe to the target. Since the currents are very small and of AC nature, the transported charge is very small. Therefore, very thin targets of 0.1 mm pose no problem at all. For our purpose this is not a limitation since the designed chuck is 3mm thick.

In our case, multiple sensors are measuring on the same target at different locations. If multiple probes are used, one can imagine that the current from one probe does not necessary flow to ground but may very well flow via another probe, which does effect the measurement. This problem can be avoided by synchronizing the excitation of the AC-signals in a proper way. The exact method depends on the manufacturer. They all do the job but in some cases the target does not have to be grounded which can be an advantage in some cases. This is a special feature and is not offered by all available systems. The system selected by us has this feature. However, using it may increase the sensor noise level, i.e. decrease the resolution and therefore we do not use this feature.

Another typical characteristic is that the probe's diameter increases when a larger range is required. When the distance between probe and target is increased, the capacitance decreases. Then, when the probe diameter is increased, so does the capacitance which then remains of measurable magnitude. A large probe means that probes can be placed less close to each other and a position measurement results in an average position of the target area. If the target has a rough surface this may actually be an advantage.

In addition these systems are sensitive for tilt. Small angles, up to 0.2 degrees, pose no problem for ranges in the order of 1 mm. When larger tilt angles are expected, the specifications should be studied carefully. In our case, such large tilt angles are not expected.

Capacitive sensors are sensitive to contamination of the space between the probe and the target. In our case the environment is clean which means that this limitation poses no problem.

The target may laterally move with respect to the sensor probe. We do not expect significant lateral movement but it grands additional design freedom.

Lastly, mounting hardware behind the probe does not influence the measurement and may be of any material which grands again additional design freedom.

C-1-3 Market survey

Capacitive sensing has been chosen as measurement technology and their general characteristics are known. In order to buy a suitable sensor system, a market survey is performed. Some manufactures specify the noise level of their sensors in terms of Root Mean Square (RMS) error while others use Peak-to-Peak (P-P) values. For comparing their specification it is assumed as rule of thumb that 8 times the RMS noise levels results in the P-P noise level. The result of the market survey is shown in Table C-1.

It is shown that some systems offer a dual range feature. This means the range of the measurement system can be changed by flipping a switch on the amplifier. Off course the noise specification also changes. This can be very handy while trouble shooting however, it is not essential for our purpose so not much weight is put on this feature.

Furthermore, it is shown is that some systems offer a digital interface. Connecting 9 analog output to external ADCs will result in a large amount of wires. Those signals should also pass through an anti-aliasing filter. This will result in extensive wiring and reconfiguring can take a lot of time. In the case of the Micro-Epsilon systems the ADCs are build in and only one or two Ethernet cables are required per unit which is a much cleaner solution. In addition, sensors with range over resolution ratios of over $2^{16} \approx 6.5 \cdot 10^4$ require high precision ADCs. 16-bit ADCs are not sufficient to perform the analog to digital conversion such that the required resolution and range are achieved at the same time. Such ADCs that are suitable for the job are specialized and expensive. Think of an additional €2,000 for 8 differential

Table C-1: *This table shows the result of the market survey for commercially available capacitive measurement systems. The aimed range is 1.0mm with a range over noise ratio of at least* $2 \cdot 10^5$. *The systems with specifications close to these values are shown in this table. As rule of thumb, it is assumed that 8 times the RMS noise levels results in the P-P noise level.*

Model	*Probe size*	*Range*	*Noise level at 1 kHz*	*Range/noise ratio*	*Price for 8 modules*	*Dual range*	*Synchronization method*	*Digital interfaces*
MicroSense								
4810	⌀10 mm	1.0 mm	23 nm (RMS)	$4.4{\cdot}10^4$	€ 22,410	No	Not inquired	No
5810	⌀10 mm	1.0 mm	6 nm (RMS)	$1.8{\cdot}10^5$	€ 35,920	No	Not inquired	No
8810	⌀10 mm	1.0 mm	5 nm (RMS)	$2.0{\cdot}10^5$	€ 26,010	No	Not inquired	No
Lion-Precision								
CPL190	⌀9.5 mm	2.0 mm	10 nm (RMS)	$2.0{\cdot}10^5$	€ 31,930	No	Cable	No
CPL290	⌀9.5 mm	0.5 mm 2.0 mm	3 nm (RMS) 10 nm (RMS)	$1.7{\cdot}10^5$ $2.0{\cdot}10^5$	€ 39,710	Yes	Cable	No
Micro-Epsilon								
CapaNCDT6200 + DL6220	⌀10 mm	1.0 mm	75 nm (P-P)	$1.0{\cdot}10^5$	€ 21,100	No	Cable	Ethernet (TCP/IP), EtherCAT
CapaNCDT6200 + DL6230	⌀10 mm	1.0 mm	12 nm (P-P)	$6.7{\cdot}10^5$	€ 23,270	No	Cable	Ethernet (TCP/IP), EtherCAT
Physik Instrumente								
E-852 + D-510.101	⌀20 mm	0.5 mm	<10 nm (RMS)	$>5.0{\cdot}10^4$	€ 21,040	Yes	Cable	No
E-509.E3 + D-510.101	⌀20 mm	0.5 mm	<13 nm (RMS)	$>4.0{\cdot}10^4$	€ 23,877	Yes	Cable	No

inputs. A digital interface is not a requirement would represent a very nice feature. Not much weight is put on this feature.

Finally, it can be seen that price to performance ratio for the Micro-Epsilon systems is very high. Performance and cost are the most important criteria and therefore this system is selected.

This section should be concluded with some final remarks. The inquired price for the Micro-Epsilon system is incomplete. It turned out that the actual price was close to € 30,000 instead of the state €23,000 because in the initial inquiry all accessories such as cables where not included. In addition it was discovered, after the sensors where ordered, that the Micro-Epsilon system performs at best as specified. The best performance is achieved at the minimum measurement distance. The Lion-Precision systems perform structurally better as specified. If this has been known on beforehand it might have influenced the choice. Still the performance of the Micro-Epsilon system is sufficient and is interfaced with the controller in a very clean way via EtherCAT. In addition, valuable time is saved that would have been required for selecting a high performance ADC that is compatible with the selected controller.

C-2 Sensor noise vs target distance

At a certain point during the process the preliminary decision was made to buy a Micro-Epsilon system. Before placing the order for 9 sensors, a test system was requested in order to experimentally validate their performance. Such experiments would expose miscommunications with the manufacturer before the actual purchase is made. The test system is used to validate the performance. First the experiment is presented, then the results of the tests are presented.

An impression of the setup can be seen in Figure C-1. The capacitive sensor probe is clamped on the right. The target is the big metal block, with a grounding wire connected to it. The target is mounted on a linear stage that can be moved with the micrometer on the left. This setup allows to accurately change the distance between target and probe.

For the measurements the digital interface is used. The main reason is that the available ADC system, a National Instruments (NI) USB-6221 or NI PCI-6220 both have a maximum resolution of 16-bit, and do therefore not have sufficient resolution to measure the sensor's noise level. By making use of the sensor's digital interface, this problem is solved.

We are interested in the Micro-Epsilon system with the DL6230 amplifier. However only a test system with a DL6220 amplifier could be provided. The functionality is the same but the DL6220 has an approximately 6 times higher noise level.

The noise level of this system is measured at different positions, the results can be seen in Figure C-2a. As can be seen, the promised noise level of 75 nm P-P can be reached but only near 0 mm target distance. The actual measurement at 0 distance has a much higher noise level since the probe was touching the target. The noise level increases linearly for increasing measurement distance. In addition, it can be seen that the rule of thumb, which assumes that 8 times the RMS noise level equals the P-P noise level is a very accurate approximation.

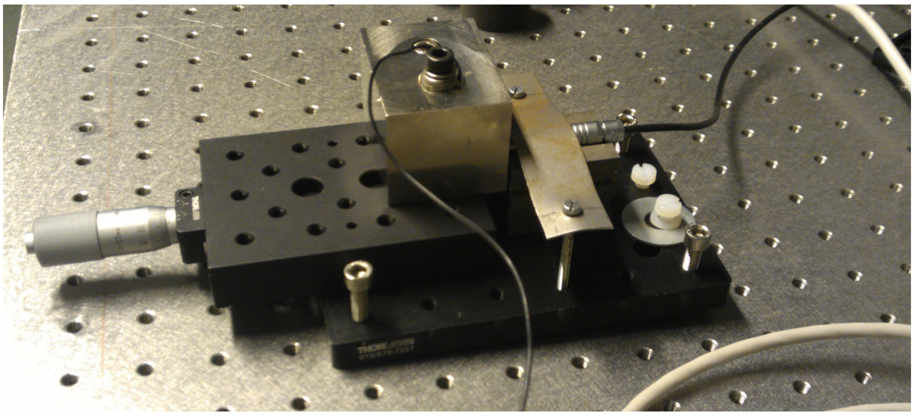

Figure C-1: *The experimental setup used to validate the sensor system's noise specification as provided by the manufacturer. The probe is clamped and the setup is places on a vibration isolation table in an optics lab. The target is mounted on a stage that can be moved by rotating the micrometer-head. This construction allows us to determine the sensor noise level as function of target distance.*

The capacitance is largest when the probe is close to the target. In combination with an approximate constant electronic noise level, the signal to noise ratio is highest near the target.

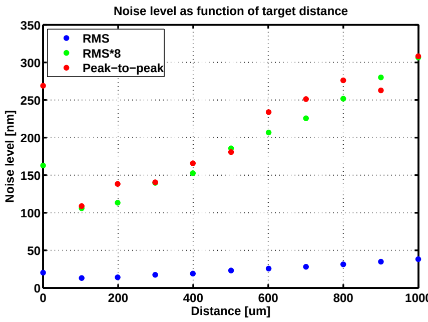

(a) This figure shows the noise level as a function of measurement distance. The results correspond to a Micro-Epsilon system with the DL6220 amplifier. The first measurement, clearly out of the trend can be explained by the fact that the probe was touching the target. This configuration is specified by Micro-Epsilon to have a noise level of 75 nm P-P.

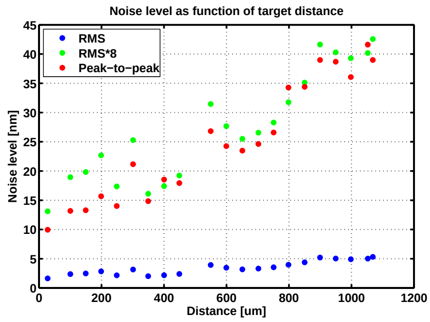

(b) This figure shows the noise level as a function of measurement distance. The results correspond to a Micro-Epsilon system with the DL6230 amplifier. This configuration is specified by Micro-Epsilon to have a noise level of 12 nm P-P.

Figure C-2: *These figures shows the noise level as a function of target distance of two Micro-Epsilon capacitive measurement systems. The minimum range is when the probe is just not touching the target. The maximum range 1 mm.*

After these measurements where performed, the Micro-Epsilon systems are ordered. When they arrived months later, the experiment was repeated with the actual DL6230 amplifier. The result shown in Figure C-2b, are similar to the results shown in Figure C-2a. The noise increases linearly with distance. Again 8 times the RMS noise level results in a well approximation of the P-P level. The resulting linear trend seems less smooth as it was for the first experiment. This is likely related to the fact that the first experiment was performed in the optic lab on the vibration isolation table, while the second experiment was performed without vibration isolation. Furthermore, this sensor is about a factor 10 more accurate and therefore are smaller noise sources more significant. Again, the best case noise level matches the specification of 12 nm P-P.

Finally, this section is concluded with a remark. The measurements have been performed using the digital interface. All filters (that could be disabled) are disabled. Still an anti aliasing filter should be present before the analog to digital conversion is performed. No specifications about this filter are provided. In the next section it is investigated if such a filter is present and if so, where its cut-off frequency has been placed.

C-3 Digital vs analog interface

The Micro-Epsilon system has a digital interface. This interface provides a clean and easy way to interface the sensor with the controller. It is expected that the output of the digital interface is filtered with an anti-aliasing filter. However no specifications about this feature are available. In addition the digital interfaces usually introduce some form of time delay due to the required processing time. In this section the digital interface is investigated. Its characteristics are determined which are used to decide if the interface can be used for our purpose. Experiments have been performed in order to obtain this information.

The advantage of Ethernet is that only two off the shelf cables are required to connect the sensors to the controller. The wiring of the analog outputs is much more comprehensive. In addition, the analog outputs have to pass through an anti-aliasing filter.

First, a small introduction to EtherCAT is provided then the experimental setup is described and finally the results are presented and discussed.

C-3-1 Difference between EtherCAT and Ethernet

The digital interface that we plan to use is the communication protocol named *EtherCAT*. It is also referred to as real time Ethernet. Ethernet, very popular for networking computers together, has some limitation concerning real-time communication. The EtherCAT protocol has been designed to overcome these limitations.

EtherCAT uses the same transmission medium as Ethernet. This means cables, connectors and hardware are identical. Ethernet and EtherCAT are identical from electrotechnical point of view. From software point of view there are important differences which relate to how a transmission (i.e. frame) over this medium is defined, handled and should be interpreted by the receiver. Everything from electrical to software point of view have been described in the standards of Ethernet and EtherCAT. Detailed technical information about the EtherCAT standard can be found in [47].

Ethernet has been designed to send large amounts of data once in a while. Each frame contains a lot of overhead which is no problem if the frame also contains a lot of data. In real-time systems, very often a small amount of data have to be send very often. Think of a sensor value that has to be transmitted every 250 μs. Because of the large overhead per transmitted frame required for normal Ethernet the transmission line will saturate quickly.

Although Ethernet is not limited to this, it is usually implemented in a star-configuration, where each device is connected to the network via a switch or router. EtherCAT however is usually implemented in a chain configuration. One device is configured as the master and is performing predefined tasks. A controller can be the master for instance. The other devices are denoted as slaves. A task can be to collect all sensor data every 250 μs. Then every 250 μs the master will send a request frame to the first slave in the chain which will resend the transmission to the next slave but with its sensor data included. This process repeats for every slave and finally the transmission is send back to the master which then interprets the data. Instead of each slave sending many frames per sensor each with their own overhead to the master, only one transmission is used which is augmented with additional information at each slave. It is possible to have multiple task on different sampling times. It is even possible to define non-time critical tasks which get a lower priority compared to the time critical tasks.

The EtherCAT network can be configured using Beckhoff EtherCAT Configurator. This is software package is freely available as an evaluation version. It can be used indefinitely but only by one user. Tasks can also be defined using this software. A complete guide on how to configure an EtherCAT network can be found in [48]. The output can be used to configure a Matlab xPC Target to obtain sensor data via EtherCAT via a normal supported Ethernet card.

C-3-2 The experiment

Some background on EtherCAT has been provided, and it is known how to interface the sensors to a Matlab xPC Target system using EtherCAT. Therefore, experiments can be performed to compare the digital with the analog output. Likely an anti-aliasing filter is used before the internal analog to digital conversion. However, this filter is not documented and it should be investigated before using the digital interface. From the results it can be concluded if the performance of the digital interface is sufficient for our application. The measurements are done together with Johan Vogel who performed much of the data processing.

The previous subsection describes how Matlab xPC Target can be interfaced with an EtherCAT system. The analog output is sampled using a NI PCI-6220 16-bit. This card cannot achieve the theoretical resolution of the sensor but this experiment is not comparing the noise levels but is comparing the frequency response. The analog output is not filtered to use it as a raw reference. This also introduces some additional noise which again is not relevant for this experiment.

Unfortunately, no photo of the setup is available. The setup consists of a shaker for which the frequency and amplitude can be manually set. A grounded body is moving laterally along the sensor probe. This way, depending on the momentary position of the body on the shaker, a quarter to about three quarters of the probe's surface has been covered. The amplitude of the shaker depends on frequency and has to be corrected manually. A lateral movement is selected as opposed to a distance measurement since in this way it is impossible for the shaker to crash against the sensor probe and damage it. For a sinusoidal input signal to the shaker, the output of the sensor is, by visual inspection on an oscilloscope also a sinusoid. Therefore, it is concluded that this capacitance variation is sufficiently linear for our purpose.

The output of the sensor is measured at both the digital and analog output using the real-time system. These measurements are done at many different excitation frequencies. These experiments are repeated at two different sample frequencies. The results are shown in Figure C-3.

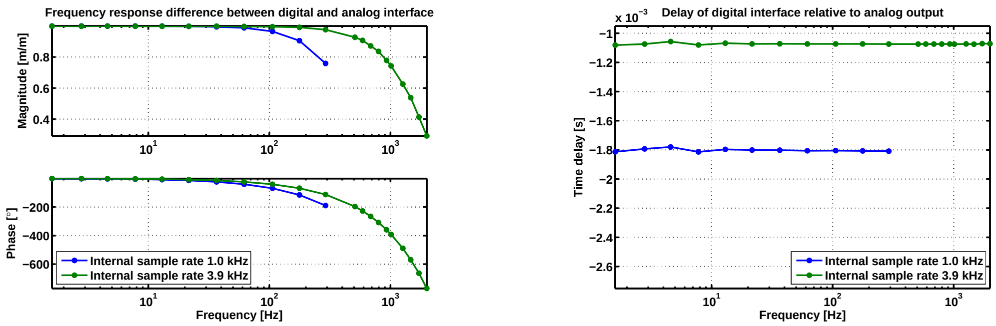

(a) The magnitude and phase of the digital output signal relative to the analog output signal for two sample frequencies.

(b) An interpretation of the phase difference, shown in Figure C-3a, as time delay. It can be seen the delay is independent of frequency.

Figure C-3: *These figures show the results used to compare the performance of the digital interface with relative to the analog output.*

It is concluded that the digital output has been filtered. Above a certain frequency, the magnitude of the digital output decreases with respect to the analog output. Also, a clear phase lag is visible. For a sampling frequency of 1 kHz already a phase lag of 65 degrees can be observed at a frequency of 100 Hz. When the sampling frequency is increased to 3.9 kHz this phase lag is reduced to 40 degrees.

In Figure C-3b the phase lag is interpreted as time-delay and as is shown, this time delay is nearly constant. The values have been checked with the manufacturer who confirmed these constant time delays corresponding to the sampling frequencies.

From these results it can be concluded that the digital output can be used. As described in Subsection 5-4-1 the controller bandwidth will end up between 10 and 20 Hz. Up to these frequencies no significant phase lag is visible and the magnitude is measured correctly for both sampling frequencies. If attempts are made to increase the bandwidth further for further development, the phase lag should be taken into account.

Appendix D

Creating in-plane fixation using repelling magnets

As stated in Subsection 5-4-6, the in-plane fixation is required to keep the chuck in its place in the *xy*-plane. The out-of plane DoFs are positioned by the levitation controller. In Subsection 5-4-6, the chosen concept is presented. In this section, another concept is presented that has been studied in detail.

The in-plane fixation has a few demands: it should provide a sufficiently *high in-plane stiffness*; it should provide *no stiffness for out-of plane directions* and it should introduce *no friction or hysteresis*. In Subsection 5-4-6, it is presented that the in-plane stiffness should at least be 1 N/mm.

The concept to implement the in-plane fixation using repelling magnets seemed to be a promising option because it would provide means to implement the in-plane fixation in a contactless manner. This means no friction and only the very limited hysteresis of the magnetization of the magnets. The idea of using a magnetic bearing system to create high stiffness in designed directions is widely used. A survey of magnetic bearing systems can be found in [49].

Earnshaw's theorem, presented in [50], states that nothing can be stably levitated using passive magnets. In this case, the levitation controller is controlling the 3 out-of-plane DoFs which can stabilize a magnetic levitated body. Since at first sight there are no fundamental restrictions, this concept is investigated further.

First, the model that is created for the analysis is introduced. Then, the results are presented and discussed and finally, the conclusions are summarized.

D-1 Model

In this part a model, describing the force between two rectangular magnets, is presented. It is created to study the feasibility of the in-plane fixation concept using repelling magnets. If so the model can also be used to size the magnets and determine their optimal orientation.

D-1-1 The magnetic flux density of a single magnet

The model, describing the force between two rectangular magnets, is a full 3D model implemented in Matlab. A magnet is placed in the origin of a space fixed Cartesian coordinate system spanned by the unit vectors $\check{x}$, $\check{y}$ and $\check{z}$. The magnetic field around the magnet is computed using analytical expressions. The analytical expressions and their derivation can be found in [51]. The most important assumptions are that the magnet must be rectangular and that the magnetic permittivity μ_m of the volume around the magnet is constant i.e. there is no iron in the neighborhood. Both assumptions are not violated in our application.

The magnet's rotations are defined using 3D Cardan angles which describe respectively a rotation around the body fixed axis: z, y and x. Cardan angles are chosen because simple rotations around just one axis can be done easily.

The model of this magnet is validated by comparing the results with a finite element model created in COMSOL Multiphysics. In Figure D-1 a comparison of the magnetic field strength can be found. It can

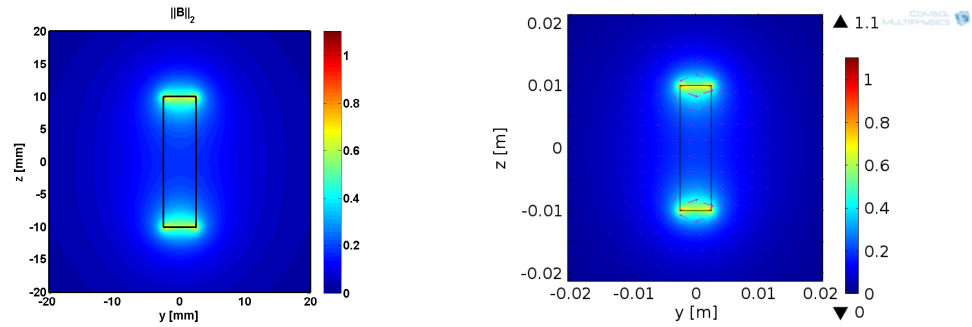

(a) Matlab model **(b)** COMSOL Multiphysics

Figure D-1: *This figure shows a comparison between a result obtained using the created model in Matlab and from a finite element analysis performed using COMSOL Multiphysics. Both models obtain their results using totally different methods. It can be seen, the results are very similar, which gives confidence that both models are valid.*

be seen both models provide very similar results but are implemented in very different ways. Therefore, it is assumed that the used analytical expressions are valid and implemented correctly.

To summarize, we have now obtained a way to compute the magnetic flux density vector B as function of the space fixed coordinates x, y and z denoted as the operator $B(x, y, z)$.

D-1-2 Forces between two magnets

Next, it is explained how forces between magnets are computed. The relative orientation between the two magnets determines the force and torque acting on both magnets. The derivatives of the forces with respect to the position of the second magnet must fulfill some requirements in order to create a suspension. The second magnet will be mounted to the chuck in order to suspend the chuck.

A second magnet is defined in the space fixed coordinates. This magnet can also be sized and rotated, which is again defined using Cardan angles.

Forces can be computed by computing the gradient of energy with respect to the position. The energy E of a magnetic field is given by:

$$E = \frac{1}{2\mu_m} \int_V \|B(x, y, z)\|_2^2 \, dV,$$

where the integral over the volume V is an integral over all of space. The derivation of this equation can be found in [52] which is an excellent recourse when studying electrodynamics. Then, the force can be computed as:

$$F = \frac{1}{2\mu_m} \nabla \left(\int_V \|B(x, y, z)\|_2^2 \, dV \right),$$

where the operator $\nabla(\cdot)$ is defined as:

$$\nabla(a) = \frac{\partial a}{\partial x}\check{x} + \frac{\partial a}{\partial y}\check{y} + \frac{\partial a}{\partial z}\check{z}.$$

In words, the operator $\nabla(\cdot)$ computes the gradient of its operant in each direction of the coordinate system.

It should be noted it is very difficult to evaluating this equation in general. When it is assumed that the magnetic flux density can be considered zero at a certain distance away from the magnet, it becomes possible to evaluate these equations numerically. This approach is easy but at the same time computationally very expensive since the $B(x, y, z)$ needs to be evaluated at many points in the volume.

Therefore, another approach is purposed which only requires evaluation of $B(x, y, z)$ at some points at the surface of the second magnets. In order to do this the second magnet is modeled as a rectangular magnet with a current loop distributed over its surface A. The force between the magnets is computed using:

$$F = \int_A (J \times B) dA.$$

This formula actually computes the Lorenz forces acting on the current-loop. It is also derived in [52]. In this equation F is a force vector, J the current density vector, dA is an infinitesimal piece of surface area of the second magnet and finally $\times$ denotes the cross product between the two vectors. Although it is very difficult to solve this equations exactly for the general case, numerically this is not very difficult.

The outside surface of the second magnet is meshed and in the center of each element the magnetic flux density is computed which is assumed to be constant over the element. The current density can be determined by:

$$J = \frac{I}{l_\perp}.$$

Here I is a vector describing the total current flowing over the surface of the magnet. Furthermore, $l_\perp$ is the length of the side of the magnet which is perpendicular to the current loop. Using the rotation matrices constructed from the Cardan angles, the vectors expressed in the magnet fixed coordinate systems are easily transformed to the space fixed coordinates. Torques around the center of the second magnet can be computed by taking the lever-arm of each element into account.

The obtained force is again validated using a COMSOL model which match closely within $\pm 4\%$.

D-2 Results

Now that an advanced model is available, it is time to investigate the interaction between two magnets and to see if suitable configurations can be obtained. The required stiffness for in-plane directions should be about 1 N/mm as is explained in Subsection 5-4-6.

In Figure D-2 a typical result is shown. Both are block magnets that have a current density of $J = 927.5$ kA/m which is a typical value for standard neodymium magnets and which is obtained from [53]. Furthermore, the magnetic permittivity μ_m is assumed to be $\mu_m = 4\pi \cdot 10^{-7}$ which is exact for vacuum and approximate for air. More details can be found in [54]. The second magnet is rotated to obtain slightly optimized results. The same kind of results can also be achieved without rotating the second magnet.

Now the magnitude of the forces are studied including how they vary with change of position, which is in the sequel denoted as stiffness. In Figure D-3 a part of the model's output is shown. This result corresponds to the magnet configuration as stated in the beginning of this section and shown in Figure D-2.

It can be seen, in the upper right plot, that there is a constant force in upward direction (from now on z-direction). This is a nice feature since it can be used to (partially) carry the weight of the chuck to relieve the actuators of the levitation controller. Furthermore it can be seen in the lower right plot that the stiffness $\partial F_z/\partial z$ can be zero so it does not influence the out-of-plane behavior.

In the upper left plot it can be seen that a constant force, which pulls the second magnet away in a in-plane direction, is present. This poses no problem since a similar construction of magnets can be mounted, to the other side of the chuck counter acting this force. As a result, the chuck will be in an equilibrium position when the forces are equal. It is more important how these forces change. Lets now look at the stiffness in y direction, defined as, $\partial F_y/\partial y$. This is shown in the lower left plot. The obtained stiffness is about 0.3 N/mm. When four of these pairs in each direction are used a stiffness larger then the required 1 N/mm is achieved. These results look promising therefore lets move on to the next step, which is the analysis of the overall effect of multiple magnet pairs on the chuck.

The idea is to place them as shown in Figure D-4. As discussed previously, each magnet pair should have an opposing pair on the other side of the chuck. Since 3 DoFs should be suspended, at least 3 sets of magnet pairs are required. For symmetry reasons because of the required in-plane stiffness, 4 sets of pairs are used. By simply adding or subtracting the forces of each pair, the total forces on the chuck can be computed.

This has been done and part of the results can be seen in Figure D-5. In the upper right plot it can be seen that there is a large force of over 4 N pushing the chuck upward while $\partial F_z/\partial z = 0$. This means that the in-plane fixation also acts as a gravity compensator which is a very nice bonus. On the down side, the stiffness $\partial F_z/\partial y$ is almost maximum which means that a movement of the chuck in the xy-plane will result in a change of force in z-direction. Unfortunately, this is not the biggest problem.

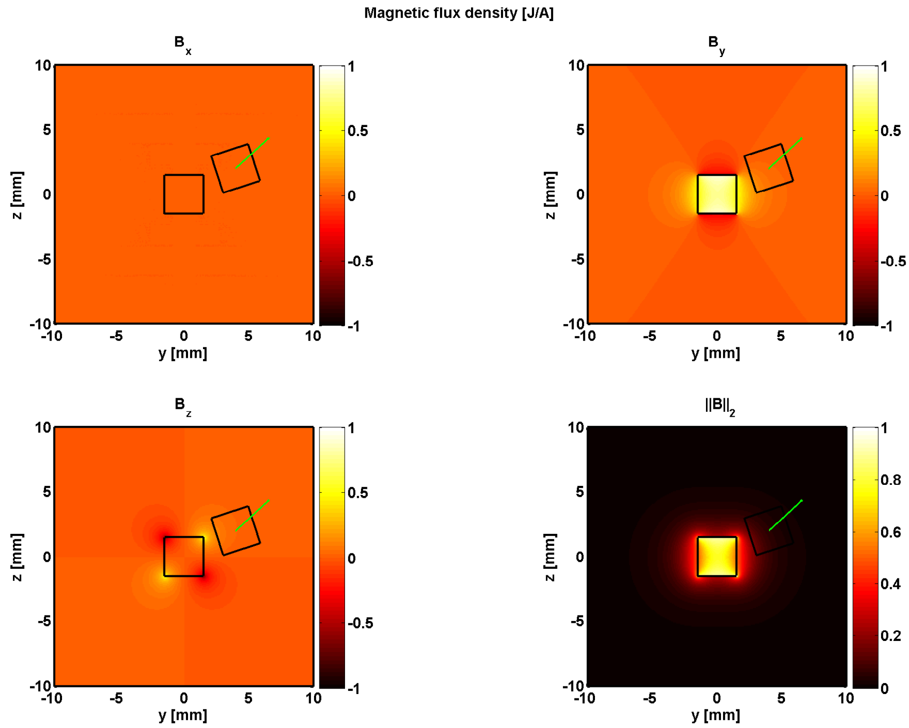

Figure D-2: *This figure shows a typical output of the model discussed in Section D-1 for a cross-sectional plane through the center of the magnet. In this case, two identical magnets of 3x3x3 mm are used. Both magnets are drawn and each magnetic flux density component of the first magnet is shown in a separate plot. Also the overall magnitude of the magnetic flux density induced by the first magnet is shown. The force experienced by the second magnet is also drawn as a green line with point of application in the center of the second magnet. This output is useful since it visualized the users input and models output which helps to detect anomalies in both the parameters and the result.*

The stiffness $\partial F_y/\partial y$ has become practically zero which means it provides no stiffness in the in-plane directions at all. This is the main function of this subsystem which is clearly not fulfilled.

The reason why $\partial F_y/\partial y$ becomes very small can be explained well. When the chuck moves in y-direction, indeed the stiffness of the four magnet pairs will try to push the chuck back. On the other side, the 4 magnet pairs responsible for the stiffness in x-direction experience a small lateral movement. When this happens, these magnet pairs start to repel the chuck further in this direction, which is actually perceived as negative stiffness in y-direction. The negative stiffness counteracts the positive stiffness resulting in a near zero in-plane stiffness.

This problem can be counteracted by making the stationary magnets wider so that the lateral movement has a smaller effect. A simulation has been done of one magnet pair where the first magnet is four times as wide. The properties of one magnet pair for this case are shown in Figure D-6. It can be seen in the lower left plot is that the in-plane stiffness of the magnet pair has decreased a lot. Because of this, the in-plane stiffness of the chuck will shown virtually no change. The reduction of the negative stiffness component is nullified by the decrease of the positive stiffness component.

When this fundamental problem became clear. No additional effort has been made to use this concept because a too in dept study, which is outside the scope of this thesis, is required to solve it since the study should include more complex shaped magnets. It has been decided to go for another, simpler concept.

D-3 Conclusion

It is time to summarize the results of the latter and repeat the conclusions.

It has been discussed that when forces between magnets are computed, the energy approach is computationally expensive. A more efficient approach is to model the second magnet as a current loop and

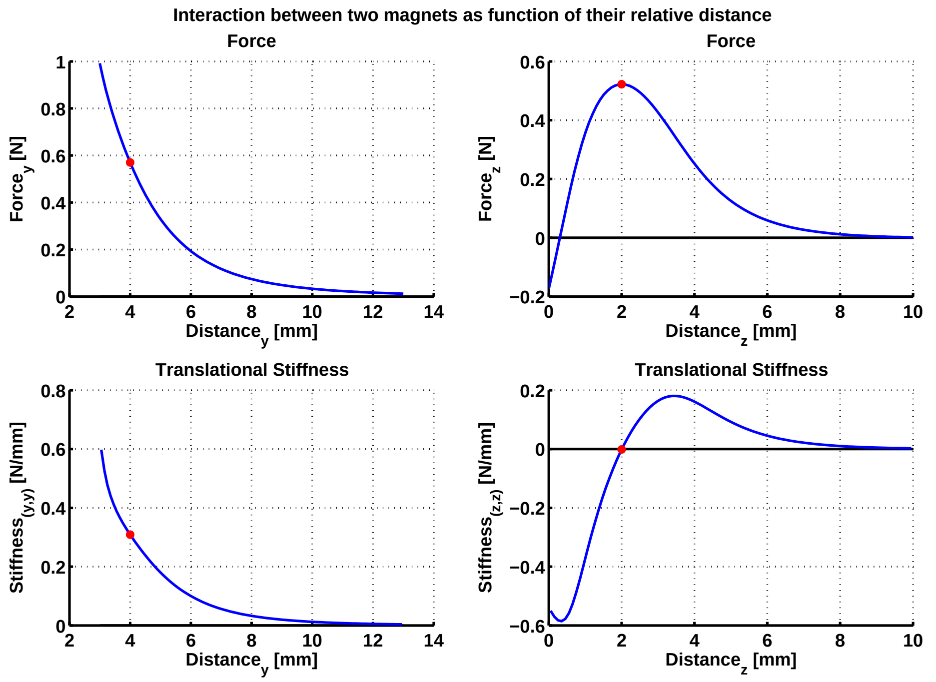

Figure D-3: *This figure shows four results as function of the relative distance between the two magnets. It shows the force in y-direction acting on the second magnet and the stiffness $\partial F_y/\partial y$ as function of distance y. It also shows the force in z-direction acting on the second magnet and the stiffness $\partial F_z/\partial z$ as function of distance z. The red dot represents the chosen work point.*

use standard equations to compute the Lorenz Forces on this current loop.

It has been shown in Section D-2, it is fundamentally difficult to create the in-plane fixation using magnets. The problem is that a magnetic pair provides stiffness in the intended direction and negative stiffness in the lateral direction. The magnet pairs are positioned at four sides of the wafer chuck and the negative stiffness cancels out the positive stiffness resulting in a (near) zero stiffness system. It may still be possible to but more complex shaped magnets must be considered, which is considered outside the scope of this research.

The stiffness in out-of-plane directions are indeed very low. In addition, a constant upward force is provided which can be used to carry a load i.e. the weight of the wafer chuck. This configuration can be deployed as gravity compensator since it provides a very low stiffness in the other directions. In order to apply it successfully as a gravity compensator, the coupled stiffness such as $\partial F_y/\partial y$ should be lowered by optimizing the design.

Because of the additional complexity and the large amount of required extra work it has been chosen not so spend additional time on this subject. It is aimed that other goals set in this thesis are also accomplished. Implementing this gravity compensator provides only a very small contribution to the work.

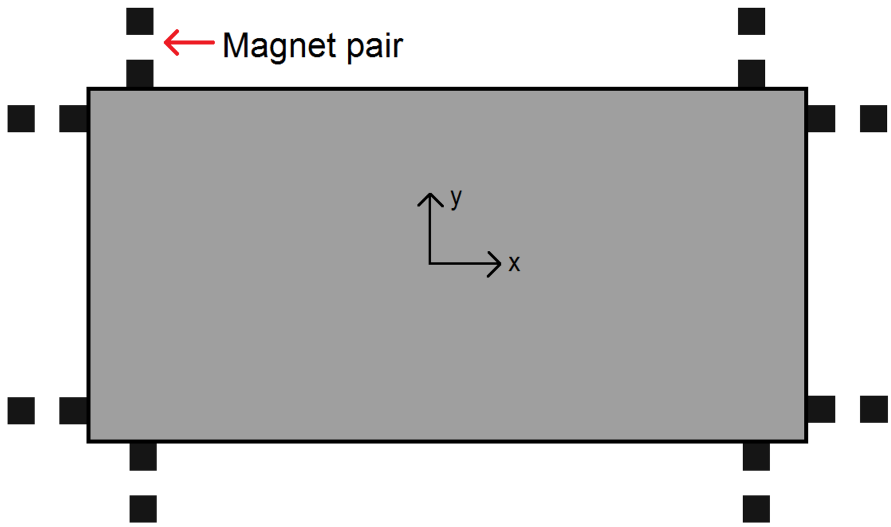

Figure D-4: *Top view of the chuck in xy-plane showing schematically the placement of the magnet pairs around the chuck.*

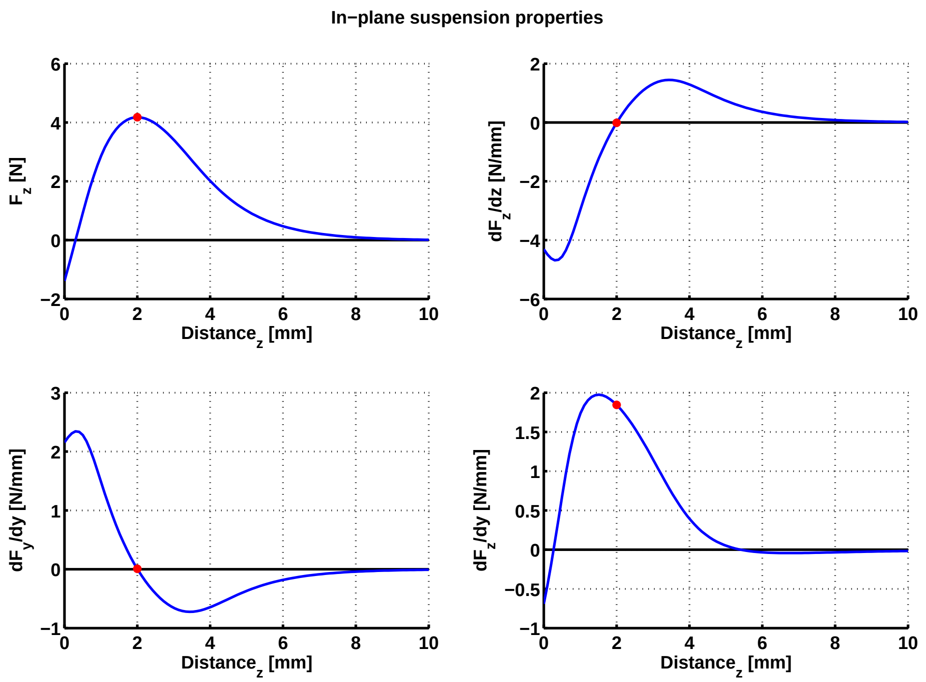

Figure D-5: *This figure shows four results as function of the relative z-distance between the two magnets. It shows the force in z-direction acting on the chuck and the stiffness $\partial F_z/\partial z$. It also shows the stiffness $\partial F_z/\partial y$ and the stiffness $\partial F_y/\partial y$. The red dot represents the chosen work point.*

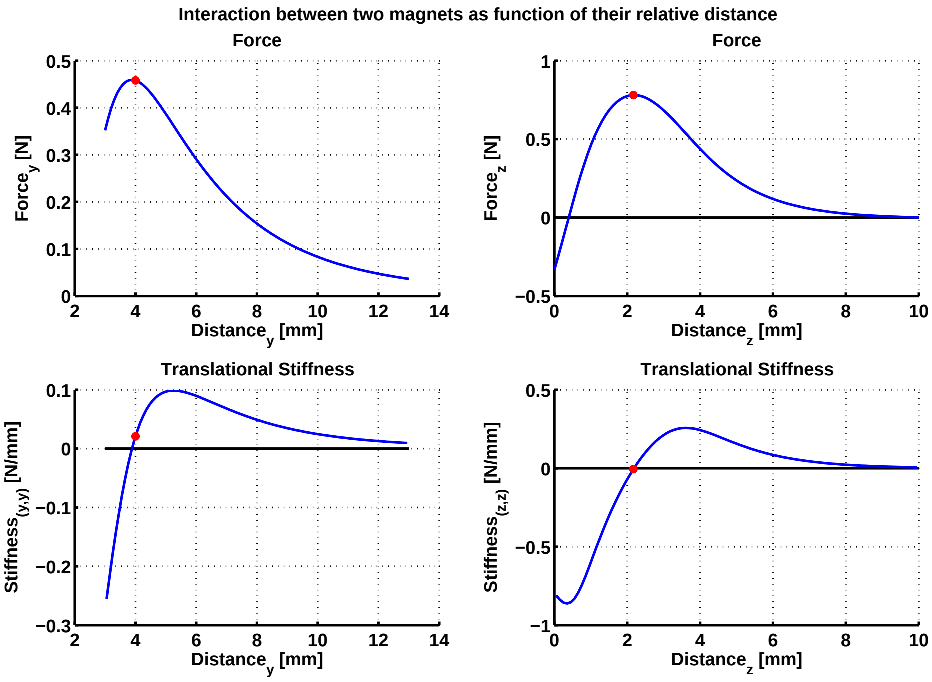

Figure D-6: *This figure shows four results as function of the relative distance between the two magnets. It shows the force in y-direction acting on the second magnet and the stiffness $\partial F_y/\partial y$ as function of distance y. It also shows the force in z-direction acting on the second magnet and the stiffness $\partial F_z/\partial z$ as function of distance z. The red dot represents the chosen work point.*

Bibliography

[1] R. Schaller, “Moore’s law: past, present and future,” *Spectrum, IEEE*, vol. 34, pp. 52–59, Jun 1997.

[2] G. Moore, “Cramming more components onto integrated circuits,” *Proceedings of the IEEE*, vol. 86, pp. 82–85, Jan 1998.

[3] “2010 update overview,” tech. rep., International technology roadmap for semiconductors, 2010.

[4] H. Butler, “Position control in lithographic equipment [applications of control],” *Control Systems, IEEE*, vol. 31, pp. 28–47, Oct 2011.

[5] V. Bakshi, *Euv Lithography*, vol. PM. SPIE Press Monograph, hardcover ed., februari 2009.

[6] J. G. Vogel, T. Arturo, J. Spronck, and R. Munnig Schmidt, “Estimation of the deformation of a plate using a limited number of sensors,” 2014.

[7] R. Mustata, M. Verhaegen, H. Ohlsson, and F. Gustafsson, “Receding horizon estimation of arbitrarily changing unknown inputs,” in *Proceedings of the 19th IFAC World Congress*, (Cape Town, Sowth Africa), pp. 5939–5944, August 24-29 2014.

[8] A. Derkevorkian, J. Alvarenga, S. Masri, H. Ryaciotaki-Boussalis, and W. Richards, “Computational studies of a strain-based deformation shape prediction algorithm for control and monitoring applications,” in *Society of Photo-Optical Instrumentation Engineers (SPIE) Conference Series*, vol. 8343 of *Society of Photo-Optical Instrumentation Engineers (SPIE) Conference Series*, Mar. 2012.

[9] A. Koevoets, J. van der Sandern, and T. Ruijl, “Thermal-elastic compensation models for position control,” in *the ASPE Annual Meeting*, 2009.

[10] F. Dai, F. Tang, X. Wang, O. Sasaki, and P. Feng, “Modal wavefront reconstruction based on zernike polynomials for lateral shearing interferometry: comparisons of existing algorithms,” *Appl. Opt.*, vol. 51, pp. 5028–5037, Jul 2012.

[11] M. Verhaegen and V. Verdult, *Filtering and System Identification; A Least Squares Approach.* Cambridge University Press, 2007.

[12] A. Alouani, T. Rice, and W. Blair, “A two-stage filter for state estimation in the presence of dynamical stochastic bias,” in *American Control Conference, 1992*, pp. 1784–1788, June 1992.

[13] G. Hostetter and J. Meditch, “Observing systems with unmmeasurable inputs,” *Automatic Control, IEEE Transactions on*, vol. 18, pp. 307–308, Jun 1973.

[14] B. Friedland, “Treatment of bias in recursive filtering,” *Automatic Control, IEEE Transactions on*, vol. 14, pp. 359–367, Aug 1969.

[15] A. Willsky and H. Jones, “A generalized likelihood ratio approach to state estimation in linear systems subjects to abrupt changes,” in *Decision and Control including the 13th Symposium on Adaptive Processes, 1974 IEEE Conference on*, vol. 13, pp. 846–853, Nov 1974.

[16] H. Ohlsson, F. Gustafsson, L. Ljung, and S. Boyd, “State smoothing by sum-of-norms regularization,” in *Decision and Control (CDC), 2010 49th IEEE Conference on*, pp. 2880–2885, Dec 2010.

[17] S. Gillijns and B. D. Moor, “Unbiased minimum-variance input and state estimation for linear discrete-time systems with direct feedthrough,” *Automatica*, vol. 43, no. 5, pp. 934 – 937, 2007.

[18] G. van der Veen, J.-W. van Wingerden, M. Bergamasco, M. Lovera, and M. Verhaegen, "Closed-loop subspace identification methods: an overview," *Control Theory Applications, IET*, vol. 7, pp. 1339–1358, July 2013.

[19] L. Ljung, "Perspectives on system identification," in *In Plenary talk at the proceedings of the 17th IFAC World Congress, Seoul, South Korea*, 2008.

[20] S. J. Qin, "An overview of subspace identification," *Computers and Chemical Engineering*, vol. 30, no. 10-12, pp. 1502 – 1513, 2006.

[21] P. Van Overschee and B. De Moor, "A unifying theorem for three subspace system identification algorithms," in *American Control Conference, 1994*, vol. 2, pp. 1645–1649 vol.2, June 1994.

[22] A. Sayed, V. Nascimento, and S. Chandrasekaran, "Estimation and control with bounded data uncertainties," *Linear Algebra and its Applications*, vol. 284, pp. 259 – 306, 1998. International Linear Algebra Society (ILAS) Symposium on Fast Algorithms for Control, Signals and Image Processing.

[23] K. Schubert, *A New Look at Robust Estimation and Identification.* University of California, Santa Barbara, 2003.

[24] M. Pilanci, O. Arikan, B. Oguz, and M. . Pinar, "Structured least squares with bounded data uncertainties.," in *ICASSP*, pp. 3261–3264, IEEE, 2009.

[25] I. Markovsky and S. Van Huffel, "Overview of total least-squares methods," *Signal Process.*, vol. 87, pp. 2283–2302, Oct. 2007.

[26] Chandrasekaran, "Parameter estimation in the presence of bounded data uncertainties," *SIAM Journal on Matrix Analysis and Applications*, vol. 19, pp. 235–252, 1998.

[27] I. CVX Research, "Software for disciplined convex programming." `http://cvxr.com/`. [Online; accessed 1-nov-2014].

[28] N. Kalantarova, M. A. Donmez, and S. S. Kozat, "A Novel Robust Approach to Least Squares Problems with Bounded Data Uncertainties," *ArXiv e-prints*, 2012.

[29] Y. Kerboua, A. Lakis, M. Thomas, and L. Marcouiller, "Hybrid method for vibration analysis of rectangular plates," *Nuclear Engineering and Design*, vol. 237, no. 8, pp. 791 – 801, 2007.

[30] J. G. Vogel, "Matlab implementation of a finite-element model of a uniform flat plate," 2014.

[31] J. G. Vogel, "Mass spring systems,." Lecture notes, 2013.

[32] P.-O. M. Lionel Zoghaib, "Damping analysis of a free aluminum plate," *Journal of Vibration and Control, SAGE Publications (UK and US)*, 2013.

[33] R. M. Schmidt, G. Schitter, and J. van Eijk, *The design of high performance mechatronics.* Delft University Press, 2011.

[34] R. R. S. Michael S. Hons, "Transfer functions of geophones and accelerometers and their effects on frequency content and wavelets," tech. rep., CREWES Research Report, 2006.

[35] "Geospace technologies geophones gs-11d." `http://www.geospace.com/geophones-gs-11d/`, 2014. [Online; accessed 13-nov-2014].

[36] R. C. Hibbeler, *Mechanics of Materials.* Pearson Prentice Hall, 2005.

[37] A. W. Leissa, "The free vibration of reactangular plates," *Journal of Sound and Vibration*, vol. 31, no. 3, pp. 257–293, 1973.

[38] T. E. ToolBox, "Typical poisson's ratios for some common materials." `http://www.engineeringtoolbox.com/poissons-ratio-d_1224.html`, 2014. [Online; accessed 15-okt-2014].

[39] M. K. Technology, "Bm-4 bench top vibration isolation platform." `http://www.minusk.com/products/bm4-vibration-isolation-platforms-bench-tops.html`, 2014. [Online; accessed 16-okt-2014].

[40] D. Fellowes, “Kinematic and quasi-kinematic constraints what they are and how they work,” tech. rep., University of Arizona, 2006.

[41] Moticont, *Linear voice coil motor.* lvcm-016-013-01 Rev. 1.

[42] S. van Veen, “Planar ferrofluid bearings for precision stages,” Master’s thesis, Delft University of Technology, 2013.

[43] G. van der Veen, *Identification of wind energy systems, PHD Thesis.* PhD thesis, Delft University of Technology, 2013.

[44] G. D. Allen, “Lectures on linear algebra and matrices,” tech. rep., Texas A&M University, 2003.

[45] L. El Ghaoui, “Inversion error, condition number, and approximate inverse of structured matrices,” *Linear Algebra and its Applications*, vol. 343-344, no. 1-3, pp. 171–193, 2002.

[46] L. Precision, “Capacitive sensor operation and optimization,” tech. rep., Lion Precision, November 2012.

[47] E. T. Group, “Technical introduction and overview.” `http://www.ethercat.org/en/technology.html`, 2014. [Online; accessed 14-okt-2014].

[48] “Ethercat configurator tutorial.” `http://http://ethercat.wiki-site.com/index.php/Main_Page`, 2014. [Online; accessed 14-okt-2014].

[49] H. Bleuler, “A survey of magnetic levitation and magnetic bearing types,” *JSME international journal. Ser. 3, Vibration, control engineering, engineering for industry*, vol. 35, pp. 335–342, sep 1992.

[50] S. Earnshaw, “On the nature of the molecular forces which regulate the constitution of the luminiferous ether.,” *Transactions of the Cambridge Philosophical Society*, vol. 6-8, pp. 1837–1846, 1839.

[51] X. Gou, Y. Yang, and X. Zheng, “Analytic expression of magnetic field distribution of rectangular permanent magnets,” *Applied Mathematics and Mechanics*, vol. 25, no. 3, pp. 297–306, 2004.

[52] D. J. Griffiths, *Introduction to Electrodynamics (3rd Edition).* Benjamin Cummings, 1998.

[53] www.Supermagnete.nl, “Physical magnet data.” `http://www.supermagnete.nl/eng/data_table.php`, 2014. [Online; accessed 9-okt-2014].

[54] P. Tipler and G. Mosca, *Physics for Scientists and Engineers.* No. pts. 1-33 in Physics for Scientists and Engineers, W. H. Freeman, 2007.

Index

Nomenclature

List of Acronyms

ADC	Analog to Digital Converter
DCSC	Delft Center for Systems and Control
DoFs	Degrees of Freedom
ICs	Integrated Circuits
LS	Least Squares
MIMO	Multiple Input Multiple Output
MSc	Master of Science
MSD	Mechatronic System Design
NI	National Instruments
OLS	Ordinary Least Squares
P-P	Peak-to-Peak
PBSID	Predictor Based Subspace IDentification
PME	Precision and Microsystems Engineering
PoI	Point of Interest
RHI	Receeding Horizon Input
RLS	Robust Least Squares
RMS	Root Mean Square
S&C	Systems and Control
SID	System IDentification
SVD	Singular Value Decomposition
ZMWN	Zero Mean White Noise
ZoH	Zero-Order Hold

List of Names

In-Plane	The DoFs acting within the chuck's plane.
Levitation controller	Controller positioning the 3 levitated DoFs of the chuck.

LS data matrix	Matrix A in a least squares problem $\min_x \|Ax + b\|_2^2$.
LS measurement vector	Vector b in a least squares problem $\min_x \|Ax + b\|_2^2$.
Out-of-Plane	The DoFs acting out of the chuck's plane.

List of Symbols

$(\cdot)^{-1}$, $(\cdot)^{\dagger}$	Respectively the inverse and left-pseudo inverse when operated on a matrix.
$\delta(\cdot)$	Operator giving the magnitude of the uncertainty on the elements of its operant.
ℓ, m, g	The amount of respectively: outputs, unknown inputs and known inputs.
$\forall(\cdot)$	All entries in the set of its operand.
$\hat{\cdot}$	The hat denotes an estimate of the variable above which it is drawn.
$\hat{a}$	The hat denotes an estimate of the variable a.
$\in$	Belongs to.
∞	Infinity.
$\mathbb{N}^0$, $\mathbb{N}^+$	The set of all natural numbers respectively starting from zero and starting from 1.
$\mathbb{R}$, $\mathbb{R}^a$, $\mathbb{R}^{a\times b}$	Respectively, the set of all real-valued scalar numbers, real-valued a-dimensional vector and real-valued a by b matrices.
$\mathrm{vec}(\cdot)$	Column wise vectorization of a matrix.
$\otimes$	Kronecker product.
Φ, $\tilde{B}$, C, D	State Space system in predictor form.
$\star$	A (block) value of no interest.
$\times$	Denotes cross product between two vectors.
A, B, C, D	State Space matrices.
E, G	State Space matrices corresponding to known inputs.
e, v, w	Zero mean white noise sequences.
K	Kalman Gain.
n	State Space model order.
r, $\bar{r}$	Respectively output residual and transformed output residual corresponding to the RHI estimator.
x, $\tilde{x}$	State Space system state.
y, u, b	Respectively the: measured outputs, unknown inputs and known inputs.